ADVANCED FIBRE REINFORCED MATERIAL: NON-CRIMP COMPOSITES

KWAME ANANE-FENIN

Submitted in Partial Fulfilment of the Requirement for the Degree of

Doctor of Philosophy

in

Mechanical Engineering

Department of Mechanical Engineering Science

in the Faculty of Engineering and the Built Environment

University of Johannesburg

South Africa

Supervisor: Professor Esther T. Akinlabi

Co-Supervisor: Professor Nicolas Perry

June, 2020

DECLARATION

I, **Kwame Anane-Fenin**, hereby declare that the research work undertaken in this thesis, is my own original research except where otherwise indicated with appropriate reference(s). Furthermore, this thesis has not been previously submitted in full or partial fulfilment of the requirements for an equivalent qualification at any other educational institution.

DEDICATION

I dedicate this thesis to my dear wife Betty, our two lovely children Paakofi and Maame Ama, and to the loving memory of my mother, Mama Fau.

ACKNOWLEDGEMENTS

"I will give thanks to you, LORD, with all my heart; I will tell of all your wonderful deeds" -Psalm 9:1.

My sincerest appreciation goes to my two supervisors, Professor Esther Titilayo Akinlabi and Professor Nicolas Perry for their insightful guidance, constructive criticisms, encouragement and support during every phase of the study period; they have contributed immensely to all the publications that have emerged out of this research. I would also like to express my profound gratitude to Professor Esther Titilayo Akinlabi for her academic mentorship, exemplary leadership and for facilitating access to the best laboratories in the world - ensuring the successful completion of this research.

I am very grateful to Professor Peter Olubambi who facilitated my first receipt of financial support from NRF. I am also profoundly grateful to Dr Stephen Akinlabi for his encouragement and support given through the provision of essential experimental tooling and reagents without which this research would not have been possible. Special gratitude also goes to members of Modern and Advanced Manufacturing System (MAMS) Research group, especially Dr Patrick Mubiayi, Dr Samuel Fatoba, Dr Samson Masebinu, Dr Frederick Madaraka and Mr Michael Olayinka Abegunde, for showing substantial interest in this research through the editing of manuscripts, insightful discussions and continued check-ups on my progress. These cherished interactions led to further refinement of the thesis. To Mr Samuel Nunu, thank you very much for the immense assistance you provided with the SEM and EDX analyses. I also need to mention the contribution of Mr Pesanai Zanamwe who provided valuable comments on manuscripts and granted me access to his laboratory. I especially want to express my appreciation to Mr Damenorty Richard Akwada for standing with me through

difficult times, spending late hours in the laboratory together, being a brother and my academic confidant; we started this academic journey together and we finished together.

I am immensely thankful to the National Research Foundation (NRF) of South Africa for their financial support. I also wish to express my profound gratitude to Saertex South Africa Ltd for donating the non-crimp fabrics used for this research; this gesture greatly influenced the successful completion of my thesis.

I would like to acknowledge the contribution of Prof Akindele Odeshi, my academic host at the University of Saskatchewan, Saskatoon Canada. The opportunity to work in your world-class laboratory was critical to my research. I am also grateful to his PhD students; Mr Tayo for his guidance and assistance with the pyrolysis equipment, and Mr Rahim for the SEM analysis. My sincerest appreciation goes to Prof Ramaswami Sammynaiken, Dr Jianfeng (Peter) Zhu and Mr Jason Maley at the Saskatchewan Structural Science Centre for the technical advice, insightful discussions and assistance with the XRD and Raman spectroscopy analysis. The experience of interacting with such seasoned researchers in a state-of-the-art facility was pivotal to the quality and depth of the research.

Special gratitude goes to my parents, Dr Kofi Anane-Fenin, who has inspired me to strive for academic excellence from childhood. To my mother - Mrs Faustina Anane-Fenin (1948-2012), who was my greatest cheerleader and instilled in me the virtues of patience and endurance; I really miss you. To my second mother – Dr (Mrs) Janet Anane-Fenin, you have restored peace and joy in our lives; I am truly grateful for your prayers and support. My appreciation goes to my in-laws, Professor and Mrs James Adu Opare, for continued encouragement, constant prayer, and support. I also acknowledge my siblings, Dr (Mrs) Ekua Bentil, Mrs Adwoa Baidoo-Williams, and Miss Effie Koomson: I appreciate all your sacrifices, prayers and support.

Finally, and most importantly, I would like to express special appreciation to the most important woman in my life, my dear wife Dr (Mrs) Betty Akua Oparebea Anane-Fenin for being my greatest supporter, motivator and prayer partner, and for showering me with love during tough times. I sincerely appreciate you. To my lovely children - Paakofi and Maame Ama, I thank you for understanding why daddy had to be away for some time. You are my pride and joy; I love you all.

ABSTRACT

Non-crimp fabric (NCF) composites combine the superior in-plane properties of unidirectional pre-impregnated tape (UDPT) and excellent out-of-plane properties of woven fabrics without their associated drawbacks of high manufacturing cost and crimping respectively. Research on such novel composite materials have mostly been parochial and focused on improving either the matrix or the reinforcement. The aim of this thesis is therefore to present a holistic and multifaceted study (in a life cycle vision of the composite) addressing the critical factors of matrix modification, dispersion quantification, testing optimisation and fibre reclamation from waste.

Opencast moulding and vacuum-assisted resin transfer moulding (VARTM) were applied in the fabrication of three (3) sets of composite plates, namely silane functionalised Titanium dioxide (TiO_2) samples, samples with non-functionalised TiO_2, and samples without TiO_2 nanoparticles. TiO_2 was chosen because of its unique chemical and physical properties such as, electrical, UV absorption, corrosion resistance, superior photocatalytic activity, photostability, and refractive index. Several characterisations to evaluate the influence of silane treatment on the mechanical and thermal properties of the NCF composites were performed. The tests conducted on the samples included impact testing, microstructural analysis, and thermogravimetric analysis (TGA). Additionally, two new approaches using gap statistics and fractal dimension were developed for quantifying the state of TiO_2 dispersion within the nanocomposite. Taguchi design of experiment, multiple response and genetic algorithm optimisations were explored for optimisation of tensile testing through the selection of optimal tab configurations. The end of life and fibre recovery were also evaluated. Pyrolysis and oxidation were used to recycle and recover carbon fibre from the NCF fibre reinforced composite plates. The recovered fibres were then characterised using a scanning electron

microscope (SEM), Brunauer-Emmett-Teller (BET) analysis, TGA, elemental analysis, X-ray diffraction (XRD), and Raman spectroscopy to investigate the influence of char.

The results and analysis conclusively showed that silane functionalisation significantly improves thermal stability ($\approx 19\%$), the integral procedural decomposition temperature (IPDT) ($\approx 12\%$), the oxidation index (OI) ($\approx 85\%$), and impact absorption energy. The two new dispersion quantification methods were used to accurately show that silane treatment improved the state of dispersion while significantly reducing agglomeration. The positive impact of silane treatment can be attributed to improved particle-matrix adhesion observed in the composites.

In order to quantify the test sample parameters and sensitivity, statistical analysis on tensile testing revealed that tab stiffness, tab taper angle and adhesive thickness were the most significant factors, and the optimal tab design configuration necessary for minimising stress concentration was to select lower tab stiffness and tab taper angle values while increasing the adhesive thickness. The recovery of carbon fibre from NCF composites via pyrolysis and oxidation revealed that the char after pyrolysis acted as a sacrificial protective covering over the fibres during oxidation. The oxidised fibres exhibited improved thermal stability, increased pore size, decreased surface area and reduced pore volume. In addition, crystallite thickness or stacking height (L_c) and crystallite width (L_a) obtained from XRD decreased after oxidation while the relative intensity (IR) from Raman characterisation increased.

This work contributes to the scientific body of research in polymer composites by presenting a holistic approach where characterisations and assessments are carried out from the manufacturing stage through to recycling and reclamation of reusable fibres.

Keywords: *Char; Dispersion quantification; Optimisation; Oxidation; Pyrolysis; and Silane coupling.*

TABLE OF CONTENTS

LIST OF TABLES

LIST OF FIGURES

GLOSSARY OF TERMS

Agglomeration	Refers to nanoparticles that have associated into a cluster composed of two or more nanoparticles.
Char	Carbonaceous layer that covers the surface of fibres due to the degradation of epoxy matrix after pyrolysis.
Circular economy	An economic system aimed at eliminating waste and the continual use of resources.
Cluster	A cluster refers to a collection of data points aggregated together because of certain similarities.
Composite materials	A material that has two or more distinct phases or constituents
Crimping	When warp and weft yarn interlace in fabric, they follow a wavy path.
Desirability index	A means for complexity reduction of multivariate quality optimization
Dispersion	The action or process of distributing things or people over a wide area
Drapeability	The spherical deformability of textile planar material without structural folds
Epoxy resin	A class of reactive prepolymers and polymers which contain epoxide groups
Finite Element Analysis	the simulation of any given physical phenomenon using the numerical technique called Finite Element Method
Fractal dimension	A ratio providing a statistical index of complexity comparing how detail in a pattern changes with the scale at which it is measured.
Fracture toughness	A property which describes the ability of a material to resist fracture
Functionalisation	The process of adding new functions, features, capabilities, or properties to a material by changing the surface chemistry of the material
Gap statistic	A standard method for determining the number of clusters in a set of data.
Hydrophobicity	The physical property of a molecule that is seemingly repelled from a mass of water

Image Segmentation	The process of partitioning a digital image into multiple segments
Impact energy	The energy required to break the material
Interfacial adhesion	Adhesion in which interfaces between phases or components are maintained by intermolecular forces, chain entanglements, or both, across the interfaces.
K-Mean algorithm	It identifies k number of centroids, and then allocates every data point to the nearest cluster, while keeping the centroids as small as possible.
Matrix	A homogeneous and monolithic material in which a fibre system of a composite is embedded
Morphology	the study of the forms of things
Nanocomposites	Nanocomposites are materials that incorporate nanosized particles into a matrix of standard material.
Nanoparticles	particles between 1 and 100 nanometres (nm) in size with a surrounding interfacial layer
Optimisation	the selection of a best element from some set of available alternatives
Oxidation	A process in which a chemical substance changes because of the addition of oxygen.
Polymer	It is a chemical compound with molecules bonded together in long repeating chains
Preforms	Form or shape beforehand or determine the shape of beforehand
Pyrolysis	The thermal decomposition of materials at elevated temperatures in an inert atmosphere.
Recycling	The process of converting waste materials into new materials and objects.
Refluxing	A technique involving the condensation of vapours and the return of this condensate to the system from which it originated
Resin	A solid or highly viscous substance of plant or synthetic origin that is typically convertible into polymers
Silane coupling agent	A class of organosilane compounds having at least two reactive groups of different types bonded to the silicon atom in a molecule
Solvolysis	The degradation of resin with the application of a solvent

Stress concentration	The accumulation of stress in a body due to sudden change in its geometry
Tab	Object used to cushion against grip loading during mechanical characterisations
Thermal stability	Ability of a material to resist the action of heat and to maintain its properties
Thermoplastic polymer	A polymer that, when heated, becomes liquid, so it can be easily formed in any desired shape.
Thermosetting polymer	A polymer that is irreversibly hardened by curing from a soft solid or viscous liquid prepolymer or resin
Warp knitting	A process whereby knitting loops are generated in the direction of production
Weft threads	
Wettability	The tendency of one fluid to spread on, or adhere to, a solid surface in the presence of other immiscible fluids

ACRONYMS AND ABBREVIATIONS

D_0	Dispersion quantity (Fractal dimension)
D_p	Dispersion parameter
G_0	Gap factor
L_a	Crystallite width
L_c	Crystallite thickness or stacking height
PSD_1	Particle spacing dispersity
PSD_2	Particle size dispersity
σ_x	Normal stress concentration
σ_y	Peel stress
τ_{xy}	Shear stress
ACARE	Aviation Research and Innovation in Europe
Al_2O_3	Alumina
ANOVA	Analysis of variance
APTMS	3-aminopropyltrimethoxysilane
BET	Brunauer-Emmet-Teller
C/N	Carbon to nitrogen ratio
CF-NE	NCF carbon fibre reinforced composite
CF-STN	NCF carbon fibre reinforced composite with TiO_2 inclusion
CNT	Carbon nanotubes
CO_2	Carbon dioxide
DTG	Derivative thermogravimetry
EDX	Energy dispersive X-ray
EoL	End of Life
FEM	Finite element method
FTIR	Fourier-transform infrared spectroscopy
FVF	Fibre volume fraction
FWHM	Full width at half maximum
GA	Genetic algorithm
H_2	Hydrogen
H_2S	Hydrogen sulphide
IPDT	Integral procedural decomposition temperature
IPTMS	3-Isocyanatopropyltrimethoxysilane
KM	Kinematic mapping

KOH	Potassium hydroxide
LCM	Liquid composite moulding
MEK	Methyl ethyl ketone MEK
MPS	3-methacryloxypropyl-trimethoxysilane
MTN	Methanol treated TiO_2
N_2	Nitrogen gas
Na	Sodium
NCF	Non-crimp fabric
NE	Neat epoxy
NH_3	Ammonia
Ni	Nickel
O and O_2	Oxygen
O/C	Oxygen content
OI	Oxidation index
PDI	Polydispersity index
PEEK	Polyetheretherketone
PMMA	Poly(methyl methacrylate)
PY-CHAR	Char covered fibres after pyrolysis
PY-CHAR-OX	Clean fibre after oxidation in air
RPSD	Radial power spectral density
RTM	Resin Transfer Moulding
SEM	Scanning Electron Microscopy
S_iO_2	Silica
SPM	Scanning probe microscope
STN	Silane functionalised TiO_2 nanocomposite
TEM	Transmission electron microscope
TGA	Thermogravimetric analysis
T_iO_2	Titania
TN	Non-functionalised TiO_2 nanocomposite
UDPT	Unidirectional Pre-impregnated Tape
UHMWPE	Ultra-high-molecular-weight polyethylene
UV	Ultraviolet
VARTM	Vacuum Assisted Resin Transfer Moulding
VF	Virgin fibre
VF-OX	Oxidised virgin fibre
XPS	X-ray photoelectron spectroscopy

XRD	X-ray Diffraction
D	Dispersion quantity (Gap statistics)
ID	$D-band$
IG	$G-band$
IR	Relative intensity
N	Aromatic layer
SN	Signal-to-noise ratio

LIST OF PUBLICATIONS

Journals

1. **K. Anane-Fenin**, E.T. Akinlabi, N. Perry, ***Quantification of nanoparticle dispersion within polymer matrix using gap statistics,*** Material Research Express. 6 (2019).
2. **K. Anane-Fenin**, E.T. Akinlabi, N. Perry, ***A Method for the Quantification of Nanoparticle Dispersion in Nanocomposites Based on Fractal Dimension***, Advances in Material Sciences and Engineering, Springer (2020) 555–564.
3. **K. Anane-Fenin**, E.T. Akinlabi, N. Perry, ***A Numerical and Statistical Approach for Optimization of Tab Design for Non-Crimp Fabric Composites***, Procedia Manuf. 35 (2019) 820–825
4. K. Anane-Fenin, E.T. Akinlabi, N. Perry, ***Carbon Fiber Surface Treatment for Enhanced Interfacial Properties: A Review***, Trends in Manufacturing and Engineering management, springer (2020). **Accepted**
5. **K. Anane-Fenin**, E.T. Akinlabi, N. Perry, ***The Effect of Silane Treated TiO2 Nanoparticles on The Thermal Performance of Polymer Composites***, Procedia CIRP (2020). **Accepted**
6. K. Anane-fenin, E.T. Akinlabi, N. Perry, ***Carbon Fiber - The Platform for Energy Storage in Batteries,*** A Review, Procedia CIRP (2020). **Under review**

Book Chapter

7. **K. Anane-Fenin**, E.T. Akinlabi, N. Perry, ***Optimization Methods for Minimizing Induced Stress During Tensile Testing of Prosthetic Composite Materials***, in: K. Kumar, J. P. Davim, (eds.), Design, Development, and Optimization of Bio-Mechatronic Engineering Products, IGI Global, USA (2019) pp. 180–206.

Peer Reviewed Conference Papers

8. **Anane-Fenin, K**., Akinlabi, E. T and Perry N, ***Quantitative Assessment of Nanoparticle Dispersion in Nanocomposites-A Review***, In: Third International Conference on Composites, Biocomposites and Nanocomposites (ICCBN 2018), Nelson Mandela Bay Stadium, Port Elizabeth, South Africa, 7-9 November 2018.
9. **Anane-Fenin, K.**, Akinlabi, E. T and Perry N, ***E-Waste Mining, An Alternative to Traditional Mining*** In: Africa, DII Conference: An International Conference on

Infrastructure Development and Investment Strategies for Africa, Livingstone, Zambia, 20 August – 1 September 2017.

10. **Anane-Fenin, K.**, Akinlabi, E. T and Perry N, ***Recycling of Fibre Reinforced Composites***, In: An International Conference on Infrastructure Development and Investment Strategies for Africa, Livingstone, Zambia, 20 August – 1 September 2017.
11. **Anane-Fenin, K.**, Akinlabi, E. T and Perry N, ***Accessing the Global Engineering Market Through Diversification of the Ghanaian Textile Industry***, in: 5th International Conference on Infrastructure Development in Africa, Johannesburg, South Africa, 10-12 July 2016.
12. Anane-Fenin, K., Akinlabi, E. T and Perry N, ***Nanotechnology and Bamboo Fibres as Avenues to Rejuvenate the Ghanaian Textile Industry***, 5th International Conference on Infrastructure Development in Africa, Johannesburg, South Africa, 10-12 July 2016.

CHAPTER ONE

INTRODUCTION

1.1 Background of the Study

The demand for light-weight but durable products has fuelled great interest in polymer composite as an alternative to conventional material in the industrial sector due to its ease of manufacture, low cost, and the possibility of optimising properties[1–5]. The category of composites leading this revolution is non-crimp fabric-based composites (NCF). In 1983 the first non-crimp fabrics (NCF) was manufactured from $\pm 45°$ plies knitted together to form a double bias fabric. Phillips [6] defines NCF ply construction as, "a textile structure constructed out of one or more laid parallel non-crimped non-woven thread plies, which are differently oriented, with different yarn densities of single thread plies and in which integration of fibre fleeces, films, foams, or other materials is possible". NCF-based composites evolved as a compromise between woven fabrics and unidirectional pre-impregnated tape (UDPT) and is distinguishable by the use of stitching. It possesses the outstanding out-of-plane properties of woven fabrics such as excellent drapeability while avoiding the problem of crimping. NCF-based composites also have the advantage of possessing the in-plane properties of UDPT but are less tedious and less expensive to manufacture.

Mechanical characterisations such as tensile and compressive testing for NCF polymer composites usually require the implementation of bonded tabs due to the low transverse compressive stress typical of such materials [7]. The existing literature on optimising these tests to minimise stresses is mostly purely experimental with some form of accompanying finite element analysis [8–13]. The implementation of advanced optimisation techniques such as genetic algorithms is not extensively explored.

The superior benefits of polymer composites make the need for control and enhancement of its mechanical, physical and chemical properties imperative. Matrix modification with nanoparticles to improve the properties of NCF composites have been extensively researched. TiO_2 nanoparticles has received a lot of interest in recent times due to their peculiar chemical, electrical, UV absorption, corrosion resistance, superior photocatalytic activity, photostability, and refractive index properties [14–18]. The incorporation of TiO_2 nanoparticles as reinforcement in polymer matrices has been successfully achieved by several researchers [17,19–24]. However, the inherently large surface area to volume ratio of the nanoparticles present a strong affinity for agglomeration [23]. Improvements to mechanical properties have only been achieved when nanoparticles are homogeneously distributed using mechanical or high-speed stirring [25], sonication [26,27], high shear mixing or melting [28,29], incorporating surfactants or compatibilisers [30] and casting solvents [31] and ultrasonic dispersion [32]. However, most of the available literature investigates non-functionalised TiO_2 nanoparticles, which makes achieving homogeneity extremely difficult. This provides a gap in the literature for examining the influence of functionalisation agents such as silane on the thermal, mechanical and fracture mechanics of the composite.

The thermal stability of epoxy-based nanocomposites, in particular, is known to be highly dependent on the state of the TiO_2 dispersion in the matrix. This means that the formation of agglomerates can negatively affect effective particle-matrix bonding which causes a reduction in the thermal stability of the nanocomposite [23]. A quantitative means of assessment is therefore an important step towards understanding the effects and relationships between bulk scale functional performance and nanoscale structures in nanocomposites [33]. Furthermore, quantification establishes a direct base for correlating the properties of the composite material to a standardised measure while providing variables for optimisation [34]. A number of researchers have proposed various approaches based on randomly distributed determinants

[35], clustering [36], interparticle spacing [37], quadrant [38–42]; [43], probability [44,45], particle volume loading [46] and fractal dimension [47]. All the above approaches are either highly sophisticated, complex or too simplistic, or theoretical with severe practical limitations. Some technical drawbacks in the existing techniques include lack of agglomeration parameters, over-reliance on only free path spacing, standard deviation as the sole basis, suitability for comparison of only similar particle concentrations, and difficulties with reference sampling.

As continual research towards optimisation of composite characterisation advances, its demand and industrial applications also rises. This situation is resulting in End of Life (EoL) waste management challenges. The core principle of the circular economy concept is value addition to EoL waste via recycling and reuse. Globally, an increase in demand for carbon fibres rose from $27000\ tonnes$ in 2009 to about $116{,}000\ tonnes$ by 2021 [48], which presents a waste management challenge in scraps and EoL products. Harsh waste disposal legislatures such as the 2000/53/ EC EU Directive make it imperative that research focuses on recycling and adequate reclamation of carbon fibre from composite waste. Several recovery techniques have been researched, and the most appealing is pyrolysis [49] which is capable of recovering solid residue, liquids and gaseous by-products. The study by Mazzocchetti et al [49] is one of the few comprehensive reports on the pyrolytic recovery of CF from waste. Their research is presently the only attempt to explore the influence of char on the surface of CF although it was limited to morphological changes. Additionally, the effect of pyrolysis, oxidation and char was limited to temperatures below $650℃$. Further research is required to investigate the influence of these parameters at more elevated temperatures.

1.2 Problem Statement

Research on non-crimp fabric composites has traditionally focused on either mechanical characterisations, failure mechanisms, drapability or a combination of these factors. Based on the literature reviewed and knowledge-gap identified, three critical areas of research have

received little or no research attention with respect to NCF composites. Firstly, mechanical testing optimisations using tools such as genetic algorithms and multiple responses are scanty and have for the most part been overlooked, yet it is important to apply such optimisation tools for precise and accurate solutions and improvement of parametric conditions. Secondly, achieving a homogeneous dispersion of nanoparticles within matrices is still very difficult [32]. Thirdly, assessments of the state of dispersion in most studies are done via visual inspection of SEM or TEM images, which is very subjective.

There is progressive improvements in fabrication and testing of composite materials coupled with climate change, global warming, stricter regulations on noise and emissions, and a progressive global shift towards greener, sustainable and efficient energy sources. This has resulted in a greater demand for composite materials which is expected to reach $120{,}000\ tonnes$ in 2021[49]. The wind energy sector is the largest consumer of NCFs since it is the primary material used for the fabrication of wind turbine blades [49]. However, the high demand implies high waste output, and with stringent directives such as the 2000/53/ EC EU Directive on waste management, research into recycling and fibre recovery techniques has become critical. Comprehensive studies conducted by Mattson [50], specifically on NCF composites, do not report on waste management or recycling and fibre recovery techniques. There is in fact no literature on NCF composites at present that is holistic and captures analyses based on a circular economy or cradle to cradle approach. Furthermore, the characteristics of the recovered fibres require a detailed examination to ensure reuse.

1.3 Research Question

The key research question based on reviewed literature and the identified knowledge gaps was as follows:

How can non-crimp fabric composites be improved up to end of life utilisation through matrix modification using functionalised nanoparticles with a perspective focusing on optimisation and quality of the characterisation approaches?

1.4 Aim

The aim of this research is to investigate and develop a holistic approach for the characterisation of non-crimp fabric composites from fabrication to fibre recovery with the emphasis on matrix modification, dispersion quantification, test parameter optimisation, and pyrolysis as a viable option for recycling and fibre recovery towards establishing a circular economy.

1.5 Objectives

The research objectives include:

1. To determine the influence of silane functionalisation of TiO_2 nanoparticles on the thermal and impact properties of NCF composite;
2. To develop two methods for quantifying the state of dispersion in the TiO_2 modified matrix;
3. To investigate and compare Taguchi, Multiple response and Genetic algorithms optimisation techniques for minimising tab induced stress concentration during tensile testing;
4. To determnine the impact of pyrolytic and oxidation conditions on the recovered carbon fibre and the influence of char formation on fibre surface.

1.6 Hypothesis Statement

In this research study, silane functionalisation is expected to significantly improve the state of nanoparticle dispersion and the thermo-mechanical properties of polymer composites. During mechanical testing, it is expected that optimising the geometry and varying material characteristics will significantly reduce the induced stress concentrations and thereby improve accuracy and consistency in test results. It is also envisaged that the process of pyrolysis coupled with oxidation will effectively recover fibre from polymer composites.

1.7 Motivation

Fibre-reinforced composites are a great resource for obtaining lighter, corrosion-resistant, flexible, biocompatible and structurally optimised materials for use across multidisciplinary fields. Although standardised testing is well-established for mechanical testing, avenues for optimising the experimental process remains under-researched. There is consequently a need to explore various optimisation techniques to address the engineering problem. Modifying the matrix properties to fabricate fibre- reinforced composites through nanoparticle inclusion has been extensively researched, however, the state of dispersion which directly correlates with the obtained properties are mostly qualitatively assessed through visual inspection. Quantification techniques for accurately assessing dispersion are necessary to investigate the full potential of composites.

There is presently a drive towards a circular economy in the composite industry, and waste minimisation through recycling and re-use to complete the circle. Due to the continued rise in demand for NCF composites, coupled with an increase in End of Life (EoL) waste and the environmental implications, the significance of developing recycling and fibre recovery approaches for secondary applications cannot be overemphasised.

1.8 Scope of Study

In this research, the theoretical data analysis and laboratory work considered only non-crimp fabric composites and TiO_2 nanoparticles. Test samples were fabricated with either open cast or vacuum-assisted resin transfer moulding (VARTM) system. Pyrolysis was the only approach used for recycling the NCF carbon fibre reinforced composites; these are well reported in detail.

1.9 Contribution to Knowledge

There is limited research on the holistic assessment of non-crimp fabric composite materials from fabrication to EoL waste management. This research contributes to the scientific body of knowledge by investigating the influence of silane treated TiO_2 on the thermal and mechanical properties of NCF composites, the development of two quantification techniques for assessing the state of nanoparticle dispersion within the matrix, the application of three optimisation techniques for tab configuration design during tensile testing to minimise induced stress concentration, and finally recycling and recovery of carbon fibre NCF with the focus on the influence of pyrolytic and oxidation conditions. The effect of char on the recovered fibre is also comprehensively explored and reported.

1.10 Structure of Thesis

This thesis is organised into five chapters with a summary at the end of each chapter, presented as follows:

Chapter One: This chapter presents a general background to fibre-reinforced polymer composites with the emphasis on optimising tests for end of life waste recycling. It offers a brief highlight of the problem statement constructed from identified gaps in a critical review of the literature. The aim, objectives, hypothesis statement, motivation, delimitation of the study and contribution to the body of knowledge are outlined.

Chapter Two: This chapter presents a general and critical review of the relevant literature. It also reports on a general but comprehensive review of non-crimp fabric composites, detailing all the manufacturing techniques and attempts at optimising tensile testing. It offers three major critical reviews highlighting identified gaps in the literature. Firstly, a detailed discussion of the effects of TiO_2 nanoparticles on the matrix is reported. Secondly, the existing methods of quantifying the state of dispersion in nanocomposites is presented. Finally, a review of existing recycling methods for fibre-reinforced composites was conducted with the emphasis on pyrolysis. The chapter concludes with a critical summary of the reviewed literature and highlights the identified gaps.

Chapter Three: In this chapter, the material, experimental procedures and quantification methodologies used to achieve the aim and objectives of this research are presented. It also offers the statistical approaches used for the data analysis to assess the influence, impact and interactions.

Chapter Four: All the findings and inferred influences, the importance, correlations and impact of this research are presented and discussed in detail.

Chapter Five: This chapter presents a result-based conclusion, which captures the summarised results and their correlation and relevance to the aim and objectives of the study. All the challenges and limitations are discussed and used as foundation for formulating recommendations for future studies and developments.

CHAPTER TWO

LITERATURE REVIEW

2.1 Introduction

The application of human-made composite materials can be traced back thousands of years. Wattle-and-daub for example, is amongst the oldest composites, dating back over 6000 years [51]. Advanced application of composites, however, dates back only some three decades, specifically in the aerospace industry [52]. The present rise in the demand for and interest in composites is primarily driven by their superior advantages over conventional materials such as wood, steel and aluminium. These advantages include superior strength and stiffness, high resistance to corrosion, excellent rigidity and lightweight, and have motivated extensive applications in automobile, wind turbine, aerospace, marine and sports equipment. A definition of a composite material is provided by Tsai [53] who states that "composite materials consist of two or more constituent materials bonded together so that the gross properties of the composite are superior to those of the constituents". Agarwal et al. also define it as "a material that has two or more distinct phases or constituents" [54]. However, the term composite material is inferred only when there is a significant difference between the physical properties of each constituent phase [50]. The two primary phases, which make up a composite material, are the dispersed or reinforcing phase and the matrix phase. The matrix is the primary phase, which is characteristically homogeneous and continuous, ductile, and accommodates the reinforcement. The secondary phase is the reinforcement incorporated within the matrix in a discontinuous nature. Reinforcements have superior strengths in comparison with the matrix and can be categorised as particles (micro and nano), whiskers, platelets, continuous and

discontinuous fibres etc. Matrix materials are primarily categorised into three groups, namely ceramics, metals and polymers [55].

2.2 Non-Crimp Fabrics

Typically, non-crimp fabrics are identified as yarn stitched unidirectional plies organised in distinct orientations [56]. Phillips [6], defines NCFs as "a textile structure constructed out of one or more laid parallel non-crimped non-woven thread plies, which are differently oriented, with different thread densities of single thread plies and in which integration of fibre fleeces, films, foams, or other materials is possible". The patent number DD000000008194A was granted to Heinrich Mauersberger in 1949 for the design and manufacturing process of a novel textile material. This patent was very important because it was the first step towards the development of an engineering fabric such as a non-crimp fabric. The patent detailed the fundamental idea of producing textiles via the application of chain-stitched seams to interlink threads that are either loose fillings or drawn parallel weft. In addition, a guide rail was used for routing the weft thread intersects with chain- seam connections. Zig-zag chain stitching seams were used for fixing process direction fed threads to the unit for stitching. Furthermore, the needle puncturing position was placed within two weft threads [57]. However, in 1983 the first NCF was developed through the knitting of plies with +45°and -45° orientations [58]. There are several categories of NCFs as shown in Figure 2.1. The high reduction in manufacturing cost of NCFs can be attributed to the manufacturing process, which is an adoption of the production systems of existing traditional textile manufacturing equipment using glass, carbon, aramid or ceramic fibres. Generally, NCFs have greatly benefited from the cost-efficiency and high automation of manufacturing techniques already developed within the textile industry such as knitting, weaving and braiding to produce dry NCF preforms [50]. Non-crimp fabrics, when used as reinforcement in composite fabrication, can be categorised into

two primary steps, namely preform manufacture using textile stitching technology and moulding via liquid composite moulding (LCM).

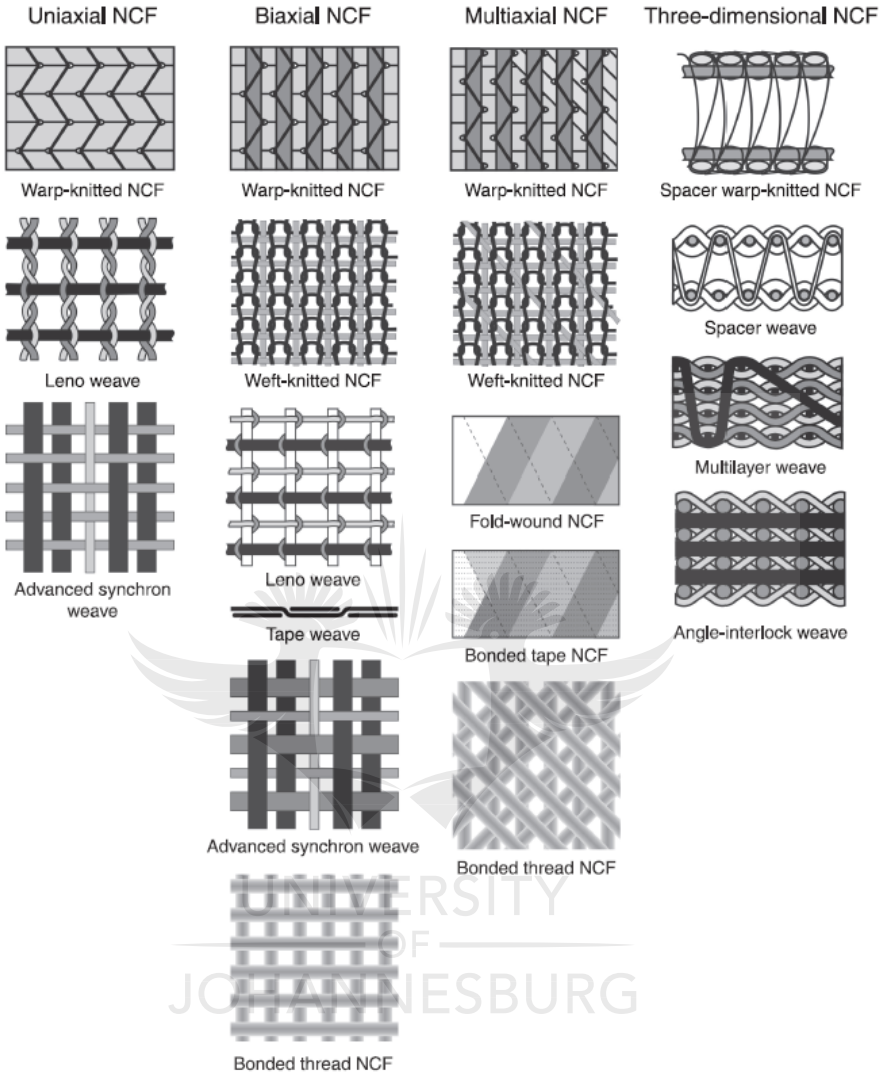

Figure 2.1 Types of Non-crimp fabrics [59]

Basically, the manufacture of preforms comprises optimal placement of non-crimp fabric tows via warp knitting using stitching yarns such as polyester or aramid [56,60,61]. Uni-, bi-, tri- and quadaxial dry preforms are manufactured using the above-stated method (Figure 2.2) followed by stacking to obtain desired thickness and geometry, and finally moulding to fabricate the component.

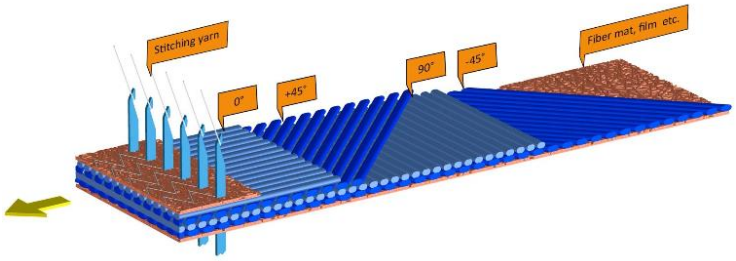

Figure 2.2 Stitching of Multiaxial NCF, source: Seuß (2014)

Warp knitting of fabrics is described as a process whereby knitting loops are generated in the direction of production. The creation of loops is carried out by compound needles carefully positioned to simultaneously move on a continuous needle bar. Several systems of yarn are necessary for the production of warp knitted fabrics [59]. During the warp knitting NCF, the formation of loops is solely for the binding reinforcement fibres or layers. Warp knitting technology and machinery are highly productive in comparison with other existing systems. The resulting warp knitted NCF has the advantage of good flexibility in terms of fibre orientation and setup of layers, however, the constraint of possessing a constant area weight and width is a limiting factor. The warp-knitting process could be coursewise or non-coursewise regarding the positioning of the thread reinforcement.

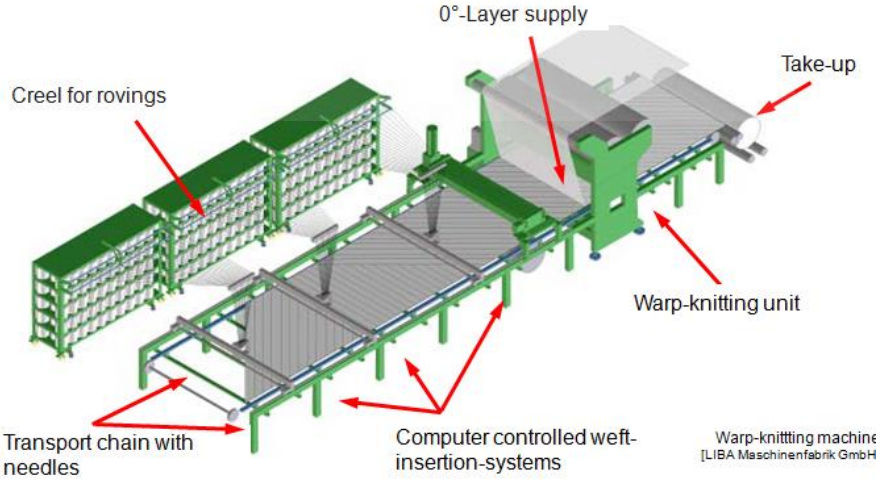

Figure 2.3 Warp-Knitting machine (diagram by Liba), source: Mattsson (2005)

A coursewise weft insertion is characterised by a single knitting loop binding both weft and warp threads while a non-course weft insertion is distinguishable by the thread positioning which is independent to the stitch length [59]. Multiaxial warp-knitting of NCFs as illustrated in Figure 2.3 is achieved with similar technology and machinery as biaxial warp-knitting however, multiaxial weft insertions are used instead of biaxial weft insertions (Arnold *et al.*, 2000; LIBA, 2007d; Parekh, 1989; Petrenz, 2009).

2.3 Non-Crimp Fabric Composite

The past six decades have seen a significant rise in the application of fibre reinforced composites in traditional mainstream industries where reductions in manufacturing cost and weight, and a high demand for flexibility in tuning properties for enhanced mechanical and structural strength, are baseline requirements [49,50,62]. Unidirectional pre-impregnated tape (UDPT) laminate intrinsically exhibit excellent in-plane properties, however, some major drawbacks are: delamination sensitivity, crack initiation and progression due to inferior interlaminar toughness during impact [63], and high fabrication cost mainly attributed to labour and storage costs [56]. The above-stated disadvantages served as inspiration for the manufacture of bidirectional woven fabrics composites, which were cheaper to manufacture, and had superior fractional toughness. Notwithstanding, woven reinforced composites exhibit out-of-plane waviness which results in significantly reduced in-plane properties in comparison to UDPT [50,64].

A third fibre reinforcement fabric was therefore developed as a compromise - bridging the excellent properties of UDPT and woven fabrics without their drawbacks of either. Non-crimp fabrics possess the enhanced drapeability of woven fabrics without the associated waviness or crimping [65] which directly contributes to lower manufacturing cost [66] and increased compressive strength [65,67].

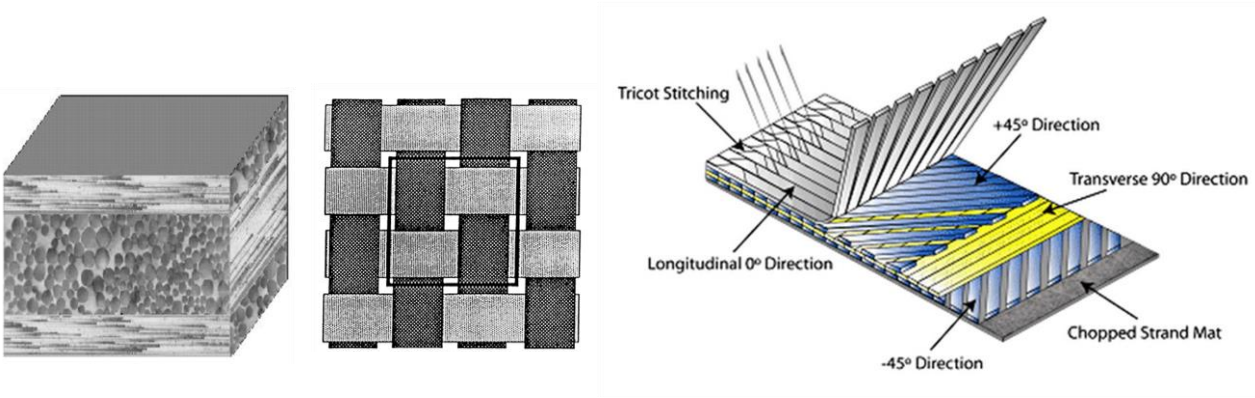

(a) (b) (c)

Figure 2.4 (a) Internal structure of UDPT [50], (b) Pain woven structure [68] and (c) Non-crimp fabric [50]

A representation of UDPT, woven and NCFs is shown in Figure 2.4 (a) (b) and (c) respectively. Furthermore, NCF reinforced composites are observed to possess improved damage tolerance and delamination resistance as a result of the stitching [69]. As alluded to earlier, the primary indicator for the transition from autoclave based UDPT to resin infusion fabricated NCF was the cost gains as presented by Bibo et al. [56] where 35% reduction in labour cost was observed for NCF composites. The cost analysis from the study further showed that in composite manufacturing, material and labour cost constituted 25% and 50% of the total cost of production respectively.

2.4 Liquid Composite Moulding Techniques

The methods developed for production of composite components are varied and can deliver products with a broad-spectrum range in quality and cost. Most composite fabrication techniques integrate systems for forming porous reinforcements into desired geometries, and then infusion with a matrix medium [64]. Nevertheless, different approaches are used to execute the two steps depending on the particular manufacturing process. The least complicated and low-cost approach is wet layup, however, the parts produced are low in quality [64,70]. Another process is via autoclave which results in products of very high quality but at a

relatively higher manufacturing cost and with bulky equipment. Liquid composite moulding (LCM) represents a category of moulding techniques, which is a compromise between wet layup and autoclave processes. This implies that parts are produced with better quality than wet layups and at a lower manufacturing cost than using autoclave. The above advantages of LCM are motivating factors for their usage in the production of the majority of composite materials [70].

LCM techniques entail soaking a fibrous material with a matrix, usually a liquid resin, and after a gelling period the composite part is formed. The process of soaking or saturation is termed infusion. A mould is normally used for the geometric shaping of the component, and the flow of the resin through the preform is accomplished through resin pressurisation and the application of a pulling vacuum or a merger of both. Several LCM variations are currently available two of which are resin transfer moulding (RTM) and vacuum assisted resin transfer moulding (VARTM) [64,71].

2.4.1 Resin Transfer Moulding (RTM) System

Resin transfer moulding (RTM) is a variant of LCM with operational procedures involving a two-sided matching mould used for forming the composite structure. Compression of the fibrous preform is carried out to create a tightly seal system using two structurally rigid moulds. Injection of a matrix, usually a thermosetting resin, is performed via at least one inlet located at different positions in the mould. To ensure effective infusion and saturation of the preforms, an injection pressure of 700 kPa is normally used [70–72]. The removal of volatiles generated during the curing of the resin can be done by connecting the outlet port to a vacuum source. Additionally, the integration of a vacuum system minimises the creation of void content and creates conditions that enables the application of lower injection pressures. Precautions must however be taken to prevent the pressure falling lower than the resin's vapour pressure to avoid the creation of voids. After the infusion is completed and the preform reaches full

saturation, the curing process is commenced via heating the mould [70–72]. The RTM process is described in Figure 2.5.

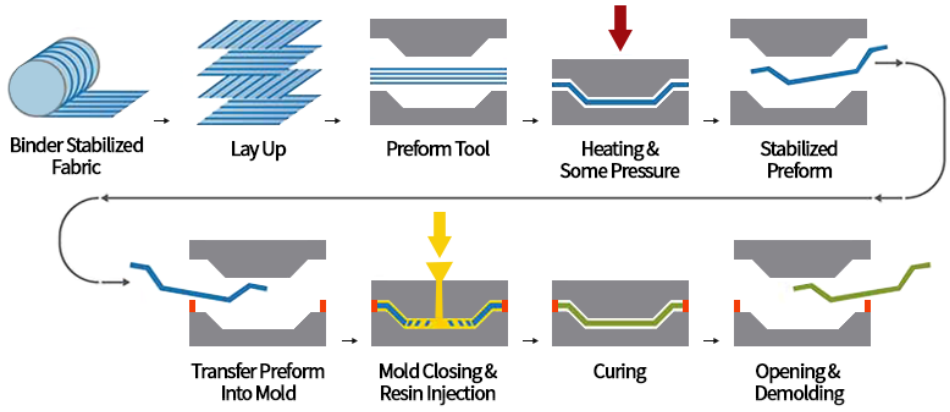

Figure 2.5 The Resin Transfer Moulding (RTM) Process [73]

RTM produces parts that are close in quality to autoclave produced components with a void content lower than 4% [74] and a high fibre volume fraction of about $60-70\%$ [75]. The use of a two-sided rigid mould ensures that the fabricated parts have high dimensional tolerance, excellent surface finish on all sides and high reproducibility. Moreover, since the injection process is conducted under pressure, reduced cycle times ($5-10\,mins$) are attainable [74] which is a motivation for adoption in large scale production of composite parts in industries such as the automotive industry [71,72]. The cost of tooling required for an RTM process is extremely high and a major drawback to mainstream adoption. The fabrication of two-sided moulds also requires high machining to tolerances plus the use of materials and designs capable of withstanding high pressures during the injection process. Furthermore, heating and pressurisation of the mould requires additional equipment [70–72].

2.4.2 Vacuum Assisted Resin Transfer Moulding (VARTM)

Vacuum assisted resin transfer moulding (VARTM) involves the use of a one-sided moulding system that sucks in the matrix material into a fibrous preform via pressurised vacuum as shown in Figure 2.6. During VARTM, a one-sided mould serves as a platform for

layering the preform before vacuum bag sealing is carried out [6,64,70]. Normally a medium with high porosity is positioned between the flexible vacuum sheet and the preform. The VARTM process has a distribution mechanism that intrinsically ensures moderate fluid flow resistance which promotes fast saturation of the mould with the resin. As the space between the mould and the vacuum bag experiences the pressure introduced by the vacuum, the atmospheric pressure outside act on the flexible vacuum bag and the fibrous preform [64,70,76]. Preform infusion is ensured by the placement of the resin inlet ports at several parts of the mould which facilitates the creation of suction force by the vacuum pressure and causing fast saturation of the preform.

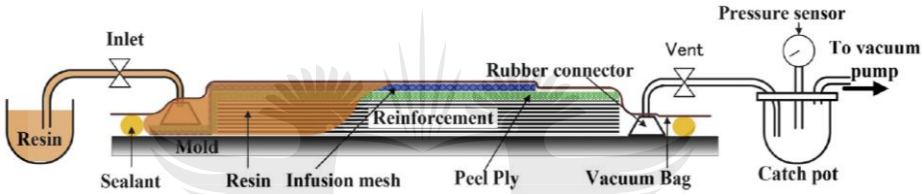

Figure 2.6 Vacuum-Assisted Resin Transfer Moulding (VARTM) [76]

In comparison to RTM the cost of tooling in VATRM is significantly less because composite fabrication is conducted on a single-sided mould, lower machining tolerances are acceptable, and cheaper. A less mechanically stiff materials can therefore be used because of the absence of high injection pressure which is a requirement for a two-sided moulding process [70]. Additionally, the presence of vacuum pressure implies that during injection and infusion of the preform with resin, the creation of void content is significantly minimised in comparison with RTM and layup processes [70–72]. The highest attainable fibre volume fraction (FVF) when fabricating with VARTM is $50 - 60\%$. The main reason for such low FVF is attributed to the low compaction pressure, limited to 1 atm, which is used for the compression of the preform during moulding [75]. The low pressure associated with the infusion process of VARTM contributes to lengthier fill and saturation times compared to the RTM process. For

large scale applications such as in wind turbine manufacture, the use of simulation programmes is often required for optimising the placement of the inlet and outlet ports primarily to ensure complete saturation of the preforms before resin curing commences [70]. Furthermore, the drawback to using a single-sided mould is that the quality of the surface finish of the vacuum sheet side is significantly inferior and of a lower tolerance than the mould side [71,72].

Even after optimising the infusion process, a challenge relating to the nature of the resin flow within the mould, which is normally inhomogeneous due to the resistance of the preform and low pressure difference, is the risk of manufacturing parts with voids and dry patches which are detrimental to the overall mechanical properties of the structure [77–80]. Therefore, to avert any possible defects from developing and to ensure efficient process control, introducing a sensor suitable for tracking and monitoring the resin flow-front evolution within the mould is vital [80]. Some of the sensors that have been applied for monitoring of the fluid flow within VARTM systems are electrical time-domain reflectometry sensors [81], pressure sensors [82] and permittivity sensors [83].

2.5 Application of Non-Crimp Fabric Composite

Non-crimp fabric composites have been applied in several fields such as the automotive, aerospace, wind and marine industries. However, there is an exponential rise in utilisation especially in the automotive, aerospace and wind power sectors. The following review therefore focuses on some significant applications in the above-stated fields. The main driving forces behind the increase in demand have been improved drapeabilty during preforming, low weight, and cheaper cost of manufacture.

2.5.1 Application in the Automotive Industry

Chevrolet pioneered the introduction of composite materials specifically with the application of glass fibre components in the design and manufacture of the Corvette in 1953. Lotus was one of the first automotive companies to successfully build a sports vehicle from glass fibre reinforced composite in 1962. Presently, NCFs are scarcely used in conventional mass production of automobile components resulting from the non-existence of reliable automated production systems [84]. Barely 5000 parts per year can be produced via resin infusion methods whereas the incorporation of automation for preforming and the moulding process will improve the rate of production to more than 50000 parts per year [59]. The limitations associated with the absence of full automation has restricted the application of NCFs to mostly high-end luxury and sports automobiles. The first reported batch manufactured NCF components were on the roof of the BMW M3 and the roof carline of the M6 [59,85]. These components were fabricated using glass fibre NCF which translated into a weight reduction of over $5kg$ compared with traditional roofs. The BMW Group, Munich, Germany, has introduced innovative approaches that apply hybrid methods for the production of components by manually gluing NCF preforms onto body-parts to enhance mechanical properties such as excellent stiffness which is required for satisfying crash standards. A typical example of the hybrid method application is the fabrication of the side frame for BMW's Hydrogen7 vehicle [85]. Lamborghini has also incorporated NCFs in the design of the boot lid of the Gallardo Spyder. For a comparative study, they also designed another boot lid with the same dimensions and geometry from aluminium. The NCF fabricated boot lid required only two (2) parts while nine (9) single parts were required when aluminium was used [85].

In Europe, the first reported use of NCF in the automotive industry was by Lotus in their 1962 sports car [59]. Non-crimp fabric composites are presently exclusively manufactured for use in high-end luxury and sports vehicles [86,87]. This is the general trend in application of

composite materials in the automotive industry. The major limiting factor for mass production of composite materials is a lack of automated systems from preform production to draping and finally moulding [59,88–90]. In the fabrication of NCF composites, the preform manufacture is the only automated section. Draping and moulding are all labour intensive. The ability to produce components with high geometric complexities is severely restricted by the drapability limitations [89]. Luxury cars are partly automated and partly manual, which means that incorporating composite materials is feasible. Increasing the current application levels for composite material use in the automotive industry however requires further investment into mitigating the limitations of draping and introducing full automation to ensure mass production possibilities without which mainstream applications will remain elusive and restricted [84].

2.5.2 Application in the Aeronautic Industry

In the aeronautic industry, the most significant motivating factors for material selection are weight reduction (which directly enhances performance) and efficiency. Composite materials are particularly suited for lightweight design applications, and further provides the requirements for complex integration of designs, superior strength-to-cost benefits, and excellent specific weight stiffness [50]. The application of composite materials in aviation can be traced to World War II particularly in the design of the British Spitfire. Hemp fibre was used for reinforcement and phenolic resins as matrix. Chronologically, glass fibre fabricated into honeycomb-core sandwich panels were introduced in 1950 while in 1960 boron/epoxy composites were developed and applied in the industry [59]. However, not until the 1970s did the introduction and application of carbon and Kevlar fibre reinforced composites within the aviation industry started gaining prominence [91]. Although aluminium, titanium and steel alloys still remain competitive materials in the dominant applications of composites materials, the drive towards sustainability, excellent mechanical and thermal properties, weight loss, efficiency and reduction in fuel consumption, and strict adherence to environmental legislation,

is contributing to higher demand and the increased significance which composite materials will assume in the future of the industry [92].

There has also been a steady rise in the percentage of composite materials over the years in the airline industry. The Airbus A340 (1990-2000) for example incorporated 17% of composite structures and components in its design while the A380 (2000-2010) model was manufactured using 25% composite parts [93]. It has been announced that the A350 XWB model which is still in production will incorporate 50% composite structures. Boeing is already leading in this regard as the Boeing 787 model consists of 50% composite components (Figure 2.7) which ultimately impacts performance and fuel consumption efficiency. The continuous and steady increase in the application of composites such as NCF is a direct consequence of the shift towards more environmentally sustainable policies, regulations and legislation from nations and institutions such as the Advisory Council for Aviation Research and Innovation in Europe [94]. Some of the set goals for the aviation industry from ACARE (2015) are curtailing carbon dioxide CO2, noise levels, and NOx by the year 2020.

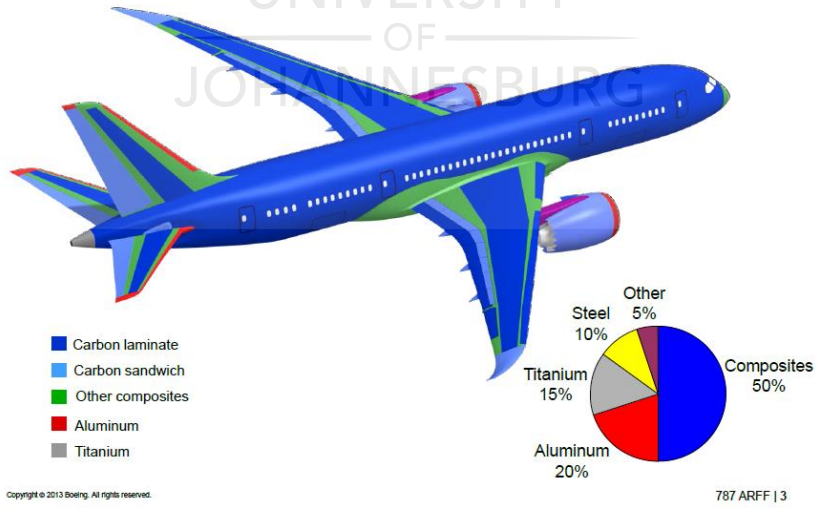

Figure 2.7 Composite content -Boeing 787 [95]

Airbus was the first to manufacture a rear pressure bulkhead (see Figure 2.8)for the commercial airlines Airbus A340-500/600. These components were fabricated with pre-

impregnated fabric, although the new design in the A380 was manufactured solely from carbon fibre NCF. It is the largest composite structural member with a dimension of $6.2mm\ X\ 5.5\ mm$ and weighs $240\ kg$. Multiaxial carbon fibre NCFs was also the main material used for manufacturing the rear cargo door of the Airbus A400M's pressurised fuselage. The aircraft is designed for the transportation of military inventories [93].

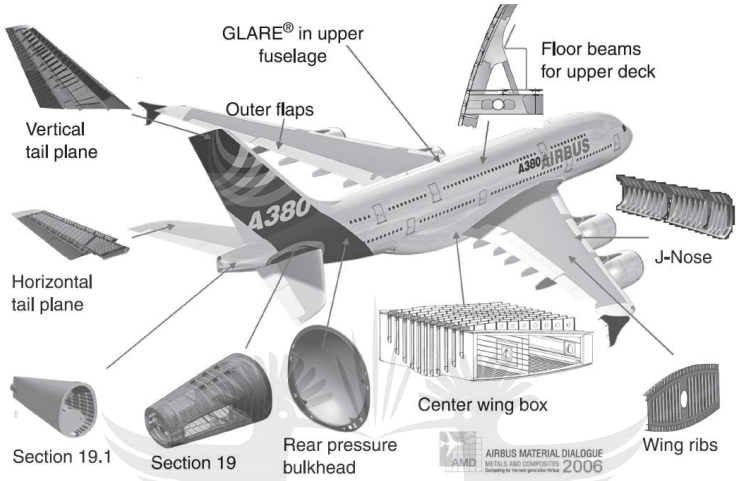

Figure 2.8 Composite application in the manufacture of Airbus A380 [96]

2.5.3 Application in the Wind Power Industry

The energy crisis in 1979 was the catalyst for the advancement of the modern-day wind energy industry. Fibre reinforced composites are highly suited for the manufacture of wind power blades because of their performance efficiency, light weight, weather and fatigue resistance, and flexibility for fabricating optimal aerodynamic shapes. In principle steel, aluminium, titanium and fibre reinforced composites (glass, carbon, aramid, Kevlar etc.) are all aerospace materials that can be used to manufacture rotor blades [97–99]. However, the basic requirements for material selection in rotor blades are excellent specific strength, modulus of elasticity, and fatigue strength. By comparison, glass/epoxy composites were observed to possess and exhibit an excellent property balance at lower cost-effective strength [100]. Fibre glass is generally known to have a low cost per unit strength and mass, and is therefore the most suited for adoption in rotor blade fabrication [101]. In a typical blade design

using NCF, the laminate build-up is normally via unidirectional, biaxial and triaxial NCF fabrics. In standard practice for normal modern rotor blades, the unidirectional NCF segment of the blade is about $50\ to\ 60\%$ of the NCF fabric [59,101]. However, in larger blade designs, triaxials are decreased in favour of $\pm 45°$ biaxial and unidirectional NCFs. Rotor shear webs are also mainly built out of $\pm 45°$ biaxial.

The wind industry is one of the largest consumers of NCF composites because its largest component (rotor blade) is made almost entirely from it. Non-crimp fabrics are often the preferred material choice because they generally address durability, cost considerations, flexibility of the manufacturing process, and suitability for the complex blade shape which is critical to the material selection [101]. In wind turbine design, specifically of rotor blades, several loading instances are incorporated in compliance with existing standards [102,103]. Significant among the loads are extreme operational loads, survival loads, and prolonged durability. The maximum load that blades can withstand in extreme conditions such as earthquakes or hurricanes is referred to as the survival load, while the maximum possible loads expected during typical workings of the turbine is termed extreme operational loads. Durability for wind turbines describes the ability to provide fail-free performance under normal circumstances throughout 20 to 25 years of standard service life [59]. Extreme design conditions are outlined in the IEC 61400 part 1[102] standards.

2.6 Matrix Modification via Introduction of Nanoparticles

2.6.1 Titanium dioxide (TiO_2) as filler in Nanocomposites

A composite material comprises a combination of reinforcement (fibre, particles or both) and matrix, which is either thermosetting or thermoplastic. Epoxy is thermosetting and widely used because of its distinguishing and excellent mechanical and thermal properties, minimal shrinkage after curing, superior chemical and corrosion resistance, and suitability for

processing under varied conditions [18]. The curing of epoxy resins leads to the formation of 3D cross-linked networks which result in brittle characteristics that limit its application [18,30]. It has been well established that the brittle nature of epoxy resin displays low resistance to crack initiation and propagation [104]. These limitations have motivated several research outputs focused on methodologies and techniques to aim at improving fracture resistance, which comprises brittleness and toughness through the introduction of nanoparticles such as alumina Al_2O_3, carbon nanotubes (CNT), silica (S_iO_2), titania (T_iO_2) and many more.

TiO_2 nanoparticles, in particular, have received a great interest in recent times due to their peculiar chemical, electrical, UV absorption, corrosion resistance, superior photocatalytic activity, photostability, and refractive index properties [14–18]. These excellent properties have been exploited for the manufacture of skincare products, food packaging, water purification systems, nanomedicine, coatings, solar cells, ion-batteries, and as reinforcement for polymer composites [105–108].

Matrix reinforcement and modifications have been carried out for epoxy [17,18], polypropylene [109], poly(butylene succinate) (PBS) [110,111], polyethylene [112], poly(vinyl butyral) [113] and poly (methyl methacrylate) [114,115] matrices to enhance the mechanical and thermal properties. Such nanocomposites have found applications in a wide variety of multidisciplinary industries such as in aerospace, automotive, semiconductors, construction, structural engineering and many more. The incorporation of nanoparticles into thermosetting polymer matrices are known to improve matrix mechanical properties such as fracture toughness, tensile modulus and strength, flexural modulus and strength and impact energy [116,117].

2.6.2 Effect of Titanium dioxide (TiO_2) on Impact and thermal properties of polymer composites

Reports from TiO_2 nanocomposites have shown significant improvements in environmental resistance, electrical, optical, mechanical, and thermal properties, [118–122]. A strong correlation between nanofiller type and volume content has been established in the literature [19,123]. Furthermore, titanium dioxide intrinsically possesses a high surface-to-volume ratio; a property that has been exploited in biomedical [105], solar cell [124] and photocatalysis applications [125]. TiO_2 polymer nanocomposites are known to exhibit considerable flame retardant properties, antibacterial behaviour and mechanical strength [24,126]. The successful synthesis of TiO_2/polymer composites have been achieved with a wide variety of matrices such as epoxy, [21,127–129], poly(methyl methacrylate) (PMMA) [130], polyamide [131], polyester [132], polyimide [133], polystyrene [134] and vinyl ester/TiO_2 [135].

Impact resistance is a pivotal mechanical characterisation but also the least understood polymer composite property. Although predicting most mechanical properties is relatively achievable, predicting the impact strength of polymer composites is impossible. Additionally, carbon fibre reinforced polymer composites are characteristically brittle and therefore particularly susceptible to impact loading [136,137]. However, the impact response of these composites is still difficult to predict as a result of the complicated fracture behaviours exhibited in the formation of delamination, matrix cracks, fibre fractures, and the separation of fibre from the matrix interface [136]. Aktaş et al. [138] observed that the damage modes due to the impact response of fibre-reinforced epoxy laminate composites are fracture and matrix cracks coupled with delamination for high and low impact energies respectively. Damage due to impact is a primary challenge since its detection is difficult, and the mechanical properties of laminates used for component manufacture may be additionally impaired. As such during

service life of material, the initiation and propagation of delaminations and cracks within the matrix as a result of low energy strikes, minimises structural integrity [139–141]. Impact susceptibility has assumed critical importance especially in the airplane industry, where thinner wing skins and fuselages are increasingly the norm to reduce manufacturing cost and weight [142].

Although laminates are observed to enhance certain mechanical in-plane properties and retard the initiation and progression of cracking within the matrix, its influence on out-of- plane properties are not clearly established [143–146]. Possessing in-situ strength is the main advantage when thin-plies are used [147–149]. Salehian and Jenabali Jahromi [135], carried out Charpy impact testing on unnotched vinyl ester matrix reinforced with TiO_2 nanoparticles. BYK C-8000 was used as the polymeric coupling agent while methyl ethyl ketone peroxide served as the curing catalyst. The resulting impact energy improved systematically until the TiO_2 loading of 2.5wt% after which a decline in the impact strength commenced upon further loading as shown in Figure 2.9. It was observed that the impact strength generally improved with smaller particle size and lower aspect ratios.

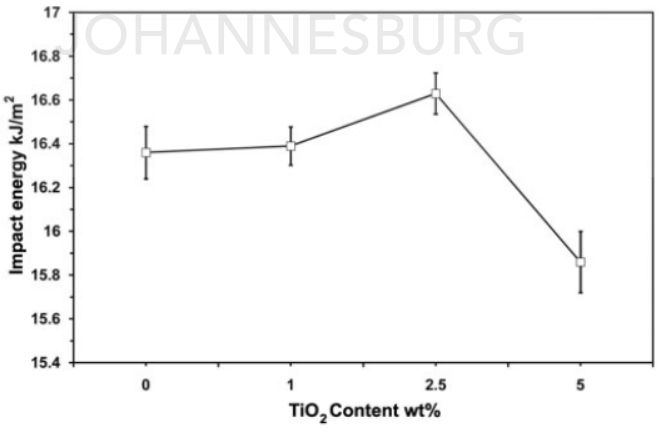

Figure 2.9 The Charpy impact energy of TiO_2 nanocomposite [135]

Dheya et al. [150] studied the effects of introducing TiO_2 and MgO nanopowder into a 90/10% blend of epoxy resin and polystyrene respectively. A significant improvement in the

impact strength using the conventional Charpy impact test was observed after the inclusion of the nanoparticle. Although the MgO reinforced nanocomposite showed a greater impact strength. Du and Wang [130] investigated the influence of introducing TiO_2 onto the surface of ultra-high-molecular-weight polyethylene (UHMWPE) fibre reinforced to improve interfacial bonding between the fibres and the PMMA matrix. The result revealed that impact resistance increased by 33% with the incorporation of $5wt\%$ TiO_2 in PMMA. Similarly, Runqin et al. [151] also observed notable improvement in the Izod impact strength when TiO_2 was introduced into a carbon reinforced PMMA composite as shown in Figure 2.10.

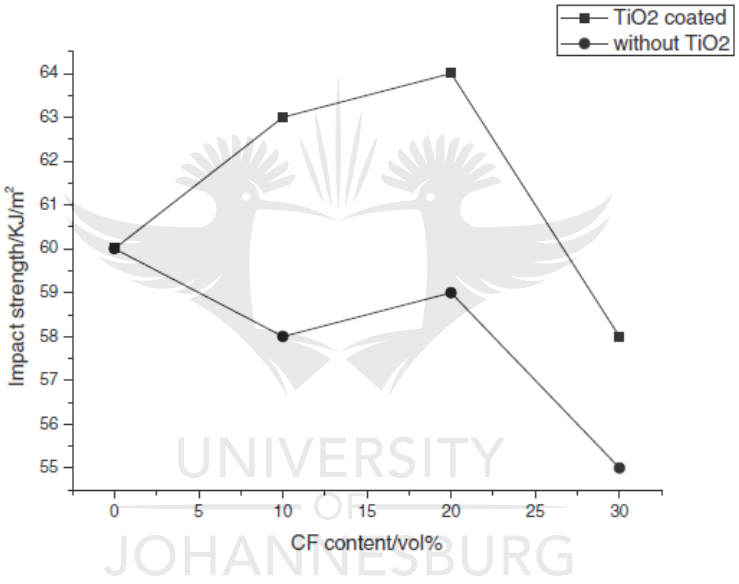

Figure 2.10 The impact strength of composites. [151]

Di et al. [152] observed that the impact strength of carbon fibre reinforced composites increased with increasing carbon fibre content because of the high impact strength of the CFs, whereas the incorporation of TiO_2 increased the impact strength as a result of the reinforcing effect of TiO_2 nanoparticles. Džunuzović et al. [153] reported on incorporating TiO_2 nanoparticles into a polystyrene matrix via in situ bulk radical polymerisation, and the resulting influence on thermal properties. The surface of the nanoparticles was modified 6-palmitate ascorbic acid (6-PAA). The surface modification facilitated suppression of the chain transfer

reaction due to the decreased mobility of molecules which subsequently enhanced the thermal and thermo-oxidative stabilities. Kumar et al. [18] also conducted a thermogravimetric analysis to study the thermal stability of TiO_2 nanocomposite prepared with epoxy resin but without particle surface treatment. To achieve homogenous dispersion, simultaneous dual mixing using ultrasonic and mechanical stirring was implemented. Additionally, to prevent degradation of the epoxy resin due to temperature rise near the ultrasonic horn, methyl ethyl ketone (MEK) was used to reduce the viscosity of the mixture. Thermal stability was observed to increase with increasing the TiO_2 content from 5 to $10wt\%$.

Singh et al. [154], investigated the effect of TiO_2 nanoparticles on the thermal properties of epoxy resin without particle surface modification. However, to decrease the matrix viscosity, methyl ethyl ketone (MEK) was added for mechanical stirring. The thermal storage for $4wt\%$ of TiO_2 nanocomposite was significantly improved by 32.88%. Chatterjee and Islam [128], while introducing TiO_2 nanoparticles used acoustic cavitation to disperse the particles in a two-part epoxy resin. The surface of the particles was not modified with any agent. The nanophase thermal stability, which was investigated via TGA revealed that, from 0.5% to 1% loading of TiO_2, the thermal stability systematically increased but reduced after a further load increase. This study is among the few that also analysed the thermal stability of the nanocomposite with integral procedural decomposition temperature (IPDT). IPDT was found to increase with particle loading with the highest thermal stability at 1%.

Zhang et al. [155] observed that although several studies have been conducted with regard to the effects of nanofillers, the results still show some inconsistencies and therefore new research with different methodologies are still needed to attain reliable data. This would lead to standards for the selection of nanofiller and possible surface treatment parameters to achieve optimal properties while limiting the side- effects of the nanoinclusion.

2.6.3 Surface Modification of TiO_2

The application of TiO_2 nanoparticles as nanofillers in polymer nanocomposites, in particular, is achievable because it is possible to conduct nanoparticle surface modifications or functionalisation [106,107]. However, the main drawback is the affinity for agglomeration formation at high concentrations which increases exponentially due to strong interparticle bonding subsequently making homogeneous dispersion extremely challenging [156,157]. Ameliorating this problem has generally been via post-mechanical or chemical treatment of TiO_2 before dispersion into a matrix [106,107,158]. The surface of TiO_2 is complicated and highly sensitive to chemical and thermal conditions such as the presence of impurity, pressure, temperature and cooling rate [159]. The surface is primarily characterised by ionic and covalent interaction of molecules, ions and atoms. Some of the bond formations observed during ionic and covalent interactions include Ti-O-Ti bond, Lewis acid site bonding, attachment of hydroxylic groups, and adsorption of chloride or sulphate residue during processing of oxidants (oxygen species or hydroperoxyl radicals) [160]. The TiO_2 surface is also covered with several defects such as alien cations, oxygen voids, crystallographic shear planes, stepped edges and line defects [159]. The numerous applications of TiO_2 can be traced to complex surface characteristics [161,162].

The chemistry of the TiO_2 surface is such that under the appropriate conditions, a large number of organic and inorganic atoms and molecules can react with it via oxidation, reduction, adsorption or dissociation. However, the dissociative or non-dissociative adsorption of H_2O is the most essential characteristic as it is directly linked with the wettability and dispersity of the TiO_2 in both aqueous and non-aqueous mediums [159]. When used as reinforcement in polymer composites, the photoactive nature of unmodified TiO_2 photoactivity causes degradation due to oxidation which subsequently results in chalking and embrittlement when subjected to sunlight or ultraviolet (UV) irradiation and moisture [157,159]. This drawback

requires some type of particle modification that influences the hydrophobicity or hydrophilicity of TiO_2 to decrease the surface photoactivity and enhance dispersion. The modifications improve organic polymer compatibility with TiO_2 by the introduction of functional groups that are capable of reacting with its organic molecules.

Several techniques for modifying TiO_2 have been researched over the years and can be categorised into four primary groups, namely modification by chemisorption through hydrogen bonding, polymer grafting onto TiO_2, polymer adsorption, and coupling agent via covalent bond formation of hydroxyl functional groups and adsorbed species [159]. The scope of this section is limited to modification using coupling agents.

2.6.4 Functionalisation of TiO_2 via Silane coupling

The TiO_2 surface is characterised by the presence of O-H species that can serve as anchor groups for covalently attaching coupling agents such as metal alkoxides, isocyantes, epoxides and organosilanes [106,159]. In recent times silane has attracted great interest in the field of surface treatment of nanoparticles for use as composite materials. The primary constituents of silane are basically silica and polymeric based organic material [163]. The chemical formulation for the resulting reaction of TiO_2 can be represented as RSiX3, where R is the organofunctional and X an amino, alkoxide, acrylate alkyl or halide group. Therefore, a siloxy derivative covalent bond is formed through the reaction between the hydroxylic O-H species on the surface of TiO_2 and the hydrolysable X components (Lin, 2006; Shokoohi, Arefazar and Khosrokhavar, 2008; Xiang, Jiang and Zhang, 2015). Generally, most organosilanes possess three (3) hydrolysable substituents attached on the centre of each silicon which facilitate the development of networks of cross-linked siloxane through the condensation of O-H groups with adsorbed silantriols and between other neighbouring silantriols [159]. Organic polymer compatibility is possible due to the presence of the R functional groups within the silane which mostly constitutes a minimum of one nonhydrolyzable aryl or an alkyl group. Furthermore,

polymer grafting onto the TiO_2 surface can take place when the substituent groups produce centres that are reactive [159,164].

Customisation of reactive substituents to target specific groups such as epoxy, acrylate, methacrylate, amino, vinyl and mercapto can be achieved. In practice, the most used types of organosilanes are the derivatives of alkoxy and chlorine[135,159]. Chlorosilanes are catalysed and therefore capable of reacting with the hydroxyl species on the surface of TiO_2 even at ambient temperatures. However, the resulting by-product of hydrogen chloride is highly toxic and detrimental to the environment. By contrast, alkoxysilanes do not readily react with TiO_2 surface silanol at ambient temperatures unless the acidic or basic co-adsorbed species facilitate catalysis. Again, contrary to chlorosilanes, alkoxysilanes produce less toxic by-products [159]. Therefore, the application of silane coupling agents grafts suitable organic functional groups onto the nanoparticle surface atoms which improves dispersion, particle-matrix bonding and physical or chemical interactions between the nanoparticles and the matrix [156,157,165]

Xiang and Zhang [164] investigated the effect of modifying the surface of TiO_2 for nanocomposite production using 3-methacryloxypropyl-trimethoxysilane (MPS) as shown in Figure 2.11. Predispersion of the TiO_2 in ethanol was conducted using ultrasonic means to enhance the efficacy of the surface treatment. Successful grafting of the silorganic functional groups onto the surface of TiO_2 was observed using Fourier transform infrared spectroscopy and thermogravimetric analysis. Additionally, the increasing MPS load content led to a corresponding increase in weight loss during the TGA.

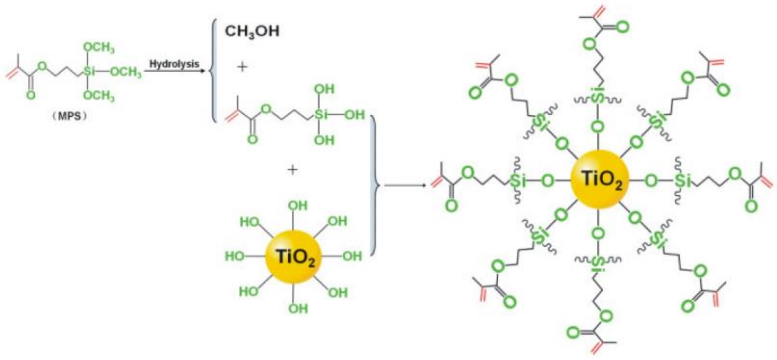

Figure 2.11 Illustration for the TiO_2 surface modification [164]

The surface modification of TiO_2 was described using three (3) steps as shown in Figure 2.11. Firstly, the hydrolysis of organosilane (MPS) takes place to transform the Si-O-CH3 groups into Si-OH groups. This is followed by a TiO_2 surface reaction of -OH groups with Si-OH groups [166] which leads to the formation of Si-O covalent bonds. In the final stage, C = C groups formation takes place on the surface of TiO_2 nanoparticles. A reaction between monomers and the C=C groups occurs and subsequently minimises aggregation [164].

2.6.5 Effect of Silane coupling agents on filler-matrix adhesion in Nanocomposites

The application of coupling agents for improving particle-matrix adhesion is critical for the design and manufacture of advanced polymer composites for structural purposes [163,167]. A broad spectrum of coupling agents are capable of achieving this purpose due to the presence of two (2) non similar functional groups; one of which chemically bonds to the polymer matrix while the other attaches to the surface of the reinforcement via absorption [168,169]. Since the introduction of glass and carbon fibre as reinforcements in composite materials, the drive towards developing different bonding methods has gained prominence [163]. Numerous research studies have recommended silane as a viable coupling agent effective in promoting bonding between polymer molecules and inorganic surfaces [170,171]. The advantages of considering silane as a coupling agent includes its commercial availability (large scale), the ability of alkoxy silane groups and a wide range of functional groups capable of bonding with

surfaces rich in OH and matrix functional groups respectively [172]. Therefore, the purpose of using silane is to enhance adhesion which subsequently influences mechanical, thermal and electrical properties [173,174].

Tee et al. [168] functionalised the surface of silver nanoparticles with silane which led to a significant enhancement in their flexural and electrical properties and the dispersity of the nanocomposite. They also reported that the coupling agent operated within the particle-matrix interface, as a 'molecular bridge' leading to covalent bond formation that consequently resulted in significant improvement in the properties of the nanocomposite [168]. Hashimoto et al. [175] reported on the 'bridging effect' while investigating the effect of silane treated TiO_2 nanoparticles on a HDPE matrix. The study observed that the silane coupling agent reduced the viscosity of the polymer thereby promoting improved wetting of the reinforcement [175,176]. However, they observed an increase in density when the silane was applied. Demjen et al. [177] investigated silane coupling agents with different functional groups on PP/Caco3 composites and observed that varying functional groups influenced their mechanical properties. The influence of over a hundred organofunctional silanes on both epoxy and polyester was investigated by Plueddemann et al. [178]. Kaynak et al. [179] also investigated several silane coupling agents and their effects on the improving the interfacial bonding within epoxy matrix and recycled rubber particles.

The use of silane for treating glass fibre has been investigated by several researchers and the findings show that improved interfacial adhesion enhances the thermal and mechanical properties [172]. A confirmation of silane treatment enhancing matrix-fibre bonding, was confirmed by Tezvergil et al. [180]. Ralph K. Witt found that allyltrimethoxysilane improves the strength of glass fibre reinforced polyester composite twice as much as when ethyltricholorosilane was used [163]. Ho and Marcolongo [163], and Ho and Marcolongo [181] reported that the hardness and local Young's modulus of the composite was negatively affected

when a silane couple agent was used. Goracci et al. [182], reported that microtensile adhesion strength between fibre and matrix improved with the application of silane solution. Zewde et al. [183] researched the role that TiO_2 surface modification plays on the thermal and mechanical properties of the epoxy nanocomposite using n-octyltriethoxysilane and 11-aminoundecyltriethoxysilane. At 0.05% loading of 11-aminoundecyltriethoxysilane functionalised TiO_2, a high silane group grafting density of 13% was observed which subsequently resulted in a significant improvement in the thermal stability of the nanocomposite.

Chen et al. [107] investigated the impact of 3-aminopropyltrimethoxysilane (APTMS) and phenyltrimethoxysilane when used as silane coupling agents. The study revealed the occurrence of covalent bonding between the silane coupling agent and the surface of the nanoparticle [184,185]. A study by Milanesi et al observed the development of a hydrophobic film resulting from the chemical bonding between Ti–O–Si and cross-linking of Si–O–Si bonds [106]. Zhao et al. [186] modified the surface of TiO_2 with 3-aminopropyltrimethoxysilane (APTMS) and 3-Isocyanatopropyltrimethoxysilane (IPTMS) and confirmed that a successful grafting of organic functional groups onto TiO_2 nanoparticles surface was achieved through an analysis of the FTIR spectra. The grafting was possible due to the formation of Ti-O-Si chemical bonds. The study also reported a significant decrease in the polydispersity index (PDI) and the hydrodynamic diameters after the silane treatment, which implies that the dispersion stability of the particles improved.

In their study, Tomovska et al. [187] implemented 3-triethoxysilyl propyl isocyanate as a silane coupling agent for the surface modification of TiO_2 nanoparticles. The establishment of the Ti-O-Si bond and the presence of a functional group on the surface of TiO_2 was demonstrated. High controllability of the TiO_2 surface characteristic was possible depending on the quantity and nature of the end-functionality electronegativity of the silane agent. A study

by Dinari and Haghighi [157] also reported a significant enhancement in the dispersion of TiO_2 nanoparticles and an improvement in the polymer matrix-particle bond when 1,3,5-triazine based silane was used as the coupling agent for modifying the surface of TiO_2. Furthermore, the inclusion of the silane treated nanoparticles improves the thermal stability of the nanocomposite. Similarly, Dalod et al. [188] investigated the in situ functionalisation of TiO_2 surface using selected silane coupling agents to obtain hydrophobicity via covalent bond formation.

2.6.6 Quantification of Dispersion

Polymer composites have in recent times attracted a lot of attention both in academia and industry as a viable alternative to traditional materials due to the ease and simplicity of processing and manufacture, low cost, and flexibility in tunability of its properties towards optimisation [1–5]. To ensure that the numerous and excellent benefits of polymer composites are fully exploited, the ability to customise and optimise through controlling and enhancing the mechanical, thermal, electrical and chemical properties is critical. The polymer composite industry has developed a huge catalogue of products, however, polymer nanocomposites are currently the most interesting and highly researched for applications in multidisciplinary fields like polymer biomaterials [4], drug delivery [1], chemical protection [5] and purification systems [3]. Studies have shown that the state of nanofiller dispersion significantly affects the microscopic and mechanical properties of polymer composites [46]. The increased use of nanoparticles as reinforcement in polymer composites has been inspired by their superior strength to weight ratio, mechanical, thermal and chemical properties. One of the challenges of introducing reinforcement into composites is [189–191]. The discrepancies between experimentation and the theoretical mechanical characterisation and properties of nanocomposites can be ascribed to ineffective dispersion [25,26,46,192].

There are three (3) possible states of dispersion, namely even dispersion, random dispersion and clustered [46,193]. Even and random dispersion states are generally preferred as they represent the measuring standard for optimal dispersion conditions, which directly correlate with improved properties. Fabricating nanocomposites possessing excellent states of dispersion is extremely challenging, and constitutes one of the main limitations in nanocomposite manufacture [25,192,194]. The presence of Van Der Waals forces between the dispersed nanoparticles is stronger than in the matrix-particle bond; this phenomenon eventually encourages the formation of agglomerates [194]. Aggregation thus occurs when the interparticle interaction is stronger than the particle-matrix interaction. Preventing agglomeration is important because it not only resists intended property augmentation but also introduces voids which are detrimental to mechanical and fatigue properties by being a source of crack initiation and failure [192]. Any attempt to enhance the properties of nanocomposites therefore depends significantly on the prevention or minimisation of agglomeration. Several properties such as mechanical (strength and stiffness) [34,195–198], thermal [199,200], electrical [197] barrier [44,201] and transparency [202] are improved when dispersion improves and agglomeration is minimised. The commonly adopted means of dispersing nanoparticles include mechanical or high-speed stirring [25], sonication [26,27], high shear mixing or melting [28,29], incorporating surfactants or compatibilisers [30] and casting solvents [31]. Generally, the process of enhancing dispersion requires a combination of these methods.

Several techniques with varying levels of sophistication and complexity have been developed for assessing states of dispersion in nanocomposites. The most commonly employed methods are microscopy based. Conventionally, visualisation and assessment of dispersed nanomaterials within the host matrix can be accomplished using images from optical microscopy [30,203], a scanning electron microscope (SEM) [204,205], a transmission

electron microscope (TEM) [37,206] or a scanning probe microscope (SPM) [207,208]. Other direct approaches include Raman spectroscopy [209], UV-visible spectroscopy [210,211], electrical conductivity [25,28] and fluorescence [212]. Spectrometry methods are limited in that they do not provide any information about the state of agglomeration and are not very useful when non-aqueous matrixes are used. The main drawbacks to these direct and visual techniques analyses are attributed to the qualitative, cumbersome, subjective, inconsistent and error-prone nature of the interpreted results [43]. Microscopy images can be further analysed using various statistical and distribution functions for quantifying dispersion. To understand the importance, effects, and relationships between bulk scale functional performance and the nanoscale structures of nanocomposites, a quantitative assessment of the extent and nature of nanomaterial dispersion within polymer matrices is a vital initial step [33]. The ability to quantify provides tools for process optimisation and critical insight into the factors that affect dispersion, and also establishes a means of standardisation for the assessment of dispersion [34].

Several research studies on methodologies for quantifying the degree of dispersion have been conducted using approaches of varying sophistication and complexity. Clark and Evans [35] characterised the state of dispersion using a random distribution determinant 'R'. In applying this concept, the state of dispersion was characterised as random when R=1. Although this approach is theoretically sound, the difficulty with selecting reference samples for comparison is a major disadvantage of this quantification method. Moore [213] proposed a formulation for dispersion quantification using the parameters of a slice index for assessing patterns, an anisotropic ratio and a variability index (VI). In their study, Bakashi et al. [36], quantified dispersion utilising a dispersion parameter (DP) which is image-based plus a cluster parameter (CP) formulated from the Delaunay triangulation. An acceptable state of dispersion is achieved when there is an increase in DP but a simultaneous decrease in CP. The

effectiveness of this technique is reliant on comparisons based on nanofillers with similar concentrations. Additionally, this method can only provide accurate quantification for an area with large nanofiller density. The state of clay dispersion as proposed by Xie et al. [37] was determined using the parameters of degree of dispersion (χ) and the mean interparticle spacing per unit volume (λ_V). The quantification of clay exfoliation in percentage was determined with (χ) while the spatial distance between clay particles was estimated using λ_V. However, the calculated state of dispersion is not comprehensive and definitively reliable although different percentages of the quantification during comparisons are generated.

The quadrant approach has been thoroughly investigated as a reliable means for dispersion quantification [38–42]. This quantification method is primarily based on computing the standard deviation of a selected region's concentration of particulate reinforcement observed in the sample image. A lower standard deviation value indicates good state of dispersion and vice versa. The main disadvantage to this technique lies in the difficulty of selecting the correct mesh size which if wrongly chosen can introduce inaccuracies and inconsistencies in the computed dispersion quantity. Due to the obvious limitation of the quadrant method previously discussed, Michael and Raeymaekers [43] proposed an improved version based on a composite index parameter formulated from a particle dispersion index and a particle size distribution index. Although their method succeeded in improving, to a large extent, the limitations of early approaches, the drawback of dependency on the quadrant to particle size was not resolved. Glaskova et al. [44], developed a methodology for dispersion quantification based on the hypothesis that state of dispersion was a factor of dispersion parameter (D) and particle size. Dispersion parameter (D) represents the probability of particles falling within a predetermined range of the particle area distribution. A high value for D is an indication of homogenous dispersion. Although this method is relatively effective in quantifying dispersion, the absence of interparticle spatial parameter limits its reliability.

Luo and Koo [45] quantified dispersion (D) using a probability density function (PDF) integrated for the evaluation of the particle spacing (mean spacing (μ)) via a computation of the statistical distribution. An increasing integral bound spacing uniformity is an indication of improvement in homogeneity in the state of dispersion. This method is however, limited by the exclusive dependency on particle free path spacing which indicates that similar states of dispersion can be estimated irrespective of the level of agglomeration. Tyson et al. [214] proposed a quantification methodology as an improvement on the Luo and Koo [45] approach using two (2) parameters namely; a dispersion quantity (D) and an agglomeration quantity (A). The dispersion quantity (D) is based on the measured interparticle spacing whereas the agglomeration quantity (A) is a derivation from the measurement of the particle sizes. The main limitation to this approach is the difficulty in choosing the most suitable distribution function.

In a recent study by Blazer et al. [46], the formulation for assessment of the quality of dispersion (β) was based on an interparticle spacing model, the volume load of the nanoparticle (ϕ) and fibre-to-particle diameter ratios (D/d). A high β value connotes a high-level dispersion quality. Lillehei et al.[47] applied fractal dimension, radial power spectral density and Minkowski functionals to successfully quantify the state of dispersion in SEM images. This study is unique as it is among the few quantification methods based on fractal dimension and radial power spectral density (RPSD). Broughton et al. [215] used a static light scattering technique based on Fourier domain optical coherence tomography, to assess the state of dispersion. Although the method was relatively effective in quantifying dispersion, it displayed major drawbacks such an output of inconsistent results and a high level of sensitivity to several extrinsic influences such as particle size and morphology.

2.7 Analysis of Stress Concentration and Application of Finite Element Analysis

The continued rise in the application of composite materials for structural parts is due to their process characteristics and excellent properties such as corrosion resistance aesthetics, flexibility, fatigue resistance, flexibility, lower cost, and ease of production [216, 217]. Accurate determination of the principal forces and stresses acting on or within composite structures is therefore essential for the selection and design of suitable composites for customised manufacture [217]. Tensile and compressive tests are the fundamental tests often used for characterisation and investigation of principal forces and mechanical properties.

2.7.1 Minimising Stress Concentration during Tensile Testing

Tensile testing is specifically effective for determining the in-plane of composite materials such as tensile strength, elastic modulus, and Poisson's ratio. The experimental setup tensile testing generally requires the use of coarse or serrated clamps for securing the test specimen at extreme ends to minimise slipping during the testing. During the clamping process, the test specimen is subjected to grip friction, axial loading and shear force [7,8,218,219]. In general, metals and their alloys can undergo tensile testing without the application of an intermediary cushioning material between the specimen and grips. On the contrary, because, fibre reinforced composites tend to display lower transverse compressive strength during tensile testing, stress cushioning materials such as tabs are essential to prevent premature failure and inconsistency in measured results [7]. The bonded tab is the most commonly used standard for tensile testing due to the advantages such as limiting transverse damage to the surface of the test specimen because of the high grip forces and reduction of induced out-of-plane stresses.

Although the application of tabs has become a standard norm, there is a major drawback in its usage. During tensile testing, tabs tend to induce high levels of stress concentrations

within the tab termination area [8]. In their study, Hart-Smith [220] concluded that tabs may in some cases not be the best option and that its use must be avoided as much as possible; where used, its selection must be carefully assessed. Local stress concentrations induced during the application of bonded tabs can result in a decrease in tensile in-plane properties. [8,9,221,222]. To ameliorate the negative effects of bonded tabs, a number of tab geometries and design parameters have been proposed. Two of the commonly used standards for tab implementation are the ASTM 3039/D3039M-14 [223] which proposes the adoption of end-tapered tabs while the ASTM5083-17 [224] and ISO 527-1:2012 [225] suggest the use of prismatic tabs. Hojo et al. [8] carried out a comparative study using a 10^{o} tapered and non-tapered (90^{o}) and found that the tensile strength values were comparatively similar and statistically insignificant.

Belingardi et al. [9] investigated the effect of both bonded and moulded tabs on the tensile strength of fibre reinforced laminate composites. After tensile testing the results showed significant and higher levels of residual stresses induced in the moulded tab test specimen. Bonded tabs with a 30^{o} bevel shape were recommend after comparative testing of several tab configurations. Application of the tabs with 30^{o} bevel shapes resulted in the lowest induction of stress concentrations in the tab termination region. A number of studies, for example the ones conducted by Adams and Adams [8] and Joyce et al. [222], advocate the utilisation of tabs since their research reveals that the intensity of the induced stress concentration from the tabs are affected by the tab geometry and that optimisation of the tab design was critical.

De Baere et al. [11], reported that although stress concentration in the tab termination region significantly reduces with the application of tapered bonded tabs, some test specimens failed prematurely due to weak adhesive bonding between the tapered region of the tab and the test coupon. Consequently 90° or straight-ended tabs were proposed as the most preferred option. To further minimise stress concentration Wisnom et al. [226] developed tensile test coupons from unidirectional fibres with gradual and symmetrical ply drop-offs forming tapers

at the grip ends. Emery paper and end tabs were still applied primarily as intermediary materials to prevent grip damage even though this novel design was successful in minimising the stress concentration. In a current study by Czel et al. [12], investigated the possibility of totally eliminating induced stress concentration during testing via a novel design of the test coupons using an interlayering of unidirectional glass and carbon fibre fabrics moulded with an epoxy matrix. The motivation for the study was also to eliminate the use of tabs in tensile testing.

Adams and Adams [8] focused specifically on tensile testing using bonded tabs and the determination and assessment of the stress concentrations using finite element analysis while the study by Belingardi et al. [9] focused on only experimental testing of moulded and bonded tabs without the compliment of finite element analysis for determination and analysis of the stress concentrations induced. An assessment of the studies reviewed and several others [8–12,222,226,227] was carried out without any rigorous statistical analysis of the influence of tab design parameters in minimising stress concentration and the significance of the parameters in optimising the tab design. Minimising the stress concentrations introduced during tensile testing via optimisation of the tab design is vital for achieving consistency and accuracy in characterised results. There is thus a need for further research and development of hybrid approaches, which utilise both statistical and finite element methodologies for customised optimisation, and for analysis of design and process parameters. The adaption and exploitation of approaches such as regression techniques, analysis of variance (ANOVA), genetic algorithms, multiple response optimisation, and the Taguchi method are essential.

2.7.2 Finite Element Analysis of NCFs

Finite element modelling is an important tool for predicting the stress behaviours of composite materials. For NCF composites in particular, several methodologies are available to simulate uni- and biaxial non-crimp fabrics, however, they are categorised under kinetic mapping [228,229] or finite element method techniques. Although kinematic mapping (KM)

is effective, it is less efficient for problems which involve boundary conditions such as friction, forming parameters like blank holder forces, and for the behaviour of materials [230]. Because of the aforementioned drawbacks of KM, FEM is the most used approach when modelling non-crimp fabrics. The classification of FEM-based approaches used for NCF analysis are: discrete, semi-discrete and continuous [231]. Indiscrete modelling uses abstract modelling based on bar elements and beams [232,233]. Meso-models for NCFs are often used to simulate different textile structure components through solid and shell elements. Multi-scale models are meso-models that are highly sophisticated, detailed, CPU-intensive and mostly required for virtual testing of the material [234,235]. However, less sophisticated meso-models are mostly implemented in many studies for the simulations of processes such as forming [231,236–238]. A semi-discrete approach to modelling involves the input of micro and mesoscale parameters directly into the finite element shape function [239–241]. Constitutive equations are applied to homogenised modelling of the NCF during a continuous modelling approach. Two main constitutive modelling approaches are preferred namely hyperelastic [242–244] and hypoelastic approaches [234,245–247]. In hyperelastic modelling, material objectivity which incorporates the assumption of rigid body rotation in relation to individual fibre tracking is achieved through covariant modelling [231]. I In hypo-elastic modelling material objectivity and fibre rotation tracking is ensured via the implementation of acceptable transformational laws or material frames between a parallel fibre frame and an existing material frame such as Naghdi's frame [245,247].

2.8 A review of Approaches for Recycling of Polymer Composites

2.8.1 Global demand trend for carbon fibre reinforced composites

T. A. Edison discovered carbon fibres in 1879 [248], although their use for light-weight high-performance composites is recent. In 1997 and 2002, carbon fibre growth rate worldwide

was 5.8% and 7–8% respectively [249]. The global production of carbon fibre increased to 28000 *tonnes* in 2006 which drove the industry worth up by between $1.4 and $5.6 *billion*. A unit of 1kg was priced at approximately $50–200 [250]. During that year the demand for carbon fibre composites especially, exceeded supply with the wind turbine industry being the biggest consumer [251]. All the market dynamics and economic indicators support the forecast of exponential growth in the composite material industry with carbon and glass fibre being the leading reinforcement materials. From 2009 to 2014, the global demand for carbon fibre rose from 27000 *tonnes* to 53,000 *tonnes*. In 2014, the composite market in US alone witnessed a 6.3% growth valued at $ 8.2 billion in comparison with previous years. This trend suggests that, based on a 6.6% annual compound growth rate, the composite market forecast will be $12 billion by the year 2020 [252]. Currently, Europe leads in the total global demand for carbon fibre by approximately 37% and a further increase of 43% is expected by 2020.

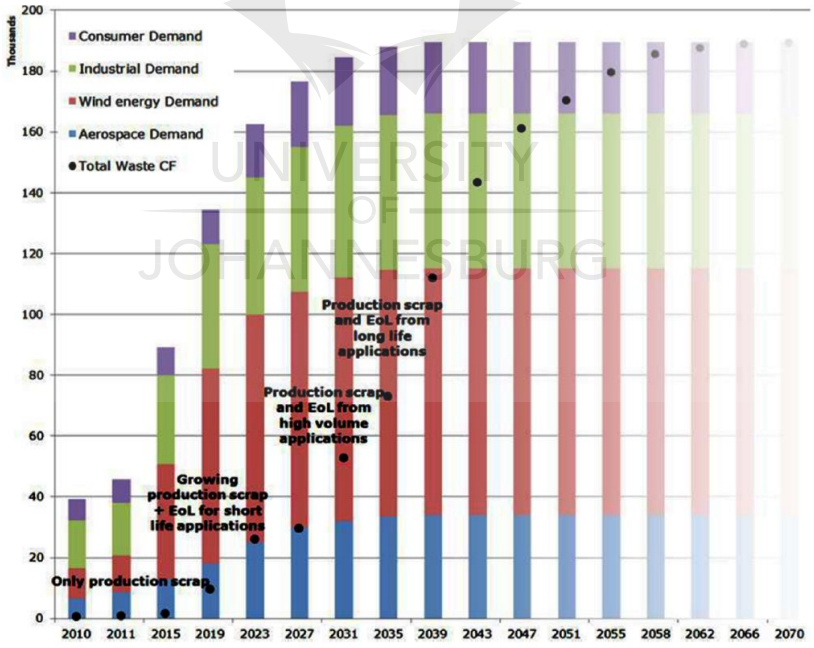

Figure 2.12 Actual and project carbon fibre demand and waste generated from 2010 to 2070 [253]

The trend in demand and regional distribution of carbon fibre reinforced composites follows a similar trend as carbon fibre. In Europe, the demand was estimated at 36.8% while

North America was 40% [252]. By 2021, this growth in demand is expected to double to approximately $116{,}000\ tons$ [254]. The primary utilisation of carbon fibre is as a polymer composite. The high exploitation has brought to the fore the critical need to address the production and End-of-life (EoL) waste.

There has been a sharp rise in scraps from carbon fibre reinforced composite production and end-of-life, particularly within the wind energy industry in 2017 [252]. The graph in Figure 2.12 shows the demand for carbon fibre reinforced composites in kilo tonnes for several industries, and the resulting projected waste is represented as black spots [253].

2.8.2 Circular Economy and Waste Management of carbon fibre reinforced composites.

The circular economy concept emphasises the restoration and regeneration of resources through efficient design [255]. The main aim of this concept is to provide protection for materials, product and resources when their effective utility is highest while significantly reducing the negative influences [256]. The pursuance of circular economy as the basis for recovering both material and energy in a society that is sustainable is difficult to achieve [257,258]. Attaining a sustainable circular economy for fibre reinforced composites presents a unique challenge, requiring the application of both recycling and conservatory approaches for dealing with production and end-of-life scrap [252]. The greatest challenge to the sustainability of fibre reinforced polymer composites is their recyclability. Increasing restrictive environmental directives and legislation on landfill disposal coupled with the detrimental impact on the environment is driving a sense of urgency for the acceleration of composite recycling processes to industrial-scale as the best solution [259].

The high demand, production and consumption of polymer composites present an end-of-life disposal problem since the majority of these materials are currently not recycled due to lack of suitable cost-effective technologies and therefore end up in landfills [252,260,261].

However, the landfill approach is becoming unsustainable and represents a high cost of disposal due to directives such as the new EC waste directive that categorises carbon fibre reinforced composites waste as chemical waste, which if not harnessed, constitutes a loss of valuable secondary raw materials [262]. Under the European Union's Waste Framework Directive [263], for example, the least preferred option for waste management is landfill although it is the cheapest disposal route. In countries such as Germany, the landfill option is illegal, and many more EU nations are following suit in opposing this method of waste management [263]. The EU legislation in its present state does not categorically issue specific regulations on composite waste. However, its disposal is captured although indirectly, in the 2000/53/ EC EU Directive where total End-of-Life vehicle weight should meet the requirements of 85% recycling and 95% recovery while restricting the utilisation of non-metals if they do not adhere to the tenets of the directive [49].

2.8.3 Technologies for recycling of Polymer Composites

Virgin carbon fibre is relatively expensive at a value of approximately $30\ €/kg$ [264] and also has a high energy input cost ranging from $183-286\ MJ/kg$ [265]. Therefore, processes that can recover carbon fibre at lower energy cost than virgin fibre manufacture, offer a more environmentally friendly and sustainable alternative which is also more economically beneficial to manufacturers. For example, pyrolysis which is one of such promising processes has been found to use only $5-10\%$ of the energy consumed during the manufacture of virgin fibre [266,267]. In the past decade, various research studies on recycling polymer composites have been undertaken and developed. These include mechanical (grinding) [259,268–274], thermal processes (incineration, pyrolysis etc) [259,260,275–284], and solvolysis [259,285–292].

A comprehensive study on the three methodologies for recycling carbon fibre reinforced waste was carried out by Pickering [270], Pimenta and Pinho [293] and Oliveux et al. [259]

specifically on the technical comparisons and re-use. All these studies concluded that the most suitable approach for recycling carbon fibre reinforced composite is the thermochemical route. Several reuse options have been proposed for polymer composite waste which includes mechanical grinding for use as filler reinforcement in the manufacture of new materials [260], thermal and chemical approaches for recovery of gasses, liquids, plastic parts and carbon fibres and incineration for energy recovery [262,280,294].

2.8.4 Mechanical Recycling Methods

This approach comprises initially shredding or crushing to downsize the composite into smaller bits followed by a grinding process which further reduces the materials into a finer product [295]. Crushing or shredding is often the standard step for all recycling techniques. Thereafter, sieving is carried out to separate resin-rich powder recyclate from fibres of varying lengths. Mechanical grinding has found greater application in the recycling of glass fibre composites [268–270]. However, there are a few studies on mechanical recycling of carbon fibre reinforced composites [271–274,295].

Mechanically ground composite waste can have two applications, namely reinforcement or filler. Virgin fillers like silica and calcium carbonate are generally inexpensive and cost less than processing ground recycled composite fillers, which make them commercially not viable. The fillers consist of sieved and sorted powdered product after grinding [259]. Schinner et al. [271] observed that thermoplastic composites could be mechanically ground and used as quality reinforcement in injection moulding. The inclusion capacity of filler materials is relatively restricted to not more than $10\,wt\%$ primarily due to the resulting decline in mechanical properties coupled with inherent challenges such as increased viscosity associated with processing at higher filler contents [270]. Although resin-rich compositions are not competitive replacement as fillers at present, they are suitable for use as an energy source. At the moment, industrial exploitation of ground carbon fibre reinforced composites is non-

existent because other treatment processes are more efficient in recovering the fibre. However, Roux et al. [296] developed a novel technique for grinding carbon fibre reinforced thermoplastics via electrodynamic fragmentation.

2.8.5 Solvolysis (Chemical Methods)

Solvolysis is the degradation of resin with the application of a solvent. The first application of solvolysis can be traced to over three (3) decades ago [297] on unsaturated polyester. In 1980, Kinstle et al. successfully broke down unsaturated polyester into its constituent monomers (glycols and carboxylic acids) and degraded styrene (fumaric acid copolymer). The hydrolysis was conducted either with or without the addition of catalysts or solvents within the temperature range of 220 and 275℃ [297]. Since then, the recovery of fibre and matrix (either thermosetting or thermoplastic) from fibre reinforced composites using varying solvents and conditions, has been achieved by several researchers [285–292,298,299]. The type of resin determines the temperature and pressure condition needed for resin degradation. Epoxy resin, for example, is more difficult to degrade than polyester resin and therefore requires higher temperatures and pressure. Carbon fibre reinforced composites have been extensively recycled using this method and its commercial viability is attracting a lot of interest.

Water is the most used solvent; either neat [249,285,297,300,301] or mixed with co-solvents such as amines, alcohols and phenols [285,297,302]. Water mixed with alkaline catalysts such as potassium hydroxide (KOH) and sodium hydroxide has also been successfully used [249,288,291,303]. Besides water, the following solvents with or without catalysts or additives have also been used, and include alcohols such as acetone, glycols, ethanol, methanol and propanol [249,289,290,292,297,299,301]. Acidic catalysts are less often used but are suitable for the degradation of highly resistant resins such as PEEK and epoxy at lower temperatures. Liu et al. [304] recovered carbon fibre from carbon fibre reinforced polymer

composites using nitric acid at a temperature of 90℃. Supercritical fluids are also attracting a lot of attention due to the tunability of recycled products through the variation of operating parameters such as pressure, temperature and volume. The main drawback of this approach is the high cost of the equipment used. This is so because of the extreme and severe operating conditions [290,298,299,302,305]. Furthermore, some catalysts and/or solvents are toxic and highly detrimental to the environment making its disposal or separation very difficult with some form of fibre damage still occurring. Meng et al. [12] recycled carbon fibre composites using supercritical water.

Solvolysis provides endless possibilities for the application of a wide spectrum of solvents, catalysts, pressures and temperatures. Its primary advantage over pyrolysis is the ability to accomplish polymer degradation at relatively low temperatures specifically for epoxy resins and unsaturated polystyrene [259]. In situations where supercritical conditions are required, the cost of recovery becomes expensive due to the high cost of reactors which experience extreme temperature and pressure conditions that promote corrosion [306]. Char formation during solvolysis is avoidable as the usage of specific reactive solvents with co-solvents or co-reactive solvent are capable of degrading specific bonds within the composite through diffusion. This makes the recovery of, monomers which cause char formation possible [259]. Pyrolysis is presently the recycling option most preferred and widely used because it is a well-established and often-used technology in the chemical processing industry. Although it enjoys widespread interest, the challenge of fibre degradation due to high process temperatures is motivating research interest into solvolytic techniques [259].

2.8.6 Thermal Recycling Methods

There are three main thermal treatment processes available for recycling composite waste which are: pyrolysis, fluidised-bed pyrolysis, and microwave-assisted pyrolysis [260,277–280,282–284,307–309].

2.8.6.1 Fluidised Bed Reactor

The fluidised bed reactor was developed by Pickering et al. [280] at the University of Nottingham (UK) for the incineration of glass fibre composites at low-temperature combustion conditions of 450℃ to recover the energy and the fibre. This process, however, has the drawback of high labour and high-energy requirements, which makes a weak business case for using this technology.

2.8.6.2 Pyrolysis

Presently, the continued generation and rise in the volume of end-of-life (EoL) composite waste is detrimental to the environment and impacts negatively on existing resources. To mitigate against impending environmental challenges, a promising solution is the utilisation of pyrolysis, which comprises a two-stage approach capable of material, fuel and chemical recovery from composite waste. During the first stage carbon fibre is recovered from reinforced composites through heating the material within a temperature range of 350 – 700℃ under inert conditions in the absence of air or oxygen [310–312]. The decomposition of the composite matrix yields a solid residue comprising fibres, fillers and char, bio-oils, and gases. Inspection of the surface of pyrolysed fibres shows the presence of deposited char and therefore cleaning of the fibres via oxidation in air is necessary to burn off the char [252]. Pyrolysis has been successfully implemented at an industrial level and its commercial viability is currently being exploited by companies such as ELG Carbon Fibre Ltd. (ELGCF) in the UK [252]. Adherent Technologies Inc. (ATI) in USA broke down the resin matrix in composites using a wet chemical, and Innoveox in France [313] developed an approach which used supercritical hydrolysis for recycling composites.

Naqvi et al. [252] conducted a comprehensive review on recycling carbon and glass fibre reinforced composites using pyrolysis with the emphasis on possibilities for re-use and the accompanying technical challenges in relation to the concept of a circular economy. The study

highlighted the economic viability of the pyrolytic recyclates and the possible inherent challenges associated with commercialisation, and concluded that the commercial viability of pyrolysis was justifiable. Several studies have shown that the application of pyrolysis in an inert environment is the most viable thermal process for the recovery of carbon fibre from composite scrap [310,314,315]. Optimisation of the process parameters of all pyrolytic processes whether flash, fast or slow, is necessary for effective and efficient recovery of fibres, fuels and chemicals [312,316–318].

In their study, Wong et al. [319], conducted a comparative analysis to extensively review the energy consumption of thermochemical (pyrolysis and combustion), chemical and mechanical methodologies for recycling fibre reinforced composites. The study revealed that the consumption of energy via pyrolysis was a moderate $30\ MJ/kg$ in comparison to the other methods. Furthermore, the other approaches were relatively more expensive, and the recovered fibres mechanically inferior. Therefore, pyrolysis seems to be the most suitable balance between a moderated production cost and best fibre quality production. Nahil and Williams et al. [275] pyrolysed composite waste manufactured from carbon fibre reinforcement in a polybenzoxazines resin matrix using a fixed bed reactor at varying temperatures. High concentrated aniline, nitrogenated and oxygenated aromatic compounds were obtained from the pyrolysis liquid while CO, CO_2, H_2, CH_4 and several hydrocarbons were derived from the pyrolysis gases. They achieved activation of carbon fibre via pyrolysis at temperatures ranging between $350–700°C$ for $1hr$ of the carbon fibre composite waste using a fixed-bed reactor. It was observed that after the oxidation of the char, the mechanical strength of the recovered fibres was comparable to that of the virgin fibre. However, an in-depth analysis of the influence of char was not carried out.

Bradna and Zima [320], used as chromatography/mass spectroscopy, to investigate the effect of pyrolysis on the thermal degradation of carbon fibre reinforced composites. The study,

however, did not report the mechanisms of pyrolysis and the product yields from pyrolysis. Meyer et al. [310], used a thermogravimetric analysis (TGA) under inert conditions to assess the thermal degradation of carbon fibre reinforced composites. Post pyrolysis treatment was not considered in the study. They were able to regulate the thermogravimetric analysis parameters to optimise both pyrolysis conditions to recover good quality fibre properties. The pyrolytic char was observed as lacking any value and should be burnt off. Giorgini et al. [311] recovered carbon fibre through pyrolysis using a batch pilot plant at temperatures of 500℃, 550℃ and 600℃. The morphology of the recovered fibres was examined with a scan electron microscope (SEM). The pyrolysed fibres were rougher and less homogenous than virgin carbon fibre. The observation of a thin char layer which was degraded through oxidation was reported, but the possible importance of char was not investigated.

2.8.6.3 Role of post-pyrolysis treatment in recovery

As earlier explained, during pyrolysis, the solid residue produced comprises char deposited on fibre. A circular economy implies that reuse is paramount. However, the presence of char contaminated surfaces limits reuse and results in fibres with inferior mechanical properties. To mitigate this drawback, post pyrolysis treatment is critical for cleaning the fibres if the primary focus is to re-introduces fibre into thermoplastic or thermosetting matrices to manufacture new composites [252]. Oxidation is the most viable method for char removal, but optimising the process parameters of temperature and residence time is difficult to achieve [275]. Nahil and Williams [275] separated char from solid residues through oxidation at 500℃ to recover the carbon fibre which had 90% of the mechanical properties of the initial virgin fibres.

2.8.6.4 Characterization of recovered fibre using the pyrolysis process

Studies by Pimenta and Pinho [293] and Oliveux et al. [259], definitively concluded that pyrolysis was the only method that produced recycled fibres with mechanical properties comparable to those of virgin fabrics, and which has large scale commercial viability for the manufacture of composite structures. Wong et al. [319], employed pyrolysis and a combustion process for comparative analysis, and the results showed that a slight reduction of approximately 10% in fibre strength of the recycled carbon fibre occurred with a significant loss of approximately 50%. From the literature it is observed that the tensile strength loss when pyrolysis is used for fibre recovery , is on average within the range of 5– 10% while that of combustion is approximately 18% [309]. To further gain insight into the recycling process, the recyclate and the recycled products must be characterised to provide the essential data regarding the thermo-chemical process. Thermogravimetric analysis (TGA) has been extensively used for characterising the thermal degradation of composite materials [321]. The generated TG and derivative thermogravimetry (DTG) curves describe the relationship between the matrix mass loss with respect to temperature. The TGA curves also provide information on the decomposition and oxidation temperatures of the resin and fibres respectively.

Giorgini et al. [311] and Kim et al. [322] reported that the decomposition temperatures of carbon fibre reinforced composites during pyrolysis was within the range of 450– 600℃ with respect to whether the sample was cured or not. The most suitable temperature range for conducting the post-pyrolysis of oxidation to clean char off the surface fibres, was found to fall within 500– 600℃ in the presence of air. The influence of the recycling process on the mechanical properties of recovered fibre was determined by Yildirir et al. [323] and Song et al. [324]. The initial fibre length, elongation at break, fibre diameter, young modulus, tensile strength and flexural properties were investigated. The study further investigated the

morphology of the recovered fibre with scan electron microscopy (SEM), Raman spectroscopy, and X-ray photoelectron spectroscopy (XPS) analysis. Das and Varughese [325], successfully identified a functional group on the surface of the recovered fibres using an attenuated total reflection linked to Fourier-transform infrared spectroscopy (ATR-FTIR). Jiang et al. [326], also detected the presence of carbonyl and carboxylic groups on the recovered fibre surface using X-ray photoelectron spectroscopy. The presence of functional groups was attributed to the effect of heating the fibre in air, which positively influences interfacial bonding. Jiang and Pickering [327], recovered fibres via pyrolysis and found active oxygenated species still present on the fibre surface which ultimately improved the fibre-epoxy bond. The characteristics of the fibre surface are influenced by the thermal and oxidation conditions. Surface defects resulting from oxidation resulted in tensile strength and crystallite size reduction.

A recent study by Mazzocchett et al. [49] validated pyrolysis as a viable recycling option for recovering carbon fibre, and investigated the effect of different oxidation conditions for char removal. The results revealed that the presence of pyrolytic char protected the fibre from excessive damage during the oxidation process. They observed the presence of oxygen-rich fibre surfaces as a result of the oxidation process which improves fibre-matrix bonding rendering the need for additional sizing unnecessary. Their research is the only study that attempts to characterise the residual char via Raman spectroscopy. The findings showed that the virgin fibres which were char-free showed sharper signals while the pyrolysed fibre exhibited broader and poorly defined peaks - clearly confirming the presence of the deposited char. After oxidation, the D and G peaks became well-defined and narrower, clearly indicating the removal of the char. The majority of such studies limited the thermal characterisation of pyrolysed and oxidised fibres to temperatures below 650℃. However, there is a need to further

investigate the influence of the char deposition at a much higher temperature during which the carbon fibre itself begins to degrade.

2.8.7 Pros and Cons of the Recycling Methodologies

Although various methods for recycling carbon fibre reinforced composites exist, the majority lack optimisation and possess significant limitations. Mechanical recycling for instance usually results in powdery materials with highly reduced value addition suitable for utilisation as fillers [270]. Also, crushing or shredding requires high energy consumption. Optimising the control of thermal recycling processes is critical to preventing unwanted chemical changes that can affect the recovered material and prevent loss of valuable constituents [266,280,326]. Although solvolysis utilises comparatively lower temperatures, it requires more chemicals than all the other processes, thereby necessitating additional avenues for the disposal of these chemicals [262]. Incineration is the most used approach for energy recovery from a mixed stream of wastes; however, some drawbacks include atmospheric pollution from emissions, loss of valuable products, and the installation of expensive equipment for gas cleaning.

2.9 Summary

The literature review highlighted and provided a holistic overview of the fundamental fabrication techniques for non-crimp fabrics, non-crimp fabric composites, and possible recycling techniques. The review focused on the basic background of NCF composites and their applications, the modification of a composite matrix via functionalised TiO_2 nanoparticles, the dispersion quantification of nanofillers, the application of finite element analysis to NCF composites, and recycling with the emphasis on pyrolysis.

Non-crimp fabrics can generally be described as unidirectional plies organised and yarn-stitched in a distinct orientation [56]. It is a compromise between unidirectional pre-

impregnated tapes (UDPT) and woven fabrics. Liquid composite moulding techniques are mostly used in the fabrication of NCF composites with vacuum assisted resin transfer moulding being the most preferred. The unique properties of NCF composites have attracted a lot of interest from researchers and applications in the aerospace, automotive and wind turbine industries.

Matrix modification has been widely explored as a research area since epoxy, which is the most, used thermosetting resin has the limitation of high brittleness after curing. The literature has shown that this characteristic results in reduced resistance to crack initiation and propagation [104]. This drawback has motivated high research outputs aimed at enhancing fracture toughness via the introduction of nanoparticles such as alumina Al_2O_3, carbon nanotubes (CNT), silica (S_iO_2), titania (T_iO_2) and many more. However, T_iO_2 is presently receiving great research attention due to its unique properties such as UV adsorption, refractive index, photocatalytic activity, photostability, and corrosion resistance [14–18]. The influence of TiO_2 on the impact strength and thermal properties of composite materials were reviewed. Most of the literature reviewed concluded that predicting the impact response of composite materials was nearly impossible due to the diverse and complicated modes of possible fractures. In general, the introduction of TiO_2 nanoparticles improved both the impact and thermal properties of the composites. The comprehensive review conducted revealed that there was no known literature on the influence of TiO_2 on the impact and thermal properties of NCF composites was non-existent.

The reviewed literature indicates that homogeneous dispersion of nanoparticles is critical for improving the mechanical and thermal properties of nanocomposites. One means of achieving this is through surface treatment or the functionalisation of nanoparticles. Silane coupling agents were identified as efficient in covalently attaching hydroxyl functional groups and species onto the surface of TiO_2, which was observed to significantly improve particle

wettability. Improving the particle-matrix interfacial adhesion consequently reduces agglomeration and promotes homogenous dispersion of the nanoparticles. Accurately quantifying the state of dispersion with a simple but effective approach is still a present challenge to researchers. Visual inspection has been the most used approach, but it is highly subjective. Quantitative methodologies that are therefore generally based on standard deviation, and distribution functions have been developed. There was clear gap in literature for a methodology that was simple implement but sophisticated enough to avoid the drawbacks of difficulties in selecting reference samples and mesh size with quadrant methods, and the inherent limitations in relying on standard deviation.

The application of finite element based approaches for modelling NCFs, such as discrete, semi-discrete and continuous methods [231], were reviewed. The most prominent approach is the use of meso-models for NCFs for simulating varied elements of the textile structure via solid and shell elements. The reviewed literature showed that meso-models with lower complexity and sophistication were normally preferred for simulations of processes such as forming [231,236–238].

The manufacturing process of virgin carbon fibre is economically expensive and requires high energy input. The economic and environmental benefits of exploring recovered fibres which is a more sustainable alternative can be harnessed. Pyrolysis in particular is very attractive since the process only consumes $5 - 10\%$ of the energy input required for the manufacture of virgin fibre [266,267]. There are only a few recent research studies on the recovery of carbon fibre through thermal techniques, but none have been conducted on non-crimp fabric composites. This therefore presents an area of novelty in this thesis.

A review of the literature relevant to this research was comprehensively presented in this chapter. The next chapter highlights the materials and methods implemented in the course of the study to achieve the aims of the research.

CHAPTER THREE

MATERIALS AND METHODS

3.1 Introduction

The methodology can be categorised under five main sections as shown in Figure 3.1. The first section focuses on the manufacturing processes and methods used in the preparation and fabrication of composite plates. In the second section, particular attention is paid to the development of two new dispersion quantification techniques. Proof of concept and validation approaches are comprehensively presented. The third section provides numerical methodologies based on finite element modelling and simulations, optimisation techniques, and statistical analysis geared towards stress concentration minimisation in the tab termination region of tensile test samples. The efficacy of three optimisation techniques is compared. To provide a holistic assessment of the composite material in accordance with a circular economy, the fourth section deals with recycling, reclamation, and the reuse of carbon fibre reinforced composites. Various post-pyrolytic treatments required for enhancing wettability are also detailed. In the final section, all the methodological approaches for the morphological, spectroscopic, chemical, thermal and physicochemical characterisations carried out during the research, are presented. A list of materials and equipment used have been provided in Table 3.1 and Table 3.2 respectively.

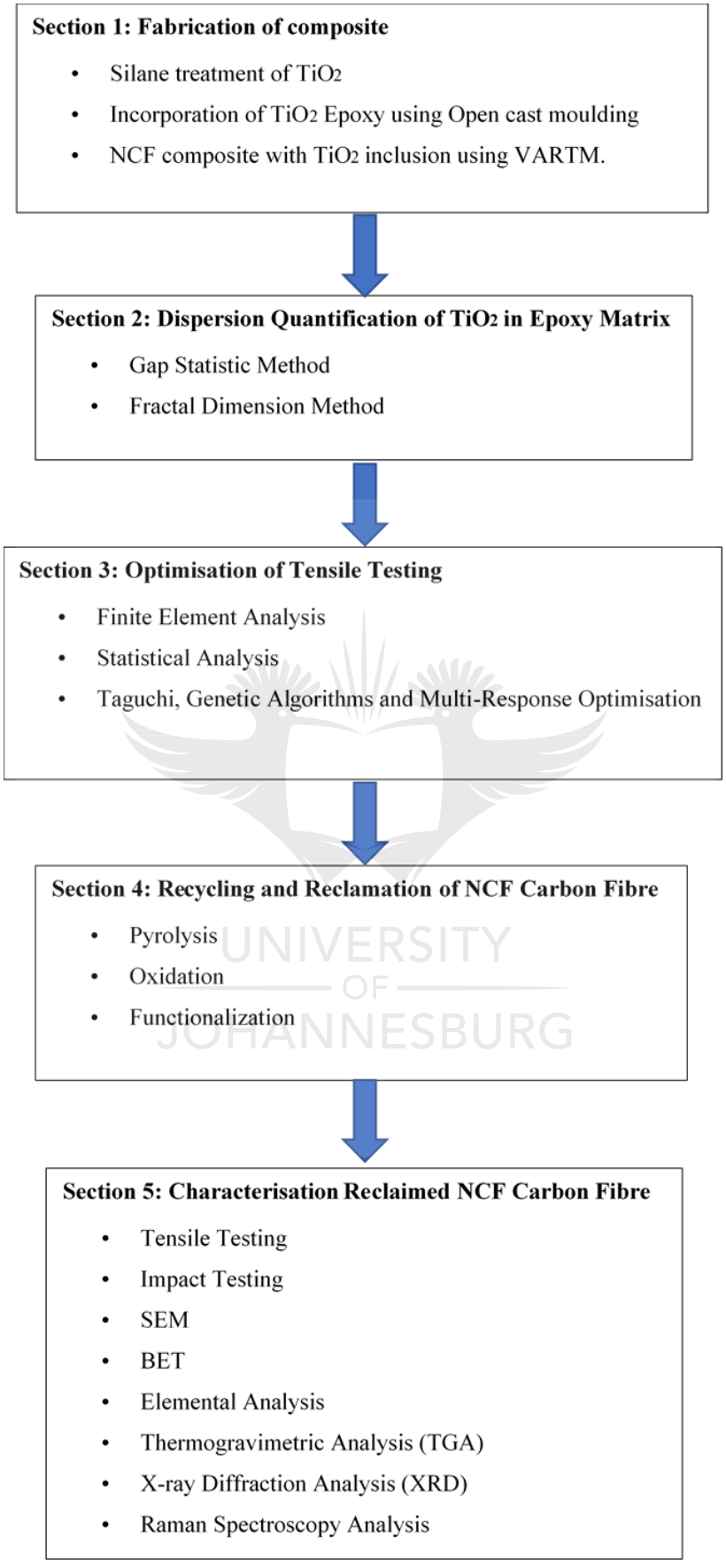

Figure 3.1 Sections of Methodology

Table 3.1 List of Materials

Material	Source	Purity
Titanium(iv) Oxide	Sigma Aldrich	≥99.5% trace metals basis
3-Aminopropyl)Triethoxysilane	Sigma Aldrich	98.0%
Carbon Fibre Non-Crimp Fabric Of ±45° Fibre Orientation (414 g/m^2 *area weight*, 3,700 tex Titer, 7.2 Mm) With 6 $g/m2$ Polyester Stitching Thread	Seartex Ltd South Africa/ Germany	-
Mirror Glaze Mold Release	Meguiars Ltd	-
Prime 20 Lv Resin	Advanced Materials Technology (Pty) Ltd	-
Prime 20 Lv Resin (1kg)	Advanced Materials Technology (Pty) Ltd	-
Spiral Bind	Advanced Materials Technology (Pty) Ltd	-
Tubing 10mm Polymide	Advanced Materials Technology (Pty) Ltd	-
PEELPLY NYLON 085g/LTX/PS 1000MM	Advanced Materials Technology (Pty) Ltd	-
Sealant Tape B1192 10x2mmx22.5m /22	Advanced Materials Technology (Pty) Ltd	-
Vac Film 450v 50mic 1.50m Tube 60 /300	Advanced Materials Technology (Pty) Ltd	-
Shade Mesh	Advanced Materials Technology (Pty) Ltd	-

Table 3.2 List of Equipment

Equipment	Manufacturer	Ananlysis
Heating Plate with magnetic stirrer	FMH Instrument	Heating and Stirring
Thermometer	FMH Instrument	Temperature analysis
Glass Open Cast Mould		Moulding
Vacuum Oven	Shel Lab Ltd	Curing and de-gassing
Vacmobile modular 2s	Shel LabLtd	Vacuum assisted Resin Transfer Moulding
Carbolite EHA one-zone model furnace	A Carbolite Ltd	Pyrolysis
Variac, and a reflux system	Variac Ltd	Refluxing
Dryer	EcoTherm Ltd	Drying fibres
Brunauer-Emmet-Teller (BET) 2460 micromeritics instrument	Micromeritics Instrument Corporation	BET Analysis
A Thermo Scientific Flash 2000	Thermo Scientific™	Elemental Analysis
TESCAN VEGA 3 XMU scanning electron microscope (SEM) with an accompanying XMAX Oxford Instrument Energy Dispersive X-Ray (EDX) analyser	Escan Analytics Ltd	SEM and EDX analysis
SDT-Q-600 thermogravimetric analyser	TA Instruments Ltd	Thermogravimetric analysis
A Rigaku Ultima IV X-Ray diffractometer	Rigaku Global Ltd	X-ray diffraction analysis
Renishaw Invia Reflex equipped with an IlluminatIRII FTIR microscope	inVia™	Raman spectroscopy analysis
100 kN capacity MTS Alliance RF/100 tensile testing equipment	MTS Alliance Ltd	Tensile Testing
Instron impact testing machine	Instron Ltd	Impact Testing
KB-45 Band Saw	ECCO Machinery™	Cutting

3.2 Fabrication of Composite Plates

The epoxy resin (PRIME 20 LV) and hardener (PRIME 20 SLOW) used for matrix preparation in this study were purchased from Advanced Materials Technology (Pty) Ltd. The non-crimp fabric of $\pm 45°$ fibre orientation ($414\ g/m^2\ area\ weight$, 3,700 tex titer, 7.2 μm) with 6 g/m^2 polyester stitching thread, donated by Seartex, was used as fibre reinforcements. The primary Nano inclusion used is commercially available titanium (IV) oxide (TiO_2) and nanoparticles ($21\ nm$), acquired from Sigma Aldrich for the fabrication of the nanocomposites.

Two sets of samples were manufactured with and without TiO_2 nanoparticle inclusion. Additionally, these samples were fabricated with two different techniques namely; open cast moulding and Vacuum assisted resin transfer moulding (see Figure 3.4and Figure 3.5). Open cast moulding was used to fabricate samples without fibre reinforcement; neat epoxy (NE), methanol treated TiO_2 (MTN), silane functionalised TiO_2 nanocomposite (STN) and non-functionalised TiO_2 nanocomposite (TN). Vacuum Assisted Resin Transfer Moulding (VARTM) was used for the fabrication of the NCF carbon fibre reinforced composite (CF-NE) and for NCF carbon fibre reinforced composite with TiO_2 inclusion (CF-STN).

3.3 Silane Functionalisation and Methanol Treatment of TiO_2

Titanium (IV) oxide nanoparticles exhibit a high affinity for agglomeration when dispersed into epoxy resin. This is due to its high hydrophilicity, which is detrimental to the properties of the fabricated composite. This drawback can be minimised through silane functionalisation. In theory, silane is capable of forming a hydrophobic film on the surface of titanium dioxide via the chemical bonding of Ti–O–Si and cross-linking of Si–O–Si bonds. Naturally, TiO_2 has a high surface-to-volume ratio which makes the reaction possible [106]. The setup included a glass beaker, thermometer and a heating plate equipped with magnetic stirring as seen in Figure 3.2.

(a) (b)

Figure 3.2 Experimental setup for functionalisation of TiO_2. (a) Glass beaker and heating plate with magnetic stirring; (b) Thermometer

The silane solution as shown in Figure 3.3 (a), was also purchased from Sigma Aldrich. The functionalisation was conducted in accordance with the procedure reported by Adhikari et al. [328]. The functionalisation was carried out by first preparing the silane solution with a liquid mixture of 95% methanol, 5% distilled water and 1% silane. To ensure homogeneity, the mixture was thoroughly stirred for 15 min. The TiO_2 (see Figure 3.3 (b)) nanoparticles were first weighed ($2.5wt\%$) then dispersed into the silane solution while continuously stirring for an additional 10 min before heating the mixture for 1 hr at 95℃ on a hotplate to facilitate evaporation of both methanol and distilled water. Further drying was performed in a vacuum oven at a temperature of 100℃ until only a dry nanoparticle residue was observed. The recovered residue was crushed and pulverised in a ceramic crucible as shown in Figure 3.3 (c), before dispersing into the matrix. To assess the influence of 95% methanol addition on TiO_2, samples were also fabricated using the silane functionalisation methodology but without the 1% silane.

(a)

(b)

(c)

Figure 3.3 (a) Silane Solution; (b) TiO_2 nanoparticles before functionalisation and (c) TiO_2 nanoparticles after functionalisation

3.4 Open Cast Moulding

A square mould fabricated from glass with inner dimensions of $200\ mm \times 200\ mm \times 5\ mm$ was used for open cast moulding as shown in Figure 3.4 (a). The inner section of the mould was lined with strips of stick-on peel plies developed for the provision of a leakproof mould to ensure easy removability after curing the composite. The open cast process requires four (4) stages, namely pre-moulding preparation, preparation of the matrix, filling of the

mould with matrix, and curing. The pre-moulding preparations involved mechanical cleaning of the mould with dry clean cloth and the application of a mould releasing agent such as Meguear's mirror glaze maximum mould release wax 8 or 87 (for hot temperatures) as shown in Figure 3.4 (b). In the second stage, the matrix was prepared by mechanically dispersing TiO_2 nanoparticles into the less viscous hardener and thereafter degassing before the addition of the epoxy with a mix ratio of 100: 26 by weight as per the manufacturer's recommendation. After the second mechanical agitation and degassing, the mixture was poured into the mould and cured in a Shel Lab Oven for 7 *hours* at a temperature of 65℃ in accordance with the manufacturer's recommendations as shown in Figure 3.4 (c). The moulding process was carried out in accordance with the methodology presented by Agrawal and Satapathy [329].

(a) (b)

(c)

Figure 3.4 Setup for conducting Open Cast Moulding. (a) Glass Mould with peelply; (b) Mould release wax; (c) Curing Oven

3.5 Vacuum Assisted Resin Transfer Moulding (VARTM) System

In this study, the fibre-reinforced samples were produced using vacuum assisted resin transfer moulding. The Vacmobile modular 2s model equipped with a single-phase $50\ mbar$ $(50\ Pa)$ VSV-20 vacuum pump and a resin trap with catching capacity of $12\ litres$ was used for the moulding process as shown in Figure 3.5.

Figure 3.5 The Vacmobile modular 2s model for VARTM

The basic items required for performing the moulding are: a spiral bind, tubing, peel ply, sealant tape, vacuum bag, mesh, mould plate, and epoxy hardener as shown in Figure 3.6. Aside from the mould plate, all the other items were purchased from Advanced Materials Technology (AMT)-South Africa.

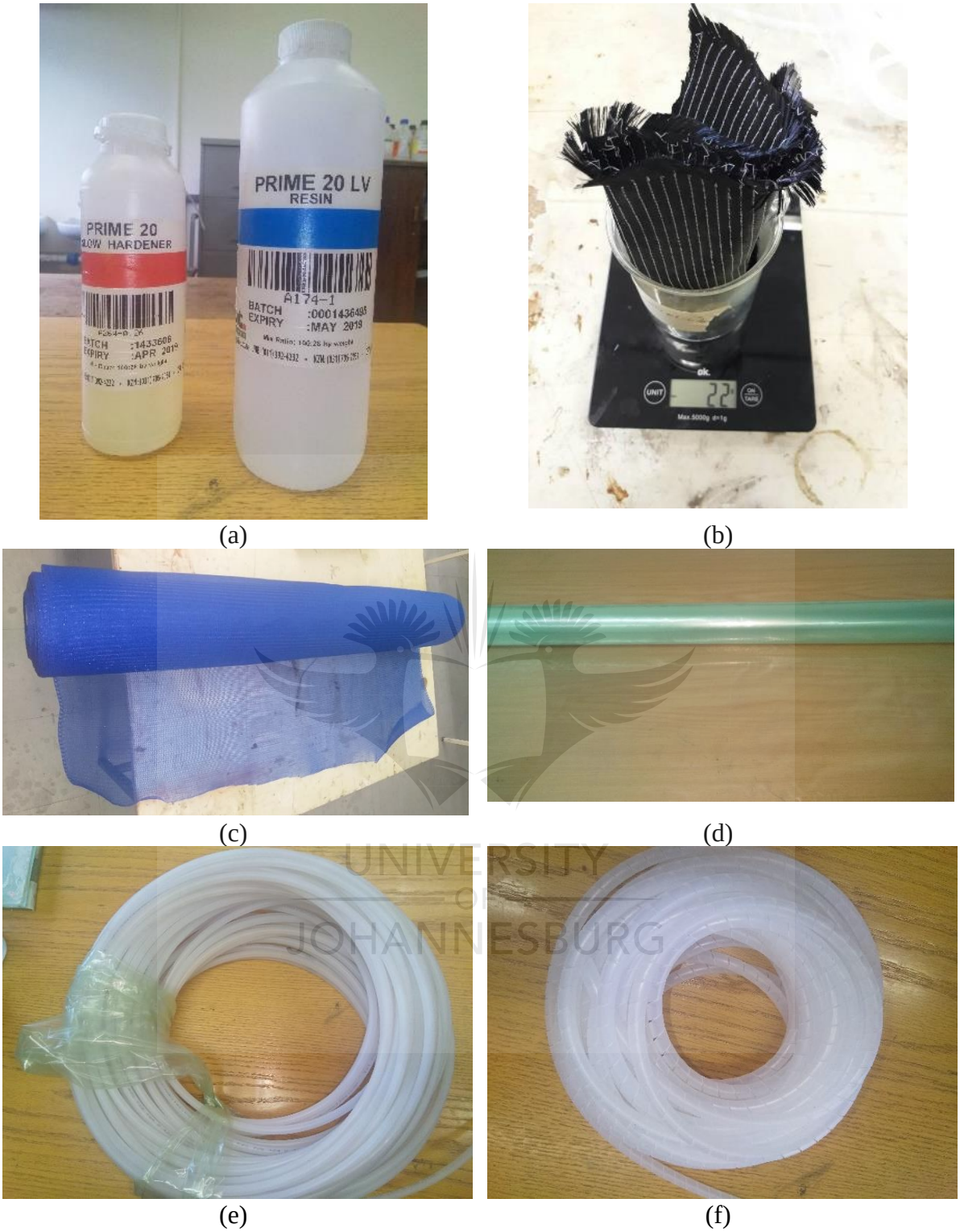

Figure 3.6 Primary items for the VARTM process. (a) Epoxy and hardener; (b) Carbon fibre; (c) Mesh; (d) Vacuum bag; (e) Tubing and (f) Spiral bind

The moulding process involved three (3) main stages, namely material preparation, mould preparation, and the moulding process. The first stage required cutting eight plies of carbon fibre non-crimp fabric (CF-NCF) with dimensions of $300\ mm \times 200\ mm$. The mesh

was cut to a quarter of the length of the CF while the peel ply dimension was cut slightly smaller than the moulding plate. One end of the mesh was wrapped around the spiral bind and sown, after which the entire stack comprising CF-NCF (bottom), peel ply (middle) and mesh and spiral bind (top) was stitched together at the two top corners as shown in Figure 3.7.

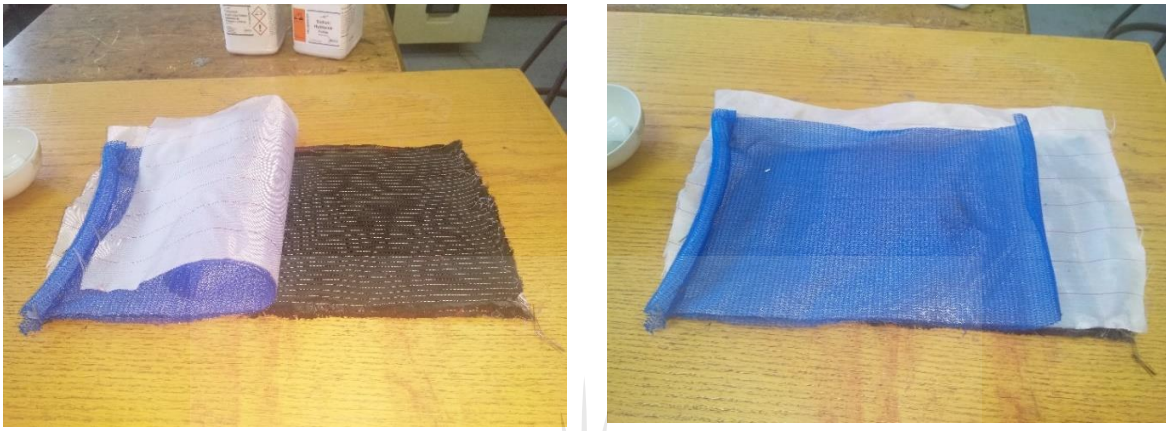

(a) (b)

Figure 3.7 Stacked Material for moulding. (a) Before corner stitching; (b) After Corner stitching

The second stage involved cleaning the stainless steel moulding plates with acetone and wiping them thoroughly to remove any debris left over from previous usage. The surface of the plates was waxed before placing the stacked materials on it. This was immediately followed by the sealant plate application along the inner edges of the plate. An inlet tubing with one end connected to the sown spiral bind, and the other end left as a suction end for matrix intake, was secured on the sealant tape. Concurrently, one end of the outlet tubing was secured onto the sealant tape and the other end connected to one of the inlet ports of the Vacmobile modular vacuum pump. Lastly, the vacuum bag was fastened onto the sealant tapes, followed by sealing the inlet tube end and starting the pump to investigate the integrity of the vacuum seal. After thorough checks to block all leakages, the outlet tube was unsealed and placed into the prepared matrix (see Figure 3.8). The infusion process is completed when the epoxy starts rising out of the outlet tube. The process was conducted in accordance with the methodology presented by

Abusrea *et al.* [76]. The recommended curing condition from the manufacturer was set at 65℃ for 7 $hours$.

(a) (b)

Figure 3.8 The VARTM Process. (a) Testing integrity of vacuum seal; (b) Process of resin infusion via vacuum suction

Mechanical agitation as a means of dispersion and mixing introduces bubbles into the matrix which results in the formation of voids and therefore degrades the mechanical strength of the composite. In this study degassing was conducted using a Shel Lab Vacuum oven at a pressure of 60 kpa for approximately 10 min before crushing the formed bubbles under atmospheric pressure (see Figure 3.9).

(a) (b)

Figure 3.9 Process of degassing. (a) Sample without degassing; (b) Epoxy Matrix placed in the vacuum oven

3.6 Quantification of Dispersion in Nanocomposites

3.6.1 Quantification using gap Statistics

3.6.1.1 Gap Statistic Estimation

Composite plates were manufactured using titanium (IV) oxide nanoparticles (21 nm), purchased from Sigma Aldrich and dispersed within an epoxy matrix at a fraction weight of 2.5 $wt\%$. The concept was tested using five models which simulate varying and commonly occurring states of dispersion. The models presented in Figure 3.10 are: uniformly dispersed (Model 1), randomly dispersed (Model 2), randomly dispersed with small agglomeration formations (Model 3), randomly dispersed with the inclusion of three large agglomerates (Model 4), and lastly randomly dispersed with a large agglomerate (Model 5).

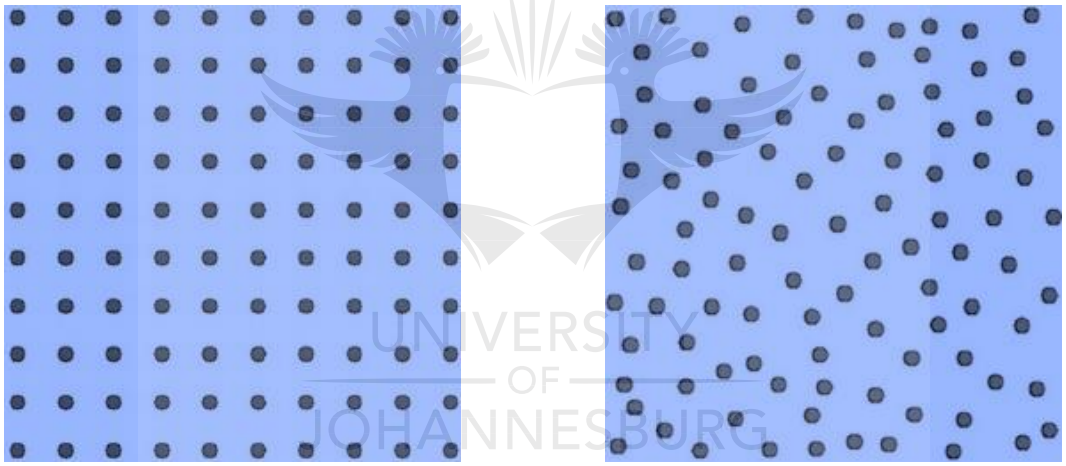

(a) (b)

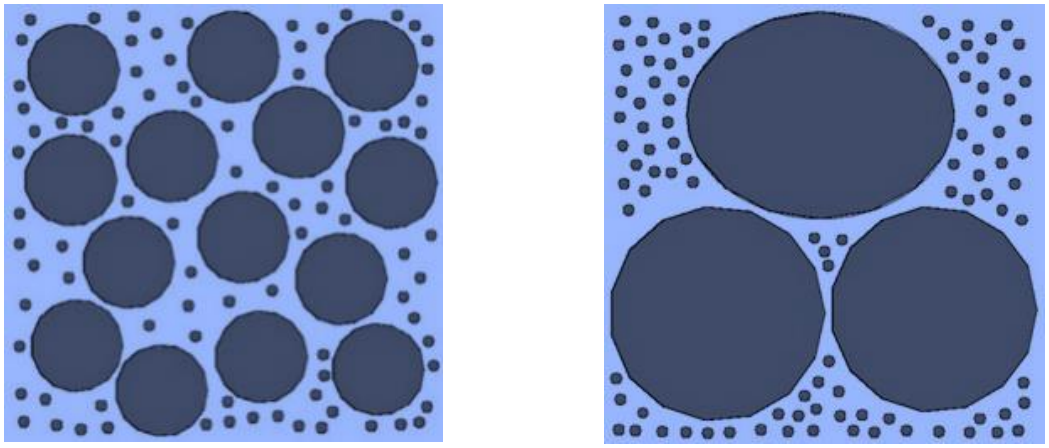

(c) (d)

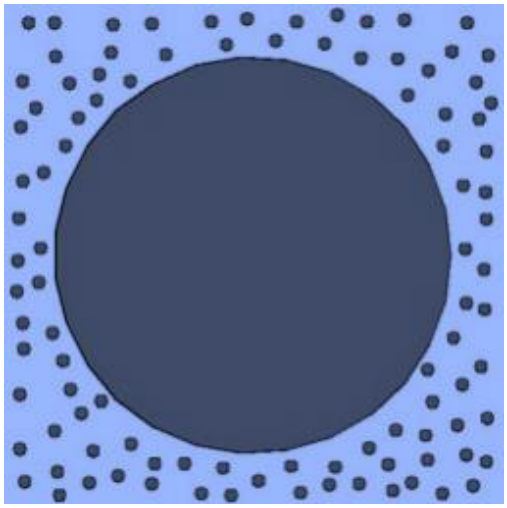

(e)

Figure 3.10 Concept models simulating possible states of particle distribution. (a) Model 1; (b) Model 2; (c) Model 3; (d) Model 4 and (e) Model 5. [330]

Tibshirani et al. [331] developed a gap statistic model, which is relatively efficient in estimating the number of clusters present within a data set. The method can incorporate the majority of the existing cluster algorithms like the K-mean and the hierarchical algorithms to quantify the variations in cluster dispersion with respect to a reference distribution. The gap criterion is effective in identifying the number of clusters, which have the largest gap value, and the optimal number of clusters is derived from a solution dataset with a tolerance range possessing the largest global or local gap value. The gap value was formulated as Equation (3.1):

$$Gap_n(k) = E_n^*\{\log(W_k)\} - \log(W_k) \tag{3.1}$$

where E_n^* is the estimated expected value derived from Monte Carlo sampling with respect to a reference distribution, n is the size of the sample dataset, k is the optimal number of clusters estimated, and W_k is the pooled within-cluster sum of squares around the cluster mean or dispersion measurement. The main disadvantage of the gap criterion is the associated high computational cost due to the application of reference data to the cluster algorithms for every cluster solution [331]. The MATLAB algorithm for computing the gap criterion is provided in Appendix A1. The resulting gap characteristics were implemented as a first principle basis in

developing the formulation of a gap factor (G_0) expressed in Equation (3.2) and illustrated in Figure 3.11 as the area between the expected and observed curves.

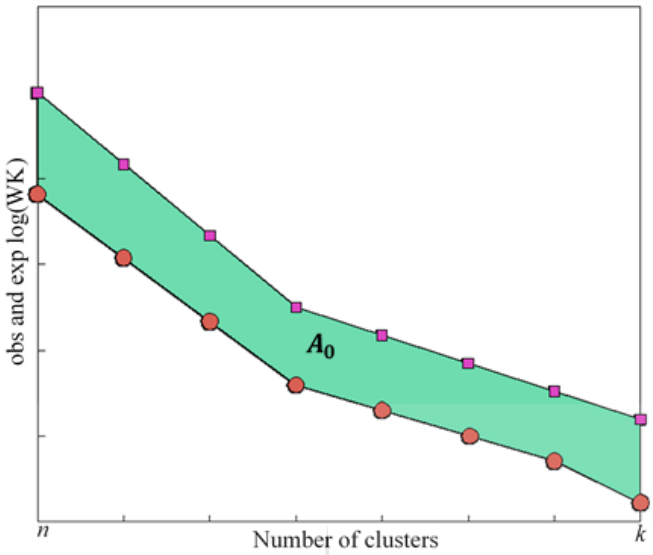

Figure 3.11 Illustrations of the Area Under a Curve Method (AUCM) for dispersion quantification. [330]

$$G_0 = \left[\int_{=1}^{k} f(x_e)dx\right] - \left[\int_{n=1}^{k} f(x_o)dx\right] \tag{3.2}$$

where G_0 is the gap factor, $f(x_e)$ is the area under the expected curve, $f(x_o)$ is the area under the observed curve, and n and k represent the initial and final inspected $k - mean$ values respectively.

The following are the assumptions adopted to ensure effectiveness and accuracy: (1) the number of particles within each model were the same to establish a standardised reference for all models, (2) the particle location and data extraction were based on a particle centroid approach, (3) the cluster analysis was conducted using the same number of inspected k values and finally (4) all the model and scanning electron microscopy (SEM) images were converted to 1500×1500 pixels.

3.6.1.2 Particle Spacing and Size Dispersity

Applying only the gap factor for the dispersion quantification is not comprehensive enough and therefore two more factors were formulated to include a dimension of particle spacing dispersity (PSD_1) and a particle size dispersity (PSD_2). PSD_1 was determined via an initial step of computing the minimum spatial distances between individual particles within an image with the MATLAB coded algorithm provided in Appendix A2. All the distances between the points on the particle boundary (B) and boundary (A) as illustrated in Figure 3.12, were computed through the formulation in Equation (3.3).

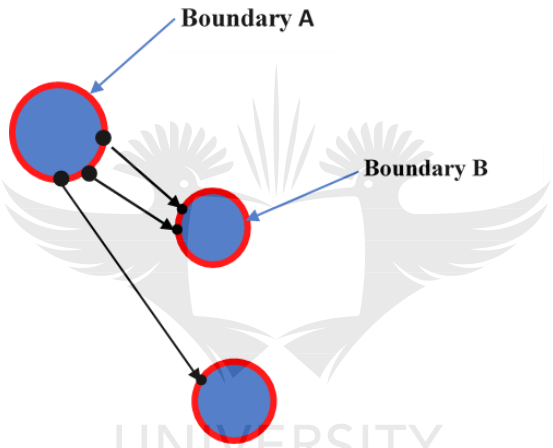

Figure 3.12 An illustration of interparticle spacing

$$S = \sqrt{(Boundary\ Ax - Boundary\ Bx)^2 + (Boundary\ Ay - Boundary\ By)^2} \qquad (3.3)$$

Where x and y represent the Cartesian coordinates of the particles A and B. The overall minimum distances were calculated for assessment of the inter particle spacing dispersity (PSD_1). Similarly, the particle size dispersity was calculated using the area of the distributed particles (PSD_2). The general expression for calculating the dispersity (PSD) is presented in Equation (3.4):

$$PSD = \left[\left(\frac{\sum {x_i}^2}{\sum x_i}\right) \Big/ \left(\frac{\sum x_i}{N}\right)\right] \tag{3.4}$$

Where x_i is the inter particle spacing or particle size while N is the number of variables. In establishing the dispersion quantity (D), a dispersion parameter (D_P) which is a summation of G_0, PSD_1 and PSD_2 (see Equation (3.5)) was formulated as shown in Equation (3.6). For a uniformly dispersed state which is considered as ideal, $D = 100\%$ as $D_P = 3$.

This means $Particle\ Size\ Dispesity$, $Particle\ spacing\ Dispersity$ and $Gap\ factor$ each have a value =1.

$$Dispersion\ Quantity\ (D) = \left(\frac{3}{D_P}\right) \times 100\% \tag{3.5}$$

$$D_P = G_0 + PSD_1 + PSD_2 \tag{3.6}$$

3.6.2 Quantification using Fractal Dimension

This technique was formulated based on the fractal dimension and variance obtained from the SEM images to quantify the state of dispersion. The five dispersion states presented in Figure 3.13 were used for the proof of concept. The fractal dimensions of black and white images obtained from image segmentation of the models were computed using a box counting method [332]. The choice of the box counting method was due to its compatibility and simplicity. The algorithm for fractal dimension estimation developed by Moisy, [333] in MATLAB was adopted (see Appendix A3). Equation (3.7) was used for calculating the fractal dimension:

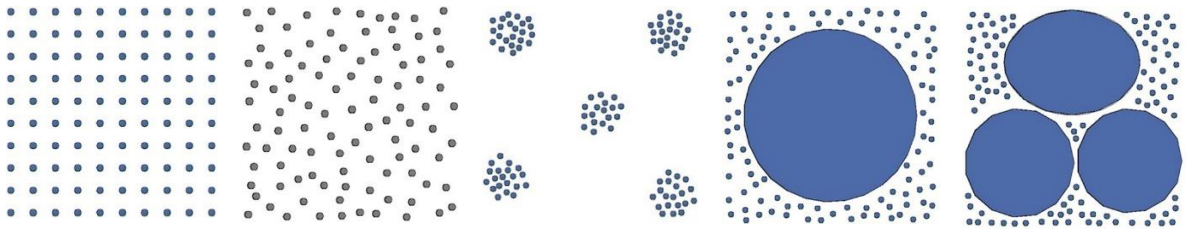

(a) (b) (c) (d) (e)

Figure 3.13 Proof of concept models; (a) Uniformly dispersed model, (b) Randomly dispersed model, (c) Cluster distribution model, (d) One large Agglomerate model and (e) One Three large Agglomerate model. [330]

$$D_f = -\frac{d\ln N}{d\ln R} \tag{3.7}$$

Where the fractal dimension is D_f for fractal set C, and N is the D-dimensional (D=1,2,3) set of R sized boxes ranging from the non-zero elements of C. R = 1, 2, 4 ... 2^P, where P is the smallest integer. D_f was eventually calculated using a second order finite difference followed by an estimation of the variances for each model. The upper boundary was set using the variance value obtained from the uniformly dispersed model (S_{UD}^2) which was considered the ideal state of dispersion. Therefore, (S_{UD}^2) was found to be 1.89×10^{-1} while a dispersion factor $(f_D) = 1.0 \times 10^{-1}$ was carefully selected. The Equation (3.8) was formulated to quantify the state of dispersion:

$$D_0 = \left(\frac{S^2}{f_D}\right) \times 100\% \tag{3.8}$$

where the dispersion quantity is (D_0) and(S^2) is the fractal dimension variance of the sample image. A perfectly homogeneous state of dispersion or ideal conditions will result in $D_0 = 100\%$. Therefore, the set boundary condition was $0\% \leq D_0 \leq 100\%$, where as $D_0 \rightarrow 100$ % dispersion improves. The measures adopted to ensure accuracy and consistency in the derived results were: converting all the model and sample SEM images to 1500×1500 pixels and ensuring that all the models used in the proof of concept had the same number of particles.

3.6.3 Image Segmentation and centroiding

Image segmentation was critical in the generation of grayscale and binary (black and white) images from which data was extracted to develop proof of concept for dispersion quantification using both gap statistics and fractal dimension. The segmentation process was accomplished via the use of a K-Mean algorithm [334]. The segmented images were then used for the extraction of critical data from the white pixels such as the area and centroid of

individual particles. The MATLAB algorithms for image segmentation, area and centroid computations are provided in Appendix A4.

3.7 Optimisation of Tab Design for Minimisation of Stress Concentration

Tensile testing is one of the oldest methods used to identify the elastic properties of materials. It is a fundamental characterisation technique applied to achieve accuracy, which is of paramount importance in material science engineering. Typically, bonded tabs are used to prevent premature failure of fibre-reinforced composites. This section presents the methodologies for finite element analysis and three optimisation approaches for comparative analysis. The objective was to optimise tab configurations, namely tab stiffness, tab thickness, tab length, tab taper angle, and adhesive thickness - with the aim of minimising induced stress concentrations in the tab termination region during testing. The response variables were the following three induced stress concentrations: normal stress (σ_x) peel stress (σ_y) and shear stress (τ_{xy}).

3.7.1 Tensile testing

Tensile testing according to the ASTM D D3039 standard [223] as depicted in Figure 3.14 was carried out on the unidirectional non-crimp fabric composite plate donated by Chomarat Ltd using 100 kN capacity MTS Alliance $RF/100$ tensile testing equipment with a crosshead speed of 2 mm/min. Ten sets of samples with 0° and 10° fibre orientations were cut with a waterjet and then tabbed with G-10 glass/epoxy rectangular tabs to specified dimensions as shown in Figure 3.15. Bonding was achieved using Hysol 907 two-part paste adhesive. Strain gauges with configurations of 0°/90° and 0°/45°/90° were also bonded to the 0° and 10° orientations respectively.

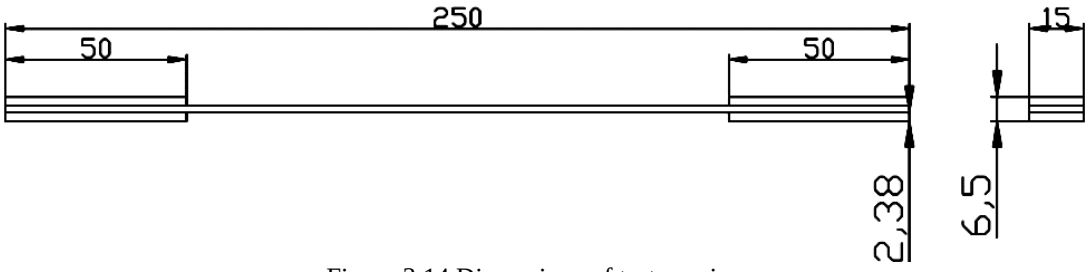

Figure 3.14 Dimensions of test specimen

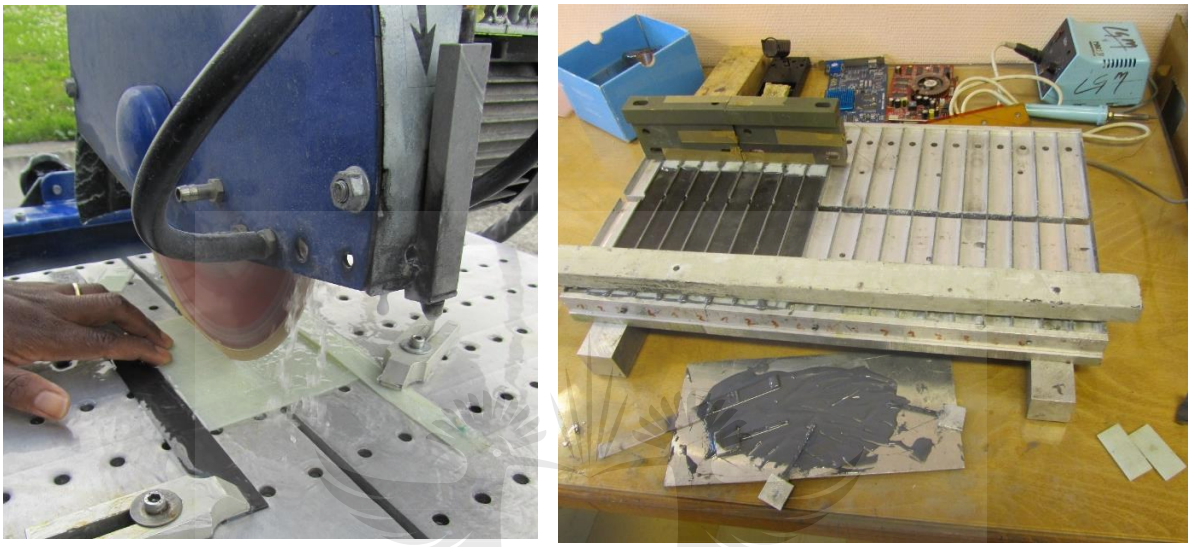

(a) (b)

Figure 3.15 Tabbing process. (a) Cutting of tabs; (b) Bonding of tabs [335]

3.7.2 Finite Element Analysis

Finite element analysis is an effective and efficient tool for modelling and simulating stress-related engineering problems. The stress concentrations induced within the tabs, the tab termination region, and the adhesive bond were comprehensively assessed and analysed. A software package ANSYS APDL Mechanical 18 was used to investigate the stress concentrations induced at the regions. All the generated and computed results were normalised. Some necessary assumptions were introduced to simplify and reduce the computational time for the modelling and simulation process. Firstly, the assumption of constant width made the use of two-dimensional models possible and adequate for analysis. Secondly, the plain stress assumption where $\sigma_z = \tau_{xz} = \tau_{yz} = 0$, was preferred to a plain strain assumption. This assumption prioritises the edges and surfaces of the sample and is specifically suitable for

composite materials as it captures the volume of the test sample [7]. Thirdly, symmetry was implemented to further simplify and reduce the number of nodes. A quarter of the specimen was used in the analysis as shown in Figure 3.16. Also, linear elastic modelling was preferred while the 8 node 183 element in ANSYS was used for meshing. To minimise errors a double layered adhesive region meshing of 2:1 aspect ratio representing the adhesive thickness was employed as shown in Figure 3.17. The design parameters were: tab thickness, tab length, tab taper angle, and adhesive thickness.

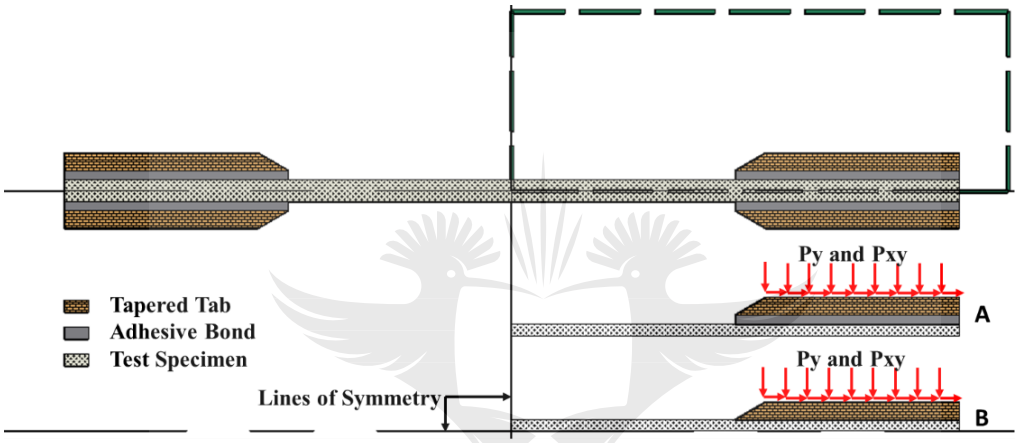

Figure 3.16 Finite element model configurations

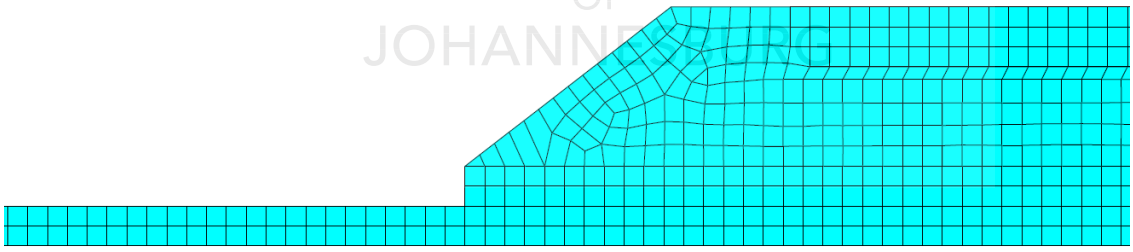

Figure 3.17 Meshing of the adhesive bonded tabs [335]

The simulation of gripping during tensile testing is critical to obtain accurate and realistic results. The equation formulated by MTS Systems Corporation [336] expressed in Equation (3.9) and Equation (3.10) for simulating the grip in the jaw clamping was employed. This equation fundamentally establishes and describes the relationship between normal gripping

traction (P_y), shear traction (P_{xy}) on the surface of the tab, and the normal (F_y) and shear forces (F_{xy}) applied, where the coefficient of friction is μand grip taper angle is Ø:

$$\frac{P_{xy}}{P_y} = \frac{\frac{F_{xy}}{A_{tab}}}{\frac{F_y}{A_{tab}}} = \frac{F_{xy}}{F_y} = \tan(\tan^{-1}(\mu) + \emptyset) \tag{3.9}$$

$\mu = 0.06, \emptyset = 15^o$

$$\frac{P_{xy}}{P_y} = \frac{F_{xy}}{F_y} = 0.33 \tag{3.10}$$

3.7.3 Taguchi Based Optimisation

The Taguchi method is a powerful tool for systematically analysing and solving engineering problems. It has contributed to the reduction or total elimination of trial and error methods in an industry which directly impacts manufacturing cost, time loss, quality and efficiency [337]. The Taguchi approach uses an orthogonal array design to significantly reduce the number of experiments which ultimately limit the effect of difficult to control factors as shown in Table 3.3 [338–340]. A loss function is used to compute the disparities between experimental and desired data. This is accomplished via conversion to a signal-noise (SN) ratio [338,340]. The SN ratio analysis is carried out using three quality characteristics namely; the lower-the-better, the higher-the-better and the nominal-the-best. The optimal parameters (see

Table 3.4) are derived from the S/N analysis for all levels of the process [338,341]. The S/N ratio formulated is shown in Equation (3.11):

$$\eta = S/N_S = -10 \log\left[\frac{1}{n}\sum_{i=1}^{n} y_i^2\right] \tag{3.11}$$

where n is the number of experimental or simulated observations and y_i is the *ith* experimental data observed [342].

Table 3.3 Taguchi Orthogonal Array Design [Taguchi L8 (25)]

Simulation no.	Factor A	Factor B	Factor C	Factor D	Factor E
1	1	1	1	1	1
2	1	1	1	2	2
3	1	2	2	1	1
4	1	2	2	2	2
5	2	1	2	1	2
6	2	1	2	2	1
7	2	2	1	1	2
8	2	2	1	2	1

Source [335]

Table 3.4 Tab design parameters and their levels

Design Factors	Symbol	Level 1	Level 2
Tab stiffness	A	32.6	132
Tab Thickness	B	0.5	1.5
Tab length	C	50	100
Tab taper angle	D	5º	90º
Adhesive thickness	E	0.25	1.5

Source [335]

3.7.4 Multi-Response (Desirability Approach)

A theoretical basis for multiple response optimisation was established by Derringer and Suich [343]. The primary motivation for developing such an approach was to overcome the drawbacks of single response optimisation techniques [344,345]. The incorporation of a desirability function was essential for integrating optimal process parameters for quantification of the optimal values. Optimal desirability values are computed using a gradient algorithm [346] as shown in Equation (3.12), Equation (3.13) and Equation (3.14) for evaluating individual desirabilities. The desirability value lies between zero (0) and one (1) for which a value close to 1 is an indication of approaching acceptable responses from settings.

Additionally, a composite desirability (D) index is calculated for generating the optimal settings for a set of responses.

$$d_i = 0 \qquad \widehat{y_i} < L_i \tag{3.12}$$

$$d_i = \left(\frac{(U_i - \widehat{y_i})}{(U_i - T_i)}\right)^{r_i} \quad T_i \leq \widehat{y_i} \leq U_i \tag{3.13}$$

$$d_i = 1 \qquad \widehat{y_i} < T_i \tag{3.14}$$

The composite desirability which is the weighted geometric mean of all the individual desirability's is calculated using Equation (3.15):

$$D = \left(\prod (d_i{}^{w_i})\right)^{\frac{1}{W}} \tag{3.15}$$

For cases where all responses have the same importance, the desirability is calculated using Equation (3.16) as:

$$D = (d_1 \times d_2 \times \ldots \times d_i)^{\frac{1}{n}} \tag{3.16}$$

where:

$d_i =$ individual desirability for the i^{th} response

$D =$ composite desirability

$L_i =$ lowest acceptable value for i^{th} response

$n =$ number of responses

$r_i =$ weight of desirability function of i^{th} response

$T_i =$ target value of i^{th} response

$U_i =$ highest acceptable value for i^{th} response

$w_i =$ importance of i^{th} response

$W = \text{sum of } w_i \text{or } \sum w_i$

$\hat{y}_i = \text{Predicted value of } i^{th} \text{ response}$

3.7.5 Genetic Algorithm Optimisation

Another optimisation approach considered was genetic algorithms (GA) for comparison with Taguchi and multiple response approaches. GAs are categorised under the family of evolutionary algorithms based on Darwin's evolution theory first developed by John Holland [347]. It is a non-linear approach, which solves optimisation problems by converging in an optimal global solution. In solving optimisation, GA uses a population's chromosomes instead of decision variables. However, all chromosome used for the evaluation of the objective function carries decision variables. Parent chromosome selection from a mating pool of suitable candidates is critical to ensure continuous production of new generations [348]. New chromosome production is achieved by using a crossover operator that selects parents via a two-by-two (binary crossover) technique which facilitates the breeding of new offspring [349–351]. Gene mutation of offspring is vital to reaching an optimal solution because of the versatility introduced into the next population's new generation [352].

The objective functions used for conducting multi-objective optimisation are shown in the regression Equations (3.17) to (3.19). Presented below is the optimisation problem formulation:

$x(1) - - - \ Tab\ stiffness$

$x(2) - - - \ Tab\ thickness$

$x(3) - - - \ Tab\ length$

$x(4) - - - \ Tab\ tapper\ angle$

$x(5) - - - \ Adhesive\ thickness$

$Lower\ bound = [32.6\ 0.5\ 50\ 5^o\ 0.25\ 1]$

$Upper\ bound = [132\ 1.5\ 100\ 90^o 1.5\ 1]$

$$\boldsymbol{y(1) = Objective\ 1 --\ equation\ for\ \sigma x(Norm)\ minimize}$$

$$\boldsymbol{y(1)} = 1.1678 + 0.001220\boldsymbol{x(1)} + 0.0309\boldsymbol{x(2)} - 0.000078\boldsymbol{x(3)} + 0.001827\boldsymbol{x(4)} - 0.1064\boldsymbol{x(5)} \quad (3.17)$$

$$\boldsymbol{y(2) = Objective\ 2 --equation\ for\ \sigma y(Norm)\ minimize}$$

$$\boldsymbol{y(2)} = 0.0583 + 0.000363\boldsymbol{x(1)} + 0.01387\boldsymbol{x(2)}0.000045\boldsymbol{x(3)} + 0.000256\boldsymbol{x(4)} - 0.01254\boldsymbol{x(5)} \quad (3.18)$$

$$\boldsymbol{y(3) = Objective\ 3 --equation\ for\ \tau xy(Norm)\ minimize}$$

$$\boldsymbol{y(3)} = 0.0332 + 0.000245\boldsymbol{x(1)} + 0.00791\boldsymbol{x(2)} + 0.000015\boldsymbol{x(3)} + 0.000269\boldsymbol{x(4)} - 0.01583\boldsymbol{x(5)} \quad (3.19)$$

3.7.6 Two -Level $\left(2^k\right)$ Factorial Design

A full factorial 2-level five factorial design was used to describe the design of experiment (DoE) for the finite element simulations. The normalised induced stress concentrations at the tab termination region data was collected for all possible combinations under study. In general, a two-level (2^k) factorial design, and k factors each with 2 levels having 2^k treatment were employed to identify important factors and their interactions. The interactions had one degree of freedom. The regression equation used for prediction is the following first order equation:

$$y = \beta_0 + \beta_1 x_1 + \beta_2 x_2 + \cdots + \beta_k x_k$$

where β_1, β_2 ... β_k are related to the main effects and interactions. While each factor's level is coded as $(coded - 1\ and + 1)$.

3.7.7 Analysis of Variance (ANOVA)

ANOVA was implemented to determine the factors that significantly influence the stress concentration within tabs during tensile testing. This was accomplished by letting y donate the total of all observation under the ith level of factor A, Y. j. denote the total of all observations under the jth level of factor B, Y ij denotes the total of observation in the $ijth$

cell, and $Y\ldots$ denote grand total of all the cell, and grand averages. This is mathematically expressed in Equation (3.20):

$$Yi.. = \sum_{j=1}^{b}\sum_{k=1}^{n} Y\ ijk\ \bar{Y}i = \frac{Yi..}{bn} \quad i = 1,2,\ldots,a$$

$$Y.j. = \sum_{j=1}^{b}\sum_{k=1}^{n} Y\ ijk\ \bar{Y}.j. = \frac{Y.j.}{an} \quad j = 1,2,\ldots,b \tag{3.20}$$

$$Yij. = \sum_{k=1}^{n} Y\ ijk\ \bar{Y}ij. = \frac{Y\ldots}{n}\ \begin{matrix} i = 1,2,\ldots,a \\ j = 1,2,..,b \end{matrix}$$

$$Y\ldots = \sum_{i=1}^{a}\sum_{j=1}^{b}\sum_{k=1}^{n} Y\ ijk\ \bar{Y}\ldots = \frac{Y\ldots}{abn}$$

The total corrected sum of squares is expressed in Equation (3.21) as:

$$\sum_{i=1}^{a}\sum_{j=1}^{b}\sum_{k=1}^{n}(Y\ ijk - \ \bar{Y})^2$$

$$= \sum_{i=1}^{a}\sum_{j=1}^{b}\sum_{k=1}^{n}[(\bar{Y}i..-\bar{Y}..) + (\bar{Y}.j.-\bar{Y}i\ldots) + (\bar{Y}ij..-\bar{Y}i..-\bar{Y}.j.+\bar{Y}\ldots)$$

$$+(\bar{Y}ijk-\bar{Y}ij.)]^2$$

$$= bn\sum_{i=1}^{a}(\bar{Y}i..-\bar{Y}\ldots)^2 + an\sum_{j=1}^{b}(\bar{Y}.j.-\bar{Y}i..-\bar{Y}.)^2$$

$$+\mathrm{n}\sum_{\mathrm{i}=1}^{\boldsymbol{a}}\sum_{\mathrm{j}=1}^{\mathrm{b}}(\bar{\mathrm{Y}}_{ij.} - \bar{Y}_{.j.} + \bar{Y}\ldots)^{\mathbf{2}}$$

$$+\sum_{i=1}^{a}\sum_{j=1}^{b}\sum_{k=1}^{n}(Y_{ijk} - \bar{Y}_{ij.})^2 \tag{3.21}$$

The total sum of the squares is partitioned into a sum of squares due to the formation of "rows" or Factor A, (SS_A); sum of squares due to "columns" or factor B, (SS_B); a sum of squares due

to the interaction between A and B, (SS_{AB}); and a sum of squares due to error, (SS_E). Equation (3.21) shows that there must be at least two replicates ($n \geq 2$) to obtain an error sum of squares. This can be expressed symbolically in Equation (3.22);

$$SS_T = SS_A + SS_B + SS_{AB} + SS_E \tag{3.22}$$

The total degrees of freedom to the sums of squares may be expressed as follows: The main effects A and B have a and b levels, respectively; this implies that $a - 1$ and $b - 1$ degrees of freedom exist as shown. The interaction degrees of freedom are the number of degrees of freedom for the two (2) main effects namely A and B; that is, $ab - 1 - (a - 1) - (b - 1) = (a - 1)(b - 1)$. Within each of the ab cells, there are $n - 1$ degrees of freedom between the n replicates; hence there are $ab(n - 1)$ degrees of freedom for error. Assuming that the model (Equation (3.22)) is adequate and that the error terms $\in_{ijk}$ are normally and independently distributed with constant varianceσ^2, then each of the ratios of mean squares MS_A/MS_E, MS_B/MS_E and MS_{AB}/MS_E are distributed as F with a – 1, b – 1, and (a – 1)(b – 1) numerator degrees of freedom, respectively, and ab(n – 1) denominator degrees of freedom, and the critical region would be the upper tail of the variance table.

The total sum of squares is computed as usual by Equations (3.23) and Equation (3.24):

$$SS_T = \sum_{i=1}^{a}\sum_{j=1}^{b}\sum_{k=1}^{n} Y_{ijk}^2 - \frac{Y^2}{abn} \tag{3.23}$$

The sums of squares for the main effects are Equations (3.24) and Equation (3.25).

$$SS_A = \sum_{i=1}^{a} \frac{Y_{i\ldots}^2}{bn} - \frac{Y_{\ldots}^2}{abn} \tag{3.24}$$

$$SS = \sum_{j=1}^{b} \frac{Y_{.j.}^2}{an} - \frac{Y_{\ldots}^2}{abn} \tag{3.25}$$

SS_{AB} is obtained in two (2) stages. The sum of squares between the ab cell totals is firstly computed ("subtotals") as in Equation (3.26):

$$SS_{subtotals} = \sum_{i=1}^{a}\sum_{j=1}^{b}\frac{Y_{ij.}^2}{n} - \frac{Y_{...}^2}{abn} \tag{3.26}$$

This sum of squares also contains SS_A and SS_B. Therefore, the second step is to compute SS_{AB} (Equation (3.27)) as

$$SS_{AB} = SS_{subtotals} - SS_A - SS_B \tag{3.27}$$

SS_E (Equation (3.28) is computed by subtraction;

$$SS_E = SS_T - SS_{AB} - SS_A - SS_B \tag{3.28}$$

or

$$SS_E = SS_T - SS_{subtotals}$$

3.8 Non-Crimp Fabric Carbon Fibre Recovery

3.8.1 Pyrolysis Experimental Setup

The recovery of carbon fibre from the carbon fibre reinforced composite was undertaken via pyrolysis. Units of 2 kg samples were weighed after cutting them into square pieces using a diamond blade cutter and placed into ceramic crucibles, which were then inserted into the reactor with the help of a furnace plunger. A Carbolite EHA one-zone model furnace equipped with an argon filled cylinder was used for the pyrolysis processes as shown in Figure 3.18. The process requires initial flushing with argon to remove air after closing the furnace lid before heating the system at a rate of 5℃/min to the predetermined temperature of 500℃ for 1 $hour$ and then cooled under argon flow of 10 l/min at a pressure of 2.5 psi. An extended tong for gripping the crucible was used to ensure centre placement of the samples in the furnace.

Figure 3.18 Pyrolysis Setup

The size of the furnace inner tube is the limiting factor with regard to the sample dimensions. The main focus was on fibre recovery and therefore pyrolysis gas and oil yields were not considered. The pyrolysis process was conducted in accordance with the procedure proposed by Mazzocchetti et al. [49].

3.8.2 Post-Pyrolysis Treatment (Oxidation)

The recovered solid residue from the pyrolysis process comprises carbon fibre coated with a carbonaceous film usually referred to as the char. In order to fully recover the fibre to have mechanical properties comparable to virgin fibre, oxidation to get rid of the char is essential. The oxidation was conducted in a Thermo scientific Thermolyne furnace as shown in Appendix A6. The char covered fibres were placed in the furnace and the temperature was set to $500℃$ and maintained at this temperature for $1\ hr$. The heating was carried out in air. The oxidation parameters were obtained from Mazzocchetti *et al.* [49].

3.8.3 Functionalisation with Nitric Acid

The primary purpose for modifying the surface of carbon fibre is to improve the wettability, effectively improving the interfacial adhesion and shear properties of the resulting composite. Several methods such as plasma and thermal treatments are also effective but relatively expensive, require high energy consumption and degrade the mechanical strength of the fibres. Therefore, an approach that increases wettability without the associated drawbacks of high cost and loss in fibre strength, was wet oxidation using nitric acid as proposed by Li [353]. This process directly influences the surface energy, the specific surface area, and the surface chemical functionality which are critical parameters for improving wettability.

The experimental setup comprised a round bottom flask, thermometer, a heating mantel regulated by a Variac, and a reflux system as shown in Figure 3.19. Char-covered recovered carbon fibre and virgin carbon fibre were treated with 6 mol nitric acid (HNO_3) obtained from a solution of 38 ml nitric acid added to 62 ml distilled water in accordance with Li [353]. During the oxidising process, 40 ml of the prepared solution was poured into the round bottom flask followed by the inclusion of the fibres whereafter the solution was heated under reflux for 5 $hours$ at a temperature of 90℃. The fibres were then removed, washed with distilled water until neutral pH was attained, and dried in an oven at 60℃ overnight.

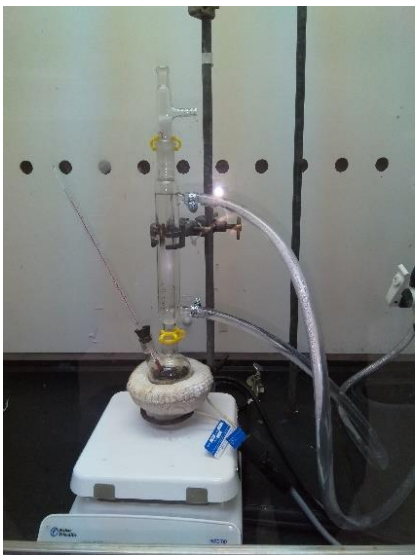

(a)

(b)

(c)

Figure 3.19 Functionalisation of virgin and recovered carbon fibre. (a) round bottom flask, thermometer, a heating mantel and reflux tubes; (b) A variac for regulating the heating mantle; (c) Drying of fibres

3.9 Materials Characterisations

3.9.1 Impact Testing

Impact Charpy tests in accordance with the ISO 179/92 standard [354]was performed on neat epoxy (NE), silane functionalised TiO_2 nanocomposite (STN) (See Figure 3.20 (a)), non-functionalised TiO_2 nanocomposite (TN), NCF carbon fibre reinforced composite (CF-NE) and NCF carbon fibre reinforced composite with TiO_2 addition (CF-STN) test specimen (See Figure 3.20 (b)). The MPX series motorised pendulum impact tester equipped with a hammer weight of 32.208 kg as shown in Appendix A6, was used for characterising the notched specimen with dimensions of $55 \times 10\ mm$ with respect to the prerequisites of the ISO 179/92 standard [354].

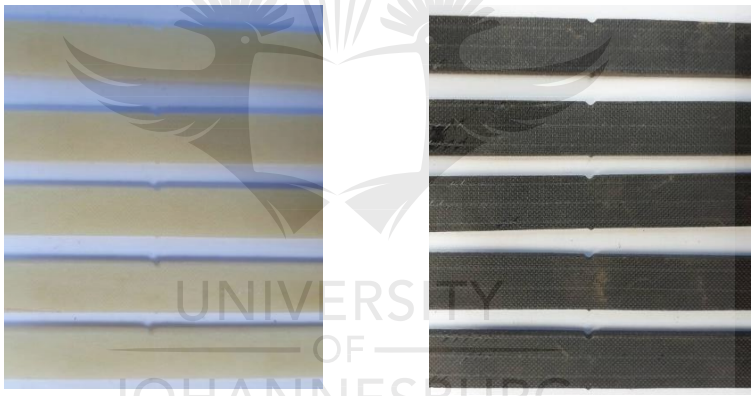

(a) (b)

Figure 3.20 Charpy impact test specimen. (a) Epoxy matrix with TiO_2 nanoparticle inclusion (b) Carbon fibre NCF with TiO_2 nanoparticle inclusion

3.9.2 Physisorption Isothermal Analysis using Brunauer Emmett Teller (BET)

The surface properties of virgin and recovered carbon fibre were characterised through a physisorption isotherm analysis. The adsorption-desorption behaviour of the carbon fibres was assessed under controlled conditions and analysed using Brunauer-Emmet-Teller (BET) methodology with an ASAP 2460 micromeritics instrument as shown in Figure 3.21(a). The carbon fibre was degassed at $250℃$ under a flow of N_2 gas for $24\ hrs$ using the Prep Flow

060 – Sample degas system micromeritics as shown in Figure 3.21 (b). During the physisorption isotherm analysis process, N_2 sorption porosimetry at $-196℃$ isotherms was investigated using BET measurements which quantify the physical adsorption of the fibre and correlates it with the specific surface area, the distribution of pore size, the total pore volume, and the adsorbent's mean pore diameter. The plots and data from the BET analysis were used for evaluating the surface area of the carbon fibre (m^2/g), while the nitrogen adsorption isotherms based on density functional theory were used to derive the pore size differential distribution curves. Additionally, the total pore volume (cm^3/g) of the carbon fibre was computed from the quantity of N_2 adsorption close to vapour pressure saturation of the N_2 gas. The experimentation was carried out with strict adherence to the procedural standards in the manufacturer's manual.

(a) (b)

Figure 3.21 Nitrogen sorption porosimetry. (a) BET equipment; (b) Degassing equipment

3.9.3 Elemental Analysis (Ultimate Analysis)

A Thermo Scientific Flash 2000 organic element analyser was used to conduct the final analysis on both the virgin and recovered carbon fibres. As a methodology, it is one of the most attractive for carrying out carbon hydrogen nitrogen (CHN) microanalysis due to its high validation quality while conducting purity analysis. As the combustion process progresses, carbon, hydrogen and nitrogen get converted into carbon dioxide, water, and nitrogen gas respectively via a variety of adsorbents. The CHN was investigated and the correlations of the adsorption behaviour of the carbon fibre to the molar ratios of O/C and H/C in accordance with D3176-15 of ASTM [355] were determined.

3.9.4 Scanning Electron Microscopy combined with Energy Dispersive X-ray Spectroscopy (SEM-EDX)

The surface morphology of virgin and recovered carbon fibres was investigated to assess the possible morphological and chemical transformations that may have occurred during pyrolysis, oxidation, and functionalisation. This was accomplished using a TESCAN VEGA 3 XMU scanning electron microscope (SEM) with an accompanying XMAX Oxford Instrument Energy Dispersive X-Ray (EDX) analyser as shown in Figure 3.22. A cross-section of the SEM composite samples was prepared by cryo-fracturing [356]. The samples were immersed in liquid nitrogen and then shattered. This method generally minimises distortions when compared to the use of shear force applied by a cutter. Sample sizes of approximately 5 mm lateral dimensions were selected for experimentation. The EDX section provides data on the chemical composition of the samples.

Figure 3.22 SEM equipped with EDX imaging

3.9.5 Thermal Analysis

3.9.5.1 Thermogravimetric Analysis (TGA)

Thermogravimetric analysis (TGA) provides a standardised method for measuring the thermal degradation of materials. Under controlled conditions and specific heating rates, samples are heated, and as the data on weight changes, temperatures and times are simultaneously documented. The TGA method is thus quantitative and focuses on thermal degradation because weight variations are a factor of temperature and time. During the TGA analysis, second-order transition characteristics of the sample absorption, adsorption, desorption, sublimation, and vapourisation can be recorded. Aside from the physical information that is captured during TGA, important chemical data such as decomposition, devolatisation, chemisorption, and solid-gas reactions can also be determined. The

determination of the rate of weight loss in relation to temperature or time is termed the derivate of the thermogravimetry (DTG).

Figure 3.23 SDT-Q-600 thermogravimetric analyser

The SDT-Q-600 Thermogravimetric Analyser manufactured by TA Instruments, as shown in Figure 3.23 was used to assess the thermal stability of composite and virgin/recovered carbon fibre samples. Composite samples were either cryofractured or cut (fibre reinforced composites). Approximately $100\,mg$ of the samples were heated for $10\,mins$ at 105℃ to ensure the elimination of any trapped moisture on samples resulting from sample preparation, prior to starting the TGA process. The TGA analysis involved heating composite and carbon fibre samples to 800℃ and 1100℃ respectively under a nitrogen inert condition of $100\,ml/min$ and a heating rate of $10℃/min$ in accordance with Mazzocchetti et al. [49]. Weight loss (TG) and weight loss rate (DTG) information was captured and used for the thermal stability analysis.

3.9.5.2 Integral Procedural Decomposition Temperature

The integral procedural decomposition temperature (IPDT) is a tool primarily used for analysing sections of a polymeric material that are volatile and also to determine the intrinsic thermal stability of the polymer matrix as illustrated in Figure 3.24. Doyle [357] developed the IPDT procedure through computation of the thermogram area summations acquired from thermogravimetric analyses. The formulation for computing IPDT as shown in Equation (3.29) was within a temperature boundary constraint of 30℃ and 800℃ which represents the initial and final temperatures:

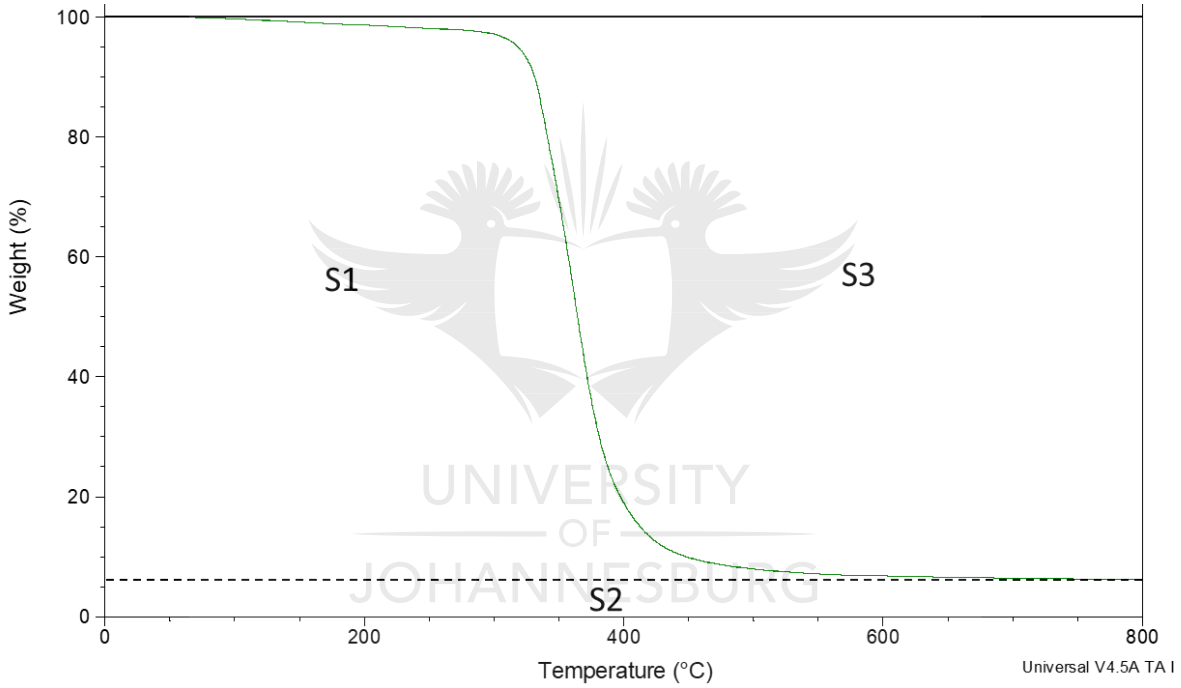

Figure 3.24 The schematic diagram of the Doyle's method for determining the IPDT

$$IPDT\ (℃) = A \times K \times (T_f - T_i) \tag{3.29}$$

$$A = \frac{S_1 + S_2}{S_1 + S_2 + S_3} \tag{3.30}$$

$$K = \frac{S_1 + S_2}{S_1} \tag{3.31}$$

where A is the total experimental curve area ratio described by the total regions within which the TGA thermogram lies, K represents the coefficient, while T_i and T_f represent the initial and final temperatures respectively.

3.9.5.3 Oxidation Index

Oxidation index (OI) is an important indexing tool used in the estimation of the flame retardant capacity of polymer composites [358]. The index is formulated based on the decomposition of the matrix with emphasis on the char residual (CR) retrieved after pyrolysis. The mathematical formulation is presented as follows in Equation (3.32):

$$OI = \frac{17.5 \times 0.4\ CR}{100} \tag{3.32}$$

3.9.6 X-Ray Diffraction Analysis (XRD)

X-ray diffraction (XRD) is a non-destructive analytical approach uniquely suited to provide comprehensive information on chemical constitution, crystallographic structure/phases, and physical and chemical properties. In this study powder XRD was used, and therefore the carbon fibre samples had to be pulverised. The standard procedure of X-ray diffraction measurements on carbon materials by Iwashita et al. [359] was adopted in this research. Powder XRD allows for the investigation and identification of solid-state material phases which is useful for analysing phase transitions, polymorphs, lattice parameters, crystallinity, crystal size, and strain.

A Rigaku Ultima IV X-Ray diffractometer as shown in Figure 3.25, which is equipped with crossbeam optics from the Saskatchewan Structural Science Center in the University of Saskatchewan was used for this study. The X-Ray diffraction uses a Cu source with a wavelength of 1.54056Å while cross-beam optics (CBO) technology provides the possibility for immediate switching between parallel and para-focusing beams. Additionally, the Rigaku Ultima IV X-Ray diffractometer has a broad 2θ scan range of $-3°$ to $162°$ The experimental

works were conducted under strict adherence to operational and specific standards provided by the Saskatchewan Structural Science Center.

Figure 3.25 The Rigaku Ultima IV X-Ray diffractometer

Crystallite characteristics were determined from the XRD data using Bragg's law and Debye-Scherrers equations. Bragg's law is capable of computing the interlayer spacing (d_{002}) and lattice constants values as shown in Equation (3.33).

$$d_{002} = \frac{\lambda}{2sin\theta} \tag{3.33}$$

where λ is the wavelength of x-ray (1.54056 Å) and 2θ is the diffraction angle. The classical Debye-Scherrer equations as shown in Equations (3.34), (3.35) and (3.36) were used for analysing the structural parameters from the XRD patterns [360]:

$$L_c = \frac{K_c\lambda}{\beta_{002}\, cos\theta_{002}} \tag{3.34}$$

$$L_a = \frac{K_a\lambda}{\beta_{011}\, cos\theta_{011}} \tag{3.35}$$

$$N = \frac{L_c}{d_{002}} \tag{3.36}$$

where β is the full width at half maximum intensity (FWHM), L_c is the crystallite thickness with its accompanying coefficient K_c (0.9), L_a is the crystallite width with its accompanying K_a (1.77), and N is the average number of aromatic layers [361]. These crystallite structural parameters are primarily influenced by pyrolysis and oxidation treatments.

3.9.7 Raman Spectroscopy Analysis

Raman spectroscopy is an approach which provides sample information that is highly chemical-specific and based on modes of molecular systems that are vibrational and rotational. It is a non-contact and non-destructive technique that is very useful in detecting and analysing chemical composition, evaluation of crystallinity, structural analysis of molecules and many more. In this study, the Renishaw Invia reflex microscope as shown in Figure 3. 26 equipped with an IlluminatIRII FTIR microscope accessory in the Saskatchewan Structural Science Center at the University of Saskatchewan, was used. The microscope is capable of very high resolutions due to the MS20 encoded stage which enables precise steps of $100\,nm$. Additionally, the Invia Reflex is equipped with lasers with excitations of $514.5\,nm$ and $785\,nm$. The automatic laser switching capabilities allow for simultaneous spectroscopy excitation of Raman and FTIR wavelengths. Several structural studies have been successfully carried out on carbon-based materials [362–364] such as graphite and carbon fibre using Raman spectroscopy, and the reliability of the results has ensured commercialisation of the technique. It is uniquely suited for the analysis of carbon-based materials because of its high sensitivity to different types of carbon structures differentiated by the generation of distinctive Raman peaks corresponding to each specific form of carbon. The intensity ratio (IR) describes the ratio of the first-order peak intensities of $D-band$ (ID) and $G-band$ (IG) [361,365] as shown in Equation (3.37). This parameter is an important indicator which determines the influence of treatments such as pyrolysis and oxidation on the crystallinity of carbon materials.

$$IR = \left(\frac{ID}{IG}\right) \tag{3.37}$$

Sample testing was undertaken at the Saskatchewan Structural Science Centre at the University of Saskatchewan. All operational standards with regard to testing were strictly adhered to.

Figure 3.26 Renishaw Invia Reflex equipped with an IlluminatIRII FTIR microscope

3.10 Summary

Two composite fabrication methodologies were adopted from the literature and manufacturer's recommendations to ensure standardised fabrication. Titanium oxide nanoparticle functionalisation was carried out based on established methods and parameters reported in the literature for silane treatment. Two formulations for dispersion quantification were developed based on reviewed literature. The first was established on the theories of gap statistics and dispersity, while the other was based on fractal dimension and variance. The quantification analysis required various algorithms, which were developed in MATLAB for activities such as image segmentation. Tab optimisation to reduce stress concentration in the tab termination region was investigated via the established literature on the finite element analysis of composite materials and the application of various optimisation techniques. Apart from the normal Taguchi, genetic algorithms and multiple response optimisations were developed to critically evaluate the influence of all design parameters and configurations on the induced stress concentration, and to further determine optimal combinations of the parameters. Analysis of variance was applied to the simulation results obtained from the finite element analysis to determine the main effects and significance of these effects via a p-value. In recycling the carbon reinforced composites, pyrolytic parameters such as optimal temperature and post-treatment oxidation temperature were based on the reviewed literature. Additionally, nitric acid functionalisation of virgin and recovered fibres was carried out in accordance with established methodologies in the literature.

The next chapter presents the results derived from quantifying the state of nanoparticle dispersion, optimising the design parameters using varying optimisation techniques, and recycling carbon fibre reinforced composites.

CHAPTER FOUR

RESULTS AND DISCUSSION

4.1 Introduction

Non-crimp fabric composites fabricated from an epoxy matrix modified through the inclusion of functionalised and non-functionalised TiO_2 nanoparticles. Then, the state of TiO_2 dispersions in the modified epoxy matrix was quantified using gap statistics and fractal dimension. Finite element modelling coupled with optimisation techniques were used to obtain optimal Tensile test specimen design parameters of the NCF composites. Thereafter impact test analysis coupled with thermal charaterisations were conducted. Lastly, the effects of pyrolysis and oxidation on reclaimed NCF carbon fibre were investigated and discussed.

4.2 Quantification of TiO_2 Nanoparticle Dispersion

4.2.1 Dispersion Quantification Using Gap Statistics

The proof of concept as presented is required in the development of simulated models (see Figure 3.1) of the possible particle dispersion and agglomeration states. Obtaining data from the models for formulation and computation involved image segmentation of the models via the K-mean algorithm [334] which transforms the model image to one that is binary, and thereafter also the location, extraction and plotting of the centroid coordinates as shown in Figure 4.1.

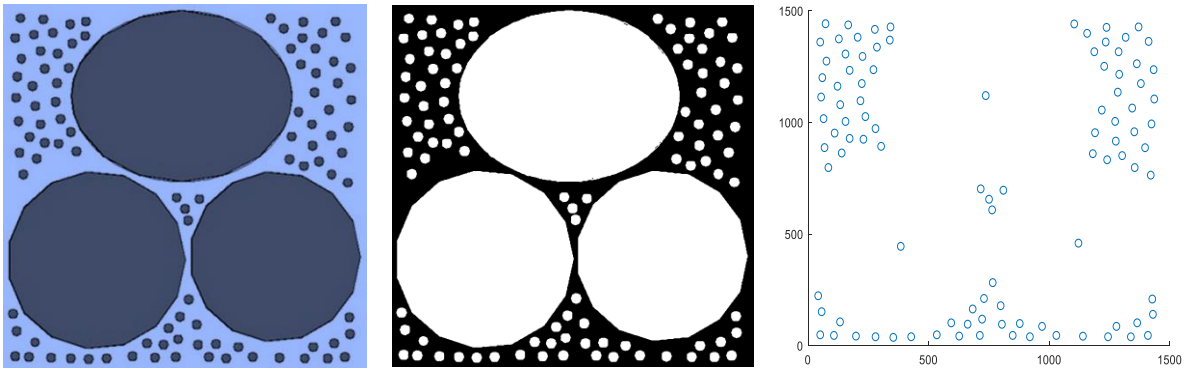

Model **Segmentation** **Particle centroid location**

Figure 4.1 The image data extraction process for Model 4 [330]

The data extracted provided numerical input for application of the gap statistic criterion to genearte both observed and expected curves as depicted in Figure 4.2. The significant observation focused on how, from Model 1 (uniform distribution) to Model 5 (highly agglomerated), the gap between the observed and expected curves progressively expanded. This obvious trend correlated with the increase in the inhomogeneity and agglomeration levels. The gap behaviour trend provided a scientific basis for the development and formulation of the gap factor (G_0) described Section 3.2.1. Consequently, the gap factor was determined as the area between the observed and expected curves; or the difference of the area under the two curves.

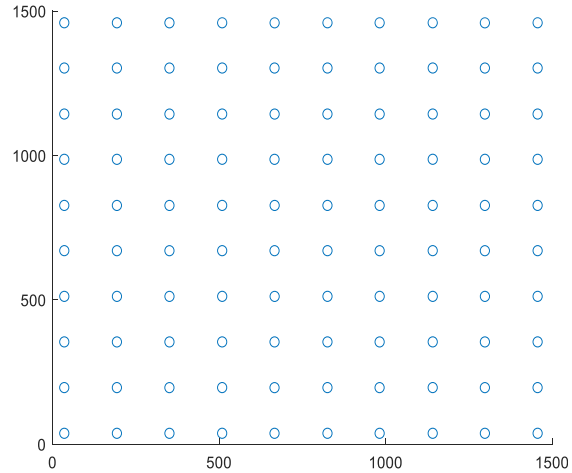

(a)

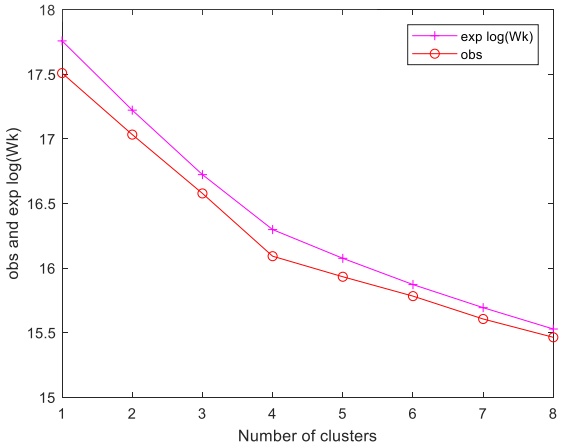

(b)

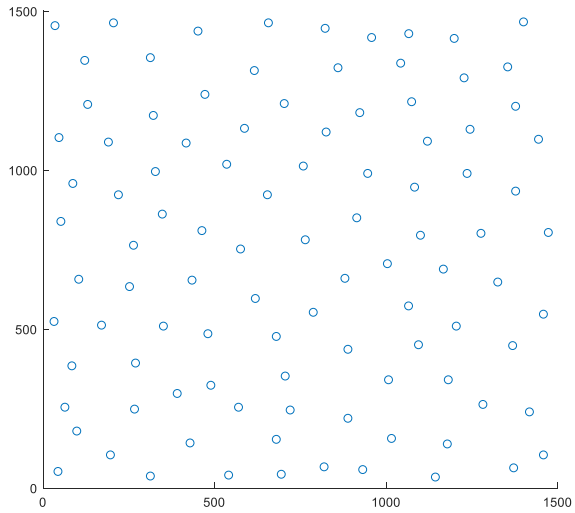

(c)

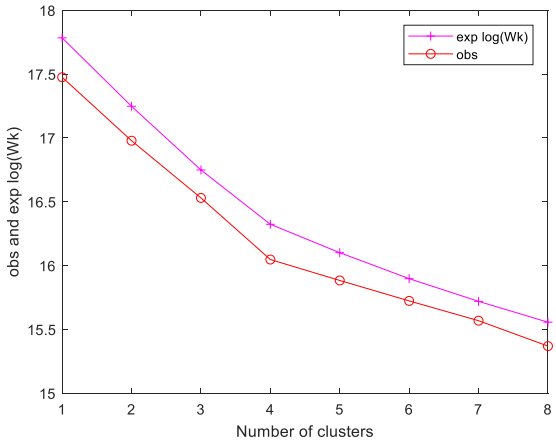

(d)

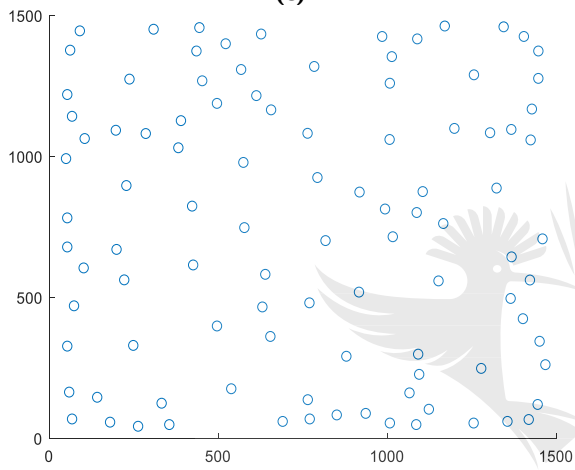

(e)

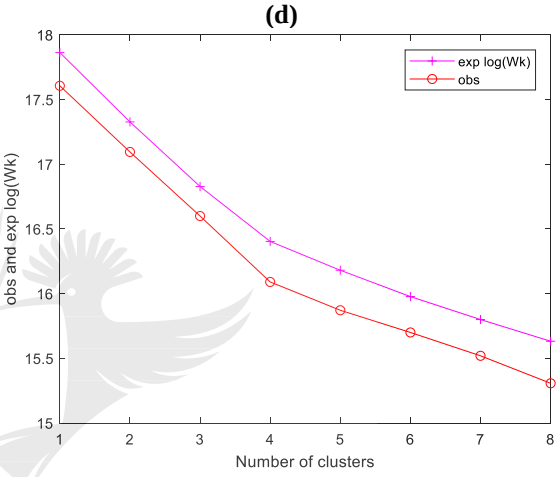

(f)

(g)

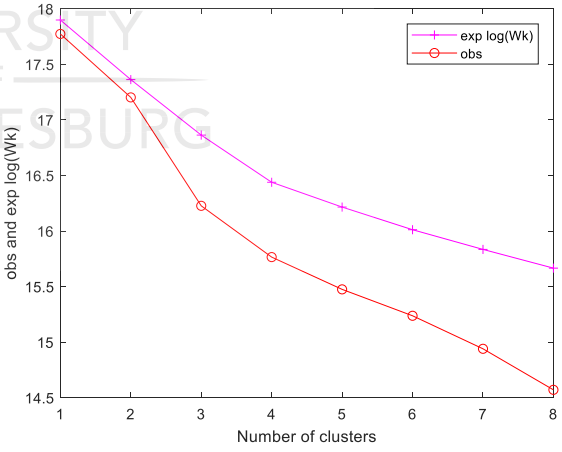

(h)

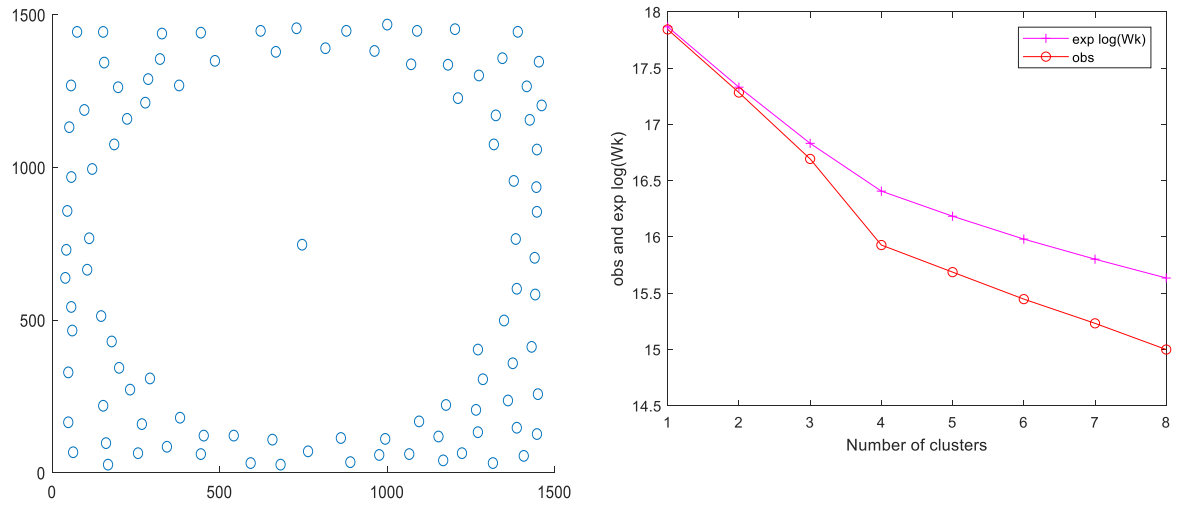

(i) **(j)**

Figure 4.2 Plotted centroids and corresponding Gap curves for Model 1 (a and b), Model 2 (c and d), Model 3 (e and f), Model 4 (g and h) and Model 5 (i and j) [330]

Thereafter, a dispersion quantity (D) was formulated from the gap factor (G_0), particle spacing dispersity (PSD_1) and particle size dispersity (PSD_2) and tested on the five simulated models. However, computing PSD_1 and PSD_2 required the calculation of critical parameters like average particle spacing and average particle size with their corresponding standard deviations; all of which were extrapolated from each of the five simulated models as reported in Table 4.1. As expected, the observed trend revealed that, Models 1, 2 and 3 showed relatively similar but lower average particle spacing in comparison with Models 4 and 5. The above observations were in agreement with the visual assessment where larger agglomerates indicating higher variations in spacing were seen for Models 4 and 5. Therefore, the average spacing standard deviation for the uniform and randomly dispersed Models (1 and 2) without agglomerations were significantly lower than the models with agglomeration. Furthermore, Models 3 to 4 which had large agglomerates showed higher average particle sizes and standard deviations than Models 1 and 2 which had the same sized particles but without agglomerates. A larger average particle spacing coupled with an associated lower standard deviation implies interparticle spacing homogeneity which is indicative of a good state of dispersion and minimal presence of agglomeration within the composite matrix.

Table 4.1 Average particle spacing and size with corresponding standard deviations for simulated model in pixels

Model	Ave. Particle Spacing	Weighted Average	Std Deviation	Ave. Particle Size	Weighted Average	Std Deviation
Model 1	7.84E+02	6.93E+02	3.75E+02	2.42E+03	2.43E+03	9.18E+01
Model 2	7.44E+02	8.06E+02	3.70E+02	2.42E+03	2.43E+03	9.18E+01
Model 3	7.71E+02	8.06E+02	4.07E+02	1.23E+04	7.12E+04	2.70E+04
Model 4	8.42E+02	1.11E+03	4.57E+02	1.45E+04	4.01E+05	7.52E+04
Model 5	9.14E+02	1.10E+03	4.59E+02	1.26E+04	9.89E+05	1.12E+05

Source [330]

Conversely, a lower average particle size coupled with a low standard deviation signifies lower levels of agglomerations and homogeneity in the distributed particles in the matrix. A positive correlation can thus be inferred between increasing average particle spacing and homogenous dispersion, while a negative correlation was observed between increasing average particle size and an increase in homogeneity in dispersion. Additionally, increasing standard deviation is negatively correlated with increasing homogeneity.

In practice three factors are known to directly affect the thermal and mechanical properties of nanocomposites, namely interparticle interactions, particle contiguity and state of particle distribution [366]. Nanocomposite elastic property, in particular, is significantly influenced by particle congruity, distribution, and size [366]. Studies have shown that nanocomposite toughness and stiffness significantly improve when the distance between individual particles is progressively reduced in comparison to the nanoparticle diameters [122,367,368]. The resulting outcome is therefore an enhanced particle-matrix interphase characterised by a three-dimensional physical network which dominates the performance of the nanocomposite [122,368]. The performance domination discussed is positive when higher dispersion homogeneity is achieved. Table 4.1 shows that, the average interparticle spacings were $7.84E+02$ and $9.14E+02$ for Models 1 and 5 respectively while their corresponding average particle sizes were $2.42E+03$ and $1.26E+04$. Clearly, the interparticle spacing for both models are greater than their average sizes; however, Model 1 was uniformly distributed

while Model 5 had large agglomerates. The smallest standard deviation for average particle spacing was $3.75E+02$ for Model 1 implying that a smaller standard deviation indicated better particle homogeneity.

However, Lou and Koo [369] however report that the reliance on standard deviations is not sufficient for exhaustive quantification of dispersion. This insufficiency associated with reliance on only average spacing, size and their standard deviations, required the implementation of an approach which incorporated gap factor, particle spacing, and size dispersity for the determination of the critical parameter known as the dispersion parameter (D_p). Consequently, a much more comprehensive method for estimation of the dispersion quantity (D) was formulated.

For Model 1 which represents a uniformly dispersed system, G_0, PSD_1 and PSD_2 all had values of approximately 1 which presented a perfect score of approximately 3 for D_p as shown in Table 4.2. The resulting dispersion quantity (D) was computed to be $99.34\% \approx 100\%$ representing an ideal state of dispersion or perfectly homogeneous system. The D for Model 5 however was found to be 3.65%; the lowest value and indicates extremely poor homogeneity in dispersion and high state of agglomeration. The emerging and expected trend in Table 4.2 indicates a progressive retrogression in dispersion percentage moving from Models 1 to 5 which is in agreement with the visual assessment of the models. Previous studies have shown that any formulation for quantifying dispersion must incorporate an agglomeration component [370]. In this study, PSD_2 represents the agglomeration parameter; hence, the PSD_2 values for Models 1 and 5 were 1 and 78.38 respectively. This means that an increase in PSD_2 correlates with an increase in the state of agglomeration. In theory, as $D \rightarrow 100\%$, the state of dispersion improves.

Table 4.2 Degree of dispersion in the simulated models

Model	G_0	PSD_1	PSD_2	D_p	D
Model 1(Uniform Distr.)	1.02	1	1	3,02	99.34%
Model 2 (Random Distr.)	1.56	1.08	1	3.64	82.42%
Model 3 (Small Agg.)	1.93	1.05	5.8	8.78	34.17%
Model 4 (Three Agg)	4.49	1.32	27.7	33.51	8.95%
Model 5 (One Agg)	2.59	1.2	78.38	8.17	3.65%

Source [330]

*Agglomeration (Agg)

4.2.1.1 Validation using real images

Although proof of concept has theoretically been established, a means of validating the methodology was vital. To achieve this, the concept was tested on real SEM images comprising varying degrees of dispersion and agglomerations of TiO_2 nanoparticles in the epoxy matrix. Four scenarios as can be observed in Figure 4.3, were used for testing the veracity, versatility and robustness of the method. All the scenarios were subjected to the initial stage of segmentation, which clearly exposed the dispersed nanoparticles as white pixels then extraction and plotting of the centroid data and finally plotting the observed and expected curves within the gap statistic criterion. To ensure reliability and accuracy all the images were scaled to a resolution of 1500×1500 pixels. The data analysis for the four scenarios is summarised in Table 4.3.

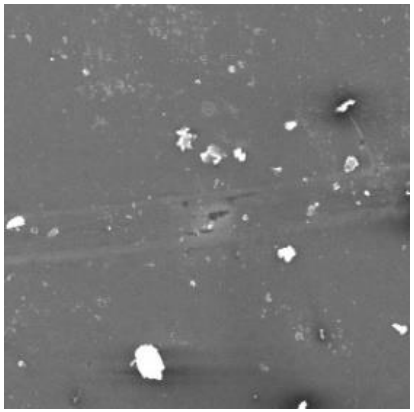

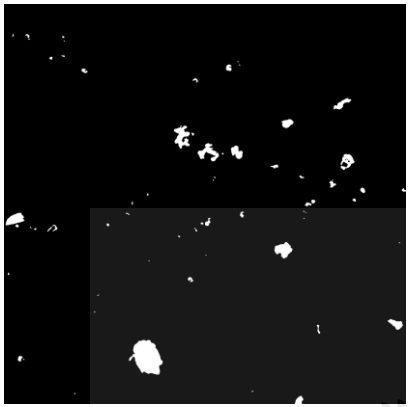

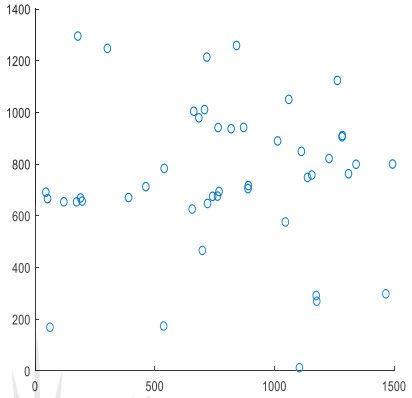

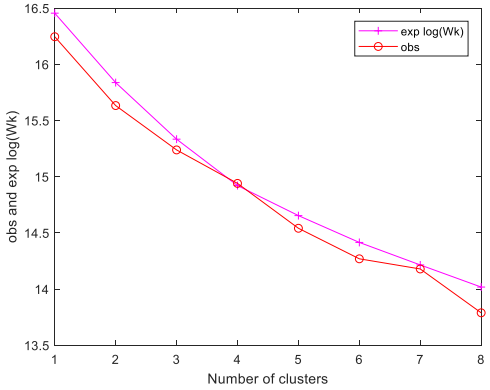

Scenario 1

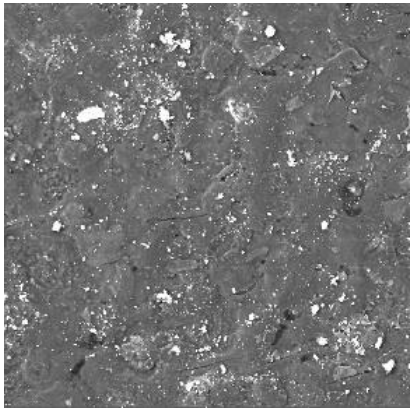

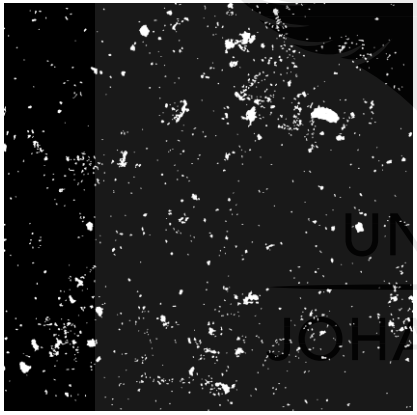

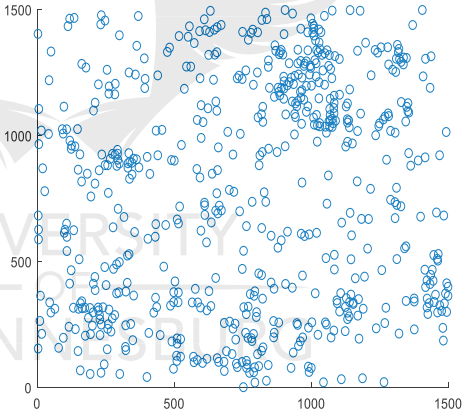

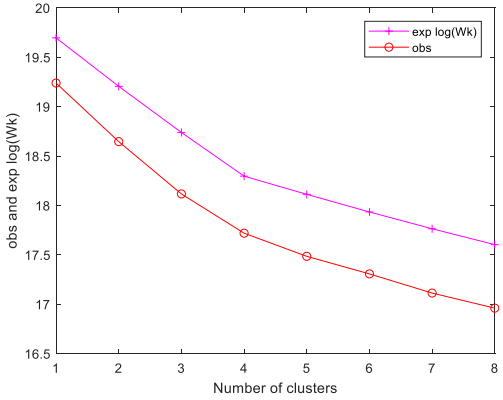

Scenario 2

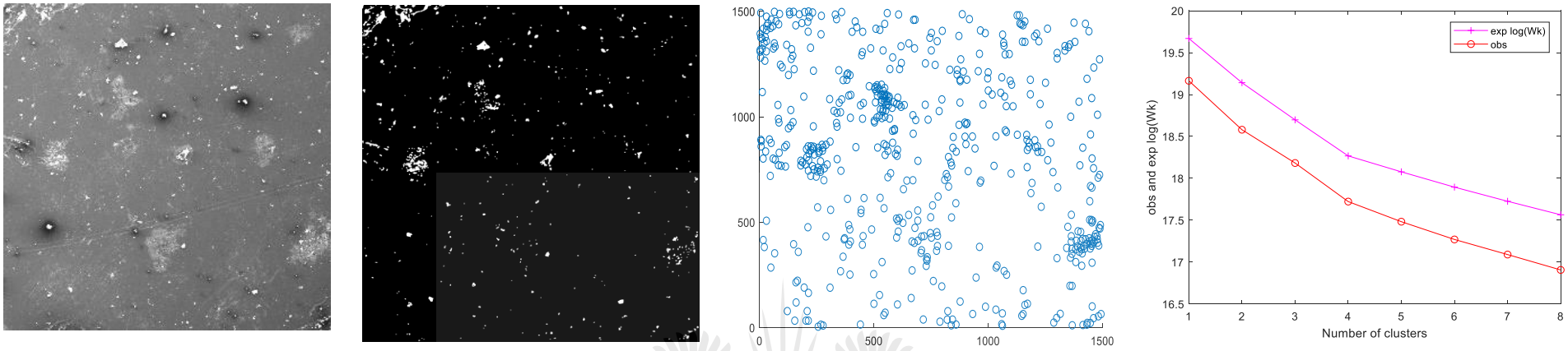

Senario 3

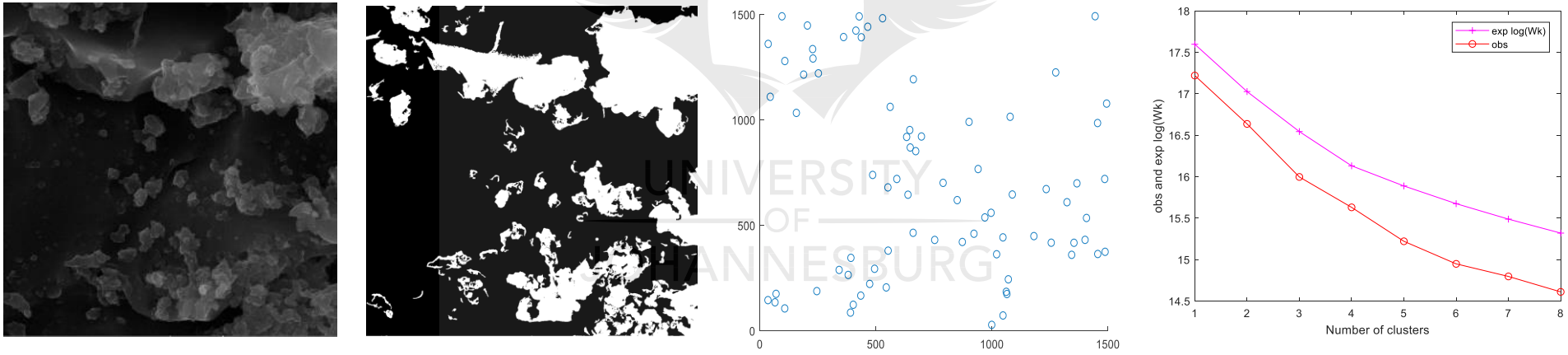

Senario 4

Figure 4.3 Data extraction process and Gap plots for real image scenarios 1, 2, 3 and 4 [330]

Table 4.3 Average particle spacing and size with corresponding standard deviations for real image scenarios in pixels

Real Images	Ave. Particle Spacing	Weighted Average	Std Deviation	Ave. Particle Size	Weighted Average	Std Deviation
Scenario 1	7.40E+02	9.46E+02	3.46E+02	6.11E+02	4.65E+03	1.59E+03
Scenario 2	7.01E+02	6.40E+02	3.59E+02	6.67E+01	3.59E+02	1.94E+02
Scenario 3	6.96E+02	7.81E+02	3.94E+02	6.40E+01	5.05E+02	1.36E+02
Scenario 4	9.03E+02	1.25E+03	3.73E+02	2.44E+03	8.13E+04	1.76E+04

Source [330]

From Table 4.3, scenarios 1, 2 and 3 had average particle spacing of $7.40E+02$, $7.01E+02$ and $6.96E+02$ respectively. These values were equivalent. However, an average spacing of $9.03E+02$ which is comparatively higher was observed for scenario 4. The high average spacing is an indication of dispersion inhomogeneity plus the presence of large agglomerates. The variations in the standard deviations of the average spacing for all the scenarios was not significant. In comparison, scenarios 1 and 4 had the highest values for average particle sizes at $6.11E+02$ and $2.44E+03$ respectively. Also, the standard deviation values of $1.59E+03$ and $1.76E+04$ for scenarios 1 and 4 respectively were greater than those of scenario 2 ($1.94E+02$) and 3 ($1.36E+02$).

It must however be noted that high values of average particle sizes and their corresponding standard deviations can have two distinct interpretations. Scenario 1 represents a situation where there is large variation in the size of nanoparticles, and smaller agglomerate sizes in the matrix. While scenario 4 represents a situation where high average particle sizes and the standard deviation is attributed to the presence of large agglomerates. The ambiguity associated with relying on standard deviations is clearly demonstrated in the above scenarios, and they are therefore not sufficient for comprehensively assessing the state of dispersion and agglomeration [36]. G_0, PSD_1, PSD_2 and the dispersion quantity (D) for the four scenarios were determined as summarised in Table 4.4. The resulting dispersion Quantity (D) was 31.02%, 28.60%, 22.95% and 7.72% for scenarios 1 to 4 respectively.

Table 4.4 Degree of dispersion for real image scenarios

Real Images	G_0	PSD_1	PSD_2	D_p	D
Scenario 1	0.79	1.28	7.6	9.67	31.02%
Scenario 2	4.21	0.91	5.37	10.49	28.60%
Scenario 3	4.06	1.12	7.89	13.07	22.95%
Scenario 4	4.07	1.39	33.38	38.84	7.72%

Source [330]

As can be seen, the most and least homogeneous scenarios were 1 and 4 respectively. The agglomeration parameter, $\boldsymbol{PSD_2}$, for scenario 1 was $\mathbf{7.6}$ while scenario 4 was $\mathbf{33.38}$. The higher $\boldsymbol{PSD_2}$ value for scenario 4 indicates that it had higher agglomeration content which is in agreement with the visual inspection.

4.2.1.2 Particle Matrix-Interphase Improvement

Improving the particle-matrix interphase is critical for enhancing the thermomechanical properties of nanocomposites. It is known that particle congruity and distribution significantly influence particle-matrix interphase. A critical analysis of the interphase regions exposes a sophisticated and complex interplay of several phenomena such as high-stress gradient, singularities of even stresses induced by particle geometry, mechanical stresses induced by shrinkage, microcracks, void content, bonding deficiencies and many more [366]. Improving particle hydrophobicity is critical to mitigating several of the discussed interphase inefficiencies. Wettability increases as hydrophobicity improve and consequently, dispersion also improves. This brings to fore the importance of functionalisation using oxidising agents coupled with cavitation processes such as ultrasonic dispersion which seek to modify the surface of the nanoparticles to enhance interphase bonding and overcome the interparticle Vander Waal forces which promotes agglomeration [32,371–373]. Silane functionalisation of TiO_2 nanoparticles was carried out on samples used in scenarios 1, 2 and 3 and was evidenced by higher D values indicating higher homogeneity and hydrophobicity. Hydrophobicity of the TiO_2 nanoparticles was accomplished through creating a film comprising $Ti-O-Si$ chemical bonding coupled with $Si-O-Si$ cross-link bonds after the silane treatment [106]. In

comparison, scenario 4 had the lowest D value because the nanocomposite was fabricated from nonfunctionalised TiO_2 nanoparticles, which exhibited higher agglomeration and lower hydrophobicity.

4.2.2 Dispersion Quantification Using Fractal Dimension

A less complicated approach has been developed based on the fractal dimension D_f where the box-counting method by Moisy [333] is adopted for computation of the variance of the fractal dimension via the segmentation of sample images. Five simulated concept models comprising dispersion states that are uniform, random, clustered and highly agglomerated were developed for testing proof of concept. The fractal dimension graphs for each model are shown in Figure 4.4. The equation developed for computing the dispersion quantity (D_0) (see section 3.2.1) was used to determine the state of dispersion in the models; a summary of the results is presented in Table 4.5**.** As expected, uniform and randomly dispersed models showed the highest D_0 values of 100% and 99.47% respectively; while the models with one and three large agglomerates had the lowest D_0 values of 15.17% and 7.13% respectively. These results are consistent with the visual assessment of the models.

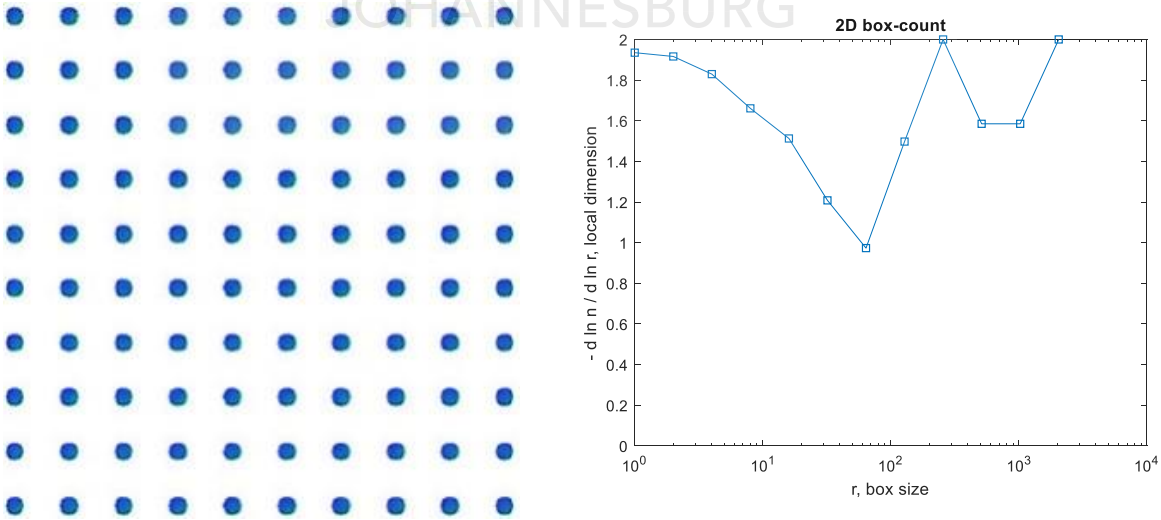

(a) (b)

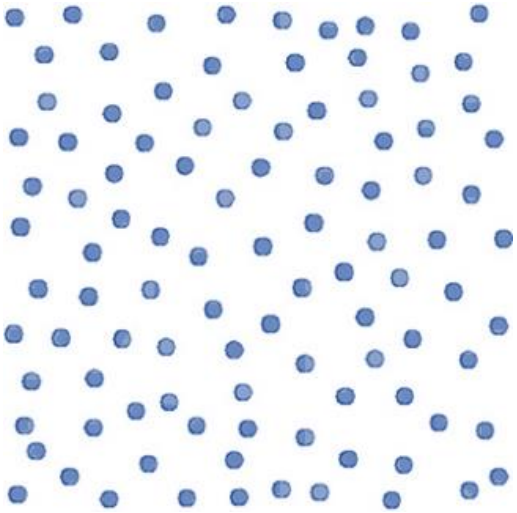

(c)

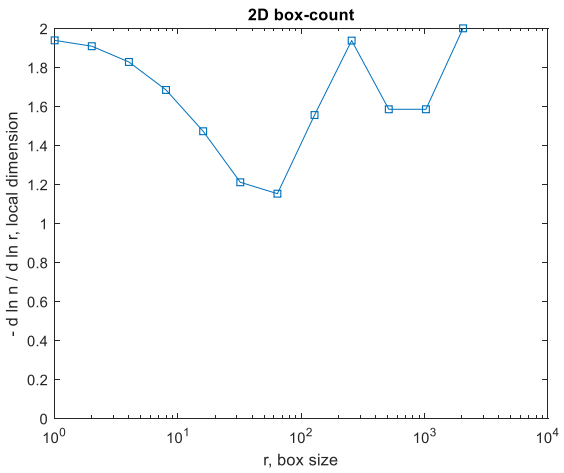

(d)

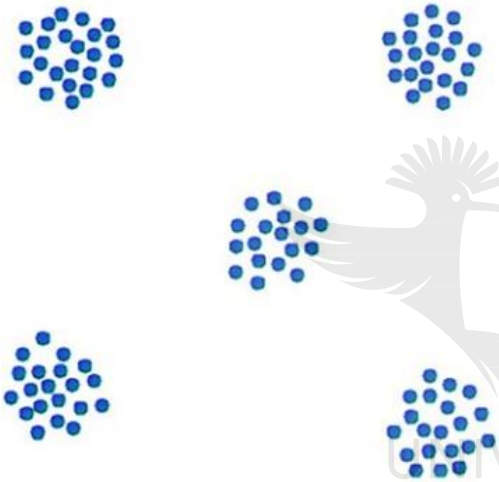

(e)

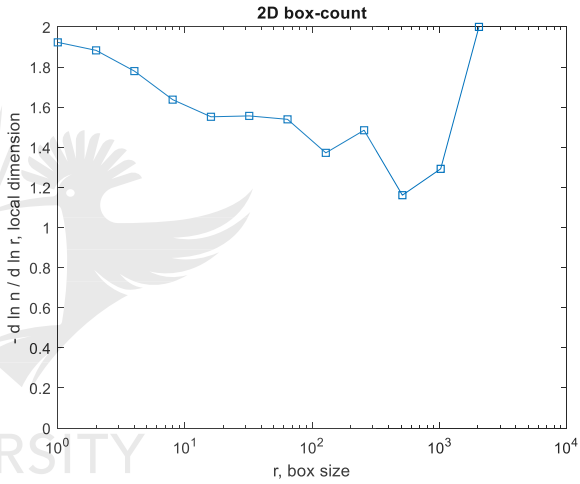

(f)

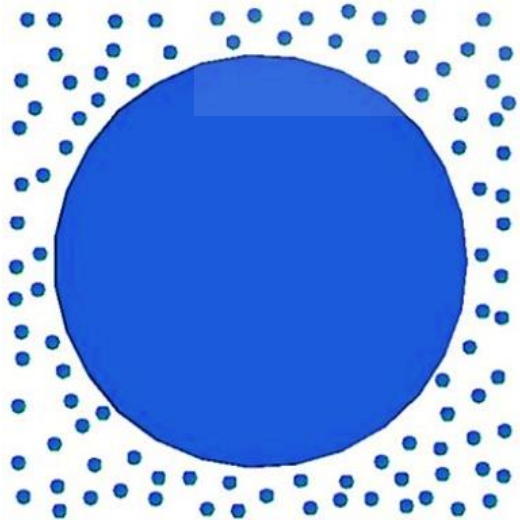

(g)

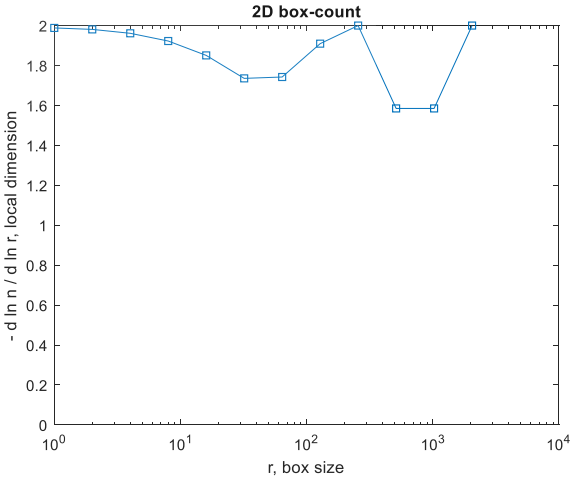

(h)

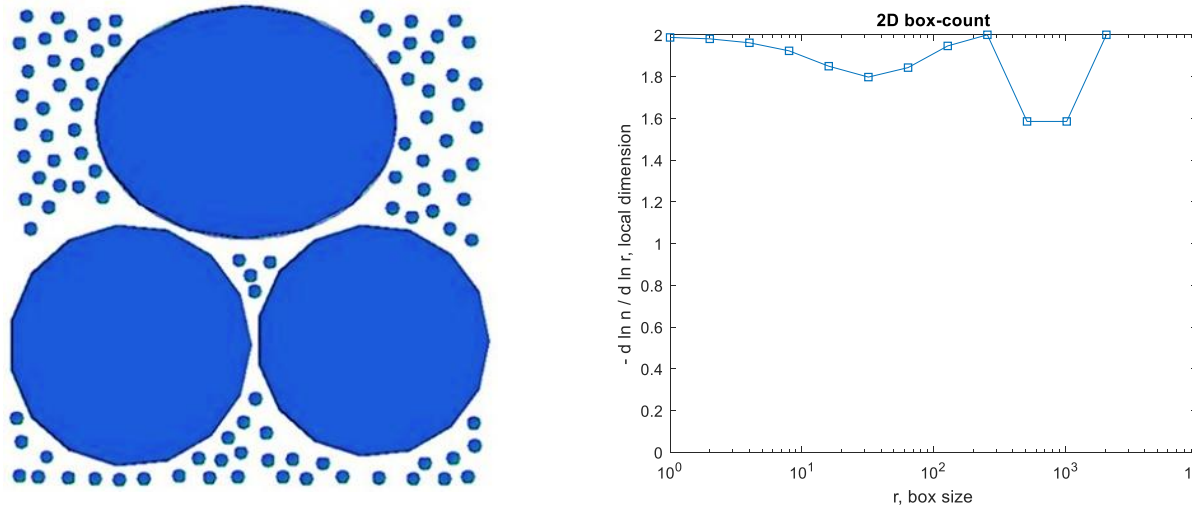

(i) (j)

Figure 4.4(a) Uniformly dispersed model, (b) Fractal dimension graph of the Uniformly dispersed model, (c) Randomly dispersed model, (d) Fractal dimension graph of the randomly dispersed model, (e) Cluster distribution model, (f) Fractal dimension graph of the cluster Distribution model, (g) One large Agglomerate model, (h) Fractal dimension graph of the One large Agglomerate model, (i) One Three large Agglomerate model, (j) Fractal dimension graph of the three large Agglomerate model [374]

The concept was theoretically proved through the results in Table 4.5, therefore the next step was a validation of the concept using real microscopy images. The three SEM images shown in Figure 4.5 were used for the validation process. All the images were captured at $5\ \mu m$ using $15\ KV$ after which they were converted to 1500×1500 pixels before generating the fractal dimension plots.

Table 4.5 Fractal Dimension, Variance and Dispersion of the concept models

Models	Fractal Dimension (D_f)	Variance (S^2)	Dispersion (D_0)
Uniformly Dispersed	1.394 ± 0.434	1.89×10^{-1}	100%
Randomly Dispersed	1.425 ± 0.315	0.099	99.47%
Clustered	1.483 ± 0.142	0.020	20.03%
One Large Agglomerate	1.837±0.123	0.015	15.17%
Three Large Agglomerates	1.877±0.084	0.007	7.13%

Source [374]

The assessment of significantly different states of dispersion is easily determined by visual inspection however, for distinguishing between very similar dispersion states, quantification tools such as the one developed in this study is required.

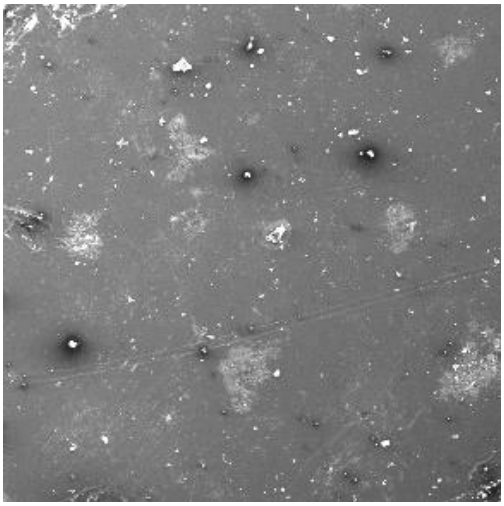

(a)

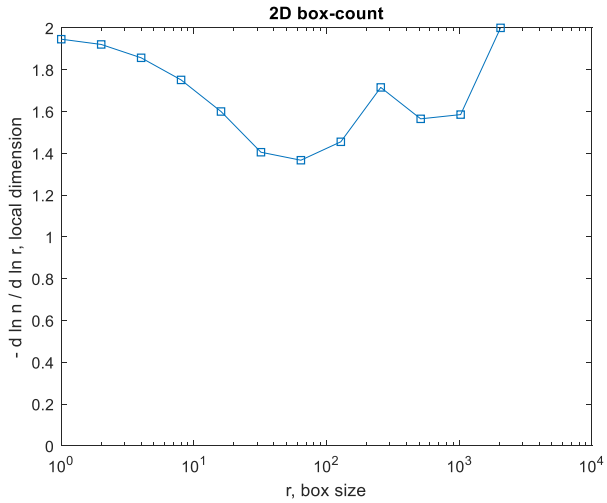

(b)

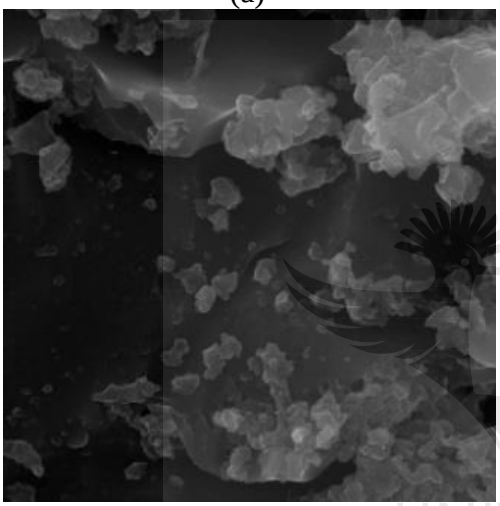

(c)

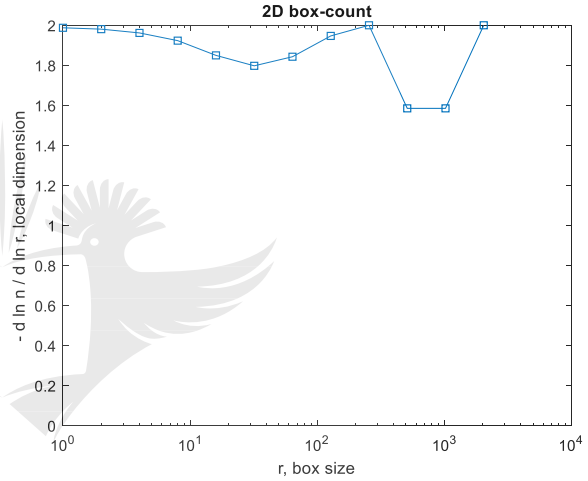

(d)

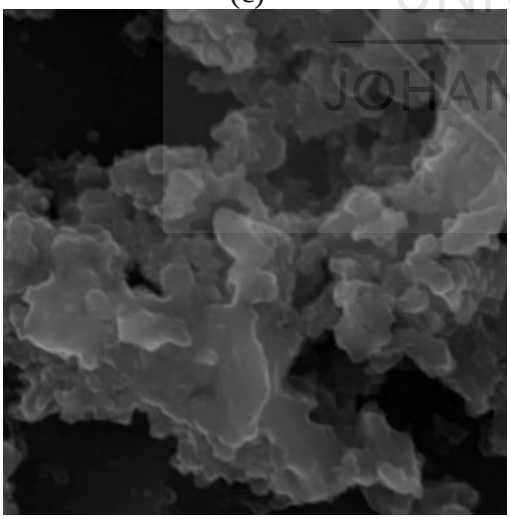

(e)

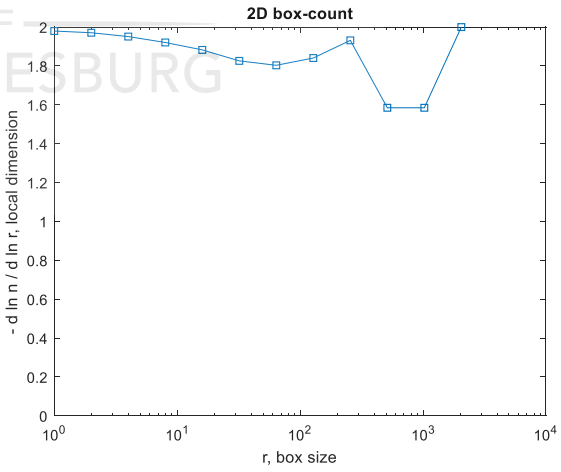

(f)

Figure 4.5 (a) Sample 1, (b) Fractal dimension graph of Sample 1, (c) Sample 2, (d) Fractal dimension graph of Sample 2, Sample 3 and (f) Fractal dimension graph of Sample 3. [374]

The SEM images were therefore carefully selected on the basis of all samples which display high levels of agglomerations. The proposed method was successfully employed to determine the degree of dispersion within the samples. Table 4.6 represents a summary of the obtained results. The dispersion quantity (D_0) was found to be 19.79%, 11.74% and 1.95% for samples 1, 2 and 3 respectively. Sample 3 in particular, was expected to have the worst state of dispersion since visual inspection shows a giant agglomerate lump.

Table 4.6 Fractal Dimension, Variance and Dispersion of real samples

Real Images	Fractal Dimension (D_f)	Variance (S^2)	Dispersion (D_0)
Sample 1	1.481±0.141	0.0198	19.79%
Sample 2	1.706±0.108	0.0117	11.74%
Sample 3	1.847±0.044	0.0019	1.95%

Source [374]

Additionally, the low dispersion percentages for all samples can be attributed to the presence of large agglomerates resulting from the use of non-functionalised TiO_2 nanoparticles. The high agglomeration levels are due to poor particle-matrix interphase characteristics such as low hydrophobicity, specific area of the particles, high interparticle Van der Waal attraction, and matrix viscosity [375] [376,377]. There are however some drawbacks to this proposed method in its current state. These include a lack of components within the dispersion equation such as particle contiguity parameters which considers interparticle spacing and an agglomeration quantity for precise assessment.

4.3 Optimisation Methods for Minimising stress Concentration in NCF composites During Tensile Testing

4.3.1 Tensile Testing

The elastic properties for non-crimp fabric glass fibre composites were obtained via an analysis of the stress-strain and shear (stress-strain) plots for 0° and 10° specimens as shown in Figure 4.6 and Figure 4.7 and Figure 4.8. The shear failure mode of the 10° G-10 glass-epoxy specimen is presented in Figure 4.9, and the obtained results are summarised in

Table 4.7. The elastic and shear modulus of the NCF composite were 132 Gpa and 7.5 Gpa respectively. The results were primarily obtained to serve as inputs for the finite element analysis.

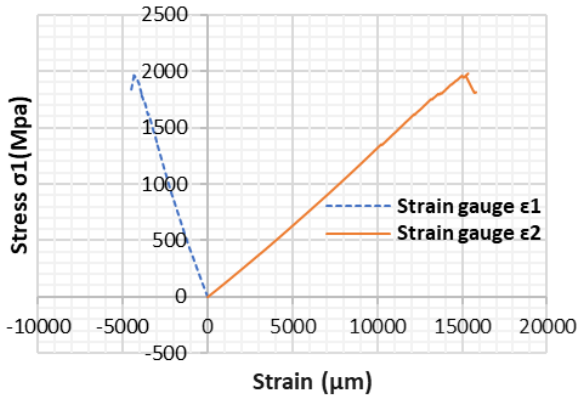

Figure 4.6 Stress-strain curve for 0º test specimen [335]

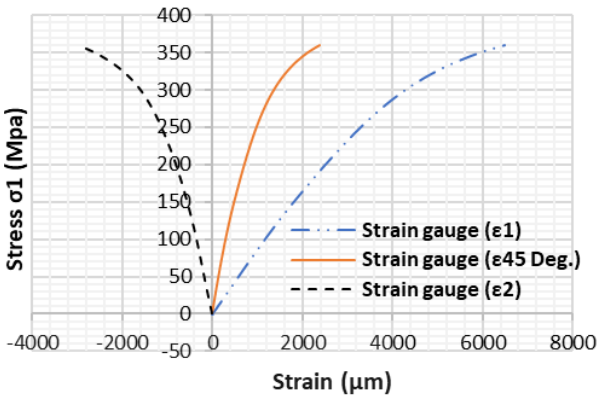

Figure 4.7 Stress-strain curve for 10º test specimen [335]

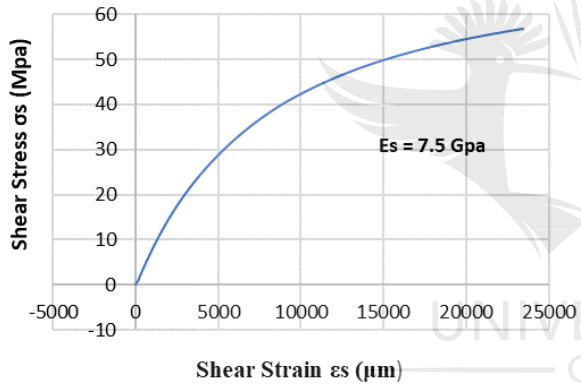

Figure 4.8 Shear (stress-strain) curve [335]

Figure 4.9 Shear failure of 10º specimen [335]

Table 4.7 Elastic properties of E-glass Non-crimp fabric

Composite	FVF (%) *	Ex (GPa)	Gxy (Gpa)	Vxy
UD-Glass/Epoxy NCF	71	132	7.5	0.307

Source [335]
*Fibre Volume Fraction

4.3.2 Finite Element Analysis

The technology for measuring induced stress concentrations directly during testing is presently non-existent and nearly impossible. However, finite element analysis provides the only feasible and effective avenue for investigating such induced stresses [8,11]. In this study, the approach proposed by Adams and Adams [8] was adopted.

Table 4.8 Material input for finite element analysis

Material Properties	UD glass NCF-epoxy*	Tab Material (G-10 glass fabric-epoxy) **	Two-part Adhesive**
Ex (GPa)	132	32.6	3.17
Ey (GPa)	10	6.9	
Es (GPa)	10	6.9	
Vxy	0.307	0.06	0.31
Vys	0.307	0.06	
Vxs	0.307	0.06	
Gxy (GPa)	7.5	3.45	
Gys (GPa)	66	10	
Gxs (GPa)	6.5	3.45	

Source [378]
*Experimental results from tensile testing

All the input parameters required for conducting finite element modelling of tensile loading are summarised in Table 4.8. The elastic modulus for the tab materials was $E = 32.6\ Gpa$ for G-10 glass fabric/epoxy [8] representing the low stiffness material and $E = 132\ Gpa$ for the non-crimp fabric composite representing the high stiffness material. After the finite element simulation of tensile loading, the area of maximum stress concentration was located at the tab termination region as shown in

Figure 4.10. The ability to minimise stress concentration at the tab termination region is essential to significantly limit testing deficiencies such as premature failures which lead to result inconsistencies, inaccuracies and extremely reduced tensile strength values.

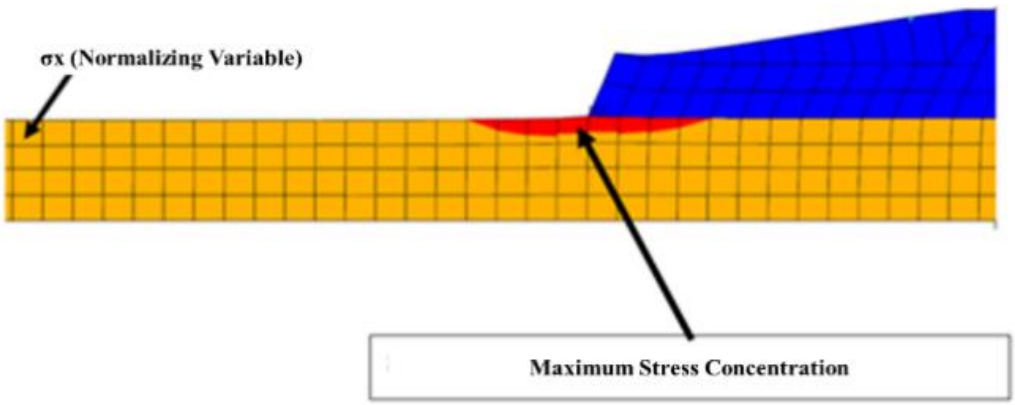

Figure 4.10 Finite element result showing the location of maximum stress concentration [335]

A summary of the normalised induced stress concentration at the tab termination region after 32 simulations using a full factorial 2-level five-factor design, is presented in Table 4.9. In this study, the five design parameters considered are: adhesive thickness, tab thickness, tab length, tap taper angle, and tab stiffness. An analysis of variance (ANOVA) was carried out to obtain the p-values which indicate the significance of each parameter as shown in Table 4. This was necessary to ascertain which factors were most significant. Since the objective was to minimise the stress concentration induced during tensile testing, the following factors had p-values less than 0.05 and therefore were the most significant: tab stiffness, tap taper angle, and adhesive thickness. The least significant factors were the tab thickness and tab length which had $P-values$ of 0.117 and 0.979 respectively for $\boldsymbol{\sigma x_{max}}$ as shown in Table 4.10. The inference from having such $p-values$ is that tab thickness ranging from 0.5 to 1.5 mm are acceptable and have no effect on induced stress concentration. The recommended rule of thumb in standard practice is to use a tab thickness, which is 1 to 4 times the thickness of the test specimen to guarantee against premature tab failure due to grip loading tab strength capable of withstanding grip loads.

Table 4.9 2-level factorial design

Tab Stiffness (Gpa)	Tab Thickness (mm)	Tab Length (mm)	Tap Tapper Angle (degrees)	Adhesive Thickness (mm)	σx_{max} (Normalised)	σy_{max} (Normalised)	τxy_{max} (Normalised)
32.6	0.5	50	90	1.5	1.193	0.070	0.038
32.6	1.5	100	90	0.25	1.394	0.126	0.084
32.6	1.5	100	90	1.5	1.251	0.104	0.057
32.6	1.5	100	5	0.25	1.151	0.045	0.031
32.6	0.5	50	90	0.25	1.297	0.079	0.053
132	1.5	50	90	1.5	1.329	0.133	0.072
132	0.5	100	5	0.25	1.500	0.145	0.096
32.6	0.5	50	5	1.5	1.201	0.082	0.045
32.6	0.5	100	90	0.25	1.285	0.083	0.055
32.6	1.5	50	5	1.5	1.199	0.081	0.044
132	1.5	100	5	1.5	1.339	0.147	0.079
32.6	1.5	50	90	0.25	1.402	0.123	0.082
32.6	1.5	50	90	1.5	1.244	0.096	0.052
132	0.5	50	90	0.25	1.591	0.164	0.108
132	0.5	100	90	0.25	1.596	0.174	0.116
132	1.5	100	90	0.25	1.655	0.198	0.132
32.6	0.5	50	5	0.25	1.151	0.045	0.031
132	1.5	100	90	1.5	1.346	0.145	0.078
32.6	0.5	100	5	1.5	1.195	0.079	0.043
32.6	1.5	50	5	0.25	1.151	0.045	0.031
132	0.5	100	90	1.5	1.313	0.130	0.070
132	0.5	100	5	1.5	1.328	0.142	0.077
32.6	0.5	100	5	0.25	1.151	0.045	0.031
32.6	0.5	100	90	1.5	1.197	0.076	0.042
132	0.5	50	5	1.5	1.338	0.147	0.079
132	1.5	50	5	0.25	1.505	0.149	0.098
132	1.5	50	90	0.25	1.651	0.191	0.127
132	1.5	50	5	1.5	1.342	0.148	0.080
132	0.5	50	5	0.25	1.501	0.148	0.098
32.6	1.5	100	5	1.5	1.198	0.080	0.044
132	1.5	100	5	0.25	1.505	0.149	0.098
132	0.5	50	90	1.5	1.299	0.119	0.064

Source [335]

Table 4.10 P-values for stress concentrations in bonded tabs

Factor	σx_{max}	σy_{max}	τxy_{max}
Tab Stiffness	0.000	0.000	0.000
Tab Thickness	0.117	0.010	0.020
Tab Length	0.979	0.581	0.612
Tab Taper Angle	0.001	0.000	0.001
Adhesive Thickness	0.000	0.000	0.001

Source [335]

A minimum thickness of 0.5 mm is recommended in the literature [7,379]. Similarly, the $P-value$ for tab length also indicates that any length ranging from 50 mm to 100 mm is acceptable. Tab length corresponding to the length of the grips is recommended [11].

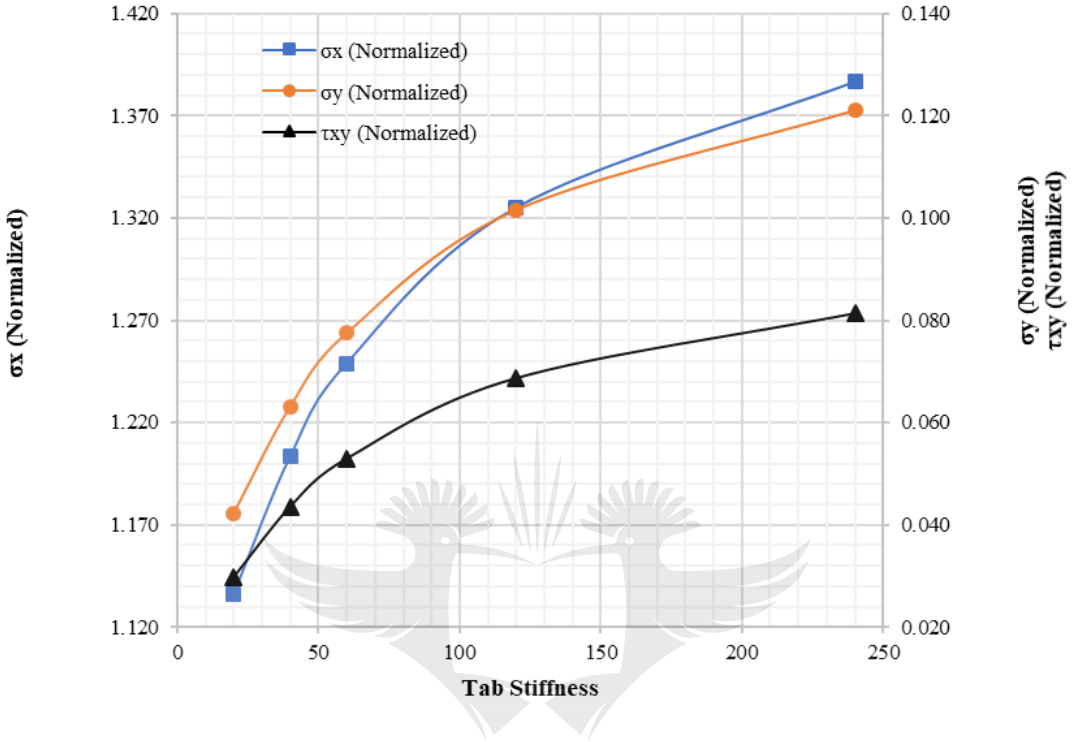

Figure 4.11 Effect of Tab stiffness on stress concentration [378]

To further investigate the effects of the tab design parameters, a finite element analysis was conducted again but over theoretically larger tab stiffness ranges of 20 – 240 Gpa, since tab stiffness was the most significant factor as observed from its $p-value$. In Figure 4.11, the trend showed that increasing tab stiffness positively correlated with an increase in all three stress concentrations in the tab termination region. The selection of tab materials with low stiffness is recommended to minimise stress concentration. The stiffness of a material indicates how compliant the material is. Material selection must therefore be guided by a compromise between material compliance and its mechanical strength capable to withstand and effectively transmit grip load to test specimen during tensile testing, since a material that is too compliant will fail under crushing and shearing load testing. The tab stiffness of the G-10 glass

fabric/epoxy ($E = 32.6\ Gpa$) meets the compliance and strength criteria and is recommended as suitable tab material [219].

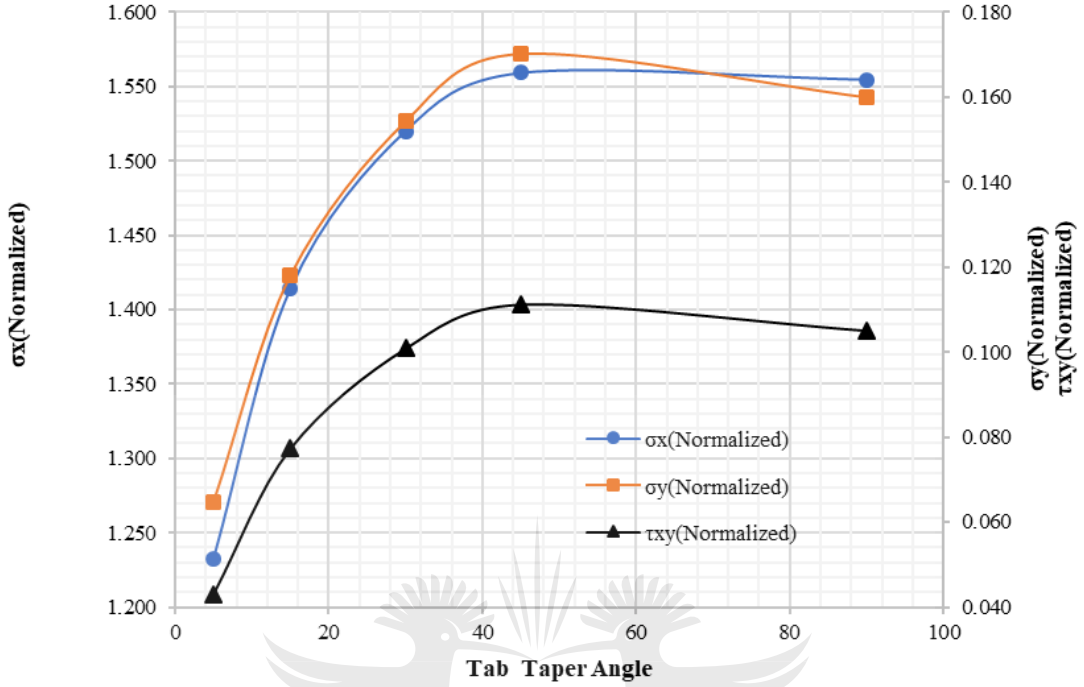

Figure 4.12 Effect of taper angle on stress concentration [378]

The shape or geometry of an object is known to significantly influence stress concentration and is a critical parameter to consider if stress minimisation is the primary goal. An increase in all three stress concentrations obtained from the finite element analysis (see Figure 4.12) showed a positive correlation with increase in the tab taper angle. Theoretically, tabs with the smallest taper angles, which are practically possible, are recommended. However, during tensile testing, the tab tapered region is not gripped and consequently susceptible to both the negative effects of peel stress (σ_y) and shear stress (τ_{xy}) which can result in premature failure in the adhesive regions with decreasing tab taper angles. In the literature, researchers have recommended taper angles within a range of 10^o to 30^o to meet the convenience of practicality and for ease of fabrication [7,380].

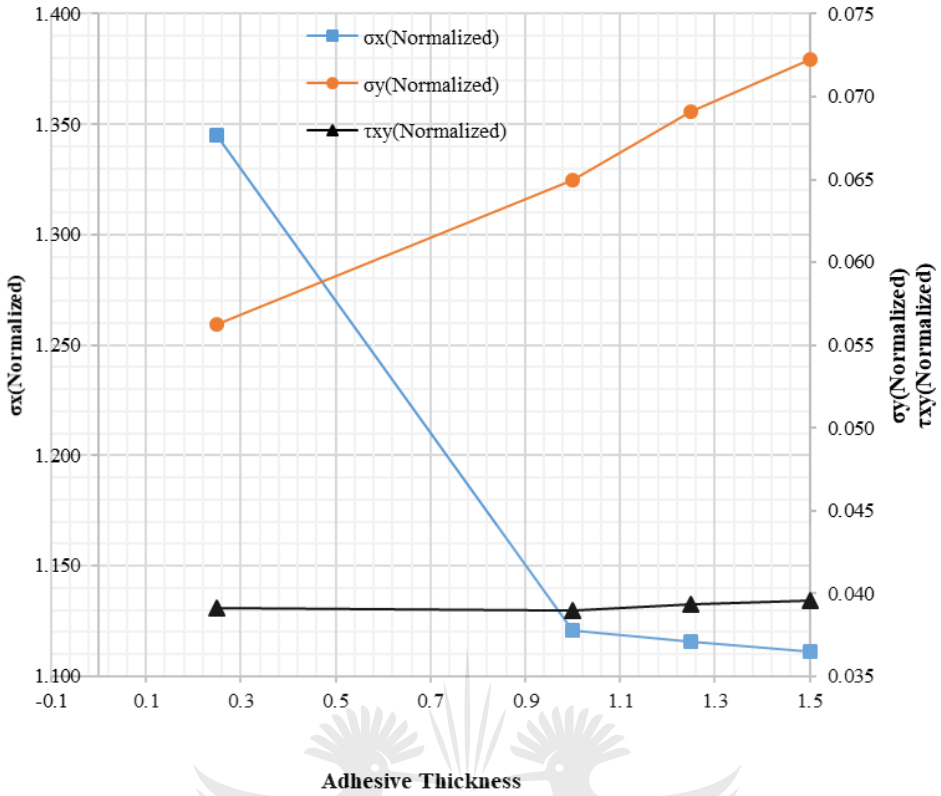

Figure 4.13 Influence of Adhesive thickness on stress concentration

The influence of adhesive thickness on all three stress concentrations was different from the two previous tab design parameters discussed. In Figure 4.13, an increase in adhesive thickness was inversely correlated to the induced normal stress concentration (σ_x) which is the predominant stress which causes premature failure at the tab termination region. Therefore, to minimise the stress the adhesive must be as thick as practically possible. However, when using tapered tabs, the inherent taper geometry can cause an increase in the peel stress (σ_y) as the adhesive thickness increases. This implies that the peel stress (σ_y) is positively correlated with an increase in adhesive thickness. The shear stress (τ_{xy}) was relatively constant.

4.3.3 Taguchi optimisation

The Taguchi $L8\ (2^5)$ orthogonal array DOE was used to analyse combinations of the design parameters to identify the configurations that minimise the stress concentrations; **σ**x_{max}**,**

σy_{max} and τxy_{max} which were computed from finite element simulations of tensile loading as seen in Table 4.11. The criteria for determination of the *SN* ratio was based on the "lower-the-better" equation. An *SN* response table was created after analysing the influence of all the design parameters as presented in Table 4.12. The optimal levels for every design factor was provided in the Table 4.13.

Table 4.11 Taguchi DOE with response stress concentration values

Simulation No.	A	B	C	D	E	σx (norm)	σy (norm)	Txy (norm)
1	32.6	0.5	50	5º	0.25	1.201	0.0817	0.0449
2	32.6	0.5	50	90º	1.50	1.193	0.0701	0.0384
3	32.6	1.5	100	5º	0.25	1.198	0.0801	0.0440
4	32.6	1.5	100	90º	1.50	1.251	0.1039	0.0566
5	132	0.5	100	5º	1.50	1.328	0.1417	0.0767
6	132	0.5	100	90º	0.25	1.596	0.1742	0.1157
7	132	1.5	50	5º	1.50	1.342	0.1484	0.0803
8	132	1.5	50	90º	0.25	1.651	0.1908	0.1265

Source [335]

Furthermore, the *SN* ratio values were computed for all the resulting induced stress concentrations. The optimal level was selected based on the highest *SN* ratio for a particular control factor level. A representation of the *SN* ratio main effects for global optimal and individual induced stresses is given in Figure 4.14. The optimised tab design configuration necessary to minimise the overall combination of the stress concentrations σx_{max}, σy_{max} and τxy_{max}, are detailed in Table 4.13. The bold text represents optimal values.

Table 4.12 The results of simulations and SN ratios values

No.	Control factors					σx_{max}	SN ratio (σx_{max})	σy_{max}	SN ratio (σy_{max})	τxy_{max}	SN ratio (τxy_{max})
	A	B	C	D	E						
1	32.6	0.5	50	5	0.25	1.201	-1.594	0.082	21.754	0.045	26.961
2	32.6	0.5	50	90	1.50	1.193	-1.535	0.070	23.082	0.038	28.304
3	32.6	1.5	100	5	0.25	1.198	-1.570	0.080	21.922	0.044	27.125
4	32.6	1.5	100	90	1.50	1.250	-1.943	0.104	19.668	0.057	24.950
5	132	0.5	100	5	1.50	1.327	-2.464	0.142	16.971	0.077	22.303
6	132	0.5	100	90	0.25	1.596	-4.060	0.174	15.178	0.116	18.731
7	132	1.5	50	5	1.50	1.342	-2.558	0.148	16.569	0.080	21.908
8	132	1.5	50	90	0.25	1.651	-4.355	0.191	14.388	0.127	17.958

Source [335]

The main effect plot provides a graphical representation of the nature of the significance via line orientation. The degree of line gradient determines the magnitude of the main effect. Factors which influence the system are thus characterised by non-horizontal lines while a horizontal line implies that the factor is not significant and has no effect on the system. Further analysis of the effects of factor interaction showed no significance which indicates that the main effect plots were sufficient for accurate interpretation of the data. An examination of the global optimal main effect plot clearly shows that tab stiffness had the greatest influence on minimising stress while tab length was horizontal reinforcing the high p-value earlier reported. Adhesive thickness was observed to be inversely correlated with increasing stiffness and stress. This implies that increasing the adhesive thickness significantly reduces induced stress concentrations at the tab termination region.

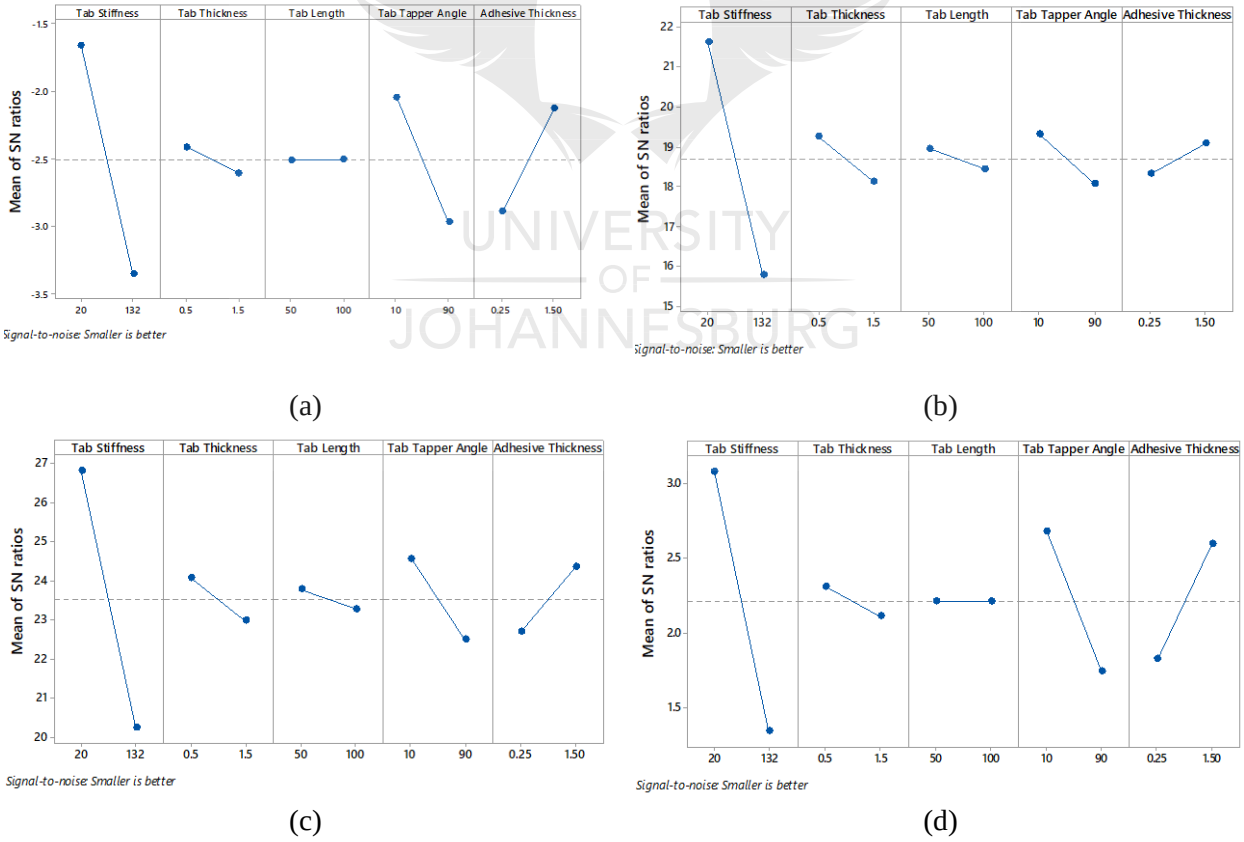

Figure 4.14 SN main effects plots for (a) $\boldsymbol{\sigma}x_{max}$ (b) $\boldsymbol{\sigma}x_{max}$ (c) $\boldsymbol{\sigma}x_{max}$ (d) global main effect [335]

The results in Table 4.13 show that the SN ratios and corresponding levels for the design factors required for minimising stress concentrations in the tab termination region were summarised as follow:; for factor A (tab stiffness) the optimal SN ratio was 3.083 at level 1, factor B (tab thickness) had an optimal SN ratio of 2.312 also at level 1, for factor C (tab length) the optimal SN ratio of 2.212 was indicated at both levels 1 and 2, and the optimal SN ratio for factor D (tab taper angle) was 2.679 at level 1. Lastly, for factor E (adhesive thickness) the optimal SN ratio value was 2.599 at level 2. Therefore, during tensile testing, the overall stress concentration effectuated due to the bonding of the tabs for this particular composite, can be minimised by implementing the optimal tab design configuration of tab stiffness = 32.6 Gpa, tab thickness = 50 mm, tab length = 50 mm or 100 mm, tab taper angle = 5° , and adhesive thickness = 1.5 mm.

Table 4.13 SN response table for the combined stress concentrations ($\boldsymbol{\sigma x_{max}}$, $\boldsymbol{\sigma y_{max}}$, $\boldsymbol{\tau xy_{max}}$)

Levels	Control factors ($\boldsymbol{\sigma x_{max}}$, $\boldsymbol{\sigma y_{max}}$, $\boldsymbol{\tau xy_{max}}$)				
	A	B	C	D	E
	Tab Stiffness	Tab Thickness	Tab Length	Tab Taper Angle	Adhesive Thickness
Level 1	3.083	2.312	2.212	2.679	14
Level 2	1.340	2.111	2.212	1.744	2.599
Delta	1.743	0.201	0.000	0.935	0.774
Rank	1	4	5	2	3

Source [335]
*Bold values show the optimal levels of design factors

4.3.4 Taguchi-Multiple Response optimisation

The second optimisation approach developed was a Taguchi multiple response hybrid where the DOE portion of the Taguchi methodology was used in combination with a desirability based multiple response optimisation. Table 4.14 shows the setup of the optimisation problem, which include factors such as the goal of minimisation, $weight = 1$ and $importance = 1$ for all the tab design factors. After the computation of the optimal outcomes for all the tab design parameters, the results are shown in Table 4.15 while the

graphical representation of the desirability components is shown in Figure 10 (the optimal values are given in red).

Table 4.14 Setup of design optimisation parameters

Response	Goal	Target	Upper	Weight	Importance
τxy (Norm)	Minimum	0.03844	0.12651	1	1
σy (Norm)	Minimum	0.07013	0.19080	1	1
σx (Norm)	Minimum	1.19333	1.65100	1	1

Source [335]

Table 4.15 Multiple response prediction (Optimised configuration)

Variable	Optimal Tab Configuration
Tab Stiffness	32.6 (Gpa)
Tab Thickness	0.5 (mm)
Tab Length	100 (mm)
Tab Taper Angle	5º
Adhesive Thickness	1.5 (mm)

Source [335]

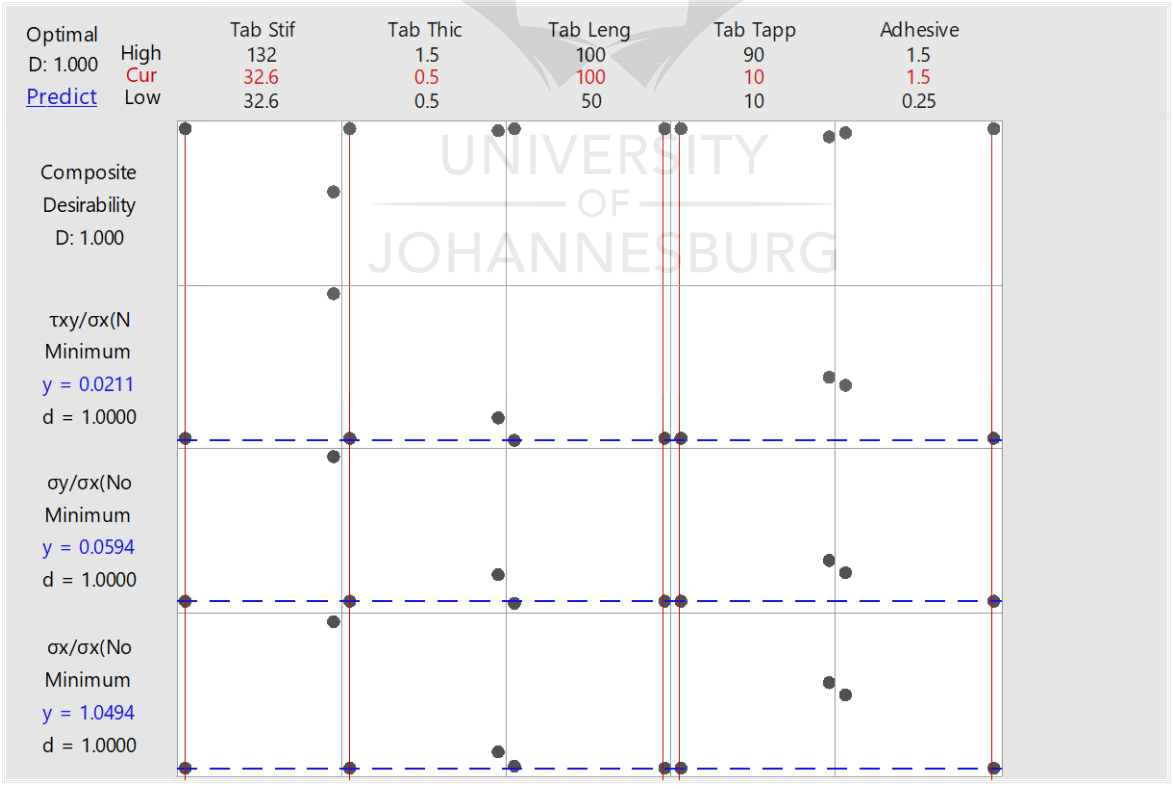

Figure 4.15 Composite desirability plot [335]

The objective for using a desirability methodology in carrying out multiple response optimisations was to derive a composite desirability equal to or close to 1. The weight and important values of 1 were selected to establish a baseline where all factors had the same influence. The optimal tab design parameters required for minimising the induced stress concentration at the tab termination region are tab stiffness ($32.6\,GPa$), tab thickness ($0.5mm$), tab length ($50mm$), tab taper angle ($5°$),and adhesive thickness ($1.5mm$). The individual desirability value was 1 for all three stress concentrations also leading to a composite desirability of also 1 as seen in Figure 4.15.

4.3.5 Taguchi-Genetic Algorithm optimisation

The second approach developed for optimising the design configuration of tabs to minimise stress concentration was a hybrid approach consisting of a combination of Taguchi design of experiments (DOE) and genetic algorithms (GA). The Taguchi L_8 (2^5) DOE section was required to generate the regression equations from the induced stress concentrations, while the GA portion used the resulting regression as the objective functions.

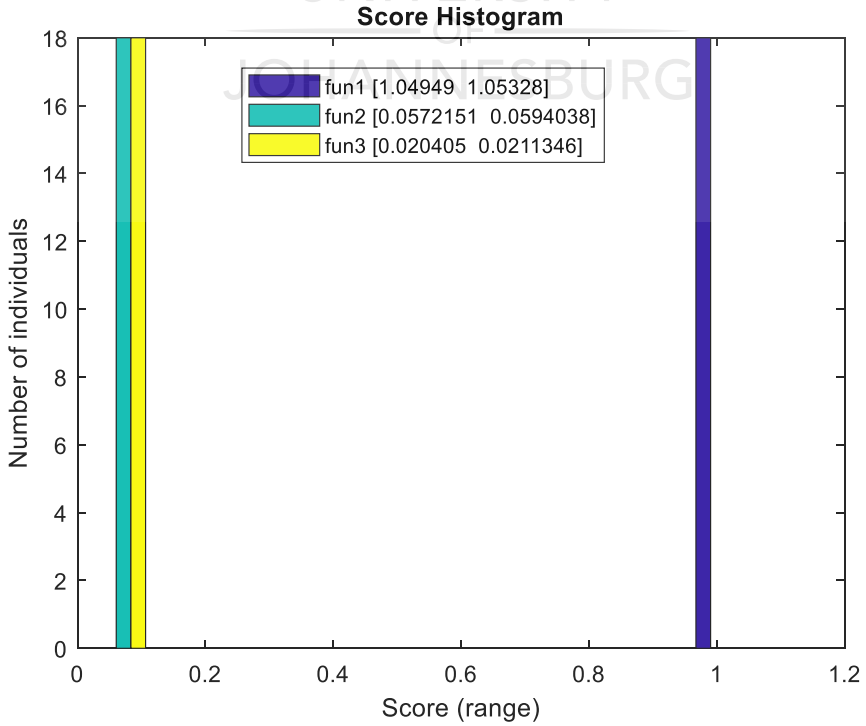

(a)

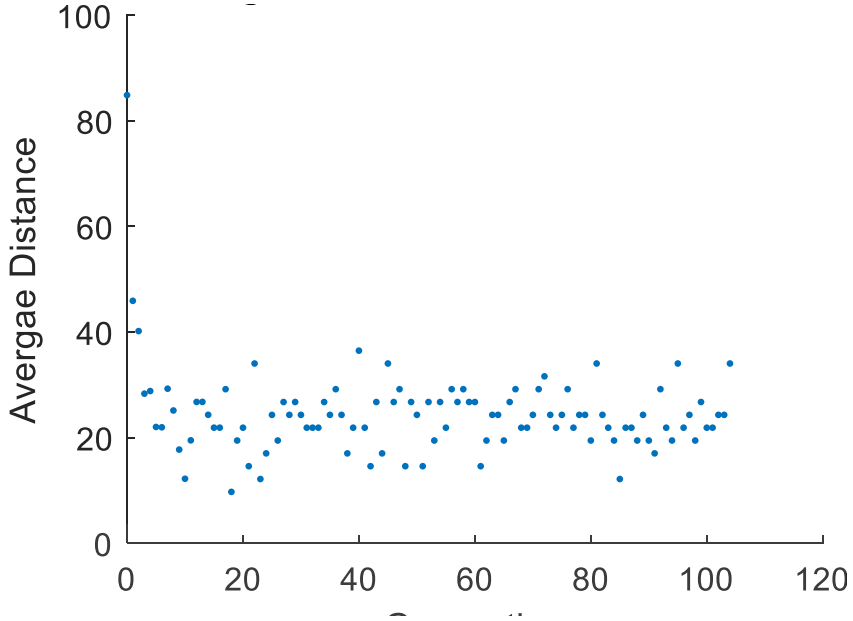

(b)

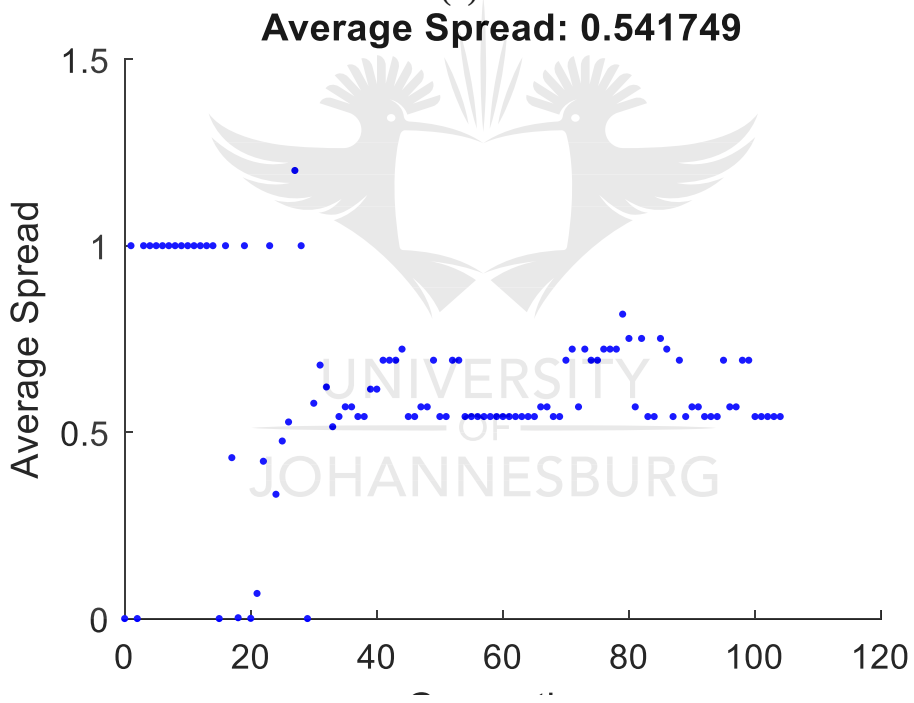

(c)

Figure 4.16 (a) Optimal Objective function (b) Average distance between individuals (c) Average Spread [335]

Table 4.16 Optimal solution for design parameters using Taguchi-GA hybrid approach

Obj. Fun 1	Obj. Fun 2	Obj. Fun 3	Tab Stiffness	Tab Thickness	Tab Length	Tap Tapper Angle	Adhesive Thickness
1.053284	0.057215	0.020405	32.6	0.5	50.004	5	1.5
1.049491	0.059404	0.021135	32.6	0.5	98.639	5	1.5

Source [335]

At the solution point, the objective function values were computed to be $[1.049491143, 0.053284701]$ for objective function 1, $[0.057215173, 0.059403764]$ for objective function 2 and $[0.020405058, 0.021134588]$ for objective function 3 as captured in Figure 4.16 (a). The average distance and spread are shown in Figure 4.16 (b) and (c) respectively and had values of 0.00107454444268082 and 0.541749461994625. After 105 generations, the optimal solution was obtained. The computational time was extremely short since the problem was linear and the solution easily attainable. The results of the attained optimal tab design configuration are outlined in Table 4.16 as follows: tab stiffness $(32.6\ GPa)$, tab thickness $(0.5\ mm)$, tab length $(50\ mm\ or\ 100\ mm)$, tab taper angle $(5°)$ and adhesive thickness $(1.5\ mm)$.

4.3.6 Comparison of Approaches

A comparison of the optimal solutions for the three optimisation approaches is given in Table 13. The results are clearly similar and in agreement with the $P - values$ obtained from ANOVA. Therefore, the induced stress concentrations in the tab termination region can be minimised by reducing tab stiffness, taper angle and increasing the adhesive thickness [8].

Table 4.17 Comparison of all optimisation techniques

Optimisation Method	Design Parameters				
	Tab Stiffness	Tab Thickness	Tab Length	Tab Taper Angle	Adhesive Thickness
Taguchi	32.6	0.5	**50/100**	5º	1.5
Taguchi – MRO	32.6	0.5	50	5º	1.5
Taguchi – GA	32.6	0.5	**50/100**	5º	1.5

MRO-Mult-Response

In comparison with the other two techniques, the Taguchi method is primarily based on the interactions between noise and controllable factors. Critical drawbacks in this technique can occur in cases where the interactions between the controllable design parameters such as

the tab stiffness, thickness, length, taper angle and adhesive thickness and noise factors such as temperature and humidity are insignificant or highly significant. A weak interaction between the design parameters and noises makes the Taguchi approach ineffective and unreliable while strong interactions compromise the capability and power of the Taguchi technique [381].

Multiple response optimisation approaches using the desirability function were very efficient for reaching optimal values and were simpler to implement compared to a GA based optimisation. The desirability function used in this study was developed by Derringer and Suich [343] and assumes that the variability within the response variables is stable, therefore making the multiple response means the primary focus of attention during optimisation. However, in situations of high multiple response variability, the assumption of this stable variability is challenged making the outcomes unreliable [382].

GA-based approaches do not have the drawback related to interaction and response variability as observed in the Taguchi method and multiple response optimisation respectively. The GA approach is the only method that can effectively handle non-linear objective functions to obtain a global solution without the drawbacks of gradient-based approaches such as getting stuck in a local minimum and the fact that performance is dependent on initial values of design variables as with the Taguchi and Multiple response optimisations. Since the problem was linear, the computational time was extremely fast. Although only three linear equations were involved in this study, for situations of an even higher number of equations with infinitely many solutions, GAs can solve large system of linear equations without the disadvantage of other techniques such as inversion of large matrixes and rounding errors [383]. The above-stated methods are suitable for optimising design parameters of the test specimen for other mechanical characterisations such as impact, compression, flexural, hardness, fatigue and many more.

4.4 Impact Test

In characterising the mechanical properties of polymer nanocomposites, impact resistance, in particular, is the least understood but one of the most important. In distinct variance with other mechanical properties, predicting the impact strength of polymer composites is not possible. Therefore, the *ASTM D*6110-18 [384] clearly states that the standard must not be used for determining design data. Consequently, the Charpy test basically seeks to provide a platform for comparative testing of different materials or configurations to investigate the absorption of localised impact energy.

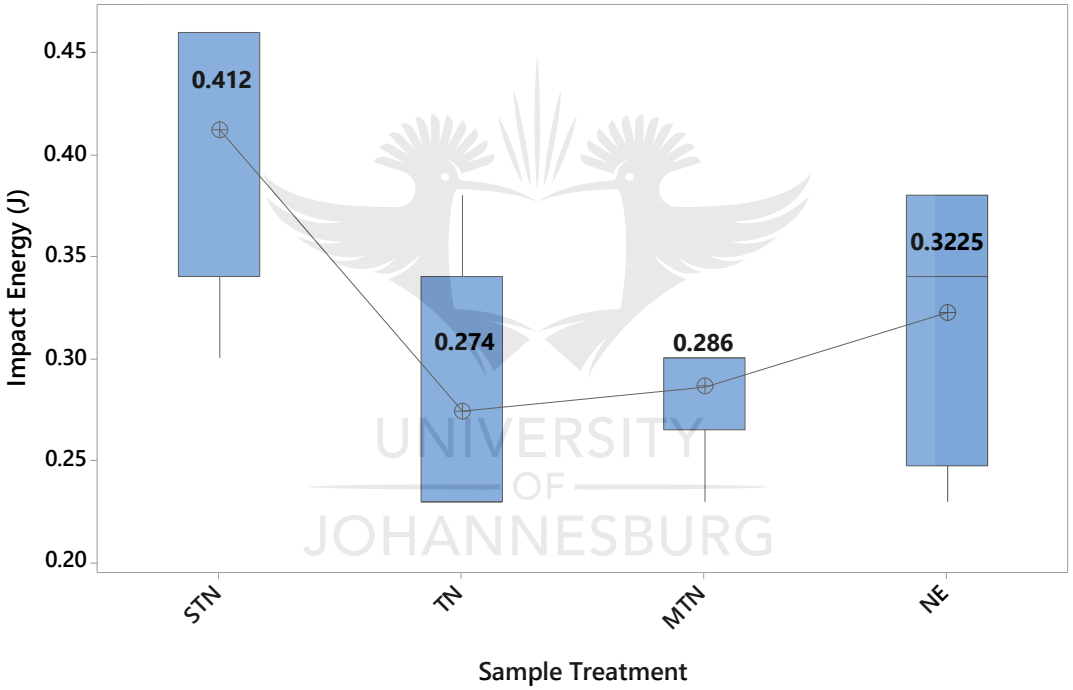

Figure 4.17 Charpy impact test results for TiO_2 Nanocomposites with and without functionalisation ((Neat epoxy (NE); Silane functionalised TiO_2 nanocomposite (STN); Non-functionalised TiO_2 nanocomposite (TN) and Methanol treated TiO_2 (MTN).

The Charpy impact test results as shown in Figure 4.17 for NE, STN, TN and methanol treated TiO_2 (MTN) nanoparticles generated impact absorption energies of $0.322\,J$, $0.412\,J$, $0.274\,J$ and $0.286\,J$ respectively. The energy absorbed improved by 28% when silane functionalised TiO_2 was incorporated into the epoxy matrix. However, the introduction of non-

functionalised and methanol treated TiO_2 decreased the energy absorbed by 15% and 11% respectively.

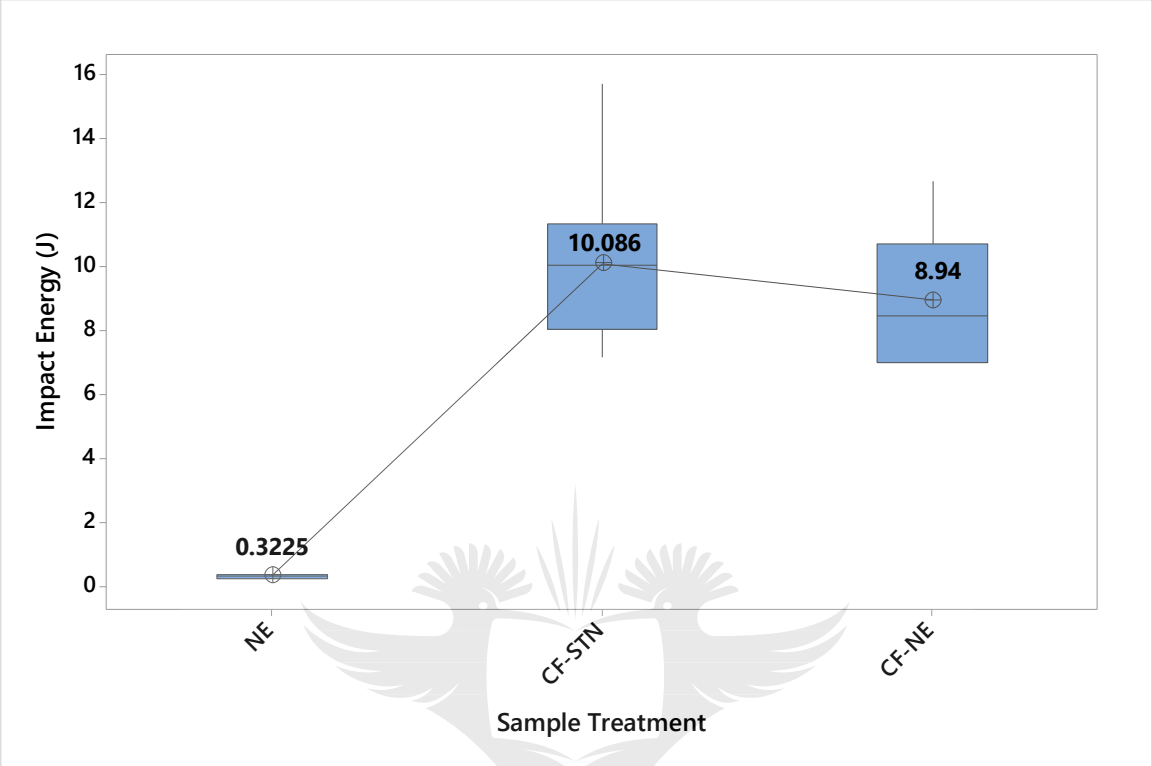

Figure 4.18 Charpy impact test result for NCF Carbon fibre reinforced composite with and without TiO_2

CF-NE and CF-STN samples were fabricated to investigate the influence of both fibre incorporation and the influence of functionalised TiO_2 on the impact energy of the composite. The impact energies presented in Figure 4.18, show that an increase of 2600% was observed for CF-NE while an increment in absorbed energy of approximately 3000% was obtained for CF-STN. As expected, the use of carbon fibre as reinforcement significantly improved the impact properties of the composite [179]; however, and more importantly, was the 13% improvement in impact energy of CF-STN as a result of incorporating silane functionalised TiO_2 nanoparticles [385].

Table 4.18 ANOVA of the average impact energies for matrix composites with or without TiO_2 reinforcement.

Source	DF	Adj SS	Adj MS	F-Value	P-Value
Sample Treatment	3	0.05845	0.019482	5.06	0.013
Error	15	0.05779	0.003853		
Total	18	0.11624			

From the results generated, the null hypothesis for the analysis of variance (see Table 4.18), stipulating that a statistical P-value of 5% significance indicates that the means are equal, was rejected. This P-Value was 0.013; implying that the applied treatments of incorporating TiO_2 functionalised and non-functionalised had different effects on the Charpy impact energy.

Table 4.19 Tukey Pairwise Comparisons of the average impact energies for epoxy matrix composites with and without TiO_2 reinforcement ((Neat epoxy (NE); Silane functionalised TiO_2 nanocomposite (STN); Non-functionalised TiO_2 nanocomposite (TN) and Methanol treated TiO_2 (MTN).

Sample Treatment	Mean	Std. Dev	Grouping
STN	0.4120	0.0716	A
NE	0.3225	0.0666	A B
MTN	0.2860	0.0313	B
TN	0.2740	0.0723	B

* Means that do not share a letter are significantly different.

Table 4.20 Tukey Simultaneous Tests for Differences of Means for epoxy matrix composites with and without TiO_2 reinforcement (Neat epoxy (NE); Silane functionalised TiO_2 nanocomposite (STN); Non-functionalised TiO_2 nanocomposite (TN) and Methanol treated TiO_2 (MTN).

Difference of Levels	Difference of Means	SE of Difference	T-Value	Adjusted P-Value
TN – STN	0.1380	0.0393	-3.52	0.015
MTN – STN	-0.1260	0.0393	-3.21	0.027
NE – STN	-0.0895	0.0416	-2.15	0.183
MTN – TN	0.0120	0.0393	0.31	0.990
NE – TN	0.0485	0.0416	1.16	0.657
NE – MTN	0.0365	0.0416	0.88	0.817

To further investigate the statistical significance of the treatments, the Tukey test at a confidence level of 95% as in Table 4.19 was applied to determine how significant the process of silane functionalisation of TiO_2 contributed to improving the impact energy of the epoxy matrix. The pairwise comparison results in Table 4.20 showed a $p - value$ of 0.015 when STN and TN were compared. The high significance was certainly due to the effects of silane

functionalisation which led to superior average impact energy. Conversely, the non-functionalised specimen (TN) displayed lower impact energies which can be attributed to the formation of large agglomeration and a poor state of dispersion [135]. The second most significant comparison was between STN and MTN which generated a $P - value$ of 0.027. Clearly, silane functionalisation improved homogeneity in nanoparticle dispersion and wettability and therefore was better at improving the impact energy by exhibiting higher average values while methanol treatment, degraded the impact properties of the epoxy matrix.

Table 4.21 ANOVA of the average impact energies of NCF Carbon Fibre reinforced composites with and without TiO_2.

Source	DF	Adj SS	Adj MS	F-Value	P-Value
Sample Treatment	2	4283.71	141.85	29.21	0.000
Error	17	82.54	4.86		
Total	19	366.26			

Similarly, ANOVA was also conducted on NE, CF-NE and CF-STN as seen in Table 4.21. The resulting $p - value$ of 0.000 indicates a high significance and a rejection of the null hypothesis where the mean impact energy values are assumed to be equal. But of greater interest was to determine whether the silane treatment had statistical significance on the fibre reinforced composites.

Table 4.22 Tukey Pairwise Comparisons of the average impact energies for NCF Carbon Fibre reinforced composites with or without TiO_2

Sample Treatment	Mean	StDev	Grouping
CF – STN	10.086	2.562	A
CF – NE	8.940	2.167	A
Neat Epoxy	0.3225	0.0723	B

Means that do not share a letter are significantly different.

Table 4.23 Tukey Simultaneous Tests for Differences of Means for NCF Carbon Fibre reinforced composites with or without TiO2

Difference of Levels	Difference of Means	SE of Difference	T-Value	Adjusted P-Value
CF-STN – NE	9.76	1.30	7.49	0.000
CF-NE – NE	8.62	1.42	6.06	0.000
CF-NE – CF-STN	-1.15	1.14	-1.01	0.583

The Tukey analysis presented in Table 4.22 and Table 4.23 clearly shows that when samples with and without silane treatment were compared the $p-value$ was 0.583 - an indication that the statistical improvement observed in the silane treatment of TiO_2 was not significant. However, the very low $p-value$ of 0.000 observed between neat epoxy and fibre reinforced samples implies that the fibre, orientation and surface morphology, and interface bonding between fibre and matrix may have contributed to the high variation in means. The influence of the above factors is thoroughly discussed in Sections 4.4.1 to 4.4.3.

4.4.1 Effect of Silane Functionalisation TiO_2 on Impact Energy of Matrix

The impact energy absorption behaviour of nanocomposites can be investigated by studying the mechanisms that are responsible for this property. The proper functioning of composite systems is primarily based on its load transfer properties. The ability of TiO_2 nanoparticles to function as reinforcement is dependent on the matrix-to-nanoparticle load transfer which is a critical metric for interfacial strength. Interfacial enhancement directly correlates with improved load transfer which leads to improved mechanical properties. Another mechanism well-known for contributing to the improvement of nanocomposite mechanical properties is the bridging phenomenon. This effect is based on the increase in nanoparticles bridging the interface cracks while particle weight fraction increases with particle size remaining constant [386]. This study confirmed the observation from previous studies that the low aspect ratio of smaller particles enhances impact properties as in STN while larger particles (agglomerate etc) can behave as flaws exhibiting high aspect ratios that create high-stress concentrations along the matrix-particle interface as in TN [135,387].

4.4.2 Effect of Silane Functionalisation TiO_2 on Impact Fracture

To evaluate the influence of flaws and agglomerates in initiating and propagating cracks in the matrix, unnotched testing is most suitable. A measure of $2.5\,wt\%$ of TiO_2 as

recommended by Salehian and Jahromi [135] was used in manufacturing the samples since a high concentration of nanoparticle inclusion tends to degrade the mechanical properties of composite materials, because of its susceptibility to increased agglomeration which introduces defects in the epoxy matrix and causes degradation of the interfacial bonding [385,388].

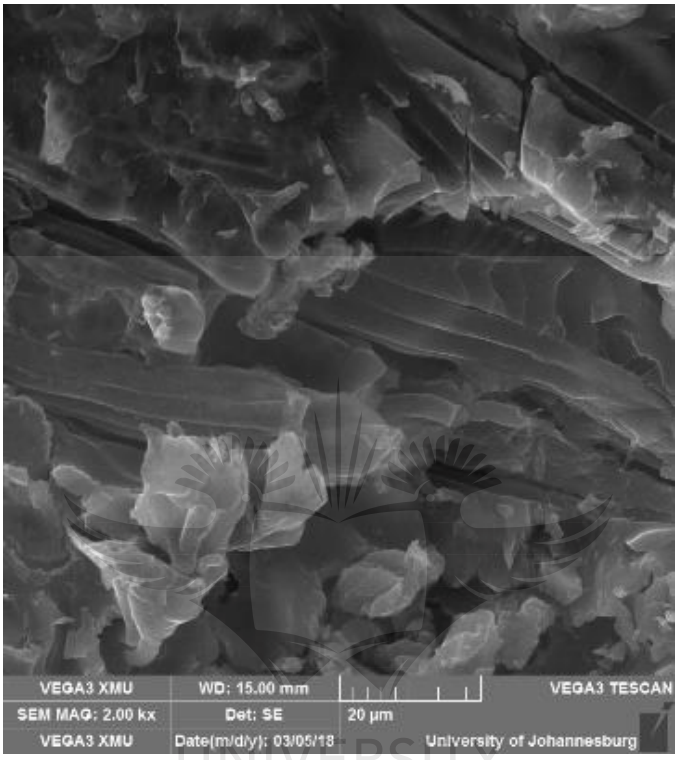

Figure 4.19 Charpy impact fracture surface of NE (0 vol% of fibre) with detail of the epoxy transversal fracture

The evaluation of the fracture surface of nanocomposites provides visual details and information about the effect of nanoparticle on fracture response and fracture mechanisms. In Figure 4.19 brittle behaviour of the neat epoxy fracture surface is observed with large smooth regions, creases, fracture steps, and hyperbolic markings along the path of the crack propagation and obvious river lines. These features are an indication of low resistance to crack propagation; a factor which results in brittle failure [135].

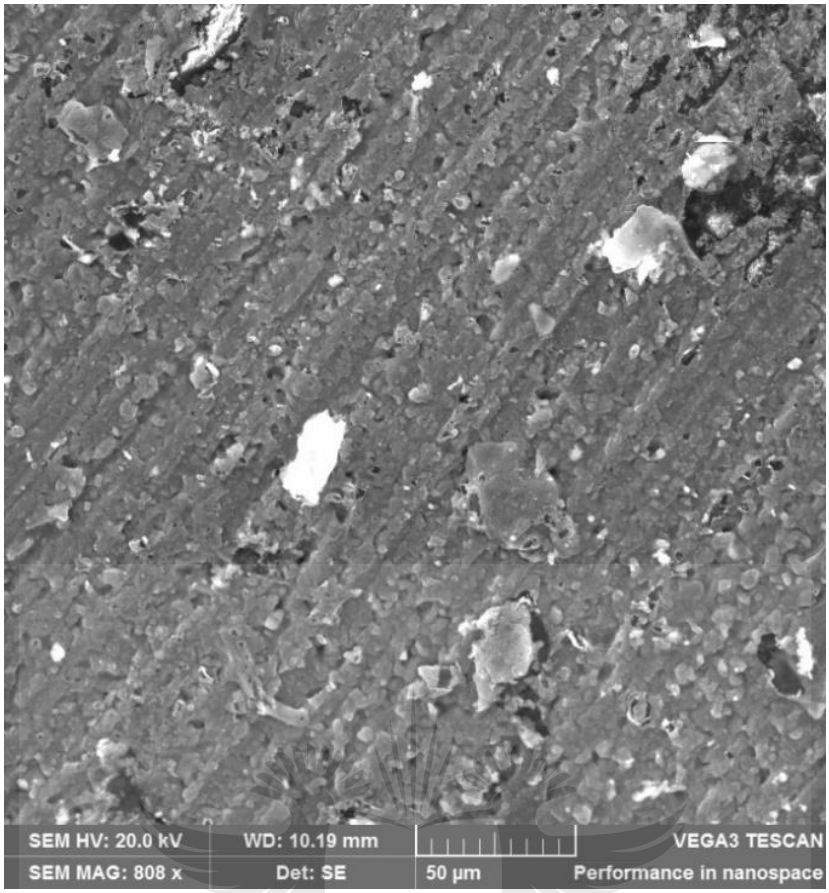

Figure 4.20 Homogenous dispersion with some agglomerations (STN)

On inclusion of the TiO_2 nanocomposites, as seen in Figure 4.20, a mostly well-spaced and homogenously distributed TiO_2 nanoparticles with only a few minor agglomerates within the polymer matrix was observed. This leads to a rough surface that serves as a hindrance to crack propagation and further as crack deflection [127,135]. The divergence of crack fronts after contacting the rigid nanoparticles results in a larger fracture surface, which correlates with increased energy absorption. Agglomerate breakage and shear lips are also observed as being primarily responsible for this type of fracture mechanism. It must be noted that the breakage of agglomerates is associated with good adhesion between particles and the matrix because weak bonding would have resulted in agglomerate pull-out.

The literature indicates that some of the toughening mechanisms include void nucleation and matrix deformation via localised inelastic shear [389], debonding at particle-

matrix interface, and crack defection at reaching agglomerates [390]. All these mechanisms were present in the functionalised samples. Shear bands developing from agglomerates are observed in Figure 4.21. The presence of the bands is an indication of the epoxy matrix undergoing plastic deformation originating from void nucleation.

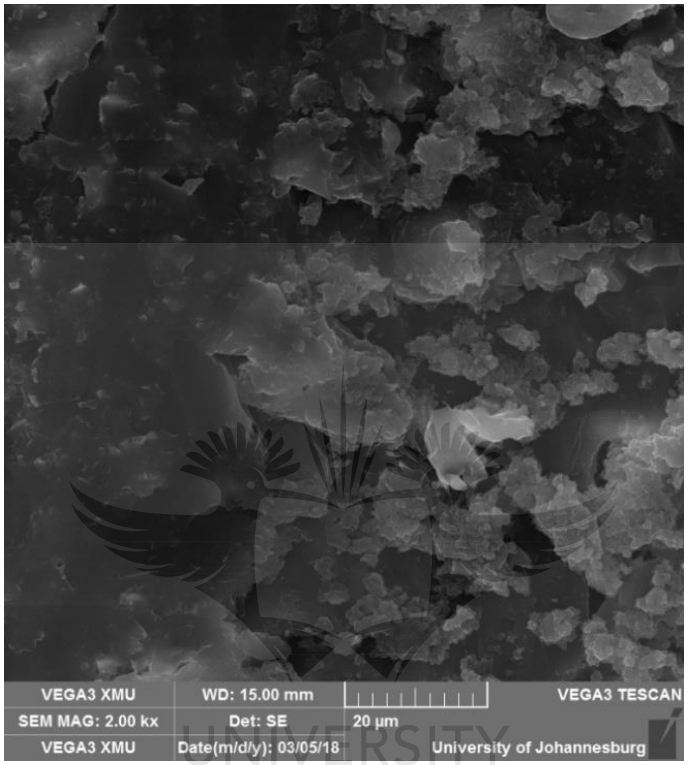

Figure 4.21 Shear bands developing from agglomeration of the TN sample

An analysis of the non-functionalised TiO_2 nanoparticles as shown in Figure 4.22, revealed the presence of both nano- and micro-reinforcing mechanisms. The nano fracture mechanisms were (1) particle pull-out, (2) interparticle crack propagation, and (3) particle crack pinning (characterised by a tail behind the particle). The micro fracture mechanisms are attributed to the presence of agglomerates which promotes (4) crack deflection. The poor energy absorbed value from the inclusion of non-functionalised TiO_2 nanoparticles can be ascribed to weak interface adhesion between the polymer chains and nanoparticles. This leads to high stress concentration along the interface which consequently results in failure of the nanocomposite [385].

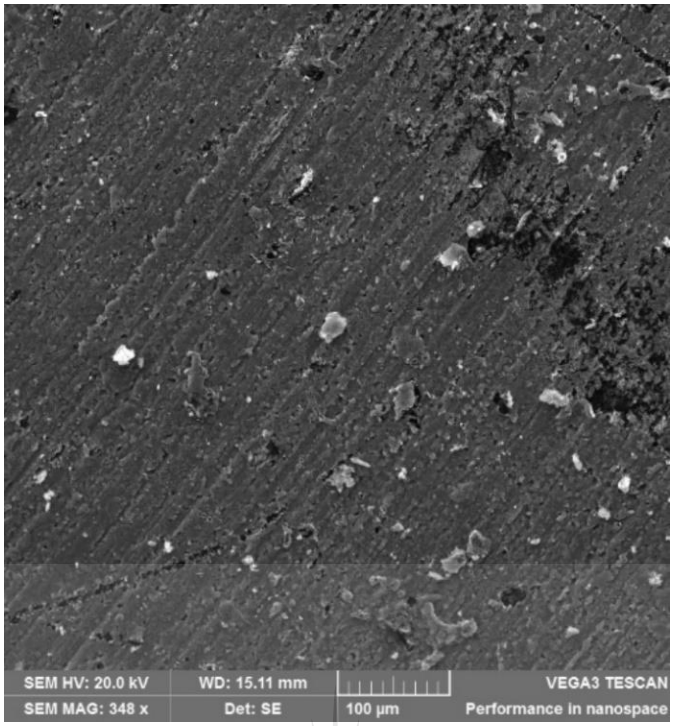

Figure 4.22 Defects in non-functionalised TiO_2 nanocomposite (TN)

However, the process of functionalisation improves the adhesion between the TiO_2 nanoparticles and epoxy matrix through the attraction of greater polymer molecules and the formation of an interphase. The silane functionalised TiO_2 nanoparticles are linked to polymer chains via strong covalent bonds [385]. Furthermore, the formation of relatively larger agglomerates when using non-functionalised TiO_2 nanoparticles hinders effective dispersion in the matrix. The inclusion of nanoparticles thus induces greater energy absorbing mechanisms which serve as obstacles to the propagation of crack re-sharpening implying that increased work is required to fracture the nanocomposite.

4.4.3 Effect of Impact Energy Absorbed on NCF Carbon Fibre

Composite impact damage response is influenced by a variety of factors, the most important being matrix toughness, impact velocity and support conditions, fibre strength and stiffness, fibre arrangement, layup and thickness [391]. During impact testing of composite materials, a portion of the associated energy is used for elastic deformation while the remaining

excess energy is consumed via other mechanisms such as delamination, matrix cracking, fibre breakage and fibre-matrix bonding. The resulting degree of damage is a function of the total energy absorbed during the impact [391].

An improvement in fibre-matrix and nanoparticle interface bonding is the main factor in enhanced impact strength. The modes of failure observed were, delamination and multiple fibre breakages, both of which are directly linked to the percentage weight selected [392]. The use of bi-axial $\pm 45^{o}$ NCF played an important role in the effective absorption of impact energy since both fibre and epoxy matrix absorbed the impact energy similar to the laminate orthotropic failure reported by Morioka, et al [393].

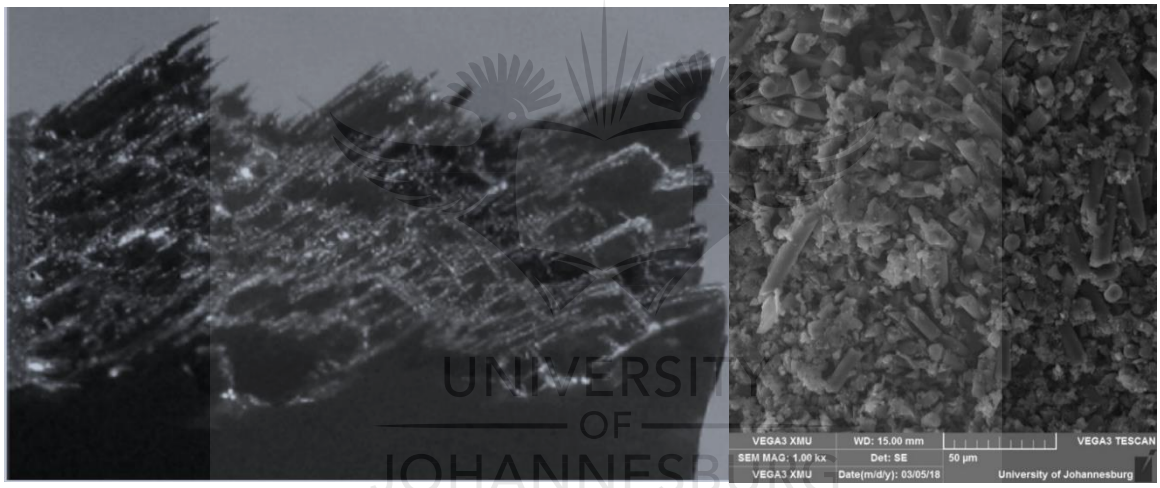

Figure 4.23 NCF CF-STN fracture profile

A high crack propagation energy was produced when cross point fibre breakages were induced at crack initiation with the crack propagation along the $\pm 45^{o}$ fibre-matrix interface in a zigzag path [394] as shown in Figure 4.23. The $\pm 45^{o}$ orientation of the ply laminates in the NCF carbon fibre exhibited pseudo-ductile characteristics, which resulted from the $+45$ laminae undergoing shearing. Both the epoxy matrix and fibres in such circumstances share the impact load [391]. It must be noted that the matrix strength is lower than the fibre strength which causes delamination to be the dominant fracture mode with accompanying transverse cracking of the matrix without breakages in the fibre. This particular behaviour has been

reported in several studies [391,395,396]. A $\pm 45^{o}$ stacked laminate shows superior impact performance compared to other stacked orientations [391,397].

In summary, three main categories of failure mechanisms occur during impact testing, which are: (1) matrix only associated fracture and plastic deformation, (2) fibre only fracture and plastic deformation, and (3) interfacial-associated mechanisms such as fibre-matrix debonding, post-bonding friction and fibre pull-out [398]. Failure mechanisms in composite materials do not depend on the constituent properties alone but also on the efficiency of interface bonding, fibre length, fibre volume and fibre orientation.

4.5 Inclusion of TiO_2 Nanoparticle towards Matrix Modification for Manufacture of NCF Composites

4.5.1 Thermal Characterisation of TiO_2 Nanocomposite

Thermogravimetric analysis (TGA) was carried out on a nanophase composite system to investigate its thermal stability. It was envisaged that the introduction of TiO_2 would positively impact the thermal stability of the composite material. Real time thermograms were generated using a universal analysis data acquisition system to analyse the thermal stability of the neat epoxy (NE), silane functionalised TiO_2 nanocomposites (STN), non-functionalised TiO_2 nanocomposites (TN), NCF carbon fibre reinforced composites (CF-NE), and NCF carbon fibre reinforced composites with TiO_2 inclusion (CF-STN) as shown in Figure 4.24. Observation of the TGA curves indicated that in general, thermal stability was enhanced by the inclusion of silane treated TiO_2 nanoparticles. The thermal stability of the composites was analysed through computation of the fractional weight as a function of the heating temperature. A sample is inferred to show higher thermal stability if it satisfies the assumption of retaining a specific fractional weight at a more elevated temperature.

Weight loss measurements were determined between the temperature ranges of 30℃ and 800℃. However, the range of importance was between 150℃ - below which weight changes

could be influenced by the absorption of water- and 700℃ - above which significant oxidation occurs [21]. The results clearly indicate that the inclusion of TiO_2 nanoparticles improves the thermal stability of neat epoxy [21,399] as in the tabulation of the decomposition temperatures for the samples with and without TiO_2 presented in Table 4.24.

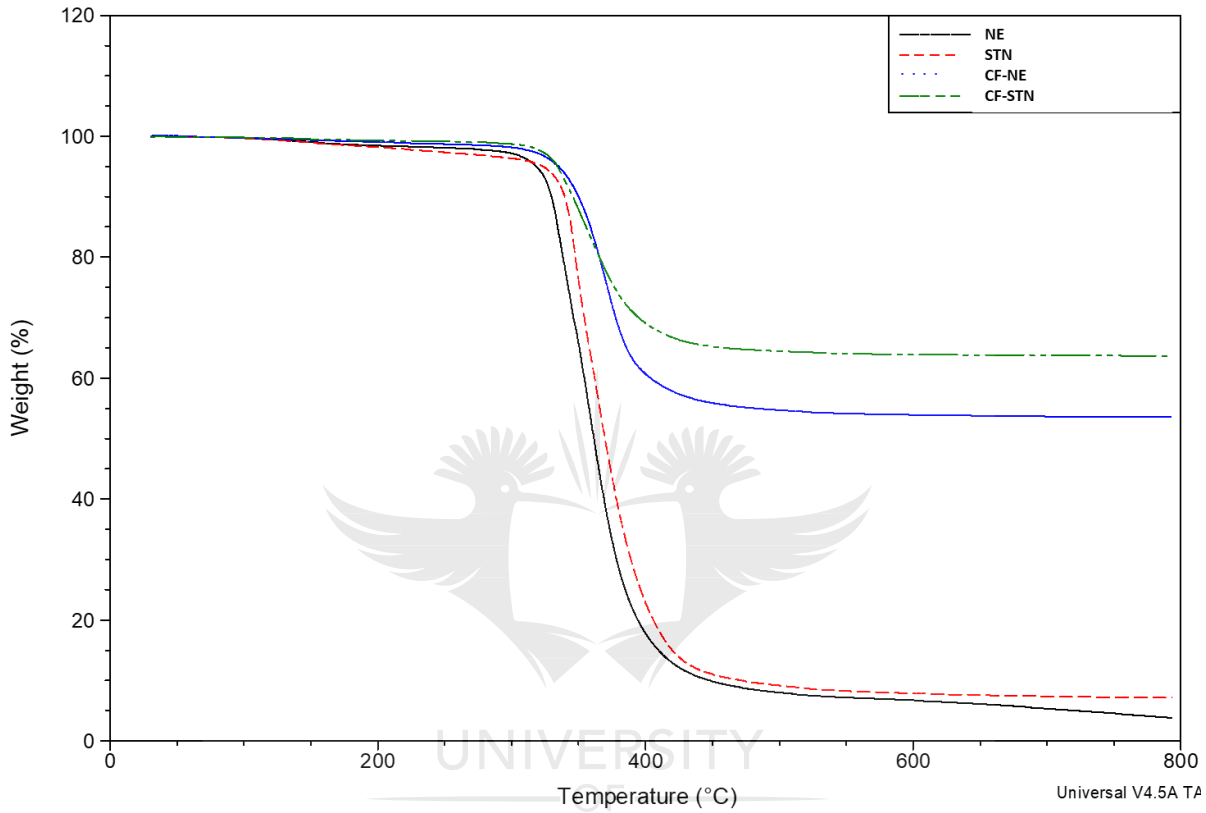

Figure 4.24 Thermogravimetric Curves for composites with and without TiO_2 (Neat epoxy (NE); Silane functionalised TiO2 nanocomposite (STN); Non-functionalised TiO2 nanocomposite (TN); NCF carbon fibre reinforced composite (CF-NE) and NCF carbon fibre reinforced composite with TiO2 inclusion (CF-STN))

The initial weight loss of 25% which is critical to comprehending the thermal stability of polymer composites manufactured with the thermosetting matrix was analysed. It was observed that the thermal stability of NE at this weight loss was significantly improved by the inclusion of TiO_2 nanoparticles from 338℃ to 347℃. Furthermore, the thermal stability for both CF-STN and CF-NE at the weight loss of 25% did not improve but remained unchanged at 365℃. However, at a weight loss of 30% and 35%, the thermal stability of the carbon fibre reinforced polymer composites was enhanced by the presence of TiO_2 from 337℃ to 394℃

and from 385℃ to 459℃ respectively. For 50% weight loss, the NE decomposition temperature was 361℃ while a thermal stability increases to 370℃ was observed for STN. Furthermore, a significant improvement in thermal stability at 75% weight loss from 383℃ to 396℃ occurred with the presence of TiO_2 nanoparticles.

Table 4.24 Thermo Gravimetric Analysis (TGA) values for neat epoxy and its composites.

Weight loss %	Degradation Temperature			
	Neat Epoxy	STN	CF-NE	CF-STN
25	338	347	365	365
30	346	354	337	394
35	350	357	385	459
50	361	370	-	-
75	383	396	-	-

Table 4.25 Char residue after 800°C

Samples	Char Residue (CR)
CF-NE	53.56%
CF-STN	63.67%
NE	3.82%
STN	7.13%
TN	6.28%

The critical weight loss at 460℃ was determined to be approximately 90% for both NE and STN and approximately 36% for the samples with CF reinforcement. During this stage, the epoxy was almost completely degraded. The low weight loss values for CF-NE and CF-STN was due to the presence of CF, which requires higher temperatures to degrade. At 800℃, the residual weight was below 8% for NE and STN and approximately 60% for the samples with CF as shown in Table 4.25. Thermosetting polymers generally exhibit relatively high cross-linking densities that contribute to its associated elevated decomposition temperature [18]. The thermal stability of epoxy-based nanocomposites, in particular, is known to be highly dependent on the state of the TiO_2 dispersion within the matrix. Consequently, the formation of agglomerates can negatively affect effective particle-matrix bonding which causes a

reduction in the thermal stability of the nanocomposite [23]. The results as discussed, shows that TiO_2 improves the overall thermal properties of the nanocomposites whether in an epoxy matrix or in fibre reinforced composites. To further improve the impact of TiO_2 on the thermal properties of the epoxy matrix, techniques and methodologies for limiting agglomerations and inhomogeneous dispersion can be implemented [18,328]. Furthermore, this study clearly establishes a basis for recycling fibre reinforced composites via pyrolysis due to the high residual weight of the CF retained even at 800℃.

4.5.2 Integral Procedural Decomposition Temperature

In this study, further characterisation of thermal stability was performed using integral procedural decomposition temperature (IPDT). Using Doyle's [357]methodology, the IDPT of NE, STN and TN were calculated and the results are summarised in Table 4.26. A positive correlation between the inclusion of TiO_2 nanoparticle and IPDT was observed. The IPDT increased by 12% when TiO_2 was introduced. Silane functionalisation contributed to the homogeneous dispersion of the particles within the matrix which is known to improve insulation and the heat resistance capabilities the TiO_2 nanoparticles [400]. The oxygen heat movement was restricted because of the presence of the particles. Heat retardation was therefore observed with the inclusion of the nanoparticles.

Table 4.26 Integral Procedural Decomposition Temperature for epoxy modified with TiO_2 nanoparticles

Samples	IPDT (°C)
NE	393.1495
TN	422.3792
STN	440.1293

Although the non-functionalised TiO_2 nanoparticles also improved the IPDT of the epoxy matrix by 7%, this was much lower than when the silane functionalised TiO_2 nanoparticles were used. This reduction in the IPDT value from 440℃ to 422℃ can be

attributed to the detrimental effect of agglomerations present in the matrix [400]. Non-homogenous dispersion is a characteristic of non-functionalised nanoparticles leading to the formation of agglomerates that are less efficient at repelling oxygen and heat [400]. IPDT is a good indicator because it encompasses or reflects the entire thermal stability of the samples from the initial decomposition stage through rapid decomposition to the final stage (char residue). Therefore, IPDT increases with the inclusion of TiO_2 and promotes the retardant properties of the matrix by influencing the behaviour of heat, oxygen and the formation of char residue.

4.5.3 Oxidation Index

Another index considered was the oxidation index (OI) which can estimate the flame-retardant capacity of composite materials [358]. The oxidation index based on char residue was determined after decomposition of the matrix for NE, STN and TN as shown in Table 4.27. The results revealed that the inclusion of silane functionalised TiO_2 nanoparticles increased the OI by 87%. The OI of non-functionalised TiO_2 nanoparticles dispersed in the epoxy matrix also improved by 65%.

Table 4.27 Oxidation Index for epoxy modified with TiO_2 nanoparticles

Samples	OI
NE	0.27
TN	0.44
STN	0.50

The increase in OI after the introduction of TiO_2 is an indication of enhanced flame resistance. It is well-established in the literature [358] that thermal stability increases with an increase in the oxidation index. The higher oxidation index values observed in STN and TN therefore indicates that they possess superior thermal stability in comparison with NE. TN had a lower OI value than STN due to the presence of agglomerates and non-uniformity of the particle distribution. OI ranging from 0.5 and above is an indication that the composite has good flame-

resistant properties [358]. Since the OI for STN was 0.5, it can be concluded that the presence of TiO_2 significantly enhanced the flame resistance of NE (0.27).

4.6 Effect of Pyrolysis and Oxidation on NCF Carbon Fibre reinforced Composite

Pyrolysis was conducted on diamond cut carbon fibre non-crimp fabric composites and virgin carbon fibre as seen in Figure 4.25. The resulting solid residue after pyrolysis, as shown in Figure 4.26, was classified as pyrolysed char covered (PY-CHAR) and pyrolysed virgin fibre (Py-VF). Further characterisation and oxidation were then successfully conducted. The virgin fibres were pyrolysed and oxidised for comparison to assess the effects of pyrolysis and oxidation treatments on the properties of samples while eliminating the bias of pyrolysis and oxidation.

(a) (b)

Figure 4.25 Samples before pyrolysis; (a) NCF carbon fibre reinforced composite, (b) Virgin NCF fabric

A visual inspection of PY-CHAR shows the brittle-like characteristic of the fibres stuck together with a carbonaceous solid residue normally referred to as char. The surface of PY-CHAR seemed rougher while the surface of PY-VF remained smooth with fibres well separated. This clearly showed that the pyro-gasification process produces char which has both positive and negative implications [49].

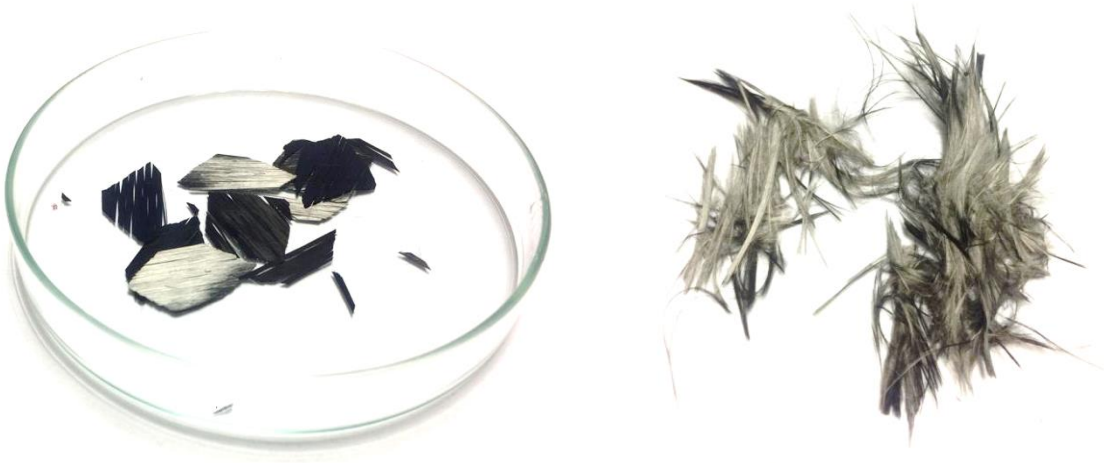

(a) (b)

Figure 4.26 Samples after pyrolysis; (a) NCF carbon fibre reinforced composite (PY-CHAR), (b) Virgin NCF fabric (PY-VF)

The two oxidation methods used were thermal treatment in air (PY-CHAR-OX) at 500℃, and reflux using nitric acid (PY-CHAR-CHEM-OX) at 90℃ as earlier reported (see Chapter 3) primarily to provide clean fibres. This provided a basis for comparing the two methods and to determine the most suitable option for fibre recovery and use as a secondary raw material. After oxidation as shown in Figure 4.27, the PY-CHAR-OX samples were well separated, smoother and looked identical to PY-VF. A visual assessment showed that the two oxidation treatments were effective in cleaning the fibres.

Figure 4.27 Char residue removed through oxidation (PY-CHAR-OX)

The fibre recovery process from manufacture to oxidation is presented in Figure 4.28. The choice of an optimal temperature for pyrolysis and oxidation is critical for the strength and surface morphology of the fibres. Studies by Meredith [401] and Mazzocchetti et al. [49] reported decreases in mechanical properties when pyrolytic and oxidation temperatures greater than 600℃ were used.

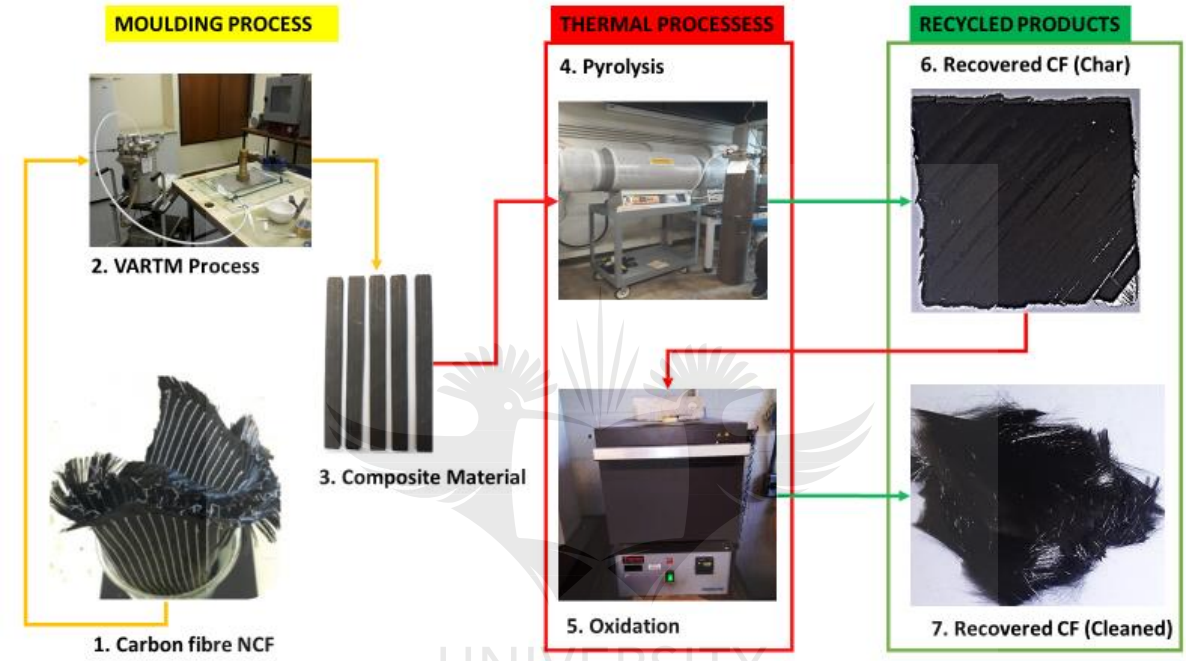

Figure 4.28 A flow chart for the recovery of NCF carbon fibre from manufacture to oxidation

Using higher temperatures increases surface oxygen fraction and effectively removes the char, but it compromises the mechanical integrity and other properties of the fibres which leads to a decrease in mechanical performance. The application of the same temperature (500℃) for both pyrolysis and oxidation established a solid foundation for the development of a continuous line thermal treatment from pyrolysis through to oxidation. The reliability of pyrolysis as a suitable methodology for the recovery and use of residue as a secondary raw material, was validated by the quality and unique characteristics of the recovered fibre.

4.7 Effect of Pyrolysis and Oxidation on the Morphology of Carbon Fibre

Morphological characterisation of the pyrolysed samples was carried out to examine the surface characteristics of the fibres and to observe the pyrolytic and oxidative footprints. Microscopy images provide insights into conducting qualitative analyses, which can also be quantitatively validated through experimentation. A critical factor during the pyrolysis of composite materials is the influence of polymer degradation both in non-oxidised and oxidised atmospheres. Therefore, in this study, an examination of the char residue deposits on the CF surface after pyrolysis and its removal after oxidation was visually conducted using scanning electron microscopy (SEM).

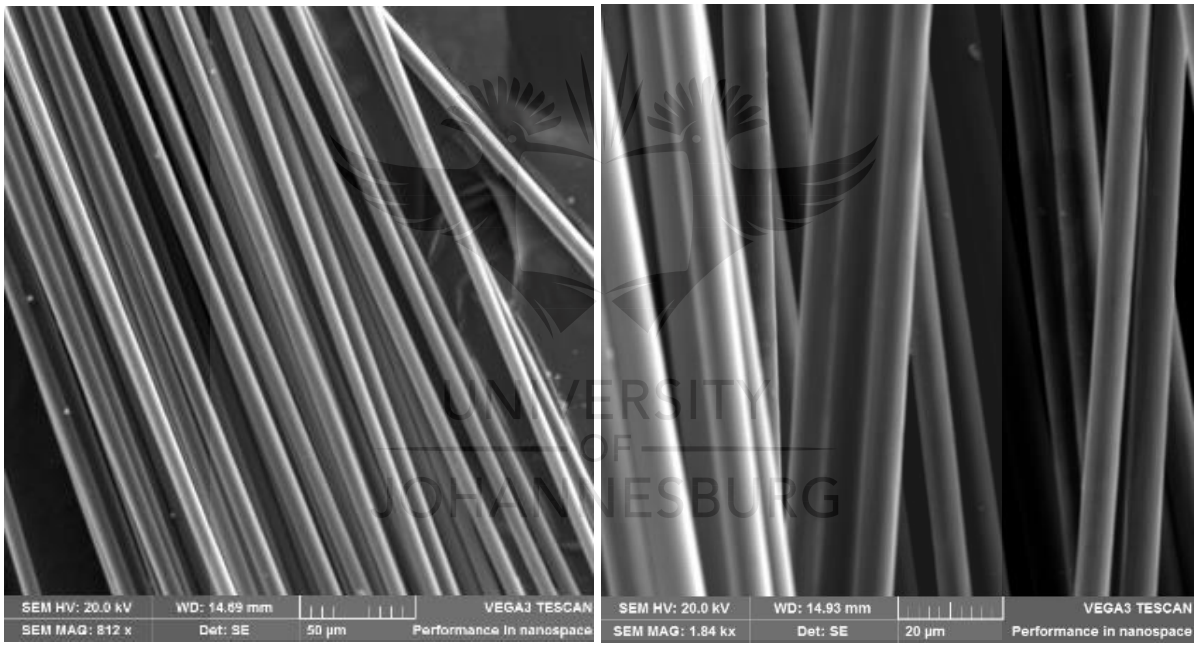

Figure 4.29 Fig. 4. SEM micrographs of virgin fibre

The pristine virgin fibre shown in Figure 4.29 was, as expected, characteristically smooth, homogenous and not linked or adhering together. The SEM micrograph presented in Figure 4.30 clearly shows that after pyrolytic treatment, the recovered solid residue obtained from the furnace comprised rough surface fibres and a spot-like layer of resin residues (PY-CHAR). The amorphous carbonaceous residue is characteristically stiff due to fibre-to-fibre adhesions.

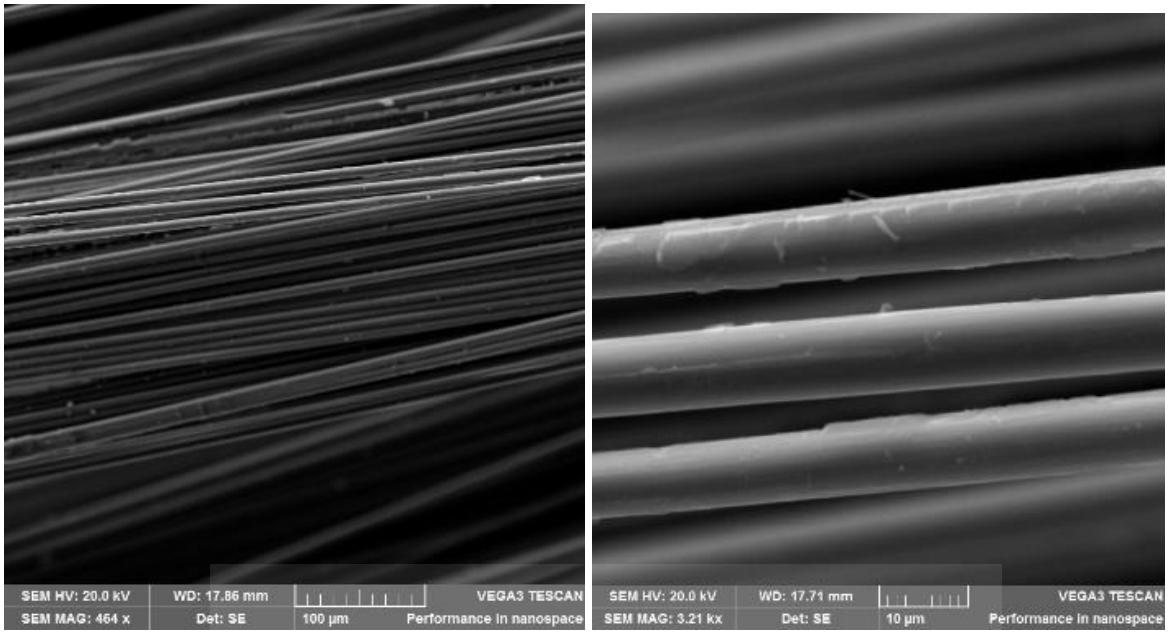

Figure 4.30 Fig. 4. SEM micrographs of carbon fibres recovered from pyrolysis (PY-CHAR).

Several studies on the reuse of the fibre for manufacture of composites have reported poor wettability attributed to the presence of char residue which subsequently causes poor fibre-matrix interfacial bonding leading to significantly low mechanical properties [49].

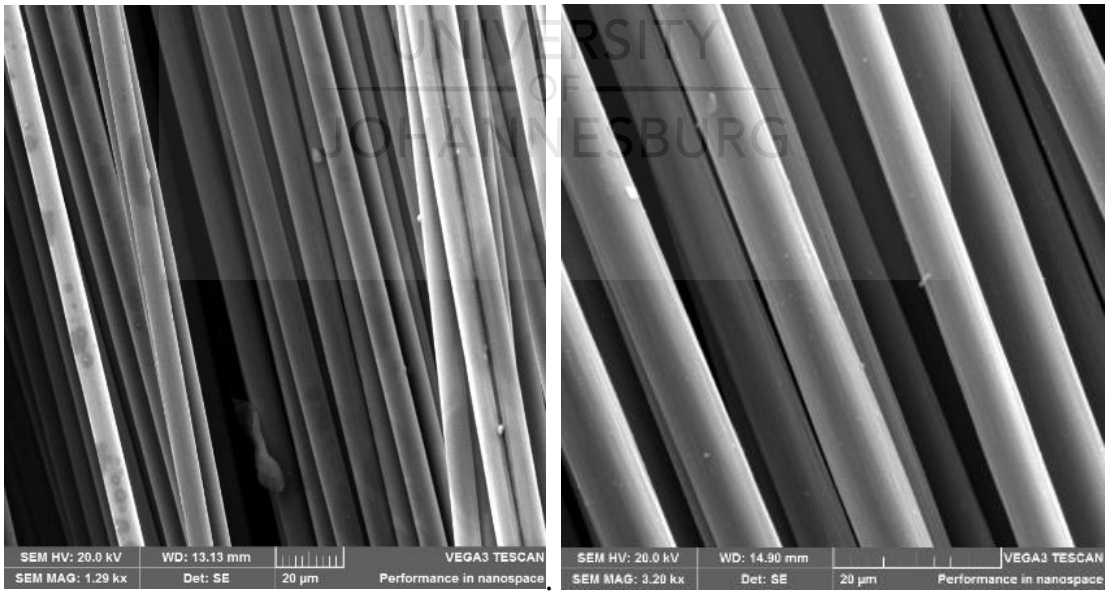

Figure 4.31 SEM micrographs of carbon fibres after oxidation in air at recovered from pyrolysis 500ºC (PY-CHAR-OX).

The process of aggressive oxidation in elevated temperatures of $500℃$ for $60\ min$ and above is often characterised by defective symptoms such as localised damage and pitting which increases the surface roughness of most fibres. This is however not the case for PY-CHAR-OX as shown in Figure 4.31: the reclaimed carbon fibre surface appears rather smooth and intact without any signs of local degradation or surface damage. This agrees with existing literature [49,252].

4.8 Effect of Pyrolysis and Oxidation on the Size of NCF Carbon Fibre

Another approach used to observe the influence of pyrolysis and oxidation on the carbon fibre was the application of SEM to measure the diameters of the samples as presented in Table 4.28. The average diameter measured from the SEM for VF was $7.20\ \mu m$ and agrees with the CF filament diameter data provided by SAERTEX South Africa (PYT) LTD. This is the total diameter inclusive of sizing. After oxidation treatment at $500℃$ for $1\ hr$, the average diameter of the sample (VF-OX) was $6.51\ \mu m$; a 10% reduction in its original size. After conducting pyrolysis of the carbon fibre reinforced composite; PY-CHAR, showed an average diameter of approximately $7.91\ \mu m$ which was a 10% size increment over the VF. This was expected and provides proof of the presence of layers of char residue deposited on the carbon fibre during the pyrolysis of the epoxy resin.

Table 4.28 Fibre size variation after pyrolysis and oxidation

Sample	Average diameter (μm)	Variation in diameter (%)
VF	7.20	-
VF-OX	6.51	- 9.58
PY-CHAR	7.91	+ 9.86
PY-CHAR-OX	6.99	- 2.91

After the oxidation of the char covered fibres in air, the resulting clean fibre (PY-CHAR-OX) showed a 3% decrease in average diameter. The reductions in diameters after oxidation are 10% and 3% for VF-OX and PY-CHAR respectively and support the claim that the char

provided some level of protection in the fibre surface to warrant the lower percentage loss in diameter [49]. Another implication is that the virgin fibre is more susceptible to oxidation degradation, a large portion of which can be attributed to surface sizing degradation. It can therefore be assumed that the amorphous carbon deposit behaves as a sacrificial film shielding the oxygen from contacting the surface of the fibres.

4.9 Effect of Pyrolysis and Oxidation on Physio-sorption Isothermal Analysis

The physio-sorption characterisation of NCF carbon fibre samples, both virgin and recovered, were evaluated using the BET (Brunauer-Emmett-Teller) method which is effective in determining gas absorption solids based on influencing factors such as surface area and surface porosity. Pyrolysis and both chemical and air oxidation played an important role in causing modifications in the microstructural and textural morphology of the carbon fibres.

Table 4.29 Physio-sorption characteristics of NCF Carbon fibre

Biochar	BET surface area [m^2/g]	Pore volume [cm^3/g]	Pore size [nm]
VF	0.44	0.0020	18.16
PY-CHAR-OX	0.60	0.0024	16.28
PY-VF-OX	1.16	0.0024	8.27
PY-CHAR	3.44	0.0055	6.38
PY-CHAR-CHEM-OX	3.56	0.0054	6.03

As VF was subjected to pyrolytic conditions of 500℃ and then oxidation in air at the same temperature for 1 hr, the BET surface area increased from 0.44 to 1.16 m^2/g which represents a 164% increase as seen in Table 4.29 for PY-VF-OX. After pyrolysis of the carbon fibre reinforced composite, the PY-CHAR BET surface area was observed to be $3.44\,m^2/g$ which is a vastly significant increase of 682% in comparison with VF. After the oxidation of PY-CHAR in air, a BET surface area of $0.6\,m^2/g$ for PY-CHAR-OX was obtained. The oxidation process reduced the BET surface by a significant margin of 473%.

The higher BET surface area of PY-CHEM-OX after chemical activation can be attributed to the presence of char. This clearly indicates that, as a means of char removal, it is less effective when compared to air oxidation as discussed during the analysis of the TGA results in section 4.11. This explains the reason for the almost identical BET values with PY-CHAR. The increase in BET surface area of PY-VF-OX can be ascribed to decomposition of the sizing agent which introduces some porosity during pyrolysis and oxidation at such elevated temperatures [402]. The significantly higher BET surface area observed with PY-CHAR can be attributed to the layer of amorphous carbonaceous material deposited during the gasification of the epoxy matrix [49,275]. The char after deposition experiences thermal cracking and deposing of some pore blocking substances through continuous volatilisation which further improves external accessibility on the surface area of the char residue [403].

The BET surface area results, as expected, were generally low and therefore required more aggressive means of activation via chemical or physical means to significantly increase the active surface area of the fibres. However, it must be noted that the objective of this study was not to improve the surface area of the carbon fibre but to obtain surface properties comparable to virgin fibre for reuse in the manufacture of composite materials. The BET surface area of virgin carbon fibre, in general, is less than $0.7\,m^2/g$. PY-CHAR-OX clearly met the surface area morphology criteria of VF by exhibiting a BET surface area of less than $0.7\,m^2/g$. Also, open porosity on the surface of fibre can be assumed as negligible or insignificant. Therefore, pyrolysis increases the BET surface area while air oxidation decreases the BET surface area.

VF, PY-VF and PY-CHAR-OX displayed relatively similar pore volumes of approximately $0.0024\ \mathrm{cm}^3/\mathrm{g}$ as observed in Table 4.29. Clearly, pyrolysis and subsequent air oxidation of VF have no significant impact on pore volume. The pore volume of PY-CHAR showed an increase from $0.0020\ cm^3/g$ to $0.0055\,cm^3/g$ representing a 175% increase

when compared with VF. After oxidation, the pore volume then decreased to $0.0024\ cm^3/g$ which is a 125% decrease. A comparison of the pore volume values of VF and PY-CHAR-OX reveals that they possessed similar pore volumes which implies that PY-CHAR-OX is suitable for direct reuse in the manufacture of composites. Pore volume thus improves with pyrolysis but degrades after oxidation in air.

PY-VF-OX exhibited a drastic reduction in pore size to $6.38\ nm$ which represents a reduction of 142%. The pore size for VF and PY-CHAR-OX were $18.16\ nm$ and $16.28\ nm$ respectively. These values are also not significantly different. The pore size of PY-CHAR after pyrolysis of the composite, however, was significantly reduced by 185%. This improvement in pore size as stated earlier is attributed to the layer of char residue deposit on the surface of the carbon fibre. After oxidation in air, the char is removed, and a large pore size representing an increase of 155% was recorded.

An inverse relationship exists between pore size and BET surface area after pyrolysis and oxidation. The pore size of both VF and PY-CHAR decreased after pyrolysis but increased after oxidation in air. The pore sizes determined for all the samples were free of both micropores and macropores. In general, micropores have diameters within the range of 1.50 to $2.0\ nm$, while macropores are characterised by diameters above 50 nm. Pore sizes between 2.0 to $50\ nm$ are considered mesopores. All the samples analysed in this study can therefore be classified as possessing mesopores. Where all pore size values range between 6 to $18\ nm$. The presence of mesopores on VF, PY-VF-OX and PY-CHAR-OX is most likely due to small flaws, wrinkles and crevices or cracks [402].

For application where gas adsorption and greater activation is the primary focus, the presence of char residue may be advantageous as the amorphous carbon deposit shows superior surface area and reduced pore size. This possible use of pyrolysed carbon fibre could provide a means for chemical functionalisation and customisation depending on the matrix used.

4.10 Effect of Pyrolysis and Oxidation on Elemental Composition of NCF Carbon Fibre

The elemental composition of recovered and virgin fibre is investigated to evaluate the effect of pyrolysis, oxidation and presence of char. The compositional data was captured using a thermal analyser and the EDX section of the Scanning Electron Microscope. The elemental compositions and atomic ratios of pyrolysed and oxidised recovered and virgin carbon fibres are presented in Table 4.30. As expected in carbon fibre samples, the most abundant element was carbon with percentages of 93.61%, 93.39%, 91.80% and 79.42% for PY-VF-OX, PY-CHAR, PY-CHAR-CHEM-OX and PY-CHAR-OX respectively, while their corresponding O/C atomic ratios were 0.0256, 0.2187, 0.0410 and 0.0256 respectively.

Table 4.30 Elemental composition of carbon fibre after pyrolysis and oxidation

Sample Name	Nitrogen (%)	Carbon (%)	Oxygen (%)	Sulphur (%)	O/C	N/C
PY-CHAR-OX	3.21	79.42	17.37	1.12	0.2187	0.0404
PY-VF-OX	4.22	93.61	2.17	1.17	0.0232	0.0451
PY-CHAR	4.22	93.39	2.39	0	0.0256	0.0452
PY-CHAR-CHEM-OX	4.44	91.80	3.76	0	0.0410	0.0484

Also, the N/C ratio values were 0.0452, 0.0404, 0.0499 and 0.0441 for PY-CHAR, PY-CHAR-OX, PY-CHAR-CHEM-OX and PY-VF-OX respectively. The oxygen and nitrogen content of PY-CHAR was 2.39% and 4.22% respectively. This comparably low polar element percentages clearly confirm a relatively inert carbon fibre surface. Similarly, the oxygen and nitrogen content of the PY-VF-OX were 2.17% and 4.22% respectively. These values even after oxidation were very low which is an indication of a highly inert surface which can be attributed to the sizing agent used and its reaction with the elevated temperature and oxygen [404]. However, for char covered carbon fibre (PY-CHAR), as oxidation in air and electrochemical oxidation progressed, an increment in oxygen content was observed. The relative oxygen content increased by 700% and 60% for PY-CHAR-OX and PY-CHAR-

CHEM-OX respectively which is indicative of a highly active fibre surface [404,405]. The relative oxygen and nitrogen contents both increased after chemical oxidation however, for oxidation by air, the oxygen content increase was significant but conversely, a slight reduction in the nitrogen content was observed. The presence of oxygen is the result of oxidation treatments and adsorbed material while nitrogen was due to some adsorption and the PAN precursor origin of the carbon fibre.

O/C and N/C ratios have a direct correlation with the interlaminar shear strength (ILSS) of composites manufactured from carbon fibre. An increase in O/C and N/C ratios improves the interlaminar shear strength [404]. It can therefore be concluded that the surface functionality of carbon fibre positively influences the interfacial properties of carbon fibre reinforced composites [404,405]. An increase in O/C is also an indication that polar functional groups have been introduced after the oxidation treatments, and often promotes good wetting [406,407]. The polar component is a critical governing parameter which influences fibre-matrix adhesion [408]. Consequently, an increase in O/C introduces surface-active sites on the surface of the fibre which facilitates a higher propensity for the formation of improved fibre-matrix chemical bonds. The enhanced interfacial adhesion of matrix to fibre occurs as a direct result of an increase in surface polarity which causes an improvement in the matrix to fibre stress transfer [409,410]. The O/C atomic ratio content of the PY-VF-OX was comparatively low and can be attributed to the sizing which influenced the oxidation process [411].

Interfacial adhesion may improve as a result of an increment in relative oxygen content, polar component and surface energy of total fibre surfaces. There is thus a direct correlation between O/C ratio, fibre surface energy, and interfacial shear strength [412]. The degree of oxygen content on the surface of the carbon fibre also influences the surface energy consisting of a polar or specific surface energy and dispersive surface energy [413]. Studies have shown that there is an approximately linear relationship between the O/C atomic ratio and surface

energy [409]. Surface energy indeed has a positive correlation with the increase in relative oxygen content [412,413].

Although the primary elemental composition was carbon, oxygen and nitrogen, the minor element observed was sulphur. The presence of such minor elements can be categorised as impurities. The level of impurities such as sulphur was seen to increase with increasing oxygen content. This indicates the development of chemical bonding between oxygen and sulphur to form acid promoting oxides such as sulphur dioxide attributed to the pre-treatment process. The presence of such impurities influences the acid-base characteristics of the carbon fibre surface [413,414]. The variability in acidic and base properties of the carbon fibre surface resulting from treatments such as oxidation correlates with both nitrogen and oxygen content increase, with oxygen being the primary contributor [413]. Any significant variation in the state of acidity on the fibre surface will affect its adhesion properties to the polymer matrix and directly influence the mechanical properties of the composite material [412,413]. An increase in relative oxygen and nitrogen content improves surface acidity especially when acidic oxidation treatments such as in the case of PY-CHAR-CHEM-OX are used [415]. This higher acidity leads to improved inter-laminar shear strength between the interface of the fibre and matrix [412–414]. Also, an increase in the O/C ratio signifies the introduction of polar functional groups which promote good wetting [407].

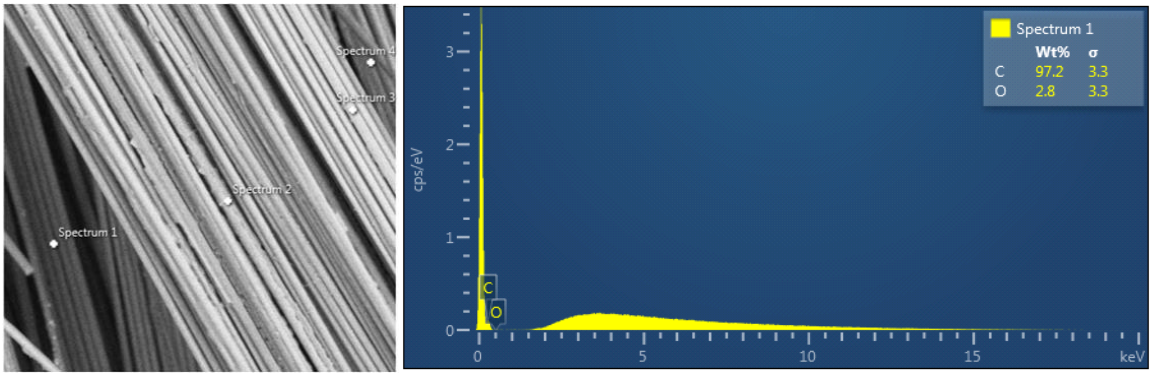

Figure 4.32 EDX compositional analysis for PY-CHAR

The EDX also showed that carbon was the dominant element on the surface of PY-CHAR at 97.2 % followed by oxygen which was 2.8 % (see Figure 4.32).

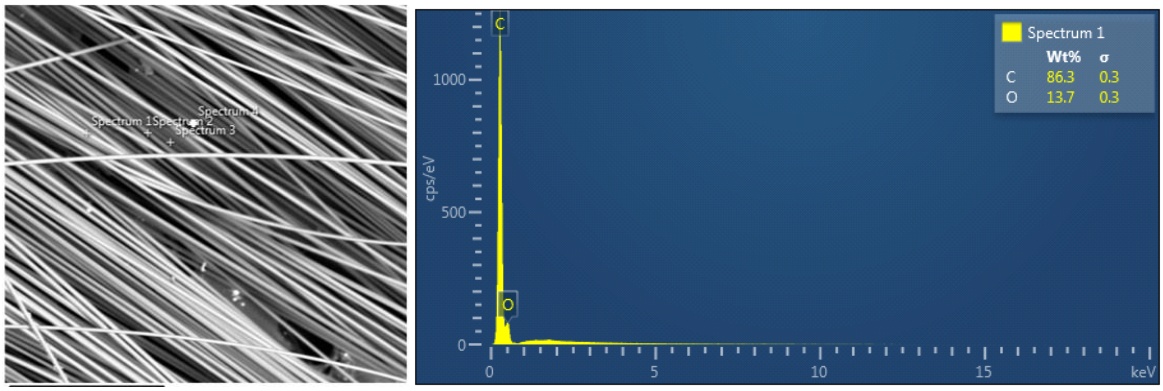

Figure 4.33 EDX compositional analysis for PY-CHAR-OX

After oxidation to remove the char layer the oxygen content increased to 13.7% shown in Figure 4.33 which corroborates the results from the elemental analysis as shown in Table 4.30. This clearly indicated a significant increase in oxygen-rich moieties on the surface of the carbon fibre.

4.11 Effect of Pyrolysis and Oxidation on the Thermal property of NCF

Thermogravimetric analysis (TGA), was carried out on the pyrolytically treated fibres with the application of steady heating from 30℃ to 1000℃ within an inert environment using nitrogen gas. This study seeks to assess the impact of oxidation treatments and the influence of char on the thermal properties of carbon fibre.

Table 4.31 Thermal degradation of pyrolysed samples during thermogravimetric analysis

Sample	Weight loss (%)		Degradation Temperature (ºC)		Residual weight at 1000ºC (%)
	Event 1	Event 2	Event 1	Event 2	
PY-CHAR	0.2	2.25	696.67	934.66	97.00
PY-CHAR-OX	1.03	-	903.27	-	96.23
PY-CHAR-CHEM-OX	0.45	3.88	160.90	932.65	95.85

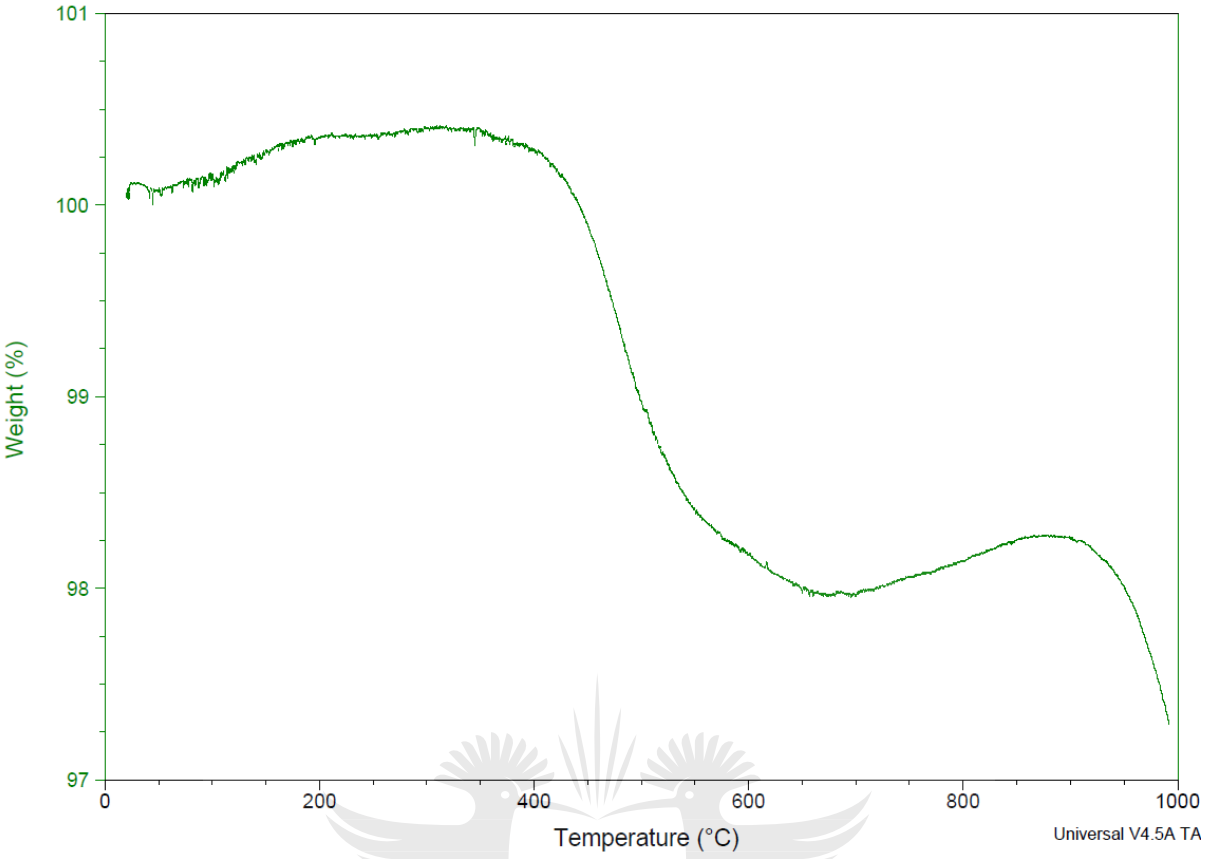

Figure 4.34 Thermogram of char covered carbon fibre (PY-CHAR)

The thermogram of PY-CHAR in Figure 4.34 shows two distinctive degradation and weight loss events occurring. The first degradation commences during the $40th$ (40.28) min at 423.15℃ (T_{onset}) with an initial weight loss of 0.2%, and continues until the $70th$ (67.51) min at 696.67 ℃ with a total weight loss of 2.44%. The second event takes place around the 90th (90.98) min at 934.66℃ with weight loss of 2.25%. A residual mass of 97% was recorded at 990℃. The first degradation event can be attributed to the decomposition of the char residue on the surface of the carbon. The second event was primarily due to the decomposition of the carbon fibre itself and any char residuals left behind. Per literature, carbon fibre starts decomposition between 650℃ – 750℃ [416]. The shape of the thermogram is indicative of a process that is not thermally stable over the temperature range (30℃ – 1000℃) in comparison with the thermogram for the PY-CHAR-OX samples.

Therefore, it may be concluded that the presence of char is detrimental to the thermal stability of carbon fibre.

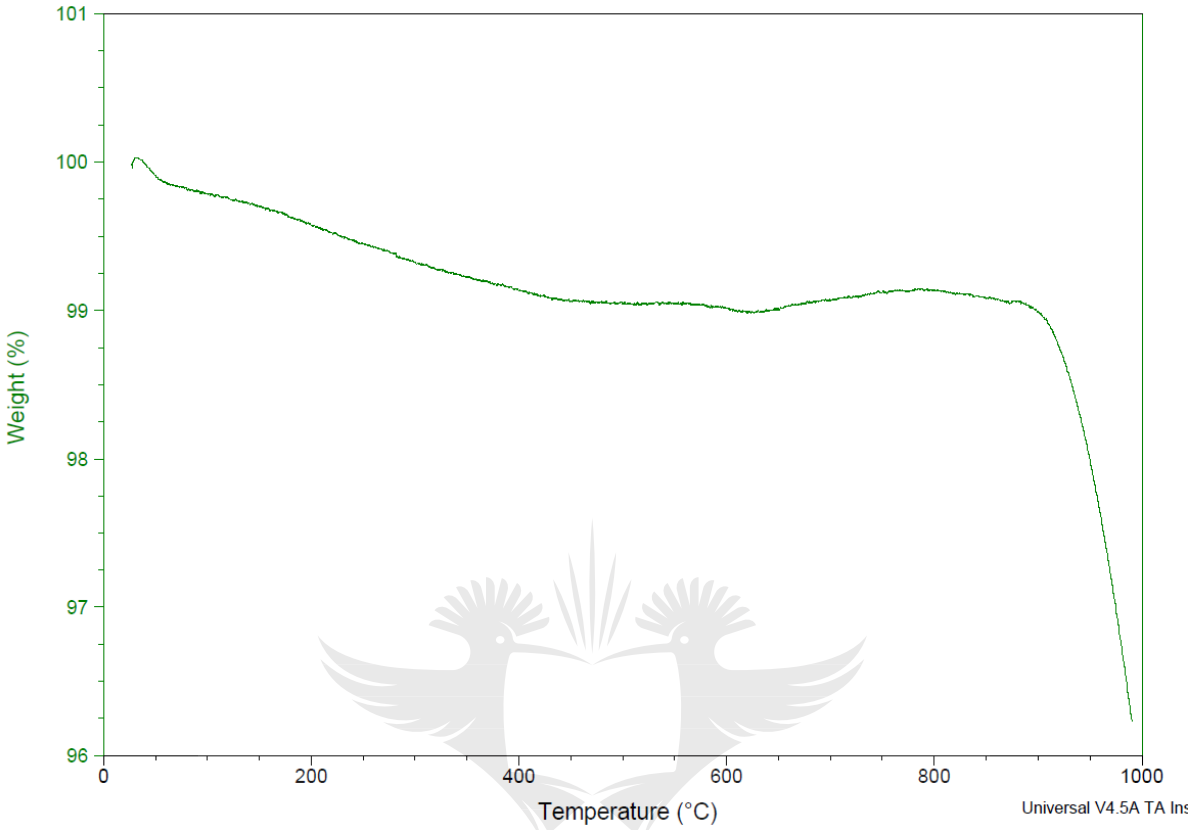

Figure 4.35 Thermogram of carbon fibre after oxidation in air @ 500℃ (PY-CHAR-OX)

Only one significant degradation event was observed when TGA was conducted on the PY-CHAR-OX sample as shown in Figure 4.35. The primary decomposition occurred within the 90th (88.27) min at 903.27℃ (T_{onset}) with a weight loss of 1.03%. At 990℃ a residual mass of 96.23% was obtained at the end of the process. The decomposition when compared to PY-CHAR can only be attributed to the degradation of the carbon fibre. The absence of the first degradation event in PY-CHAR clearly proves that the oxidation in air at 500℃ for 1hr completely removed the char residue. The shape of the thermogram up to 900℃ is characterised by relatively low variation and can be described as having a good thermal stability compared with PY-CHAR and PY-CHAR-CHEM-OX. Consequently, oxidation

drastically improves the thermal stability of the carbon fibre and provides a basis for reuse as a secondary raw material in manufacturing composite materials.

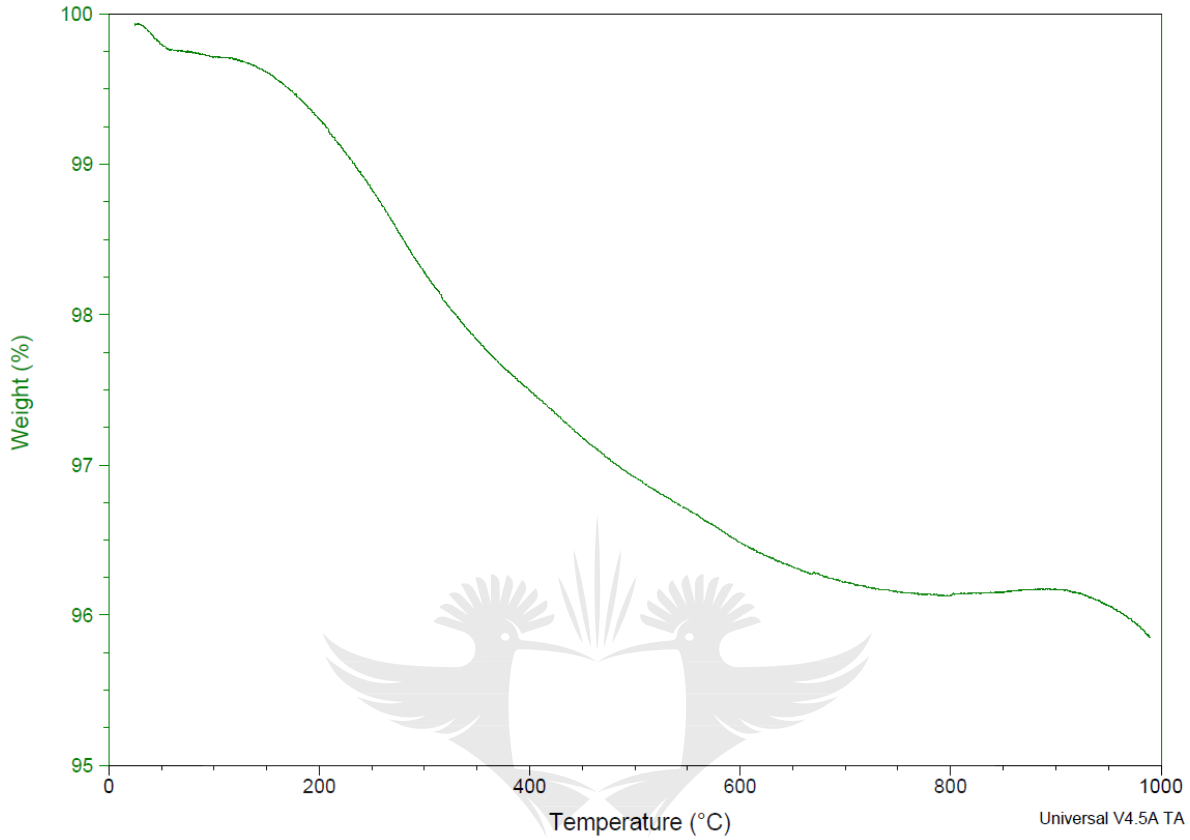

Figure 4.36 Thermogram of carbon fibre after chemical oxidation using nitric acid (PY-CHAR-CHEM-OX)

PY-CHAR samples were also oxidised using nitric acid via refluxing and heating for comparison with air oxidation. The resulting samples, PY-CHAR-CHEM-OX, were also subjected to a TGA analysis to ascertain the veracity of the methodology and its impact on the char covered fibres. The generated thermogram was similar to that of PY-CHAR and double degradation events were observed. The first decomposition occurred within the 14th (14.16) min at 160.90℃ (T_{onset}) with a corresponding weight loss of 0.45%. The decomposition process continued to the 70th (73.77) min at 758.21℃ with a total weight loss of 3.85%. The second event began at a decomposition temperature of 932.65℃ within the 90th (91.30) min with a weight loss of 3.88%. The first event can also be attributed to the degradation of residual char present on the fibre surface [49,315]. This observation implies that

the chemical oxidation process is not efficient for the removal of char residue. The second event resulted from the degradation of both char and carbon fibre. The shape of the thermogram is clearly analogous to that of the PY-CHAR and is thermally unstable in comparison to PY-CHAR-OX. The residual mass percentage at the end of the process was 95.85%.

The residual mass percentages recorded establishes a trend of PY-CHAR> PY-CHAR-OX. This trend is significant in confirming the importance of char with regards to thermal properties of carbon fibre. The fact that PY-CHAR had the highest residual mass implies that the char provided some level of protection to the fibres and thus minimised the rate of degradation in comparison with PY-CHAR-OX which were char free [49]. Therefore, in situations where high thermal resistance of carbon fibre is the priority and not mechanical strength, char covered fibres may be more suitable. In most literature oxidation after pyrolysis is a critical component in the recycling of carbon fibre reinforced composites. However, this study has shown that the presence of char can be exploited for thermal applications and for the customised activation of fibres.

4.12 Effect of Pyrolysis and Oxidation on Crystallinity of NCF Carbon Fibre

The XRD technique was used to characterise the pyrolysed and oxidised fibres to further explore the effect of the presence of char and the influence of oxidation on carbon fibre at crystalline level. Figure 4.37 shows the XRD spectra for PY-CHAR-OX and PY-CHAR samples. Two distinctive widened diffractogram reflection patterns with angles (θ) approximately situated at 25° and 44° were observed for both PY-CHAR-OX and PY-CHAR. The broadened peaks at 44° were significant as this indicated the presence of an amorphous structural aspect [417].

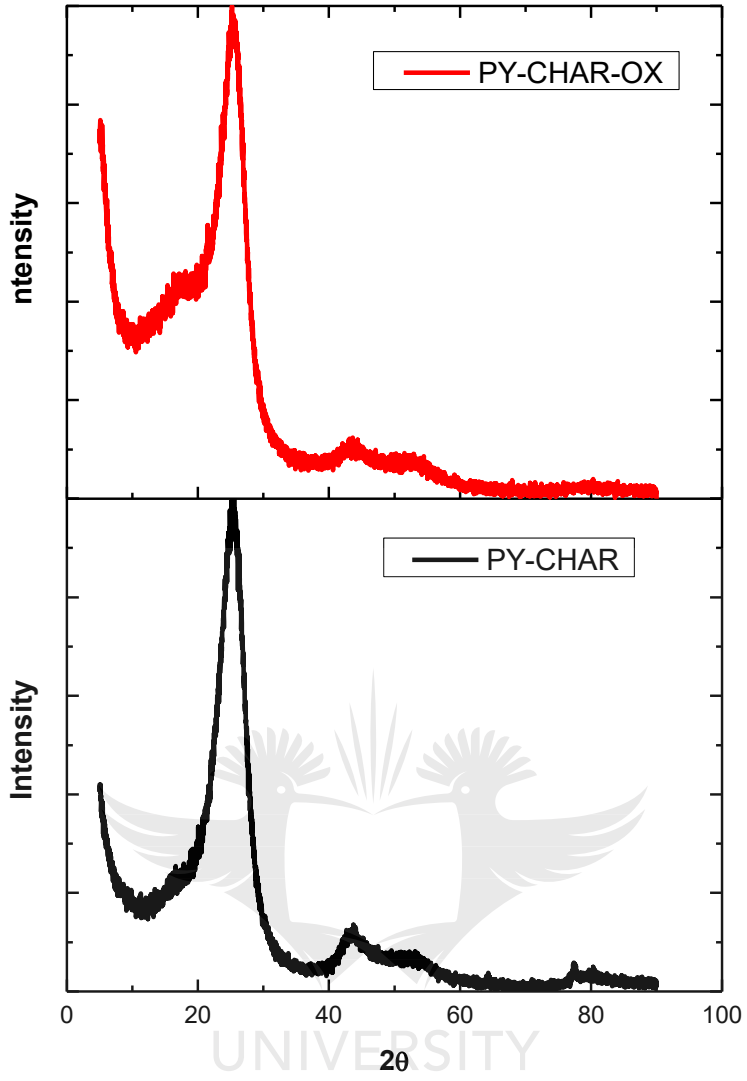

Figure 4.37 XRD spectra of oxidised (PY-CHAR-OX) and char covered (PY-CHAR) carbon fibre

The peaks reflected were at angles 25° and 44° corresponding to the 002 and 011 diffraction line, respectively. Furthermore, the presence of an amorphous structure is a positive indicator of the presence of char residuals or some form of activation on the surface of the carbon fibres. A summary of the structural parameters extracted from the peaks generated during XRD diffraction is presented in Table 4.32, where a comparison of oxidised recovered carbon fibre and char covered recovered carbon fibre was conducted. From the analysis, the interlayer spacing represented by d_{002} for PY-CHAR and PY-CHAR-OX were determined to be 3.58 Å and 3.57 Å respectively.

Table 4.32 XRD peak characterisation of d_{002} and d_{011} for PY-CHAR-OX and PY-CHAR

Sample	002 peak			011 peak	
	d_{002} (Å)	L_c (Å)	N	d_{011} (Å)	L_a (Å)
PY-CHAR	3.57	15.71	4.40	2.06 Å	93.91
PY-CHAR-OX	3.58	13.14	3.67	2.05 Å	17.87

These values were approximately the same and lie closer to the lower end of the disordered carbon material range and in agreement with the established literature where disordered carbon materials display interlayer spacing within the range of $3.4 \sim 8$ Å [418–421]. The interlayer spacing(d_{002}) of carbon fibre is known to be significantly higher than a purely graphitic material [361].

The interlayer spacing (d_{011}) was 2.06 Å for PY-CHAR and 2.05 Å for PY-CHAR-OX. These results are also consistent with other studies [361,418]. The results revealed that for all cases, the interlayer spacing was approximately the same even after the oxidation processes. Additionally, oxidation is known to introduce some level of activation that impacts the crystalline structure of the fibres [361,422,423]. The crystallite structural parameters primarily influenced by pyrolysis and oxidation include crystallite thickness (L_c), crystallite width L_a and the number of aromatic layers (N) [361]. The full width at half maximum intensity (FWHM) is the parameter used in XRD analysis to calculate the crystallite. The FWHM was measured from the corrected diffraction profile. Further analysis was conducted using the Scherrer equation [419] which incorporates the FWHM to analyse patterns of the X-ray diffraction for the determination of critical parameters, namely the crystallite width or lateral size (L_a) and the crystallite thickness or stacking height (L_c). L_a and L_c are mostly sufficient for characterising the diffractogram reflections for most carbon-based materials. The other components of the Scherrer equation were used for the computation of the crystallite parameters which included the first Scherrer constant $k_c$with a numerical value of 0.9 for the 002 diffraction line and k_a which represents the diffraction line 011 with a value of 1.77.

The L_c values were 15.71 Å for PY-CHAR and 13.14 Å for PY-CHAR-OX while the La values were 93.91 Å and 17.87 Å for PY-CHAR and PY-CHAR-OX respectively. The crystallite thickness or stacking height (L_c) decreased by 16% after the oxidation process. This should normally have resulted in a widening of the interlayer spacing [424]. But on the contrary, it had no significant effect on the d_{002} value which remained constant at approximately 3.6 Å. However, the crystallite width (L_a) values decreased significantly by 80% after the post-treatment oxidation to remove the char. This huge difference in the crystallite width can be attributed to the reduction process that takes place during oxidation when the evacuation of carbon atoms occurs at the edge of the crystallites. Consequently, the reduction process induces an increase in crystallinity disorder and introduces imperfection within the layer stacking.

A morphological analysis via SEM which captured the char residuals coupled with the higher BET surface area and smaller mesopores diameter (see section 4.7 and 4.9) of the PY-CHAR compared to PY-CHAR-OX, significantly contributed to the huge difference in the L_a values. Increasing the surface area of the carbon fibre therefore increases L_c and L_a, while reducing the pore size also increases L_c and L_a. The significantly higher values of L_a compared to L_c implies that the graphitic order further extends in the direction of the planes rather than perpendicular to the planes [417].

Another important parameter obtained from the XRD analysis was the average number of aromatic layers (N). The calculation of N was also based on the interlayer spacing (d_{002}) and the crystallite thickness or stacking height (L_c) [417] (see section 3.2). The average aromatic layer for PY-CHAR was 4.40 and 3.67 for PY-CHAR-OX. The L_c and L_a values of the PY-CHAR represents a stacking of less than 5-layer planes. This structural layout, therefore, indicates the presence of randomly distributed layers with random active sites [361]. The structure of the chars is composed of nanosized aromatic layers and disordered carbon.

The aromatic layers are known to form stacks that often pile up in $2-3$ up to $8-10$ while the disordered carbon forms a "turbostratic structure" within the aromatic layer and cross-linkage structures comprising periphery aliphatic chains [425]. Pyrolysis thus increases the aromatic layers, crystallite width, and thickness while oxidation has a decreasing effect on the crystallite parameters consequently increases the disorder.

4.13 Raman Spectroscopy

Microstructural analysis of carbon-based materials is essential for the characterisation of its properties, and Raman spectroscopy in particular is an important experimental method for accessing and assessing such information. To further investigate the influence of oxidation treatment and the effect of char on the pyrolysed carbon fibre, Raman spectroscopy was conducted. The microscopic section of the equipment allowed for precise guidance of the probe which ensured that a precise recording of the spectra at the preferred region of interest was accomplished as shown in Figure 4.38.

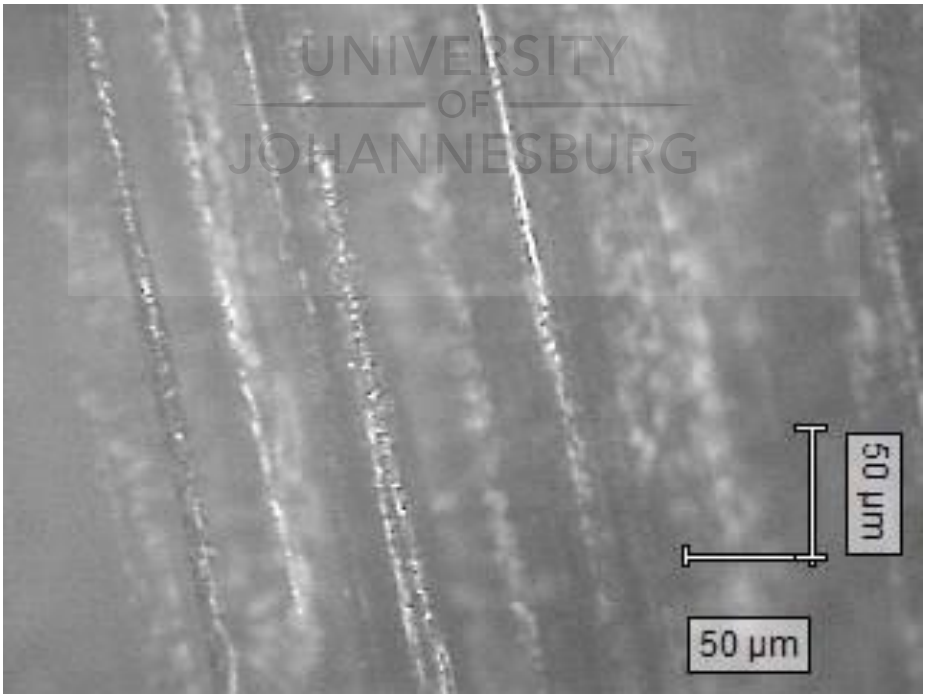

Figure 4.38 Microscopic view of carbon fibre using the Raman spectrometer probe

Sadesky [426] methodology was adopted for analysing the Raman spectra. The spectra observed in Figure 4.39 are well-known signals in the literature for conditions of absorption - usually representative of carbonaceous materials with graphitic ($G\ peak$) and amorphous carbon ($D\ peak$).

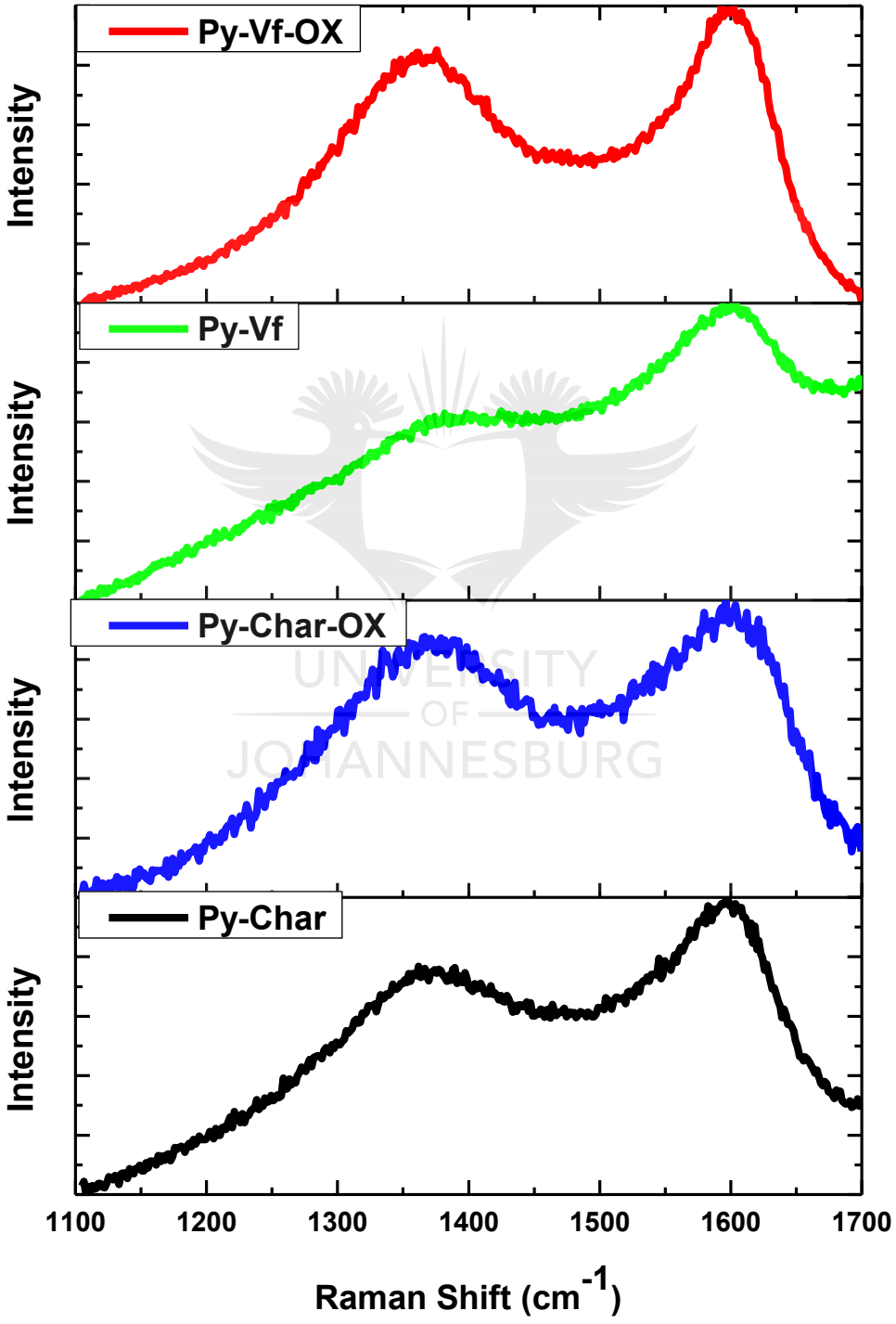

Figure 4.39 Raman spectra for pyrolysed and oxidised carbon fibre samples

The Raman spectra analysis is summarised in Table 4.33 where the $D\ band$ peak positions for PY-CHAR and PY-VF were $1384.58\ cm^{-1}$ and $1381.35\ cm^{-1}$ respectively while that for PY-CHAR-OX and PY-VF-OX were $1367.42\ cm^{-1}$ and $1367.17\ cm^{-1}$ respectively. A slight reduction in the peak position is observed after oxidation. For the $G\ band$, the peak positions were approximately $1600\ cm^{-1}$. From Figure 4.39, PY-CHAR and PY-VF had a wider band than PY-CHAR-OX and PV-VF-OX which were oxidised.

Table 4.33 A summary of the peak positions, peak intensities and the intensity ratio for non-oxidised and oxidised samples

Sample	Peak Position				Peak Intensity		IR = $\left(\frac{ID}{IG}\right)$
	D-band	FWHM (D)	G-band	FWHM (G)	D-band	G-band	
PY-CHAR	1384.58	206.54	1595.95	113.23	3576.61	4157.05	0.8604
PY-CHAR-OX	1367.42	196.93	1596.67	112.24	1433.59	1488.42	0.9632
Py-VF	1381.35	250.94	1619.72	177.92	4895.97	7476.43	0.6549
Py-VF-OX	1367.17	228.93	1596.22	96.11	5018.32	5188.85	0.9671

The different frequencies of the G and $D\ bands$ for graphitic and amorphous carbonaceous materials are attributed to the varying crystallite and induced stresses characteristic within these carbon domains [427]. For carbon materials, the Raman spectra are often categorised into first- and second-order regions. For purposes of this study, the first order which lies within the region of $1100 - 1800\ cm^{-1}$, was the primary focus because this is the region where the G and $D\ bands$ can be observed. The $G\ band$ is characterised by a graphite vibration mode known as E_{2g}, and is ascribed to the occurrence of a stretching vibration at a frequency of $\sim 1580\ cm^{-1}$ within the aromatic layers. Consequently, the carbon sp^2 atom pairs experience the motion of in-plane stretching during the E_{2g} mode of vibration [428]. The G band is the only band observed within the first-order region of the Raman spectra when pure or perfect graphite is analysed. The sp^2 G band is therefore the primary Raman signature.

The $D\ band$, also known as the defective band lies within the $1350\ cm^{-1}$ band and is commonly attributed to the degradation of local lattice and translational symmetries or to the

vibration mode of the graphite crystallite A_{1g} [429,430]. The $D-peak$ is caused by the induced defects or disorder on the sp^2 structure [49,427]. The intensity of the $D\ band$ can, therefore, be quantified by the disorder which is mainly activated by defects during processes like oxidation and all types of activation. The $D-band$ is clearly wider and is an indication of the presence of carbon materials that are poorly crystallised. This could possibly be the result of interstitials caused by sp^3 carbon residuals [431].

The above concept of using double resonance for a given phonon branch and laser energy to excite the $D\ mode$ of a Raman spectrum was first proposed by Thomsen and Reich [432], while Matthews et al. [429], investigated the dispersion and origin of the $D\ band$ in carbon materials. These two studies provided the physical basis for exciting, graphite's 2-D electron and phonon dispersion curves and deduced that in the Brillouin zone electronic transition takes place only in the region of the K point. Both studies concluded that there was a correlation of proportionality between band intensities and the state of carbonaceous materials organisation.

In this study an analysis of the peak intensities for the $D\ band$ showed a significant decrease (see Table 4.33) after the samples underwent oxidation. This decrease can be attributed to an increased state of structural organisation [433]. In the first-order Raman spectrum, the non-oxidised samples showed well-resolved D and G bands of equivalent intensities. However, after oxidation, both the D and G bands became slightly narrower with their maxima shifting towards lower frequencies and increased intensity ratios (IR). The parameters that influence the relative intensity (IR) include post pyrolysis treatments such as oxidation, crystallinity and carbon material disorder which affects the crystallite size. The IR increased after the oxidation process for each sample. Researchers including Lespade [365]showed that the structure of the carbon material is related to the intensity ratio $(IR = ID/IG)$ of the two first-order D and G bands [361,365]. The disorder within the carbon fibre was characterised using the intensity ratio where an increase in IR represented an increase in

the degree of disorder. The peak positions for oxidised and non-oxidised fibres were very close meaning that the oxidation treatment was just sufficient for removal of the residual char but did not modify the core region of the carbon fibre.

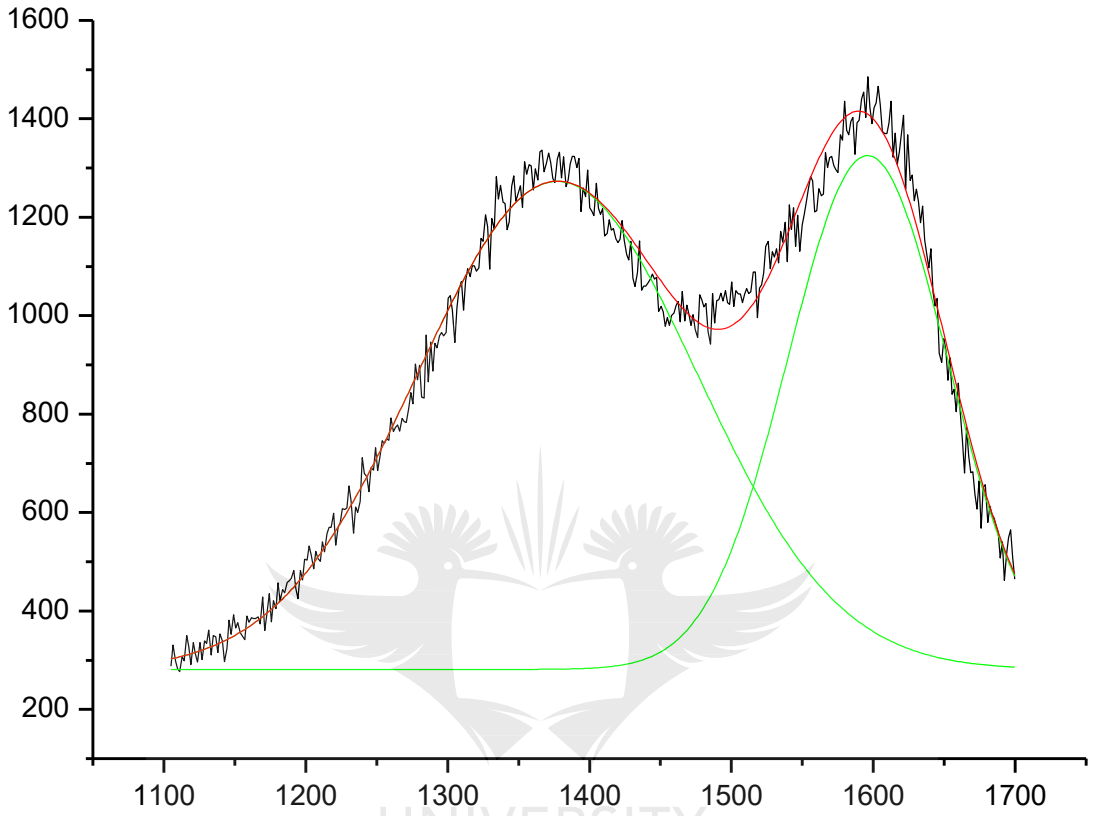

Figure 4.40 Lorentzian fitting of peaks

The Raman spectra of all the samples were subjected to deconvolution to provide a basis for the separation of the first-order D and G peaks via fitting Lorentzian shaped curves because they provide the best fits for the experimental data as shown in Figure 4.40 Lorentzian fitting of peaks during the analysis, particular attention was focused on defining the most appropriate baseline for comparison of one spectrum to another. In this regard, a linear baseline was selected as the most appropriate for all spectra. The results suggest that the oxidation process affected the Raman band positioning. The $G\ band$ positions exhibited no significant difference after oxidation. However, a slight variation in the $D\ band$ positions was observed after

oxidation. A shift towards a lowered wave number occurred after the oxidation process. This shift may possibly result from the high disorder or poor organisation [434].

4.14 Summary

Results from the computations and characterisations were analysed and discussed in this chapter. Thermal analysis using TGA revealed that in general, the incorporation of silane functionalised TiO_2 nanoparticles significantly improves the thermal stability of polymer composites due to improved particle-matrix bonding. A positive correlation was observed between enhanced thermal stability and improved dispersion with corresponding reduction in agglomeration when silane treated TiO_2 nanoparticles were used. Furthermore, indices such as IPDT and OI increased with the inclusion of TiO_2. A p-value of 0.015 for nanocomposite samples with silane treated TiO_2 clearly indicates that the treatment significantly influenced the Charpy impact energy in a positive manner. SEM characterisation revealed the occurrence of agglomeration breakage and not pull-outs for STN samples which is evidence of improvement in particle-matrix bonding.

Two approaches for quantifying dispersion of nanoparticles were successfully developed and validated based on gap statistics and fractal dimension of the two methodologies, gap statistic was the most comprehensive. It incorporated agglomeration factors and was not dependent on some probability distribution function and standard deviation. The approaches were versatile, robust and sophisticated, but not limited by the complexities of other approaches.

Analysis of variance (ANOVA) was conducted on finite element analyis data of the induced stress concentrations when variable tab configurations were investigated. The results showed that designing tabs with lower stiffness and taper angle while simultaneously increasing adhesive thickness significantly minimised the stress concentration at the tab

termination region. Taguchi, Taguchi-multiple response and Taguchi-genetic algorithm approaches were also implemented for the determination of optimal tab design parameters. All the approaches were equally efficient in converging at the optimal values of tab stiffness ($32.6\ GPa$), tab thickness ($0.5\ mm$), tab length ($50\ mm\ or\ 100\ mm$), tab taper angle (5°) and adhesive thickness ($1.5\ mm$).

The application of pyrolysis and oxidation on NCF reinforced composites for carbon fibre recovery was successfully achieved. To investigate the influence of char deposits, morphological and thermal characterisations were also conducted. The SEM results revealed that virgin fibre was highly susceptible to oxidation degradation while the char on the pyrolyzed samples acted as a sacrificial shield preventing oxygen from reaching the fibre surface. Furthermore, BET analysis showed that after pyrolysis fibre surface area and pore volume increased and decreased after oxidation. Pore size, however, decreased after pyrolysis and increased during oxidation. The observation from the XRD analysis revealed that carbon fibre's crystallite interlayer spacing was not impacted by both pyrolysis and oxidation, but the crystallite thickness (L_c), crystallite width (L_a) and the number of aromatic layers (N) were significantly influenced by oxidation in air. L_c and L_a increased with increase in surface area and reduction in pore size. The Raman spectroscopy results showed that the oxidation process significantly reduced the intensity of $D\ band$ peaks while a slight increase in the intensity ratio was observed. Furthermore, after oxidation sharper and narrower D and $G\ peaks$ were observed with a Raman band shift towards lower wave numbers which was evidence of char-free fibres.

CHAPTER FIVE

CONCLUSIONS AND RECOMMENDATIONS

5.1 Introduction

The objective of this research was to present a holistic approach for characterising non-crimp fabric composites where the emphasis is placed on modification of the matrix during fabrication, dispersion quantification of the nano-inclusions, minimising stress concentration during mechanical testing via optimisation techniques, and the application of pyrolysis and oxidation for the reclamation of carbon fibre from NCF composite waste. A circular economy approach that considers the composite from fabrication to fibre recovery was thus adopted.

A comprehensive literature review highlighted the manufacture of non-crimp fabric materials and the fabrication of non-crimp fabric composites. The review identified the difficulties and drawbacks of non-functionalised nanoparticles before inclusion in a matrix. Furthermore, the limitations of existing methodologies for quantifying the dispersed nanoparticles were highlighted. Possible recycling options for carbon fibre reinforced composites were extensively reviewed emphasising their pros and cons.

The knowledge gap identified included the lack of a comprehensive report characterising NCF composites from fabrication to fibre recovery. The application of dispersion quantification methodologies, which are not reliant on some probability distribution function, was limited. Furthermore, studies on characterising and investigating the effects of char were also limited.

Details of all the methodologies and experimental procedures applied in this research study were reported in Chapter 3. The functionalisation of TiO_2 nanoparticles before the

fabrication of composites with both open cast moulding and vacuum assisted resin transfer moulding was presented. A detailed description of two new approaches for quantifying dispersion using gap statistics and fractal dimensions were developed. The implementation of finite element analysis, statistical analysis and optimisation techniques were employed in stress concentration minimisation during tensile testing. The processes of recycling and reclamation of carbon fibre from NCF composite waste using pyrolysis followed by oxidation were presented. Thereafter, comprehensive characterisations including mechanical testing, scan electron microscopy, BET, elemental analysis, thermogravimetric analysis (TGA), X-ray diffraction analysis (XRD) and Raman spectroscopy analysis were offered.

5.2 Conclusions

The results and discussion as presented in Chapter 4 constituted studies from matrix modification, and characterisations and fibre reclamation via pyrolysis. The samples produced for experimentation included neat epoxy (NE), silane functionalised TiO_2 nanocomposites (STN), non-functionalised TiO_2 nanocomposites (TN), NCF carbon fibre reinforced composites (CF-NE) and NCF carbon fibre reinforced composite with TiO_2 inclusion (CF-STN).

It is obvious that dispersion plays a key role in the thermal and mechanical properties of composites. Two methodologies for assessing the state of dispersion were therefore developed, namely, dispersion quantification using gap statistics and dispersion quantification using fractal dimension. Proof of concept using simulated models and validation with real images was carried out. The gap statistic approach was the most comprehensive approach which used a gap factor (G_0), particle spacing dispersity (PSD_1) and particle size dispersity (PSD_2) to determine the dispersion quantity (D). The simulated models revealed that average particle size and its corresponding standard deviation for models and real samples with agglomerates and large variations in particle sizes were greater than those with consistent particles sizes and

minimal agglomerates. Furthermore, the presence of larger agglomerates correlated with higher variation in interparticle spacing. Homogeneous dispersion was thus characterised by lower standard deviation of the interparticle spacing. However, studies have shown that standard deviation is not a reliable metric for quantifying dispersion. Hence, a much more comprehensive quantification with PSD_2 representing the agglomeration factor which increases as the state of agglomeration increases, was formulated. An agglomeration parameter is critical for accuracy in quantification. An improvement in the state of dispersion was observed as $D \rightarrow 100\%$. For an ideal condition of same sized and uniformly distributed particles, G_0, PSD_1 and PSD_2 each must have a value of one (1).

The second quantification approach developed was less complicated and was based on the variance (S^2) of the fractal dimension D_f. As S^2 increases the dispersion quantity $(D_0) \rightarrow 100\%$ and homogeneity is improved. This methodology was successfully tested with simulated models during proof of concept and validated with real SEM images. The techniques developed are easy to implement, ensure reliable and consistent outputs, are very robust with some level of sophistication but without the complexities of other techniques, and are versatile enough to analyse both optical and electron microscopy images. These quantification methods serve as a means of establishing standardised benchmarks for characterising the state of dispersion.

An investigation into optimising the tab design configurations to minimise stress concentration within the tab termination region during tensile testing of NCF was carried out. To determine the statistical significance of each parameter, analysis of variance (ANOVA) was used after finite element analysis, which is the most effective means of analysing stress concentrations. The most significant factors were found to be tab stiffness, tap taper angle and adhesive thickness with corresponding P-values of approximately 0.000 for all the stress concentrations; σx_{max}, σy_{max} and τxy_{max}. The finite element analysis showed that increasing tab stiffness and taper angle directly increased the stress concentrations within the tab termination

region. Therefore, selection of tab materials with low stiffness and designing the tabs with lower taper angles was recommended. The results also revealed that in general increasing adhesive thickness decreases induced stress concentrations. However, in the case of tapered tabs, the peel stress (σ_y) increased with increasing adhesive thickness.

Three optimisation techniques, namely Taguchi, Taguchi-multiple response and Taguchi-genetic algorithm approach, were applied to obtain the optimal tab design parameters. The results showed that all the approaches were efficient in converging at the same optimal values of tab stiffness ($32.6\ GPa$), tab thickness ($0.5\ mm$), tab length ($50\ mm\ or\ 100\ mm$), tab taper angle ($5°$) and adhesive thickness ($1.5\ mm$). Comparatively, GA-based approaches are not limited by the challenges of interaction and response variability as seen with the Taguchi approach and multiple response optimisation respectively. Furthermore, a GA approach does not have the drawbacks of gradient-based approaches and can handle non-linear objective functions. Lastly, performance is not dependent on an initial design variable.

The impact strength of NE, STN, TN, methanol treated TiO_2 (MTN), CF-NE and CF-STN were determined as $0.322\ J$, $0.412\ J$, $0.274\ J$, $0.286\ J$, $8.98\ J$ and $10.086\ J$ respectively via the Charpy impact test. Analysis of variance (ANOVA) and a Tukey pairwise comparison was conducted to ascertain the significance of introducing silane treated TiO_2 nanoparticles. A P-Value of 0.013 was obtained indicating that the application of different treatments to the TiO_2 nanoparticles was significant from the ANOVA. The Tukey pairwise comparison test between TN and STN gave a P-value of 0.015. This clearly showed that silane treatment significantly affected the Charpy impact energy by improving the particle-matrix.

The fractured surfaces from the Charpy impact tests were investigated using SEM to evaluate the influence of nanoparticles on fracture response and mechanisms. The fracture behaviour of NE was characteristically brittle with large smooth regions, creases, fracture steps and hyperbolic markings along the path of the crack propagation and obvious river lines. These

characteristics clearly describe low resistance to crack propagation. The SEM image of the STN samples showed mostly homogenous dispersion with some sparsely distributed agglomerates of the nanoparticles attributed to the silane treatment. Improved particle-matrix bonding was observed in the large fracture surfaces attributed to rigid nanoparticles and diverging crack fronts resulting in increased energy absorption. Furthermore, the presence of agglomerate breakage and not pull-out clearly indicated strong particle-matrix adhesion. The SEM examination of the TN samples revealed nano fracture mechanisms associated with poor particle-matrix bonding and high presence of agglomeration such as particle pull-outs, interparticle crack propagation, particle crack pinning and crack deflection. These results clearly demonstrate the importance of silane functionalisation. Finally, the impact failure mechanisms observed after SEM examination of the fracture surfaces of NCF composites can be grouped into three main categories, namely (1) matrix only associated fracture and plastic deformation, (2) fibre only fracture and plastic deformation, and (3) interfacial-associated mechanisms such as fibre-matrix debonding, post-bonding friction and fibre pull-out.

After conducting the TGA analysis on NCF samples with and without TiO_2, it was observed that in most instances significant improvements in thermal stability were achieved with the introduction of TiO_2 nanoparticles. At the critical initial weight loss of 25%, the thermal stability of NE improved significantly from 338℃ to 347℃ after the introduction of TiO_2 nanoparticles. Thermal stability improvements were only pronounced for CF-STN and CF-NE after a 30% weight loss. Further enhancements in thermal stability were also observed from $50\% - 70\%$ weight loss with the inclusion of TiO_2 nanoparticles. At 460℃, 90% weight loss occurred, and the epoxy resin had completely degraded. The high weight of 60% at 800℃ for CF-STN clearly justifies the application of processes such as pyrolysis as an effective means of reclaiming carbon fibre. The treatment of the TiO_2 nanoparticles with silane solution ensured improvement in the particle-matrix bonding. This contributed to improving

homogeneity in the dispersion of the nanoparticles. A strong correlation was established between thermal stability and the dispersion state of particles where agglomeration is detrimental to particle-matrix bonding [23].

Further examination of the thermal stability of samples was carried out using the integral procedural decomposition temperature (IPDT) methodology. The inclusion of TiO_2 nanoparticle correlated positively with an increase in IPDT values. There was an increase of 7% and 12% and in the IPDT values after the introduction of silane treated and nontreated TiO_2 Respectively. An increase in IPDT is an established indication of improved heat retardation primarily due to the restriction in the oxygen heat movement caused by the presence of nanoparticles. The oxidation index (OI) was used in the estimation of the flame-retardant capacity of the NE, STN and TN; 0.27, 0.44 and 0.50 respectively. An 87% increase in OI was observed when NE and STN were compared. It is known in the literature that OI ranging from 0.5 and above indicates an increase in thermal stability and consequently enhancement in the flame resistance.

The reclamation of carbon fibre from NCF reinforced composites was successfully conducted via pyrolysis and oxidation. After the pyrolytic (500℃) process, an examination of the fibre morphology was carried out using the SEM. The resulting solid residue comprised fibres with brittle-like characteristics covered and bonded together with a carbonaceous solid residue known as char. Thereafter, the char was effectively removed by oxidation in air at 500℃. The oxidation process is critical to achieving the circular economy component of re-use as secondary raw material; char covered fibres are known to show poor fibre-matrix adhesion due to poor wettability which severely degrades the mechanical properties of the resulting composite when compared to virgin fibre. Furthermore, the capability of using the same temperature for pyrolysis and oxidation established a platform for developing a continuous thermal line treatment from pyrolysis to oxidation. In general, most fibres tend to

experience defects such as pitting and localised damage when subjected to elevated oxidation temperatures. However, the surface morphology of PY-CHAR-OX appeared very smooth without local and surface damage. This can be attributed to the protective action of the char.

To further investigate the influence of char during oxidation, the fibre diameters of virgin and pyrolyzed samples were determined using the SEM. A 10% reduction in virgin carbon fibre filament diameter was observed after oxidation. After pyrolysis, a 10% increase in fibre diameter was observed. This increase was clearly due to the deposition of char on the surface of the fibre. The removal of the char through oxidation resulted in a diameter decrease of only 3%. This lower percentage reduction is also proof that the presence of char acts as a protective cover during oxidation. Clearly the virgin fibre was highly susceptible to oxidation degradation while the char on the pyrolysed samples acted as a sacrificial shield preventing oxygen from reaching the fibre surface.

The physio-sorption characteristics of the recovered NCF carbon fibres were investigated using the Brunauer-Emmett-Teller (BET) method. The BET surface area analysis showed that after pyrolysis the fibre surface area increases by 682% while oxidation decreased it by 473%. The relatively higher surface area of PY-CHAR was due to the deposition of the amorphous carbon material from the gasification of the epoxy matrix. Since surface activation was not the objective of this study priority was given to achieving recovered fibre (PY-CHAR-OX) surface areas as close to those of virgin fibre (VF). Although the BET surface area for VF was 0.44 m^2/g, the acceptable surface area for virgin carbon fibre from the literature falls within the range of values less than 0.7 m^2/g. Therefore, PY-CHAR-OX (0.6 m^2/g) clearly satisfies the above-stated criteria and provides a justification for applying pyrolysis as a viable approach for reclamation fibre from composite waste. In general, pore volume was found to increase after pyrolysis, and decrease after oxidation. However, pore size exhibited an inverse

relationship with BET surface area such that pore size decreased after pyrolysis but increased after oxidation. in air.

The elemental composition of the recovered fibres was evaluated using a thermal analyser and the EDX unit of the SEM to investigate the effect of pyrolysis and oxidation. In the elemental composition of the comprised carbon, oxygen, nitrogen and sulphur, carbon, as expected, was the dominant element. A comparison of PY-CHAR and PY-CHAR-OX showed an oxygen composition of 2.39% and 17.37% respectively. The corresponding O/C atomic ratios were also 0.0256 and 0.2187 respectively. The comparably lower oxygen percentage of PY-CHAR is indication of an inert fibre surface which consequently decreases fibre-matrix bonding. After oxidation, the increase in O/C coupled with an increase of over 700% in oxygen content of PY-CHAR-OX, implied that surface active sites which promote surface polarity were introduced onto the fibre surface. This facilitates a higher propensity for the formation of improved fibre-matrix chemical bonds and therefore wetting is enhanced. The presence of minor constituent elements such as sulphur enhances the acid-base properties of the fibre and is critical in improving fibre-matrix adhesion.

The impact of pyrolysis and oxidation on the thermal property of carbon fibre was investigated using TGA under heating conditions from 30℃ to 1000℃. Two distinguishable events on the thermogram of PY-CHAR were observed after TGA with the decomposition of the char layer attributed to the first event while the second event was due to the decomposition of the carbon fibre itself. The two events coupled with the shape of the thermogram clearly represents low thermal stability and an indication that the presence of char negatively influences thermal stability. However, the thermogram for PY-CHAR-OX had only one event which corresponded to the decomposition of the carbon fibre itself. Higher thermal stability could be deduced from the shape of the thermogram and the occurrence of just one event. The lack of char on the fibre surface due to its removal via oxidation therefore positively impacts

thermal stability. Nevertheless, the residual weights for PY-CHAR and PY-CHAR-OX were approximately 97% and 96% respectively. The slightly higher residual of PY-CHAR supports the conclusion that the char layer has thermal protection capabilities.

Investigating the effects of pyrolysis and oxidation on the crystallinity of the recovered carbon fibre was carried out using XRD. The two peaks observed on the diffractograms from the XRD spectra of PY-CHAR-OX and PY-CHAR samples were reflected at 25° and 44° corresponding to the 002 and 011 diffraction lines respectively. The interlayer spacings of d_{002} and d_{011} for both PY-CHAR and PY-CHAR-OX were approximately equal with d_{002} closer to the lower end of the disordered carbon material range disorder range of 3.4 Å. Pyrolysis and oxidation thus did not significantly influence the crystallite interlayer spacing of the carbon fibre. The most critical crystallite structural parameters that were affected by oxidation treatment were the crystallite thickness (L_c), crystallite width (L_a) and the number of aromatic layers (N). After oxidation of the char covered reclaimed carbon fibre, the L_c decreased by 16%, L_a saw a significant reduction of 80%, and N also slightly decreased. The high decrease in L_a can be attributed to the evacuation of carbon atoms from the crystallite edge during the reduction reaction of oxidation. Furthermore, the results show that as the surface area of carbon fibre increases, L_c and L_a tend to increase while a reduction in pore size also increases L_c and L_a.

Raman spectroscopy was also used to explore the effects of pyrolysis, oxidation and the presence of char on the microstructure of carbon fibre. Two absorptions or well-resolved peaks were present in both oxidised and non-oxidised fibres. A significant reduction in the $D\ band$ peak intensities was observed after the oxidation process which was attributed to improvement in the structural organisation. The intensity ratio of the oxidised fibres was slightly higher than the pyrolysed fibres. Furthermore, the signal sharpness of the oxidised samples coupled with the broadness and in some cases poorly defined peaks of the pyrolysed samples provide an

indication of deposited char residue and resin on the surface of the fibres. Additionally, the aggressive oxidation conditions of $500℃$ for $60\,min$ caused a sharper, narrower D and $G\ peaks$, a change in position of the Raman band, and a shift towards lower wave numbers which was evidence of char-free fibres.

5.3 Recommendations for Future Research

This research provides a holistic approach by successfully addressing critical gaps in literature related to improving non-crimp fabric reinforced composites using active particles, quantification of the particle dispersion after matrix modification, improving testing through optimisation approaches and reclamation of quality fibre for end of life utilisation. Although this research study has been comprehensive, further investigations are still required in some critical areas. These include:

1. The greatest limitation to mainstream use of fibre-reinforced composites is the lack of a continuous automation process from fabric manufacture to composite fabrication. Non-crimp fabrics are uniquely suited for complete automation due to the fact that existing automation processes in the textile industry were adopted for the manufacture of preforms. A significant advancement will be a combination of preform manufacture, draping and Vacuum assisted resin transfer moulding processes.

2. Existing dispersion quantification techniques rely on 2D images, however, the newly developed approaches in this study can be modified to analyse 3D images. Furthermore, a stepwise increase in magnifications can be used to generate various images that can be employed to give a better representation of the dispersion state within the entire sample.

3. The importance of char after pyrolysis has not been sufficiently explored; further studies are required to investigate the properties of the carbonaceous layer. A study into its possible role in activation and functionalisation of the fibres is necessary.

4. Presently, there is no published literature on the use of recovered activated carbon fibre for adsorption purposes. Future studies will benefit from focusing on the use of such fibres for biogas upgrades.

5. The application of optimised process parameters for both pyrolysis and post pyrolysis processes are critical to enhance the quality of reclaimed fibres. Further studies are required to establish the optimal parameters required to gain insight into the impact of the pyrolysis.

Since the current literature on economic assessment, energy analysis and environmental impact analyses of pyrolysis on carbon fibre reinforced composites is scanty or non-existent, this field will greatly benefit from further exploration.

REFERENCES

[1] V.H. DeLeon, T.D. Nguyen, M. Nar, N.A. D'Souza, T.D. Golden, Polymer nanocomposites for improved drug delivery efficiency, Mater. Chem. Phys. 132 (2012) 409–415. doi:10.1016/j.matchemphys.2011.11.046.

[2] H. Li, W.T.S. Huck, Polymers in nanotechnology, Curr. Opin. Solid State Mater. Sci. 6 (2002) 3–8. doi:10.1016/S1359-0286(02)00008-6.

[3] H. Cong, M. Radosz, B.F. Towler, Y. Shen, Polymer-inorganic nanocomposite membranes for gas separation, Sep. Purif. Technol. 55 (2007) 281–291. doi:10.1016/j.seppur.2006.12.017.

[4] R. a Hule, D.J. Pochan, Polymer Nanocomposites for Biomedical Applications, MRS Bull. 32 (2007) 354–358. doi:10.1557/mrs2007.235.

[5] D.R. Paul, L.M. Robeson, Polymer nanotechnology: Nanocomposites, Polymer (Guildf). 49 (2008) 3187–3204. doi:10.1016/j.polymer.2008.04.017.

[6] B.J. Phillips, Multidisciplinary Optimization of a CFRP Wing Cover, Cranfield University, 2009. doi:10.1260/0957456042880200.

[7] M. Alfano, F. Furgiuele, R. Rangarajan, A.J. Lew, B. Krull, J. Patrick, K. Hart, S. White, N. Sottos, Daniel O. Adams, Donald F. Adams, Tabbing Guide for Composite Test Specimens, Compos. Joints Connect. 40 (2011) 341–362. doi:10.1007/s40799-016-0094-9.

[8] D.O. Adams, D.F. Adams, Tabbing Guide for Composite Test Specimens, (2002). http://www.dtic.mil/docs/citations/ADA411472 (accessed September 28, 2017).

[9] G. Belingardi, D.S. Paolino, E.G. Koricho, Investigation of influence of tab types on tensile strength of E-glass/epoxy fiber reinforced composite materials, in: Procedia Eng., 2011: pp. 3279–3284. doi:10.1016/j.proeng.2011.04.541.

[10] M. Hojo, Y. Sawada, H. Miyairi, Influence of clamping method on tensile properties of unidirectional CFRP in 0° and 90° directions - round robin activity for international standardization in Japan, Composites. 25 (1994) 786–796. doi:10.1016/0010-4361(94)90139-2.

[11] I. De Baere, W. Van Paepegem, J. Degrieck, On the design of end tabs for quasi-static and fatigue testing of fibre-reinforced composites, Polym. Compos. 30 (2009) 381–390. doi:10.1002/pc.20564.

[12] J. Czél, G., Meisam, M.R. Wisnom, Hybrid specimens eliminating stress concentrations in tensile and compressive testing of unidirectional composites, Compos. Part A Appl. Sci. Manuf. 91 (2016) 436–447. doi:10.1016/j.compositesa.2016.07.021.

[13] G. Cz??l, M. Jalalvand, M.R. Wisnom, Hybrid specimens eliminating stress concentrations in tensile and compressive testing of unidirectional composites, Compos. Part A Appl. Sci. Manuf. 91 (2016) 436–447. doi:10.1016/j.compositesa.2016.07.021.

[14] J.L.H. Chau, C.T. Tung, Y.M. Lin, A.K. Li, Preparation and optical properties of titania/epoxy nanocomposite coatings, Mater. Lett. 62 (2008) 3416–3418. doi:10.1016/j.matlet.2008.02.058.

[15] X. Chen, S.S. Mao, Titanium dioxide nanomaterials: Synthesis, properties, modifications and applications, Chem. Rev. 107 (2007) 2891–2959. doi:10.1021/cr0500535.

[16] X. Wang, Y. He, R.-M. Wang, Z.-M. Wu, P. Song, W. Zhai, Preparation of epoxy-acrylate copolymer@nano-TiO2 Pickering emulsion and its antibacterial activity, Prog. Org. Coatings.

87 (2015) 122–128. doi:10.1016/j.porgcoat.2015.05.019.

[17] B. Wetzel, P. Rosso, F. Haupert, K. Friedrich, Epoxy nanocomposites - fracture and toughening mechanisms, Eng. Fract. Mech. 73 (2006) 2375–2398. doi:10.1016/j.engfracmech.2006.05.018.

[18] K. Kumar, P.K. Ghosh, A. Kumar, Improving mechanical and thermal properties of TiO2-epoxy nanocomposite, Compos. Part B Eng. 97 (2016) 353–360. doi:10.1016/j.compositesb.2016.04.080.

[19] C.B. Ng, L.S. Schadler, R.W. Siegel, Synthesis and mechanical properties of TiO2-epoxy nanocomposites, Nanostructured Mater. 12 (1999) 507–510. doi:10.1016/S0965-9773(99)00170-1.

[20] Y. Zhou, E. White, M. Hosur, S. Jeelani, Effect of particle size and weight fraction on the flexural strength and failure mode of TiO2 particles reinforced epoxy, Mater. Lett. 64 (2010) 806–809. doi:10.1016/j.matlet.2010.01.016.

[21] H.A. Al-Turaif, Effect of nano TiO2 particle size on mechanical properties of cured epoxy resin, Prog. Org. Coatings. 69 (2010) 241–246. doi:10.1016/j.porgcoat.2010.05.011.

[22] V.M.. Evora, A. Shukla, Fabrication, characterization, and dynamic behavior of polyester/TiO2 nanocomposites, Mater. Sci. Eng. A. 361 (2003) 358–366. doi:10.1016/S0921-5093(03)00536-7.

[23] A. Chatterjee, M.S. Islam, Fabrication and characterization of TiO2-epoxy nanocomposite, Mater. Sci. Eng. A. 487 (2008) 574–585. doi:10.1016/j.msea.2007.11.052.

[24] G. Polizos, E. Tuncer, I. Sauers, K.L. More, Physical properties of epoxy resin/titanium dioxide nanocomposites, Polym. Eng. Sci. 51 (2011) 87–93. doi:10.1002/pen.21783.

[25] J. Sandler, M.S.P. Shaffer, T. Prasse, W. Bauhofer, K. Schulte, A.H. Windle, Development of a dispersion process for carbon nanotubes in an epoxy matrix and the resulting electrical properties, Polymer (Guildf). 40 (1999) 5967–5971. doi:10.1016/S0032-3861(99)00166-4.

[26] Y.Y. Huang, E.M. Terentjev, Dispersion of carbon nanotubes: Mixing, sonication, stabilization, and composite properties, Polymers (Basel). 4 (2012) 275–295. doi:10.3390/polym4010275.

[27] R. Bandyopadhyaya, E. Nativ-Roth, O. Regev, R. Yerushalmi-Rozen, Stabilization of Individual Carbon Nanotubes in Aqueous Solutions, Nano Lett. 2 (2002) 25–28. doi:10.1021/nl010065f.

[28] P. Pötschke, A.R. Bhattacharyya, A. Janke, Melt mixing of polycarbonate with multiwalled carbon nanotubes: Microscopic studies on the state of dispersion, in: Eur. Polym. J., Pergamon, 2004: pp. 137–148. doi:10.1016/j.eurpolymj.2003.08.008.

[29] F. Bensadoun, N. Kchit, C. Billotte, S. Bickerton, F. Trochu, E. Ruiz, A study of nanoclay reinforcement of biocomposites made by liquid composite molding, Int. J. Polym. Sci. 2011 (2011) 1–10. doi:10.1155/2011/964193.

[30] R. Rastogi, R. Kaushal, S.K. Tripathi, A.L. Sharma, I. Kaur, L.M. Bharadwaj, Comparative study of carbon nanotube dispersion using surfactants, J. Colloid Interface Sci. 328 (2008) 421–428. doi:10.1016/j.jcis.2008.09.015.

[31] N. Jouault, D. Zhao, S.K. Kumar, Role of casting solvent on nanoparticle dispersion in polymer nanocomposites, Macromolecules. 47 (2014) 5246–5255. doi:10.1021/ma500619g.

[32] M.S. Goyat, S. Rana, S. Halder, P.K. Ghosh, Facile fabrication of epoxy-TiO2nanocomposites: A critical analysis of TiO2impact on mechanical properties and toughening mechanisms, Ultrason. Sonochem. 40 (2018) 861–873. doi:10.1016/j.ultsonch.2017.07.040.

[33] S.R. Bakshi, R.G. Batista, A. Agarwal, Quantification of carbon nanotube distribution and property correlation in nanocomposites, Compos. Part A Appl. Sci. Manuf. 40 (2009) 1311–1318. doi:10.1016/j.compositesa.2009.06.004.

[34] A.M.K. Esawi, K. Morsi, A. Sayed, M. Taher, S. Lanka, Effect of carbon nanotube (CNT) content on the mechanical properties of CNT-reinforced aluminium composites, Compos. Sci. Technol. 70 (2010) 2237–2241. doi:10.1016/j.compscitech.2010.05.004.

[35] P.J. Clark, F.C. Evans, Distance to Nearest Neighbor as a Measure of Spatial Relationships in Populations, Ecology. 35 (1954) 445–453. doi:10.2307/1931034.

[36] S.R. Bakshi, R.G. Batista, A. Agarwal, Quantification of carbon nanotube distribution and property correlation in nanocomposites, Compos. Part A Appl. Sci. Manuf. 40 (2009) 1311–1318. doi:10.1016/j.compositesa.2009.06.004.

[37] S. Xie, E. Harkin-Jones, Y. Shen, P. Hornsby, M. McAfee, T. McNally, R. Patel, H. Benkreira, P. Coates, Quantitative characterization of clay dispersion in polypropylene-clay nanocomposites by combined transmission electron microscopy and optical microscopy, Mater. Lett. 64 (2010) 185–188. doi:10.1016/j.matlet.2009.10.042.

[38] D. Kim, J.S. Lee, C.M.F. Barry, J.L. Mead, Microscopic measurement of the degree of mixing for nanoparticles in polymer nanocomposites by TEM images, Microsc. Res. Tech. 70 (2007) 539–546. doi:10.1002/jemt.20478.

[39] H.A. Gleason, Society Some Applications of the Quadrat Method, Bull. Torrey Bot. Club. 47 (1920) 21–33. doi:10.2307/2480223.

[40] A. Yazdanbakhsh, Z. Grasley, B. Tyson, R.K. Abu Al-Rub, Dispersion quantification of inclusions in composites, Compos. Part A Appl. Sci. Manuf. 42 (2011) 75–83. doi:10.1016/j.compositesa.2010.10.005.

[41] L.T. Fan, Y. ming Chen, F.S. Lai, Recent developments in solids mixing, Powder Technol. 61 (1990) 255–287. doi:10.1016/0032-5910(90)80092-D.

[42] M. Rhodes, Introduction to Particle Technology, Wiley, 2008. doi:10.1002/9780470727102.

[43] M.D. Haslam, B. Raeymaekers, A composite index to quantify dispersion of carbon nanotubes in polymer-based composite materials, Compos. Part B Eng. 55 (2013) 16–21. doi:10.1016/j.compositesb.2013.05.038.

[44] T. Glaskova, M. Zarrelli, A. Borisova, K. Timchenko, A. Aniskevich, M. Giordano, Method of quantitative analysis of filler dispersion in composite systems with spherical inclusions, Compos. Sci. Technol. 71 (2011) 1543–1549. doi:10.1016/j.compscitech.2011.06.009.

[45] Z.P. Luo, J.H. Koo, Quantifying the dispersion of mixture microstructures, J. Microsc. 225 (2007) 118–125. doi:10.1111/j.1365-2818.2007.01722.x.

[46] C. Balzer, M. Armstrong, B. Shan, Y. Huang, J. Liu, B. Mu, Modeling Nanoparticle Dispersion in Electrospun Nanofibers, Langmuir. 34 (2018) 1340–1346. doi:10.1021/acs.langmuir.7b03726.

[47] P.T. Lillehei, J.-W. Kim, L.J. Gibbons, C. Park, A quantitative assessment of carbon nanotube dispersion in polymer matrices, Nanotechnology. 20 (2009) 325708. doi:10.1088/0957-

4484/20/32/325708.

[48] E. Witten, M. Thomas, K. Michael, Composites Market Report 2015, Ind. Verstärkte Kunstoffe. (2015) 1–44. http://www.eucia.eu/userfiles/files/Composites_Market Report_2015.pdf.

[49] L. Mazzocchetti, T. Benelli, E. D'Angelo, C. Leonardi, G. Zattini, L. Giorgini, Validation of carbon fibers recycling by pyro-gasification: The influence of oxidation conditions to obtain clean fibers and promote fiber/matrix adhesion in epoxy composites, Compos. Part A Appl. Sci. Manuf. 112 (2018) 504–514. doi:10.1016/j.compositesa.2018.07.007.

[50] D. Mattsson, Mechanical performance of NCF composites, PhD Thesis, Lulea Univ. Technol. (2005) 172. doi:10.1021/jp401923v.

[51] G.D. Shaffer, An Archaeomagnetic Study of a Wattle and Daub Building Collapse, J. F. Archaeol. 20 (1993) 59. doi:10.2307/530354.

[52] S.W. Tsai, Composites design, Think Composites, 1987.

[53] S.W. Tsai, Strength Characteristics of Composite Materials., (1965). https://apps.dtic.mil/docs/citations/ADA307777 (accessed August 23, 2019).

[54] B.D. Agarwal, L.J. Broutman, K. Chanshekhara, Analysis and performance of fiber composites, 4th ed., John Wiley & Sons, 2017. https://www.wiley.com/en-us/Analysis+and+Performance+of+Fiber+Composites%2C+4th+Edition-p-9781119389989 (accessed August 23, 2019).

[55] NASA, Fiber-Reinforced Polymer Composite Material Fiber-Reinforced Polymer Composite, Matrix. (1996) 1–9. https://kscddms.ksc.nasa.gov/Reliability/Documents/Preferred_Practices/2210.pdf (accessed August 23, 2019).

[56] G.A. Bibo, P.J. Hogg, M. Kemp, Mechanical characterisation of glass- and carbon-fibre-reinforced composites made with non-crimp fabrics, Compos. Sci. Technol. 57 (1997) 1221–1241. doi:10.1016/S0266-3538(97)00053-5.

[57] H. Mauersberger, VerfahrenzurHerstellung von Kettenstichware, 1954.

[58] P. Steggal, Developing multiaxial non-crimp reinforcements for the cost effective solution, in: 31st Int. SAMPE Tech. Conf., 1999: pp. 26–30.

[59] S. V. Lomov, Non-crimp fabric composites: Manufacturing, properties and applications, Woodhead Pub, 2011. doi:10.1533/9780857092533.

[60] H.B. Dexter, G.H. Hasko, Mechanical properties and damage tolerance of multiaxial warp-knit composites, Compos. Sci. Technol. 56 (1996) 367–380. doi:10.1016/0266-3538(95)00107-7.

[61] P.J. Hogg, A. Ahmadnia, F.J. Guild, The mechanical properties of non-crimped fabric-based composites, Composites. 24 (1993) 423–432. doi:10.1016/0010-4361(93)90249-8.

[62] S.L. Iyer, R. Sen, Advanced Composites Materials in Civil Engineering Structures, ASCE, 1991. https://cedb.asce.org/CEDBsearch/record.jsp?dockey=0069838 (accessed September 26, 2019).

[63] A.P. Mouritz, K.H. Leong, I. Herszberg, A review of the effect of stitching on the in-plane mechanical properties of fibre-reinforced polymer composites, Compos. Part A Appl. Sci. Manuf. 28 (1997) 979–991. doi:10.1016/S1359-835X(97)00057-2.

[64] J.I. Kim, Y.T. Hwang, K.H. Choi, H.J. Kim, H.S. Kim, Prediction of the vacuum assisted resin transfer molding (VARTM) process considering the directional permeability of sheared woven fabric, Compos. Struct. 211 (2019) 236–243. doi:10.1016/j.compstruct.2018.12.043.

[65] K. Vallons, I. Duque, S.V. Lomov, I. Verpoest, Loading direction dependence of the tensile stiffness, strength and fatigue life of biaxial carbon/epoxy NCF composites, Compos. Part A Appl. Sci. Manuf. 42 (2011) 16–21. doi:10.1016/J.COMPOSITESA.2010.09.009.

[66] N. Tessitore, A. Riccio, A novel FEM model for biaxial non-crimp fabric composite materials under tension, Comput. Struct. 84 (2006) 1200–1207. doi:10.1016/J.COMPSTRUC.2006.01.024.

[67] B. Yang, V. Kozey, S. Adanur, S. Kumar, Bending, compression, and shear behavior of woven glass fiber–epoxy composites, Compos. Part B Eng. 31 (2000) 715–721. doi:10.1016/S1359-8368(99)00052-9.

[68] Z. ming Huang, The mechanical properties of composites reinforced with woven and braided fabrics, Compos. Sci. Technol. 60 (2000) 479–498. doi:10.1016/S0266-3538(99)00148-7.

[69] K. Dransfield, C. Baillie, Y.-W. Mai, Improving the delamination resistance of CFRP by stitching—a review, Compos. Sci. Technol. 50 (1994) 305–317. doi:10.1016/0266-3538(94)90019-1.

[70] C. Polowick, Optimizing Vacuum Assisted Resin Transfer Moulding (VARTM) Processing Parameters to Improve Part Quality, 2013.

[71] S.G. Advani, E.M. Sozer, E.M. Sozer, Process Modeling in Composites Manufacturing, CRC Press, 2002. doi:10.1201/9780203910061.

[72] A.A. Baker, M.L. Scott, Composite Materials for Aircraft Structures, Third Edition, American Institute of Aeronautics and Astronautics, Inc., Washington, DC, 2016. doi:10.2514/4.103261.

[73] Molding – SONGWOL TECHNOLOGIES, (n.d.). http://songwoltech.com/en/molding/ (accessed September 27, 2019).

[74] L. Khoun, D. Maillard, M.N. Bureau, Effect of process variables on the performance of glass fibre reinforced composites made by high pressure resin transfer moulding, in: Proc. 12th Annu. Automot. Compos. Conf. Exhib. (ACCE 2012), 2012: p. 380. https://nrc-publications.canada.ca/eng/view/accepted/?id=f1b008ab-a89d-43a5-8d01-ee328d85eefe (accessed September 27, 2019).

[75] M. Schwartz, Innovations in materials manufacturing, fabrication, and environmental safety, CRC Press, 2010. doi:10.1201/b10386.

[76] M.R. Abusrea, S.W. Han, K. Arakawa, N.S. Choi, Bending strength of CFRP laminated adhesive joints fabricated by vacuum-assisted resin transfer molding, Compos. Part B Eng. 156 (2019) 8–16. doi:10.1016/j.compositesb.2018.08.041.

[77] P.A. Sreekumar, K. Joseph, G. Unnikrishnan, S. Thomas, A comparative study on mechanical properties of sisal-leaf fibre-reinforced polyester composites prepared by resin transfer and compression moulding techniques, Compos. Sci. Technol. 67 (2007) 453–461. doi:10.1016/J.COMPSCITECH.2006.08.025.

[78] C.H. Park, A. Lebel, A. Saouab, J. Bréard, W. Il Lee, Modeling and simulation of voids and saturation in liquid composite molding processes, Compos. Part A Appl. Sci. Manuf. 42 (2011) 658–668. doi:10.1016/J.COMPOSITESA.2011.02.005.

[79] R. Matuzaki, D. Seto, M. Naito, A. Todoroki, Y. Mizutani, Analytical prediction of void

formation in geometrically anisotropic woven fabrics during resin transfer molding, Compos. Sci. Technol. 107 (2015) 154–161. doi:10.1016/J.COMPSCITECH.2014.12.013.

[80] M. Nauheimer, R. Relan, U.H. Thygesen, H. Madsen, B. Olesen, K. Kirkeby, A Stochastic Spatio-Temporal Model of the Flow-Front Dynamics in a Vacuum Assisted Resin Transfer Moulding Process, IFAC-PapersOnLine. 51 (2018) 383–388. doi:10.1016/j.ifacol.2018.09.175.

[81] A. Dominauskas, D. Heider, J.W. Gillespie, Electric time-domain reflectometry sensor for online flow sensing in liquid composite molding processing, Compos. Part A Appl. Sci. Manuf. 34 (2003) 67–74. doi:10.1016/S1359-835X(02)00232-4.

[82] F. Zhang, B. Cosson, S. Comas-Cardona, C. Binetruy, Efficient stochastic simulation approach for RTM process with random fibrous permeability, Compos. Sci. Technol. 71 (2011) 1478–1485. doi:10.1016/J.COMPSCITECH.2011.06.006.

[83] B. Yenilmez, E. Murat Sozer, A grid of dielectric sensors to monitor mold filling and resin cure in resin transfer molding, Compos. Part A Appl. Sci. Manuf. 40 (2009) 476–489. doi:10.1016/J.COMPOSITESA.2009.01.014.

[84] B. Sköck-Hartmann, T. Gries, Automotive applications of non-crimp fabric composites, in: S. V Lomov (Ed.), Non-Crimp Fabr. Compos. Manuf. Prop. Appl., Woodhead Publishing Limited, Cambridge, 2011.

[85] M. Derks, F. Birzle, H. Pfitzer, CFK-Technologie bei der BMW Group – Heute/ Zukunft, in: VDI (Ed.), Kunststoffe Im Automob., VDI, Düsseldorf, 2007.

[86] P. Feraboli, A. Masini, Development of carbon/epoxy structural components for a high performance vehicle, Compos. Part B Eng. 35 (2004) 323–330. doi:10.1016/j.compositesb.2003.11.010.

[87] O. Schauerte, W. Schreiber, A. Finkbeiner, E. Ene, D. Starmann, Der Einsatz von leistungsfähigen Kunststoffen im Bugatti Veyron, in: VDI (Ed.), Kunststoffe Im Automob., VDI, Düsseldorf, 2007.

[88] C. Köth, Pulver, Kohle, Kosten: ein neuartiges Pulver senkt die Herstellungskosten von CFK- und GFK-Verbundwerkstoffen; die Serienanwendung rückt damit in greifbare Nähe, Automob. Ind. 48 (2003) 94–95.

[89] T.C. Grundmann, Automatisiertes Preforming für schalenförmige komplexe Faserverbundbauteile, Shaker, 2009. https://www.booklooker.de/Bücher/Angebote/autor=Grundmann+Tim+Christian&titel=Automatisiertes+Preforming+für+schalenförmige+komplexe+Faserverbundbauteile (accessed September 29, 2019).

[90] A. Geßler, Textile Integrationstechniken zur Herstellung vorkonfektionierter Verstärkungsstrukturen für FVK “INTEX,” 2002. https://www.tib.eu/de/suchen/id/tema%3ATEMA20030901950/Textile-Integrationstechniken-zur-Herstellung-vorkonfektionierter/ (accessed September 29, 2019).

[91] D. Gay, S. V Hoa, Composite materials : design and applications, CRC Press, 2007. https://books.google.com.gh/books/about/Composite_Materials.html?id=qqEeAQAAIAAJ&redir_esc=y (accessed September 29, 2019).

[92] M. Kalanchiam, M. Chinnasamy, Advantages of composite materials in aircraft structures, World Acad. Sci. Eng. Technol. 71 (2012) 597–601. https://www.semanticscholar.org/paper/Advantages-of-Composite-Materials-in-Aircraft-

Kalanchiam-Chinnasamy/e143e0f9fcf5f8222b6b695217ce0e861c1d080e (accessed September 29, 2019).

[93] P. Middendorf, C. Metzner, Aerospace applications of non-crimp fabric composites, in: S. V. Lomov (Ed.), Non-Crimp Fabr. Compos. Manuf. Prop. Appl., Woodhead Publishing Limited, Cambridge, 2011.

[94] ACARE, Advisory Council for Aviation Research and Innovation in Europe (ACARE), Activity Summary,2015, 2015. https://www.acare4europe.org/sites/acare4europe.org/files/document/ACARE Annual report 2014-15vs0 7 25Sept15.pdf (accessed September 30, 2019).

[95] Boeing, 787 Aircraft Rescue and Firefighting Composite Structure, 2013. http://www.boeing.com/assets/pdf/commercial/airports/faqs/787_composite_arff_data.pdf (accessed September 29, 2019).

[96] Airbus, Airbus Material Dialogue, Bremen, 2006.

[97] T. Ackermann, L. Söder, Wind energy technology and current status: a review, Renew. Sustain. Energy Rev. 4 (2000) 315–374. doi:10.1016/S1364-0321(00)00004-6.

[98] C. Soutis, Fibre reinforced composites in aircraft construction, Prog. Aerosp. Sci. 41 (2005) 143–151. doi:10.1016/J.PAEROSCI.2005.02.004.

[99] L.M. Wyatt, Materials for MW sized aerogenerators Part 2. Materials characteristics, Mater. Des. 4 (1983) 880–884. doi:10.1016/0261-3069(83)90087-0.

[100] C.W. Kensche, Fatigue of composites for wind turbines, Int. J. Fatigue. 28 (2006) 1363–1374. doi:10.1016/j.ijfatigue.2006.02.040.

[101] G. Adolphs, C. Skinner, Non-crimp fabric composites in wind turbines, in: S. V. Lomov (Ed.), Non-Crimp Fabr. Compos. Manuf. Prop. Appl., Woodhead Publishing Limited, Cambridge, 2011.

[102] M. of Energy, Wind Energy in Denmark, Research and technological Development, 1990, 1990.

[103] P. Friis, Large Scale Wind Turbines, Operating Hours and Energy Production, Elsam Project A/S. Internal Report, 1993, 1993.

[104] D. Pinto, L. Bernardo, A. Amaro, S. Lopes, Mechanical properties of epoxy nanocomposites using titanium dioxide as reinforcement - A review, Constr. Build. Mater. 95 (2015) 506–524. doi:10.1016/j.conbuildmat.2015.07.124.

[105] A. Rabenau, The Role of Hydrothermal Synthesis in Preparative Chemistry, Angew. Chemie Int. Ed. English. 24 (1985) 1026–1040. doi:10.1002/anie.198510261.

[106] F. Milanesi, G. Cappelletti, R. Annunziata, C.L. Bianchi, D. Meroni, S. Ardizzone, Siloxane-TiO2 hybrid nanocomposites. the structure of the hydrophobic layer, J. Phys. Chem. C. 114 (2010) 8287–8293. doi:10.1021/jp1014669.

[107] Q. Chen, N.L. Yakovlev, Adsorption and interaction of organosilanes on TiO2 nanoparticles, Appl. Surf. Sci. 257 (2010) 1395–1400. doi:10.1016/j.apsusc.2010.08.036.

[108] J. Zhao, M. Milanova, M.M.C.G. Warmoeskerken, V. Dutschk, Surface modification of TiO2 nanoparticles with silane coupling agents, Colloids Surfaces A Physicochem. Eng. Asp. 413 (2012) 273–279. doi:10.1016/j.colsurfa.2011.11.033.

[109] S. Daneshpayeh, F. Ashenai Ghasemi, I. Ghasemi, M. Ayaz, Predicting of mechanical properties of PP/LLDPE/TiO<inf>2</inf> nano-composites by response surface methodology, Compos. Part B Eng. 84 (2016) 109–120. doi:10.1016/j.compositesb.2015.08.075.

[110] R. Neppalli, V. Causin, E.M. Benetti, S.S. Ray, A. Esposito, S. Wanjale, M. Birajdar, J.M. Saiter, A. Marigo, Polystyrene/TiO2 composite electrospun fibers as fillers for poly(butylene succinate-co-adipate): Structure, morphology and properties, Eur. Polym. J. 50 (2014) 78–86. doi:10.1016/j.eurpolymj.2013.11.002.

[111] P.M. Chou, M. Mariatti, A. Zulkifli, S. Sreekantan, Evaluation of the flexural properties and bioactivity of bioresorbable PLLA/PBSL/CNT and PLLA/PBSL/TiO 2 nanocomposites, Compos. Part B Eng. 43 (2012) 1374–1381. doi:10.1016/j.compositesb.2011.11.023.

[112] D.L. Tran, V.G. Nguyen, H.T. Tran, H. Thai, D.H. Mai, M.T. Vu, Effect of titanium dioxide on the properties of polyethylene/TiO2 nanocomposites, Compos. Part B Eng. 45 (2012) 1192–1198. doi:10.1016/j.compositesb.2012.09.058.

[113] K. Nakane, T. Kurita, T. Ogihara, N. Ogata, Properties of poly(vinyl butyral)/TiO2 nanocomposites formed by sol - Gel process, Compos. Part B Eng. 35 (2004) 219–222. doi:10.1016/S1359-8368(03)00066-0.

[114] Y. Chen, A. Lin, F. Gan, Improvement of polyacrylate coating by filling modified nano-TiO2, Appl. Surf. Sci. 252 (2006) 8635–8640. doi:10.1016/j.apsusc.2005.11.083.

[115] N. Patra, M. Salerno, P.D. Cozzoli, A.C. Barone, L. Ceseracciu, F. Pignatelli, R. Carzino, L. Marini, A. Athanassiou, Thermal and mechanical characterization of poly(methyl methacrylate) nanocomposites filled with TiO2nanorods, Compos. Part B Eng. 43 (2012) 3114–3119. doi:10.1016/j.compositesb.2012.04.028.

[116] M. Hussain, Y. Oku, A. Nakahira, K. Niihara, Effects of wet ball-milling on particle dispersion and mechanical properties of particulate epoxy composites, Mater. Lett. 26 (1996) 177–184. doi:10.1016/0167-577X(95)00223-5.

[117] D.K. Shukla, S. V. Kasisomayajula, V. Parameswaran, Epoxy composites using functionalized alumina platelets as reinforcements, Compos. Sci. Technol. 68 (2008) 3055–3063. doi:10.1016/j.compscitech.2008.06.025.

[118] F. El-Tantawy, K. Kamada, H. Ohnabe, In situ network structure, electrical and thermal properties of conductive epoxy resin-carbon black composites for electrical heater applications, Mater. Lett. 56 (2002) 112–126. doi:10.1016/S0167-577X(02)00401-9.

[119] F. El-Tantawy, K. Kamada, H. Ohnabe, A novel way of enhancing the electrical and thermal stability of conductive epoxy resin-carbon black composites via the Joule heating effect for heating-element applications, J. Appl. Polym. Sci. 87 (2003) 97–109. doi:10.1002/app.10851.

[120] V.G. Nguyen, H. Thai, D.H. Mai, H.T. Tran, D.L. Tran, M.T. Vu, Effect of titanium dioxide on the properties of polyethylene/TiO2 nanocomposites, Compos. Part B Eng. 45 (2013) 1192–1198. doi:10.1016/J.COMPOSITESB.2012.09.058.

[121] S.K. Jain, R. Gupta, S. Chandra, Evaluation of acoustical characteristics of ultrasonic transducer backing materials at high hydrostatic pressures, Ultrasonics. 36 (1998) 37–40. doi:10.1016/S0041-624X(97)00153-4.

[122] R.P. Singh, M. Zhang, D. Chan, Toughening of a brittle thermosetting polymer: Effects of reinforcement particle size and volume fraction, J. Mater. Sci. 37 (2002) 781–788. doi:10.1023/A:1013844015493.

[123] B. Wetzel, F. Haupert, K. Friedrich, M.Q. Zhang, M.Z. Rong, Mechanical and Tribological

Properties of Microparticulate and Nanopaticulate Reinforced Polymer Composites, Iccm. (2013) 1–10. http://www.iccm-central.org/Proceedings/ICCM13proceedings/SITE/PAPERS/Paper-1021.pdf (accessed August 20, 2019).

[124] G. Liu, H.G. Yang, J. Pan, Y.Q. Yang, G.Q.M. Lu, H.M. Cheng, Titanium dioxide crystals with tailored facets, Chem. Rev. 114 (2014) 9559–9612. doi:10.1021/cr400621z.

[125] J. Deng, L.Y. Lim, W. Li, Z. Jiang, Y. Lai, D. Gong, Y. Zhang, J. Huang, Z. Chen, Y. Tang, Correction: Titanate and titania nanostructured materials for environmental and energy applications: a review, RSC Adv. 5 (2015) 82632–82632. doi:10.1039/c5ra90088c.

[126] D.Y. Wang, Y.P. Song, J.S. Wang, X.G. Ge, Y.Z. Wang, A.A. Stec, T. Richard Hull, Double in situ approach for the preparation of polymer nanocomposite with multi-functionality, Nanoscale Res. Lett. 4 (2009) 303–306. doi:10.1007/s11671-008-9242-1.

[127] B. Bittmann, F. Haupert, A.K. Schlarb, Preparation of TiO2/epoxy nanocomposites by ultrasonic dispersion and their structure property relationship, Ultrason. Sonochem. 18 (2011) 120–126. doi:10.1016/j.ultsonch.2010.03.011.

[128] A. Chatterjee, M.S. Islam, Fabrication and characterization of TiO2-epoxy nanocomposite, Mater. Sci. Eng. A. 487 (2008) 574–585. doi:10.1016/j.msea.2007.11.052.

[129] L. Chang, Z. Zhang, C. Breidt, K. Friedrich, Tribological properties of epoxy nanocomposites I. Enhancement of the wear resistance by nano-TiO2 particles, in: Wear, Elsevier, 2005: pp. 141–148. doi:10.1016/j.wear.2004.09.005.

[130] G. Du, J.J. Wang, The mechanical properties of surface treated UHMWPE fibers and TiO2 reinforced PMMA composite, Surf. Interface Anal. 49 (2017) 940–944. doi:10.1002/sia.6247.

[131] J.L. Yang, Z. Zhang, H. Zhang, The essential work of fracture of polyamide 66 filled with TiO2 nanoparticles, Compos. Sci. Technol. 65 (2005) 2374–2379. doi:10.1016/j.compscitech.2005.06.008.

[132] X. Yinghong, W. Xin, Y. Xujie, L. Lude, Nanometre-sized TiO2 as applied to the modification of unsaturated polyester resin, Mater. Chem. Phys. 77 (2003) 609–611. doi:10.1016/S0254-0584(02)00114-1.

[133] J.W. Zha, Z.M. Dang, T. Zhou, H.T. Song, G. Chen, Electrical properties of TiO2-filled polyimide nanocomposite films prepared via an in situ polymerization process, Synth. Met. 160 (2010) 2670–2674. doi:10.1016/j.synthmet.2010.10.024.

[134] Y.H. Park, S.H. Jeong, S.M. Yi, B.H. Choi, Y.R. Kim, I.K. Kim, M.K. Kim, S.W. Son, Analysis for the potential of polystyrene and TiO 2 nanoparticles to induce skin irritation, phototoxicity, and sensitization, Toxicol. Vitr. 25 (2011) 1863–1869. doi:10.1016/j.tiv.2011.05.022.

[135] H. Salehian, S.A. Jenabali Jahromi, Effect of titanium dioxide nanoparticles on mechanical properties of vinyl ester-based nanocomposites, J. Compos. Mater. 49 (2015) 2365–2373. doi:10.1177/0021998314546140.

[136] M.H.B. and N.G. Cagri Uzay, Impact Energy Absorption Capacity of Fiber Reinforced Polymer Matrix (FRP) Composites, in: Conf. Int. J. Arts Sci., 2016: pp. 211–220. https://ssrn.com/abstract=2782304 (accessed August 21, 2019).

[137] D. Garcia-Gonzalez, M. Rodriguez-Millan, A. Rusinek, A. Arias, Low temperature effect on impact energy absorption capability of PEEK composites, Compos. Struct. 134 (2015) 440–449. doi:10.1016/j.compstruct.2015.08.090.

[138] M. Aktaş, C. Atas, B.M. Içten, R. Karakuzu, An experimental investigation of the impact response of composite laminates, Compos. Struct. 87 (2009) 307–313. doi:10.1016/j.compstruct.2008.02.003.

[139] E. V. González, P. Maimí, P.P. Camanho, C.S. Lopes, N. Blanco, Effects of ply clustering in laminated composite plates under low-velocity impact loading, Compos. Sci. Technol. 71 (2011) 805–817. doi:10.1016/j.compscitech.2010.12.018.

[140] E. V. González, P. Maimí, J.R. Sainz de Aja, P. Cruz, P.P. Camanho, Effects of interply hybridization on the damage resistance and tolerance of composite laminates, Compos. Struct. 108 (2014) 319–331. doi:10.1016/j.compstruct.2013.09.037.

[141] Y. Liv, G. Guillamet, J. Costa, E. V. González, L. Marín, J.A. Mayugo, Experimental study into compression after impact strength of laminates with conventional and nonconventional ply orientations, Compos. Part B Eng. 126 (2017) 133–142. doi:10.1016/j.compositesb.2017.05.074.

[142] N.H. Nash, T.M. Young, P.T. McGrail, W.F. Stanley, Inclusion of a thermoplastic phase to improve impact and post-impact performances of carbon fibre reinforced thermosetting composites - A review, Mater. Des. 85 (2015) 582–597. doi:10.1016/j.matdes.2015.07.001.

[143] S. Sihn, R.Y. Kim, K. Kawabe, S.W. Tsai, Experimental studies of thin-ply laminated composites, Compos. Sci. Technol. 67 (2007) 996–1008. doi:10.1016/j.compscitech.2006.06.008.

[144] R. Amacher, J. Cugnoni, J. Botsis, L. Sorensen, W. Smith, C. Dransfeld, Thin ply composites: Experimental characterization and modeling of size-effects, Compos. Sci. Technol. 101 (2014) 121–132. doi:10.1016/j.compscitech.2014.06.027.

[145] J. Renart, G. Guillamet, P. Linde, J. Costa, J.A. Mayugo, A. Turon, Damage occurrence at edges of non-crimp-fabric thin-ply laminates under off-axis uniaxial loading, Compos. Sci. Technol. 98 (2014) 44–50. doi:10.1016/j.compscitech.2014.04.014.

[146] Y.C. Ho, H. Sasayama, J. Yanagimoto, Mechanical properties and drawing process of multilayer carbon-fiber-reinforced plastic sheets with various prepreg thicknesses, Adv. Mech. Eng. 9 (2017). doi:10.1177/1687814017692695.

[147] G.J. Dvorak, N. Laws, Analysis of Progressive Matrix Cracking In Composite Laminates II. First Ply Failure, J. Compos. Mater. 21 (1987) 309–329. doi:10.1177/002199838702100402.

[148] A. Arteiro, G. Catalanotti, A.R. Melro, P. Linde, P.P. Camanho, Micro-mechanical analysis of the in situ effect in polymer composite laminates, Compos. Struct. 116 (2014) 827–840. doi:10.1016/j.compstruct.2014.06.014.

[149] P.P. Camanho, P. Linde, A. Arteiro, G. Catalanotti, A.R. Melro, Micro-mechanical analysis of the effect of ply thickness on the transverse compressive strength of polymer composites, Compos. Part A Appl. Sci. Manuf. 79 (2015) 127–137. doi:10.1016/j.compositesa.2015.09.015.

[150] B.M. Dheya, F.M. Hussien, I.G. Dway, Studying the Impact Strength of (Epoxy with TiO 2 and MgO) Composite, Eng. Technol. J. 29 (2011) 1971–1978. https://www.iasj.net/iasj?func=fulltext&aId=31870 (accessed August 7, 2019).

[151] H. Runqin, N. Fenglian, C. Qiuxiang, Mechanical properties of TiO 2-filled CNT/PMMA composites, J. Exp. Nanosci. 12 (2017) 308–318. doi:10.1080/17458080.2017.1335889.

[152] J. Di, C. Chunhua, W. Jie, Effect of TiO2 deposition on the mechanical properties of a carbon-fiber-reinforced bismaleimide composite, Mech. Compos. Mater. 49 (2013) 261–266.

doi:10.1007/s11029-013-9342-6.

[153] E. Džunuzović, V. Vodnik, K. Jeremić, J.M. Nedeljković, Thermal properties of PS/TiO2 nanocomposites obtained by in situ bulk radical polymerization of styrene, Mater. Lett. 63 (2009) 908–910. doi:10.1016/j.matlet.2009.01.039.

[154] S.K. Singh, S. Singh, A. Kumar, A. Jain, Thermo-mechanical behavior of TiO2 dispersed epoxy composites, Eng. Fract. Mech. 184 (2017) 241–248. doi:10.1016/j.engfracmech.2017.09.005.

[155] J. Zhang, S. Deng, Y. Wang, L. Ye, L. Zhou, Z. Zhang, Effect of nanoparticles on interfacial properties of carbon fibre-epoxy composites, Compos. Part A Appl. Sci. Manuf. 55 (2013) 35–44. doi:10.1016/j.compositesa.2013.08.005.

[156] S. Mallakpour, P. Asadi, Synthesis and structural characterization of novel bionanocomposite poly(ester-imide)s containing TiO 2 nanoparticles, S-valine, and L-tyrosine amino acids moieties, Polym. Bull. 68 (2012) 53–67. doi:10.1007/s00289-011-0519-7.

[157] M. Dinari, A. Haghighi, Surface modification of TiO2 nanoparticle by three dimensional silane coupling agent and preparation of polyamide/modified- TiO2 nanocomposites for removal of Cr (VI) from aqueous solutions, Prog. Org. Coatings. 110 (2017) 24–34. doi:10.1016/j.porgcoat.2017.04.044.

[158] M. Iijima, M. Kobayakawa, H. Kamiya, Tuning the stability of TiO2 nanoparticles in various solvents by mixed silane alkoxides, J. Colloid Interface Sci. 337 (2009) 61–65. doi:10.1016/j.jcis.2009.05.007.

[159] F. Lin, Preparation and Characterization of Polymer TiO 2 Nanocomposites via In-situ Polymerization, 2006. https://pdfs.semanticscholar.org/caf4/fd28ace7cd9422132e9a4ab4eaf3ba95fc24.pdf (accessed August 7, 2019).

[160] D.H. (David H. Solomon, D.G. (David G. Hawthorne, Chemistry of pigments and fillers, Wiley, 1983. https://books.google.com.gh/books/about/Chemistry_of_pigments_and_fillers.html?id=gPlTAAAAMAAJ&redir_esc=y (accessed August 20, 2019).

[161] V.E. Henrich, P.A. Cox, The surface science of metal oxides, Cambridge University Press, 1994. https://books.google.com.gh/books/about/The_Surface_Science_of_Metal_Oxides.html?id=xzVhQgAACAAJ&redir_esc=y (accessed August 20, 2019).

[162] U. Diebold, The surface science of titanium dioxide, Surf. Sci. Rep. 48 (2003) 53–229. doi:10.1016/S0167-5729(02)00100-0.

[163] A. Voet, REINFORCEMENT OF ELASTOMERS BY FILLERS: REVIEW OF PERIOD 1967-1976., J. Polym. Sci. Macromol. Rev. 15 (1980) 327–373. doi:10.1002/pol.1980.230150107.

[164] B. Xiang, G. Jiang, J. Zhang, Surface modification of TiO2 nanoparticles with silane coupling agent for nanocomposite with poly(butyl acrylate), Plast. Rubber Compos. 44 (2015) 148–154. doi:10.1179/1743289815Y.0000000007.

[165] M.A. Neouze, U. Schubert, Surface modification and functionalization of metal and metal oxide nanoparticles by organic ligands, Monatshefte Fur Chemie. 139 (2008) 183–195. doi:10.1007/s00706-007-0775-2.

[166] Y. Djaoued, S. Badilescu, P.V. Ashrit, D. Bersani, P.P. Lottici, R. Brüning, Low Temperature

Sol-Gel Preparation of Nanocrystalline TiO2 Thin Films, J. Sol-Gel Sci. Technol. 24 (2002) 247–254. doi:10.1023/A:1015305328932.

[167] E.P. Plueddemann, Silane Coupling Agents, 2nd ed., Plenum Press, New York, 1991. doi:10.1007/978-1-4899-2070-6.

[168] D.I. Tee, M. Mariatti, A. Azizan, C.H. See, K.F. Chong, Effect of silane-based coupling agent on the properties of silver nanoparticles filled epoxy composites, Compos. Sci. Technol. 67 (2007) 2584–2591. doi:10.1016/j.compscitech.2006.12.007.

[169] J.P. Matinlinna, L.V.J. Lassila, M. Ozcan, A. Yli-Urpo, P.K. Vallittu, An introduction to silanes and their clinical applications in dentistry., Int. J. Prosthodont. 17 (2004) 155–64. http://www.ncbi.nlm.nih.gov/pubmed/15119865 (accessed August 20, 2019).

[170] K.L. Mittal, Silanes and other coupling agents, 2004. https://books.google.com.gh/books?id=5JrlC5Cs6xIC&pg=PA49&lpg=PA49&dq=Mittal,+K.+L.+(1992).+Silane+and+Other+Coupling+Agents,&source=bl&ots=75Gjw3vwu1&sig=ACfU3U0MOGTy1QUL2ax13hYpctNKci4U0g&hl=en&sa=X&ved=2ahUKEwjwiIefpZLkAhX4SRUIHZoIAf8Q6AEwBnoECAkQAQ#v= (accessed August 20, 2019).

[171] M.W. Daniels, L.F. Francis, Silane adsorption behavior, microstructure, and properties of glycidoxypropyltrimethoxysilane-modified colloidal silica coatings, J. Colloid Interface Sci. 205 (1998) 191–200. doi:10.1006/jcis.1998.5671.

[172] S. Shokoohi, A. Aref Azar, Effect of coupling agents on polymer-filler surface interactions, morphology and properties of fiber-reinforced thermoplastics, J. Reinf. Plast. Compos. 28 (2009) 2131–2142. doi:10.1177/0731684408091705.

[173] M. Abdelmouleh, S. Boufi, M.N. Belgacem, A. Dufresne, A. Gandini, Modification of cellulose fibers with functionalized silanes: Effect of the fiber treatment on the mechanical performances of cellulose-thermoset composites, J. Appl. Polym. Sci. 98 (2005) 974–984. doi:10.1002/app.22133.

[174] M. Abdelmouleh, S. Boufi, A. Ben Salah, M.N. Belgacem, A. Gandini, Interaction of silane coupling agents with cellulose, Langmuir. 18 (2002) 3203–3208. doi:10.1021/la011657g.

[175] M. Hashimoto, H. Takadama, M. Mizuno, T. Kokubo, Enhancement of mechanical strength of TiO2/high-density polyethylene composites for bone repair with silane-coupling treatment, Mater. Res. Bull. 41 (2006) 515–524. doi:10.1016/j.materresbull.2005.09.014.

[176] B. Chmielewska, L. Czarnecki, J. Sustersic, A. Zajc, The influence of silane coupling agents on the polymer mortar, Cem. Concr. Compos. 28 (2006) 803–810. doi:10.1016/j.cemconcomp.2006.04.005.

[177] Z. Demjén, B. Pukánszky, E. Földes, J. Nagy, Interaction of silane coupling agents with CaCO3, J. Colloid Interface Sci. 190 (1997) 427–436. doi:10.1006/jcis.1997.4894.

[178] E.P. Plueddemann, H.A. Clark, L.E. Nelson, K.R. Hoffmann, Silane coupling agents for reinforced plastics, Mod. Plast. 39 (1962).

[179] C. Kaynak, C. Celikbilek, G. Akovali, Use of silane coupling agents to improve epoxy-rubber interface, Eur. Polym. J. 39 (2003) 1125–1132. doi:10.1016/S0014-3057(02)00381-6.

[180] A. Tezvergil, L.V.J. Lassila, A. Yli-Urpo, P.K. Vallittu, Repair bond strength of restorative resin composite applied to fiber-reinforced composite substrate., Acta Odontol. Scand. 62 (2004) 51–60. http://www.ncbi.nlm.nih.gov/pubmed/15124783 (accessed August 20, 2019).

[181] E. Ho, M. Marcolongo, Effect of coupling agents on the local mechanical properties of

bioactive dental composites by the nano-indentation technique, Dent. Mater. 21 (2005) 656–664. doi:10.1016/j.dental.2004.09.002.

[182] C. Goracci, O. Raffaelli, F. Monticelli, B. Balleri, E. Bertelli, M. Ferrari, The adhesion between prefabricated FRC posts and composite resin cores: Microtensile bond strength with and without post-silanization, Dent. Mater. 21 (2005) 437–444. doi:10.1016/j.dental.2004.07.012.

[183] B. Zewde, P. Pitliya, D. Raghavan, The role of surface modified TiO2 nanoparticles on the mechanical and thermal properties of CTBN toughened epoxy nanocomposite, J. Mater. Sci. 51 (2016) 9314–9329. doi:10.1007/s10853-016-0179-y.

[184] C.T. Dinh, T.D. Nguyen, F. Kleitz, T.O. Do, Shape-controlled synthesis of highly crystalline titania nanocrystals, ACS Nano. 3 (2009) 3737–3743. doi:10.1021/nn900940p.

[185] Y.R. De Miguel, A. Ahniyaz, B. Faure, I. Villaluenga, G. Salazar-Alvarez, G. Berriozabal, L. Bergström, Dispersion and surface functionalization of oxide nanoparticles for transparent photocatalytic and UV-protecting coatings and sunscreens, Sci. Technol. Adv. Mater. 14 (2013) 023001. doi:10.1088/1468-6996/14/2/023001.

[186] J. Zhao, M. Milanova, M.M.C.G. Warmoeskerken, V. Dutschk, Surface modification of TiO2 nanoparticles with silane coupling agents, Colloids Surfaces A Physicochem. Eng. Asp. 413 (2012) 273–279. doi:10.1016/j.colsurfa.2011.11.033.

[187] R. Tomovska, V. Daniloska, J.M. Asua, Surface modification of TiO 2 nanoparticles via photocataliticaly induced reaction: Influence of functionality of silane coupling agent, Appl. Surf. Sci. 264 (2013) 670–673. doi:10.1016/j.apsusc.2012.10.091.

[188] A.R.M. Dalod, O.G. Grendal, S.L. Skjærvø, K. Inzani, S.M. Selbach, L. Henriksen, W. Van Beek, T. Grande, M.A. Einarsrud, Controlling Oriented Attachment and in Situ Functionalization of TiO2 Nanoparticles during Hydrothermal Synthesis with APTES, J. Phys. Chem. C. 121 (2017) 11897–11906. doi:10.1021/acs.jpcc.7b02604.

[189] T.W. Chou, L. Gao, E.T. Thostenson, Z. Zhang, J.H. Byun, An assessment of the science and technology of carbon nanotube-based fibers and composites, Compos. Sci. Technol. 70 (2010) 1–19. doi:10.1016/j.compscitech.2009.10.004.

[190] P.M. Ajayan, L.S. Schadler, C. Giannaris, A. Rubio, Single-walled carbon nanotube-polymer composites: Strength and weakness, Adv. Mater. 12 (2000) 750–753. doi:10.1002/(SICI)1521-4095(200005)12:10<750::AID-ADMA750>3.0.CO;2-6.

[191] A.M.K. Esawi, M.M. Farag, Carbon nanotube reinforced composites: Potential and current challenges, Mater. Des. 28 (2007) 2394–2401. doi:10.1016/j.matdes.2006.09.022.

[192] M. Šupová, G.S. Martynková, K. Barabaszová, Effect of Nanofillers Dispersion in Polymer Matrices: A Review, Sci. Adv. Mater. 3 (2011) 1–25. doi:10.1166/sam.2011.1136.

[193] J. Jancar, J.F. Douglas, F.W. Starr, S.K. Kumar, P. Cassagnau, A.J. Lesser, S.S. Sternstein, M.J. Buehler, Current issues in research on structure-property relationships in polymer nanocomposites, Polymer (Guildf). 51 (2010) 3321–3343. doi:10.1016/j.polymer.2010.04.074.

[194] D. Qian, E.C. Dickey, R. Andrews, T. Rantell, Load transfer and deformation mechanisms in carbon nanotube-polystyrene composites, Appl. Phys. Lett. 76 (2000) 2868–2870. doi:10.1063/1.126500.

[195] F.H. Gojny, M.H.G. Wichmann, B. Fiedler, K. Schulte, Influence of different carbon nanotubes on the mechanical properties of epoxy matrix composites - A comparative study, Compos. Sci. Technol. 65 (2005) 2300–2313. doi:10.1016/j.compscitech.2005.04.021.

[196] J. Tsai, C.T. Sun, Effect of Platelet Dispersion on the Load Transfer Efficiency in Nanoclay Composites, J. Compos. Mater. 38 (2004) 567–579. doi:10.1177/0021998304042397.

[197] J. Vera-Agullo, A. Glória-Pereira, H. Varela-Rizo, J.L. Gonzalez, I. Martin-Gullon, Comparative study of the dispersion and functional properties of multiwall carbon nanotubes and helical-ribbon carbon nanofibers in polyester nanocomposites, Compos. Sci. Technol. 69 (2009) 1521–1532. doi:10.1016/j.compscitech.2008.11.032.

[198] K.P. Ryan, M. Cadek, V. Nicolosi, D. Blond, M. Ruether, G. Armstrong, H. Swan, A. Fonseca, J.B. Nagy, W.K. Maser, W.J. Blau, J.N. Coleman, Carbon nanotubes for reinforcement of plastics? A case study with poly(vinyl alcohol), Compos. Sci. Technol. 67 (2007) 1640–1649. doi:10.1016/j.compscitech.2006.07.006.

[199] J. Hong, J. Lee, C.K. Hong, S.E. Shim, Effect of dispersion state of carbon nanotube on the thermal conductivity of poly(dimethyl siloxane) composites, Curr. Appl. Phys. 10 (2010) 359–363. doi:10.1016/j.cap.2009.06.028.

[200] S. Wang, R. Liang, B. Wang, C. Zhang, Dispersion and thermal conductivity of carbon nanotube composites, Carbon N. Y. 47 (2009) 53–57. doi:10.1016/j.carbon.2008.08.024.

[201] G. Gorrasi, M. Tortora, V. Vittoria, E. Pollet, B. Lepoittevin, M. Alexandre, P. Dubois, Vapor barrier properties of polycaprolactone montmorillonite nanocomposites: Effect of clay dispersion, Polymer (Guildf). 44 (2003) 2271–2279. doi:10.1016/S0032-3861(03)00108-3.

[202] T. Glaskova, M. Zarrelli, A. Aniskevich, M. Giordano, L. Trinkler, B. Berzina, Quantitative optical analysis of filler dispersion degree in MWCNT-epoxy nanocomposite, Compos. Sci. Technol. 72 (2012) 477–481. doi:10.1016/j.compscitech.2011.11.029.

[203] T. Kashiwagi, J. Fagan, J.F. Douglas, K. Yamamoto, A.N. Heckert, S.D. Leigh, J. Obrzut, F. Du, S. Lin-Gibson, M. Mu, K.I. Winey, R. Haggenmueller, Relationship between dispersion metric and properties of PMMA/SWNT nanocomposites, Polymer (Guildf). 48 (2007) 4855–4866. doi:10.1016/j.polymer.2007.06.015.

[204] J.Z. Kovacs, K. Andresen, J.R. Pauls, C.P. Garcia, M. Schossig, K. Schulte, W. Bauhofer, Analyzing the quality of carbon nanotube dispersions in polymers using scanning electron microscopy, Carbon N. Y. 45 (2007) 1279–1288. doi:10.1016/j.carbon.2007.01.012.

[205] P.T. Lillehei, J.-W. Kim, L.J. Gibbons, C. Park, A quantitative assessment of carbon nanotube dispersion in polymer matrices, Nanotechnology. 20 (2009) 325708. doi:10.1088/0957-4484/20/32/325708.

[206] H. Jinnai, Transmission electron microtomography in polymer research, Polymer (Guildf). 50 (2009) 1067–1087. doi:10.1016/j.polymer.2008.12.023.

[207] S. V Kalinin, S. Jesse, J. Shin, A.P. Baddorf, M.A. Guillorn, D.B. Geohegan, Scanning probe microscopy imaging of frequency dependent electrical transport through carbon nanotube networks in polymers, Nanotechnology. 15 (2004) 907–912. doi:10.1088/0957-4484/15/8/006.

[208] A. Trionfi, D.A. Scrymgeour, J.W.P. Hsu, M.J. Arlen, D. Tomlin, J.D. Jacobs, D.H. Wang, L.-S. Tan, R.A. Vaia, Direct imaging of current paths in multiwalled carbon nanofiber polymer nanocomposites using conducting-tip atomic force microscopy, J. Appl. Phys. 104 (2008) 083708. doi:10.1063/1.3000458.

[209] N. Izard, D. Riehl, E. Anglaret, Exfoliation of single-wall carbon nanotubes in aqueous surfactant suspensions: A Raman study, Phys. Rev. B. 71 (2005) 195417. doi:10.1103/PhysRevB.71.195417.

[210] J. Yu, N. Grossiord, C.E. Koning, J. Loos, Controlling the dispersion of multi-wall carbon

nanotubes in aqueous surfactant solution, Carbon N. Y. 45 (2007) 618–623. doi:10.1016/j.carbon.2006.10.010.

[211] V. Georgakilas, A. Bourlinos, D. Gournis, T. Tsoufis, C. Trapalis, A. Mateo-Alonso, M. Prato, Multipurpose Organically Modified Carbon Nanotubes: From Functionalization to Nanotube Composites, J. Am. Chem. Soc. 130 (2008) 8733–8740. doi:10.1021/ja8002952.

[212] M.J. O'Connell, Band Gap Fluorescence from Individual Single-Walled Carbon Nanotubes, Science (80-.). 297 (2002) 593–596. doi:10.1126/science.1072631.

[213] G.A. Moore, Is quantitative metallography quantitative?Applications of Modern Metallographic Techniques, in: W.D. Forgeng, L.J. Toman (Eds.), ASTM STP 480, American Society forTesting and Materials, Philadelphia, Pennsylvania, 1970: pp. 3–48.

[214] B.M. Tyson, R.K. Abu Al-Rub, A. Yazdanbakhsh, Z. Grasley, A quantitative method for analyzing the dispersion and agglomeration of nano-particles in composite materials, Compos. Part B Eng. 42 (2011) 1395–1403. doi:10.1016/j.compositesb.2011.05.020.

[215] W.R. Broughton, T. Koukoulas, P. Woolliams, J. Williams, S.S. Rahatekar, Assessment of nanoparticle loading and dispersion in polymeric materials using optical coherence tomography, Polym. Test. 32 (2013) 1290–1298. doi:10.1016/j.polymertesting.2013.08.004.

[216] J. Kadhim Oleiwi, A. Namah Hadi, Design of Prosthetic Foot from Polymer Materials Reinforced by Carbon Fibers, Eng. Technol. J. . (2016).

[217] D.A. Berry, Composite Materials for Orthotics and Prosthetics, J. Prosthetists Orthot. (1987).

[218] R.J. Coguill, D.F. Adams, Selection of the proper wedge grip surface for tensile testing composite materials, in: Int. SAMPE Symp. Exhib., 1999. http://www.scopus.com/inward/record.url?eid=2-s2.0-0033309663&partnerID=tZOtx3y1.

[219] D. Adams, Tabbing composite test specimens: When and why, High-Performance Compos. 19 (2011).

[220] L.. Hart-Smith, Mechanically-Fastened Joints for Advanced Composites -Phenomenological Consideration and Simple Analyses, in: E.M. Lenoe, D.W. Oplinger, J.J. Burke (Eds.), Fourth Conf. Fibrous Compos. Struct. Des., Plenum Press, San Diego, CA, USA, 1978: pp. 543–574.

[221] J.M. Hodgkinson, Mechanical testing of advanced fibre composites, CRC Press, 2000.

[222] P.J. Joyce, M.G. Violette, T.J. Moon, Finite element analysis of unidirectional composite compression test specimens: A parametric study, Compos. Mater. Testing, Des. Accept. Criteria. 1416 (2002) 30–68. doi:Doi 10.1520/Stp10630s.

[223] ASTM International, ASTM D3039/D3039M-14 Standard Test Method for Tensile Properties of Polymer Matrix Composite Materials, Annu. B. ASTM Stand. (2014) 1–13. doi:10.1520/D3039.

[224] ASTM D5083 - 17, ASTM D5083 - 17 Standard Test Method for Tensile Properties of Reinforced Thermosetting Plastics Using Straight-Sided Specimens, (n.d.). https://www.astm.org/Standards/D5083.htm (accessed September 28, 2017).

[225] ISO 527-1:2012, ISO 527-1:2012 - Plastics -- Determination of tensile properties -- Part 1: General principles, (n.d.). https://www.iso.org/standard/56045.html (accessed September 28, 2017).

[226] S.R. Wisnom, M. R., Khan, B., Hallett, Size effects in unnotched tensile strength of unidirectional and quasi-isotropic carbon/epoxy composites, Compos. Struct. 84 (2008) 21–28.

doi:10.1016/J.COMPSTRUCT.2007.06.002.

[227] M.R. Wisnom, J.W. Atkinson, Reduction in tensile and flexural strength of unidirectional glass fibre-epoxy with increasing specimen size, Compos. Struct. 38 (1997) 405–411. doi:10.1016/S0263-8223(97)00075-5.

[228] P. Potluri, S. Sharma, R. Ramgulam, Comprehensive drape modelling for moulding 3D textile preforms, Compos. - Part A Appl. Sci. Manuf. 32 (2001) 1415–1424. doi:10.1016/S1359-835X(01)00040-9.

[229] S.G. Hancock, K.D. Potter, The use of kinematic drape modelling to inform the hand lay-up of complex composite components using woven reinforcements, Compos. Part A Appl. Sci. Manuf. 37 (2006) 413–422. doi:10.1016/j.compositesa.2005.05.044.

[230] K. Vanclooster, Forming of multilayered fabric reinforced thermoplastic composites, 2009.

[231] F.J. Schirmaier, D. Dörr, F. Henning, L. Kärger, A macroscopic approach to simulate the forming behaviour of stitched unidirectional non-crimp fabrics (UD-NCF), Compos. Part A Appl. Sci. Manuf. 102 (2017) 322–335. doi:10.1016/j.compositesa.2017.08.009.

[232] B. Ben Boubaker, B. Haussy, J.-F. Ganghoffer, Discrete models of fabric accounting for yarn interactions, Rev. Eur. Des Éléments Finis. 14 (2007) 653–675. doi:10.3166/reef.14.653-675.

[233] A.A. Skordos, C. Monroy Aceves, M.P.F. Sutcliffe, A simplified rate dependent model of forming and wrinkling of pre-impregnated woven composites, Compos. Part A Appl. Sci. Manuf. 38 (2007) 1318–1330. doi:10.1016/j.compositesa.2006.11.005.

[234] P. Badel, E. Vidal-Sallé, P. Boisse, Computational determination of in-plane shear mechanical behaviour of textile composite reinforcements, Comput. Mater. Sci. 40 (2007) 439–448. doi:10.1016/j.commatsci.2007.01.022.

[235] P. Badel, E. Vidal-Sallé, P. Boisse, Large deformation analysis of fibrous materials using rate constitutive equations, Comput. Struct. 86 (2008) 1164–1175. doi:10.1016/j.compstruc.2008.01.009.

[236] F. Fritz, A. Oeckerath, D. Magagnato, A. Schön, L. Kärger, F. Henning, S. Galkin, A. Bernath, Development and validation of a CAE chain for unidirectional fibre reinforced composite components, Compos. Struct. 132 (2015) 350–358. doi:10.1016/j.compstruct.2015.05.047.

[237] F. Härtel, P. Böhler, P. Middendorf, An Integral Mesoscopic Material Characterization Approach, Key Eng. Mater. 611–612 (2014) 280–291. doi:10.4028/www.scientific.net/kem.611-612.280.

[238] G. Creech, A.K. Pickett, Meso-modelling of Non-crimp Fabric composites for coupled drape and failure analysis, J. Mater. Sci. 41 (2006) 6725–6736. doi:10.1007/s10853-006-0213-6.

[239] N. Hamila, P. Boisse, Simulations of textile composite reinforcement draping using a new semi-discrete three node finite element, Compos. Part B Eng. 39 (2008) 999–1010. doi:10.1016/j.compositesb.2007.11.008.

[240] N. Hamila, P. Boisse, S. Chatel, Semi-discrete shell finite elements for textile composite forming simulation, Int. J. Mater. Form. 2 (2009) 169–172. doi:10.1007/s12289-009-0518-5.

[241] S. Bel, N. Hamila, P. Boisse, F. Dumont, Finite element model for NCF composite reinforcement preforming: Importance of inter-ply sliding, Compos. Part A Appl. Sci. Manuf. 43 (2012) 2269–2277. doi:10.1016/j.compositesa.2012.08.005.

[242] J. HUETINK, On Anisotropy , Objectivity and Invariancy in finite thermo – mechanical

deformations, in: 9th Int. ESAFORM Conf. Mater. Form., 2006: pp. 355–358. http://doc.utwente.nl/59600/1/esaform2006_huetink.pdf.

[243] Y. Aimène, E. Vidal-Sallé, B. Hagège, F. Sidoroff, P. Boisse, A hyperelastic approach for composite reinforcement large deformation analysis, J. Compos. Mater. 44 (2010) 5–26. doi:10.1177/0021998309345348.

[244] E. Guzman-Maldonado, N. Hamila, P. Boisse, J. Bikard, Thermomechanical analysis, modelling and simulation of the forming of pre-impregnated thermoplastics composites, Compos. Part A Appl. Sci. Manuf. 78 (2015) 211–222. doi:10.1016/j.compositesa.2015.08.017.

[245] P. Badel, S. Gauthier, E. Vidal-Sallé, P. Boisse, Rate constitutive equations for computational analyses of textile composite reinforcement mechanical behaviour during forming, Compos. Part A Appl. Sci. Manuf. 40 (2009) 997–1007. doi:10.1016/j.compositesa.2008.04.015.

[246] M.A. Khan, T. Mabrouki, E. Vidal-Sallé, P. Boisse, Numerical and experimental analyses of woven composite reinforcement forming using a hypoelastic behaviour. Application to the double dome benchmark, J. Mater. Process. Technol. 210 (2010) 378–388. doi:10.1016/j.jmatprotec.2009.09.027.

[247] D. Dörr, F.J. Schirmaier, F. Henning, L. Kärger, A viscoelastic approach for modeling bending behavior in finite element forming simulation of continuously fiber reinforced composites, Compos. Part A Appl. Sci. Manuf. 94 (2017) 113–123. doi:10.1016/j.compositesa.2016.11.027.

[248] R.J. Diefendorf, High modulus carbon fibre processes, (1976) 315–323. doi:10.1021/bk-1976-0021.ch022.

[249] R. Piñero-Hernanz, C. Dodds, J. Hyde, J. García-Serna, M. Poliakoff, E. Lester, M.J. Cocero, S. Kingman, S. Pickering, K.H. Wong, Chemical recycling of carbon fibre reinforced composites in nearcritical and supercritical water, Compos. Part A Appl. Sci. Manuf. 39 (2008) 454–461. doi:10.1016/J.COMPOSITESA.2008.01.001.

[250] A.T. Serkov, M.B. Radishevskii, Status and prospects for production of carbon fibres based on polyacrylonitrile, Fibre Chem. 40 (2008) 24–31. doi:10.1007/s10692-008-9012-y.

[251] A. Jacob, European production of reinforced plastics up 6% in 2006, Reinf. Plast. 51 (2007) 38–41. doi:10.1016/S0034-3617(07)70387-9.

[252] S.R. Naqvi, H.M. Prabhakara, E.A. Bramer, W. Dierkes, R. Akkerman, G. Brem, A critical review on recycling of end-of-life carbon fibre/glass fibre reinforced composites waste using pyrolysis towards a circular economy, Resour. Conserv. Recycl. 136 (2018) 118–129. doi:10.1016/j.resconrec.2018.04.013.

[253] S.J. Pickering, T.. Turner, Research and development in support of carbon fibre recycling., in: Compos. Adv. Mater. Expo Comb. Strength. Unsurpassed Innov., 2014.

[254] E. Witten, T. Kraus, M. Kühnel, Composites Market Report 2015 Market developments, trends, outlook and challenges, 2015. www.avk-tv.de (accessed July 29, 2019).

[255] S. Zhong, J.M. Pearce, Tightening the loop on the circular economy: Coupled distributed recycling and manufacturing with recyclebot and RepRap 3-D printing, Resour. Conserv. Recycl. 128 (2018) 48–58. doi:10.1016/J.RESCONREC.2017.09.023.

[256] L.A. Akanbi, L.O. Oyedele, O.O. Akinade, A.O. Ajayi, M. Davila Delgado, M. Bilal, S.A. Bello, Salvaging building materials in a circular economy: A BIM-based whole-life performance estimator, Resour. Conserv. Recycl. 129 (2018) 175–186.

doi:10.1016/J.RESCONREC.2017.10.026.

[257] J. Kirchherr, D. Reike, M. Hekkert, Conceptualizing the circular economy: An analysis of 114 definitions, Resour. Conserv. Recycl. 127 (2017) 221–232. doi:10.1016/J.RESCONREC.2017.09.005.

[258] R. Hoogmartens, J. Eyckmans, S. Van Passel, A Hotelling model for the circular economy including recycling, substitution and waste accumulation, Resour. Conserv. Recycl. 128 (2018) 98–109. doi:10.1016/J.RESCONREC.2017.09.015.

[259] G. Oliveux, L.O. Dandy, G.A. Leeke, Current status of recycling of fibre reinforced polymers: Review of technologies, reuse and resulting properties, Prog. Mater. Sci. 72 (2015) 61–99. doi:10.1016/j.pmatsci.2015.01.004.

[260] A.M. Cunliffe, P.T. Williams, Characterisation of products from the recycling of glass fibre reinforced polyester waste by pyrolysis☆, Fuel. 82 (2003) 2223–2230. doi:10.1016/S0016-2361(03)00129-7.

[261] M. Buggy, L. Farragher, W. Madden, Recycling of composite materials, J. Mater. Process. Technol. 55 (1995) 448–456. doi:10.1016/0924-0136(95)02037-3.

[262] G. Jiang, S.J. Pickering, E.H. Lester, T.A. Turner, K.H. Wong, N.A. Warrior, Characterisation of carbon fibres recycled from carbon fibre/epoxy resin composites using supercritical n-propanol, Compos. Sci. Technol. 69 (2009) 192–198. doi:10.1016/j.compscitech.2008.10.007.

[263] A. Jacob, Composites can be recycled, Reinf. Plast. 55 (2011) 45–46. doi:10.1016/S0034-3617(11)70079-0.

[264] D.A. Baker, T.G. Rials, Recent advances in low-cost carbon fiber manufacture from lignin, J. Appl. Polym. Sci. (2013). doi:10.1002/app.39273.

[265] Y.S. Song, J.R. Youn, T.G. Gutowski, Life cycle energy analysis of fiber-reinforced composites, Compos. Part A Appl. Sci. Manuf. 40 (2009) 1257–1265. doi:10.1016/j.compositesa.2009.05.020.

[266] S. Pimenta, S.T. Pinho, Recycling carbon fibre reinforced polymers for structural applications: Technology review and market outlook, Waste Manag. 31 (2011) 378–392. doi:10.1016/j.wasman.2010.09.019.

[267] R.A. Witik, R. Teuscher, V. Michaud, C. Ludwig, J.A.E. Månson, Carbon fibre reinforced composite waste: An environmental assessment of recycling, energy recovery and landfilling, Compos. Part A Appl. Sci. Manuf. 49 (2013) 89–99. doi:10.1016/j.compositesa.2013.02.009.

[268] D.A. Steenkamer, J.L. Sullivan, On the recyclability of a cyclic thermoplastic composite material, Compos. Part B Eng. 29 (1998) 745–752. doi:10.1016/S1359-8368(98)00016-X.

[269] J. Palmer, O.R. Ghita, L. Savage, K.E. Evans, Successful closed-loop recycling of thermoset composites, Compos. Part A Appl. Sci. Manuf. 40 (2009) 490–498. doi:10.1016/J.COMPOSITESA.2009.02.002.

[270] S.J. Pickering, Recycling technologies for thermoset composite materials—current status, Compos. Part A Appl. Sci. Manuf. 37 (2006) 1206–1215. doi:10.1016/J.COMPOSITESA.2005.05.030.

[271] G. Schinner, J. Brandt, H. Richter, Recycling Carbon-Fiber-Reinforced Thermoplastic Composites, J. Thermoplast. Compos. Mater. 9 (1996) 239–245. doi:10.1177/089270579600900302.

[272] C.E. Kouparitsas, C.N. Kartalis, P.C. Varelidis, C.J. Tsenoglou, C.D. Papaspyrides, Recycling of the fibrous fraction of reinforced thermoset composites, Polym. Compos. 23 (2002) 682–689. doi:10.1002/pc.10468.

[273] K. Ogi, T. Nishikawa, Y. Okano, I. Taketa, Mechanical properties of ABS resin reinforced with recycled CFRP, Adv. Compos. Mater. 16 (2007) 181–194. doi:10.1163/156855107780918982.

[274] J. Palmer, L. Savage, O.R. Ghita, K.E. Evans, Sheet moulding compound (SMC) from carbon fibre recyclate, Compos. Part A Appl. Sci. Manuf. 41 (2010) 1232–1237. doi:10.1016/J.COMPOSITESA.2010.05.005.

[275] M.A. Nahil, P.T. Williams, Recycling of carbon fibre reinforced polymeric waste for the production of activated carbon fibres, J. Anal. Appl. Pyrolysis. 91 (2011) 67–75. doi:10.1016/j.jaap.2011.01.005.

[276] F.A. López, O. Rodríguez, F.J. Alguacil, I. García-Díaz, T.A. Centeno, J.L. García-Fierro, C. González, Recovery of carbon fibres by the thermolysis and gasification of waste prepreg, J. Anal. Appl. Pyrolysis. 104 (2013) 675–683. doi:10.1016/J.JAAP.2013.04.012.

[277] V. Marković, S. Marinković, A study of pyrolysis of phenolic resin reinforced with carbon fibres and oxidized pan fibres, Carbon N. Y. 18 (1980) 329–335. doi:10.1016/0008-6223(80)90004-4.

[278] A. Torres, I. de Marco, B.M. Caballero, M.F. Laresgoiti, J.A. Legarreta, M.A. Cabrero, A. González, M.J. Chomón, K. Gondra, Recycling by pyrolysis of thermoset composites: characteristics of the liquid and gaseous fuels obtained, Fuel. 79 (2000) 897–902. doi:10.1016/S0016-2361(99)00220-3.

[279] S. Feih, E. Boiocchi, G. Mathys, Z. Mathys, A.G. Gibson, A.P. Mouritz, Mechanical properties of thermally-treated and recycled glass fibres, Compos. Part B Eng. 42 (2011) 350–358. doi:10.1016/J.COMPOSITESB.2010.12.020.

[280] S.J. Pickering, R.M. Kelly, J.R. Kennerley, C.D. Rudd, N.J. Fenwick, A fluidised-bed process for the recovery of glass fibres from scrap thermoset composites, Compos. Sci. Technol. 60 (2000) 509–523. doi:10.1016/S0266-3538(99)00154-2.

[281] L.O. Meyer, K. Schulte, E. Grove-Nielsen, CFRP-Recycling Following a Pyrolysis Route: Process Optimization and Potentials, J. Compos. Mater. 43 (2009) 1121–1132. doi:10.1177/0021998308097737.

[282] Y. Zheng, Z. Shen, S. Ma, C. Cai, X. Zhao, Y. Xing, A novel approach to recycling of glass fibers from nonmetal materials of waste printed circuit boards, J. Hazard. Mater. 170 (2009) 978–982. doi:10.1016/J.JHAZMAT.2009.05.065.

[283] E. Lester, S. Kingman, K.H. Wong, C. Rudd, S. Pickering, N. Hilal, Microwave heating as a means for carbon fibre recovery from polymer composites: a technical feasibility study, Mater. Res. Bull. 39 (2004) 1549–1556. doi:10.1016/J.MATERRESBULL.2004.04.031.

[284] D. Åkesson, Z. Foltynowicz, J. Christéen, M. Skrifvars, Microwave pyrolysis as a method of recycling glass fibre from used blades of wind turbines:, Http://Dx.Doi.Org/10.1177/0731684412453512. (2012). doi:10.1177/0731684412453512.

[285] G. Oliveux, J.-L. Bailleul, E.L.G. La Salle, Chemical recycling of glass fibre reinforced composites using subcritical water, Compos. Part A Appl. Sci. Manuf. 43 (2012) 1809–1818. doi:10.1016/J.COMPOSITESA.2012.06.008.

[286] I. Okajima, M. Hiramatsu, Y. Shimamura, T. Awaya, T. Sako, Chemical recycling of carbon

fiber reinforced plastic using supercritical methanol, J. Supercrit. Fluids. 91 (2014) 68–76. doi:10.1016/J.SUPFLU.2014.04.011.

[287] Y. Liu, J. Liu, Z. Jiang, T. Tang, Chemical recycling of carbon fibre reinforced epoxy resin composites in subcritical water: Synergistic effect of phenol and KOH on the decomposition efficiency, Polym. Degrad. Stab. 97 (2012) 214–220. doi:10.1016/J.POLYMDEGRADSTAB.2011.12.028.

[288] C.C. Knight, C. Zeng, C. Zhang, B. Wang, Recycling of woven carbon-fibre-reinforced polymer composites using supercritical water, Environ. Technol. 33 (2012) 639–644. doi:10.1080/09593330.2011.586732.

[289] P. Yang, Q. Zhou, X.-X. Yuan, J.M.N. van Kasteren, Y.-Z. Wang, Highly efficient solvolysis of epoxy resin using poly(ethylene glycol)/NaOH systems, Polym. Degrad. Stab. 97 (2012) 1101–1106. doi:10.1016/J.POLYMDEGRADSTAB.2012.04.007.

[290] P. Xu, J. Li, J. Ding, Chemical recycling of carbon fibre/epoxy composites in a mixed solution of peroxide hydrogen and N,N-dimethylformamide, Compos. Sci. Technol. 82 (2013) 54–59. doi:10.1016/J.COMPSCITECH.2013.04.002.

[291] J.A. Onwudili, E. Yildirir, P.T. Williams, Catalytic Hydrothermal Degradation of Carbon Reinforced Plastic Wastes for Carbon Fibre and Chemical Feedstock Recovery, Waste and Biomass Valorization. 4 (2013) 87–93. doi:10.1007/s12649-013-9204-4.

[292] E. Yildirir, J.A. Onwudili, P.T. Williams, Recovery of carbon fibres and production of high quality fuel gas from the chemical recycling of carbon fibre reinforced plastic wastes, J. Supercrit. Fluids. 92 (2014) 107–114. doi:10.1016/J.SUPFLU.2014.05.015.

[293] S. Pimenta, S.T. Pinho, Recycling carbon fibre reinforced polymers for structural applications: Technology review and market outlook, Waste Manag. 31 (2011) 378–392. doi:10.1016/j.wasman.2010.09.019.

[294] A.M. Cunliffe, N. Jones, P.T. Williams, Recycling of fibre-reinforced polymeric waste by pyrolysis: thermo-gravimetric and bench-scale investigations, J. Anal. Appl. Pyrolysis. 70 (2003) 315–338. doi:10.1016/S0165-2370(02)00161-4.

[295] A. Molnar, Recycling Advanced Composites, Seattle, Washington, 1995. https://p2infohouse.org/ref/05/04014.pdf (accessed September 21, 2019).

[296] M. Roux, C. Dransfeld, N. Eguémann, L. Giger, Processing and recycling of a thermoplastic composite fibre/peek aerospace part, in: 16th Eur. Conf. Compos. Mater. ECCM 2014, Seville, Spain, 2014. http://www.escm.eu.org/eccm16/assets/0607.pdf (accessed September 21, 2019).

[297] K.H. Yoon, A.T. DiBenedetto, S.J. Huang, Recycling of unsaturated polyester resin using propylene glycol, Polymer (Guildf). 38 (1997) 2281–2285. doi:10.1016/S0032-3861(96)00951-2.

[298] P. Feraboli, H. Kawakami, B. Wade, F. Gasco, L. DeOto, A. Masini, Recyclability and reutilization of carbon fiber fabric/epoxy composites, J. Compos. Mater. 46 (2012) 1459–1473. doi:10.1177/0021998311420604.

[299] J. Li, P.-L. Xu, Y.-K. Zhu, J.-P. Ding, L.-X. Xue, Y.-Z. Wang, A promising strategy for chemical recycling of carbon fiber/thermoset composites: self-accelerating decomposition in a mild oxidative system, Green Chem. 14 (2012) 3260. doi:10.1039/c2gc36294e.

[300] I. Okajima, K. Yamada, T. Sugeta, T. Sako, Waste Treatment Technologies. Decomposition of Epoxy Resin and Recycling of CFRP with Sub- and Supercritical Water., KAGAKU KOGAKU RONBUNSHU. 28 (2002) 553–558. doi:10.1252/kakoronbunshu.28.553.

[301] K. Suyama, M. Kubota, M. Shirai, H. Yoshida, Effect of alcohols on the degradation of crosslinked unsaturated polyester in sub-critical water, Polym. Degrad. Stab. 91 (2006) 983–986. doi:10.1016/J.POLYMDEGRADSTAB.2005.08.003.

[302] W. Dang, M. Kubouchi, H. Sembokuya, K. Tsuda, Chemical recycling of glass fiber reinforced epoxy resin cured with amine using nitric acid, Polymer (Guildf). 46 (2005) 1905–1912. doi:10.1016/J.POLYMER.2004.12.035.

[303] Y. Shibasaki, J. Kadokawa, H. Tagaya, B. Hatano, C. Kato, Decomposition reactions of epoxy resin and polyetheretherketone resin in sub- and supercritical water, J. Mater. Cycles Waste Manag. 6 (2004) 1–5. doi:10.1007/s10163-003-0098-2.

[304] Y. Liu, L. Meng, Y. Huang, J. Du, Recycling of carbon/epoxy composites, J. Appl. Polym. Sci. 94 (2004) 1912–1916. doi:10.1002/app.20990.

[305] K. El Gersifi, G. Durand, G. Tersac, Solvolysis of bisphenol A diglycidyl ether/anhydride model networks, Polym. Degrad. Stab. 91 (2006) 690–702. doi:10.1016/J.POLYMDEGRADSTAB.2005.05.021.

[306] P. Kritzer, Corrosion in high-temperature and supercritical water and aqueous solutions: a review, J. Supercrit. Fluids. 29 (2004) 1–29. doi:10.1016/S0896-8446(03)00031-7.

[307] F.A. López, O. Rodríguez, F.J. Alguacil, I. García-Díaz, T.A. Centeno, J.L. García-Fierro, C. González, Recovery of carbon fibres by the thermolysis and gasification of waste prepreg, J. Anal. Appl. Pyrolysis. 104 (2013) 675–683. doi:10.1016/j.jaap.2013.04.012.

[308] L.O. Meyer, K. Schulte, E. Grove-Nielsen, CFRP-recycling following a pyrolysis route: Process optimization and potentials, in: J. Compos. Mater., 2009. doi:10.1177/0021998308097737.

[309] M.A. Nahil, P.T. Williams, Recycling of carbon fibre reinforced polymeric waste for the production of activated carbon fibres, J. Anal. Appl. Pyrolysis. 91 (2011) 67–75. doi:10.1016/j.jaap.2011.01.005.

[310] L.O. Meyer, K. Schulte, E. Grove-Nielsen, CFRP-recycling following a pyrolysis route: Process optimization and potentials, J. Compos. Mater. 43 (2009) 1121–1132. doi:10.1177/0021998308097737.

[311] L. Giorgini, T. Benelli, L. Mazzocchetti, C. Leonardi, G. Zattini, G. Minak, E. Dolcini, M. Cavazzoni, I. Montanari, C. Tosi, Recovery of carbon fibers from cured and uncured carbon fiber reinforced composites wastes and their use as feedstock for a new composite production, in: Polym. Compos., 2015. doi:10.1002/pc.23440.

[312] T.R. Abdou, D.C.R. Espinosa, J.A.S. Tenório, Recovering of Carbon Fiber Present in an Industrial Polymeric Composite Waste through Pyrolysis Method while Studying the Influence of Resin Impregnation Process: Prepreg, in: REWAS 2016, Springer International Publishing, Cham, 2016: pp. 313–318. doi:10.1007/978-3-319-48768-7_49.

[313] C. Morin, A. Loppinet-Serani, F. Cansell, C. Aymonier, Near- and supercritical solvolysis of carbon fibre reinforced polymers (CFRPs) for recycling carbon fibers as a valuable resource: State of the art, J. Supercrit. Fluids. 66 (2012) 232–240. doi:10.1016/J.SUPFLU.2012.02.001.

[314] L. Giorgini, T. Benelli, L. Mazzocchetti, C. Leonardi, G. Zattini, G. Minak, E. Dolcini, C. Tosi, I. Montanari, Pyrolysis as a way to close a CFRC life cycle: Carbon fibers recovery and their use as feedstock for a new composite production, in: AIP Conf. Proc., American Institute of Physics, 2014: pp. 354–357. doi:10.1063/1.4876851.

[315] J.A. Onwudili, N. Miskolczi, T. Nagy, G. Lipóczi, Recovery of glass fibre and carbon fibres

from reinforced thermosets by batch pyrolysis and investigation of fibre re-using as reinforcement in LDPE matrix, Compos. Part B Eng. 91 (2016) 154–161. doi:10.1016/j.compositesb.2016.01.055.

[316] A.C. Louwes, L. Basile, R. Yukananto, J.C. Bhagwandas, E.A. Bramer, G. Brem, Torrefied biomass as feed for fast pyrolysis: An experimental study and chain analysis, Biomass and Bioenergy. 105 (2017) 116–126. doi:10.1016/J.BIOMBIOE.2017.06.009.

[317] K.M. Habib Al Razi, Resourceful recycling process of waste desktop computers: A review study, Resour. Conserv. Recycl. 110 (2016) 30–47. doi:10.1016/J.RESCONREC.2016.03.017.

[318] L.D. Poulikakos, C. Papadaskalopoulou, B. Hofko, F. Gschösser, A. Cannone Falchetto, M. Bueno, M. Arraigada, J. Sousa, R. Ruiz, C. Petit, M. Loizidou, M.N. Partl, Harvesting the unexplored potential of European waste materials for road construction, Resour. Conserv. Recycl. 116 (2017) 32–44. doi:10.1016/J.RESCONREC.2016.09.008.

[319] K. Wong, C. Rudd, S. Pickering, X. Liu, Composites recycling solutions for the aviation industry, Sci. China Technol. Sci. 60 (2017) 1291–1300. doi:10.1007/s11431-016-9028-7.

[320] P. Bradna, J. Zima, Compositional analysis of epoxy matrices of carbon-fibre composites by pyrolysis—gas chromatography/mass spectrometry, J. Anal. Appl. Pyrolysis. 24 (1992) 75–85. doi:10.1016/0165-2370(92)80006-8.

[321] D. Bücheler, A. Kaiser, F. Henning, Using Thermogravimetric Analysis to Determine Carbon Fiber Weight Percentage of Fiber-Reinforced Plastics, Compos. Part B Eng. 106 (2016) 218–223. doi:10.1016/J.COMPOSITESB.2016.09.028.

[322] K.-W. Kim, H.-M. Lee, J.-H. An, D.-C. Chung, K.-H. An, B.-J. Kim, Recycling and characterization of carbon fibers from carbon fiber reinforced epoxy matrix composites by a novel super-heated-steam method, J. Environ. Manage. 203 (2017) 872–879. doi:10.1016/J.JENVMAN.2017.05.015.

[323] E. Yildirir, N. Miskolczi, J.A. Onwudili, K.E. Németh, P.T. Williams, J. Sója, Evaluating the mechanical properties of reinforced LDPE composites made with carbon fibres recovered via solvothermal processing, Compos. Part B Eng. 78 (2015) 393–400. doi:10.1016/J.COMPOSITESB.2015.04.003.

[324] C. Song, F. Wang, Y. Liu, X. Wang, B. Yang, Recycling carbon fiber from composite waste and its reinforcing effect on polyvinylidene fluoride composite: Mechanical, morphology, and interface properties, Polym. Compos. 38 (2017) 2544–2552. doi:10.1002/pc.23845.

[325] M. Das, S. Varughese, A Novel Sonochemical Approach for Enhanced Recovery of Carbon Fiber from CFRP Waste Using Mild Acid–Peroxide Mixture, ACS Sustain. Chem. Eng. 4 (2016) 2080–2087. doi:10.1021/acssuschemeng.5b01497.

[326] G. Jiang, S.J. Pickering, G.S. Walker, K.H. Wong, C.D. Rudd, Surface characterisation of carbon fibre recycled using fluidised bed, Appl. Surf. Sci. 254 (2008) 2588–2593. doi:10.1016/j.apsusc.2007.09.105.

[327] G. Jiang, S.J. Pickering, Structure–property relationship of recycled carbon fibres revealed by pyrolysis recycling process, J. Mater. Sci. 51 (2016) 1949–1958. doi:10.1007/s10853-015-9502-2.

[328] J. Adhikari, B. Biswas, S. Chabri, N.R. Bandyapadhyay, P. Sawai, B.C. Mitra, A. Sinha, Effect of functionalized metal oxides addition on the mechanical, thermal and swelling behaviour of polyester/jute composites, Eng. Sci. Technol. an Int. J. 20 (2017) 760–774. doi:10.1016/j.jestch.2016.10.016.

[329] A. Agrawal, A. Satapathy, Experimental Investigation of Micro-sized Aluminium Oxide Reinforced Epoxy Composites for Microelectronic Applications, Procedia Mater. Sci. (2014). doi:10.1016/j.mspro.2014.07.295.

[330] K. Anane-Fenin, E.T. Akinlabi, N. Perry, Quantification of nanoparticle dispersion within polymer matrix using gap statistics, Mater. Res. Express. 6 (2019). doi:10.1088/2053-1591/ab1106.

[331] R. Tibshirani, G. Walther, T. Hastie, Estimating the number of clusters in a data set via the gap statistic, J. R. Stat. Soc. Ser. B (Statistical Methodol. 63 (2001) 411–423. doi:10.1111/1467-9868.00293.

[332] S.R. Nayak, J. Mishra, G. Palai, A modified approach to estimate fractal dimension of gray scale images, Optik (Stuttg). 161 (2018) 136–145. doi:10.1016/j.ijleo.2018.02.024.

[333] F. Moisy, Fractal dimension using the "box-counting" method for 1D, 2D and 3D sets, (2008). https://www.mathworks.com/matlabcentral/fileexchange/13063-boxcount?focused=5083247&tab=example (accessed September 30, 2018).

[334] J. Macqueen, Some methods for classification and analysis of multivariate observations, Proc. Fifth Berkeley Symp. Math. Stat. Probab. 1 (1967) 281–297. doi:citeulike-article-id:6083430.

[335] K. Anane-Fenin, E.T. Akinlabi, N. Perry, Optimization Methods for Minimizing Induced Stress During Tensile Testing of Prosthetic Composite Materials, in: 2019: pp. 180–206. doi:10.4018/978-1-5225-8235-9.ch008.

[336] MTS Systems Corporation, Series 647 hydraulic wedge grips reference manual, 2013.

[337] R.A. Wysk, B.W. Niebel, P.H. Cohen, T.W. Simpson, Taguchi's Robust Design Method, Manuf. Process. Integr. Prod. Process Des. (2000) 1–9.

[338] T. Kivak, G. Samtaş, A. Çiçek, Taguchi method based optimisation of drilling parameters in drilling of AISI 316 steel with PVD monolayer and multilayer coated HSS drills, Meas. J. Int. Meas. Confed. 45 (2012) 1547–1557. doi:10.1016/j.measurement.2012.02.022.

[339] K. Palanikumar, Experimental investigation and optimisation in drilling of GFRP composites, Meas. J. Int. Meas. Confed. 44 (2011) 2138–2148. doi:10.1016/j.measurement.2011.07.023.

[340] I. Asiltürk, H. Akkuş, Determining the effect of cutting parameters on surface roughness in hard turning using the Taguchi method, Meas. J. Int. Meas. Confed. 44 (2011) 1697–1704. doi:10.1016/j.measurement.2011.07.003.

[341] A. Gupta, H. Singh, A. Aggarwal, Taguchi-fuzzy multi output optimization (MOO) in high speed CNC turning of AISI P-20 tool steel, Expert Syst. Appl. 38 (2011) 6822–6828. doi:10.1016/j.eswa.2010.12.057.

[342] N. Mandal, B. Doloi, B. Mondal, R. Das, Optimization of flank wear using Zirconia Toughened Alumina (ZTA) cutting tool: Taguchi method and Regression analysis, Meas. J. Int. Meas. Confed. 44 (2011) 2149–2155. doi:10.1016/j.measurement.2011.07.022.

[343] G. Derringer, R. Suich, Simultaneous-Optimization of Several Response Variables, J. Qual. Technol. 12 (1980) 214–219. http://www.asq.org/data/subscriptions/jqt_open/1980/oct/jqtv12i4derringer.pdf.

[344] R.K. Bhushan, Multiresponse Optimization of Al Alloy-SiC Composite Machining Parameters for Minimum Tool Wear and Maximum Metal Removal Rate, J. Manuf. Sci. Eng. (2013). doi:10.1115/1.4023454.

[345] C. Kuo, Z. Li, C. Wang, Multi-objective optimisation in vibration-assisted drilling of CFRP/Al stacks, Compos. Struct. 173 (2017) 196–209. doi:10.1016/j.compstruct.2017.04.026.

[346] M. Balaji, K. Venkata Rao, N. Mohan Rao, B.S.N. Murthy, Optimization of drilling parameters for drilling of TI-6Al-4V based on surface roughness, flank wear and drill vibration, Meas. J. Int. Meas. Confed. 114 (2018) 332–339. doi:10.1016/j.measurement.2017.09.051.

[347] J.H. Holland, Adaptation in Natural and Artificial Systems, Ann Arbor MI Univ. Michigan Press. (1975). doi:10.1137/1018105.

[348] H. Abarghooei, H. Arabi, S.H. Seyedein, B. Mirzakhani, Modeling of steady state hot flow behavior of API-X70 microalloyed steel using genetic algorithm and design of experiments, Appl. Soft Comput. J. 52 (2017) 471–477. doi:10.1016/j.asoc.2016.10.021.

[349] S.N. Sivanandam, S.N. Deepa, Introduction to genetic algorithms, 2008. doi:10.1007/978-3-540-73190-0.

[350] M. Affenzeller, S. Winkler, S. Wagner, A. Beham, Genetic Algorithms and Genetic Programming, Simulation. 20093626 (2009). doi:10.1201/9781420011326.

[351] S. Sumathi, P. Surekha, Computational Intelligence Paradigms: Theory andApplications Using MATLAB, CRC Press, Taylor & Francis Group, 2016.

[352] R.L. Haupt, S.E. Haupt, Practical Genetic Algorithms, (2016).

[353] J. Li, The effect of surface modification with nitric acid on the mechanical and tribological properties of carbon fiber-reinforced thermoplastic polyimide composite, Surf. Interface Anal. 41 (2009) 759–763. doi:10.1002/sia.3089.

[354] ISO 179-1:2010 - Plastics -- Determination of Charpy impact properties -- Part 1: Non-instrumented impact test, (n.d.). https://www.iso.org/standard/44852.html (accessed July 23, 2019).

[355] ASTM, Ultimate analysis D3176 − 15, (n.d.). doi:10.1520/d3176-15.

[356] A.E. Vladár, Strategies for scanning electron microscopy sample preparation and characterization of multiwall carbon nanotube polymer composites, NIST Spec. Publ. 1200-17. 1 (2015) 1–16. doi:10.6028/NIST.SP.1200-17.

[357] C.D. Doyle, Estimating Thermal Stability of Experimental Polymers by Empirical Thermogravimetric Analysis, Anal. Chem. 33 (1961) 77–79. doi:10.1021/ac60169a022.

[358] S.M. Lee, Reference book for composites technology, Technomic Pub. Co, 1989.

[359] N. Iwashita, C.R. Park, H. Fujimoto, M. Shiraishi, M. Inagaki, Specification for a standard procedure of X-ray diffraction measurements on carbon materials, Carbon N. Y. 42 (2004) 701–714. doi:10.1016/j.carbon.2004.02.008.

[360] B. Sakintuna, Y. Yürüm, S. Çetinkaya, Evolution of carbon microstructures during the pyrolysis of Turkish Elbistan Lignite in the temperature range 700-1000°C, Energy and Fuels. 18 (2004) 883–888. doi:10.1021/ef0301809.

[361] J.-S. Roh, Structural Study of the Activated Carbon Fiber using Laser Raman Spectroscopy, Carbon Lett. 9 (2008) 127–130. doi:10.5714/CL.2008.9.2.127.

[362] L.J. Hardwick, H. Buqa, P. Novák, Graphite surface disorder detection using in situ Raman microscopy, Solid State Ionics. 177 (2006) 2801–2806. doi:10.1016/j.ssi.2006.03.032.

[363] M. Perraki, A. Proyer, E. Mposkos, R. Kaindl, G. Hoinkes, Raman micro-spectroscopy on diamond, graphite and other carbon polymorphs from the ultrahigh-pressure metamorphic Kimi Complex of the Rhodope Metamorphic Province, NE Greece, Earth Planet. Sci. Lett. 241 (2006) 672–685. doi:10.1016/j.epsl.2005.11.014.

[364] T. Hirai, J. Compan, K. Niwase, J. Linke, Laser Raman microprobe analysis of graphite exposed to edge plasma in the TEXTOR tokamak, J. Nucl. Mater. 373 (2008) 119–122. doi:10.1016/j.jnucmat.2007.05.040.

[365] P. Lespade, R. Al-Jishi, M.S. Dresselhaus, Model for Raman scattering from incompletely graphitized carbons, Carbon N. Y. 20 (1982) 427–431. doi:10.1016/0008-6223(82)90043-4.

[366] A. Kampouroglou, E.P. Sideridis, Influence of particle contiguity and interphase on the stiffness of particulate epoxy composites, Polym. Bull. 74 (2017) 4619–4644. doi:10.1007/s00289-017-1964-8.

[367] J. Lee, Fracture of glass bead/epoxy composites: on micro-mechanical deformations, Polymer (Guildf). 41 (2002) 8363–8373. doi:10.1016/s0032-3861(00)00187-7.

[368] H. Zhang, Z. Zhang, K. Friedrich, C. Eger, Property improvements of in situ epoxy nanocomposites with reduced interparticle distance at high nanosilica content, Acta Mater. 54 (2006) 1833–1842. doi:10.1016/j.actamat.2005.12.009.

[369] Z.P. Luo, J.H. Koo, Quantifying the dispersion of mixture microstructures, J. Microsc. 225 (2007) 118–125. doi:10.1111/j.1365-2818.2007.01722.x.

[370] B.M. Tyson, R.K. Abu Al-Rub, A. Yazdanbakhsh, Z. Grasley, A quantitative method for analyzing the dispersion and agglomeration of nano-particles in composite materials, Compos. Part B Eng. 42 (2011) 1395–1403. doi:10.1016/j.compositesb.2011.05.020.

[371] M.S. Goyat, P.K. Ghosh, Impact of ultrasonic assisted triangular lattice like arranged dispersion of nanoparticles on physical and mechanical properties of epoxy-TiO2 nanocomposites, Ultrason. Sonochem. 42 (2018) 141–154. doi:10.1016/j.ultsonch.2017.11.019.

[372] P.K. Ghosh, A. Pathak, M.S. Goyat, S. Halder, Influence of nanoparticle weight fraction on morphology and thermal properties of epoxy/TiO2 nanocomposite, J. Reinf. Plast. Compos. 31 (2012) 1180–1188. doi:10.1177/0731684412455955.

[373] R. Gupta, M. Agrawal, M. Prateek, A. Biswas, A. Hooda, M.S. Goyat, Synthesis of nano-textured polystyrene/ZnO coatings with excellent transparency and superhydrophobicity, Mater. Chem. Phys. 193 (2017) 447–452. doi:10.1016/j.matchemphys.2017.03.011.

[374] K. Anane-Fenin, E.T. Akinlabi, N. Perry, A Method for the Quantification of Nanoparticle Dispersion in Nanocomposites Based on Fractal Dimension, (2020) 555–564. doi:10.1007/978-981-13-8297-0_57.

[375] P.C. Ma, N.A. Siddiqui, G. Marom, J.K. Kim, Dispersion and functionalization of carbon nanotubes for polymer-based nanocomposites: A review, Compos. Part A Appl. Sci. Manuf. 41 (2010) 1345–1367. doi:10.1016/j.compositesa.2010.07.003.

[376] H.M. Naguib, M.A. Ahmed, Z.L. Abo-Shanab, Silane coupling agent for enhanced epoxy-iron oxide nanocomposite, J. Mater. Res. Technol. 7 (2018) 21–28. doi:10.1016/j.jmrt.2017.03.002.

[377] A.R.M. Dalod, L. Henriksen, T. Grande, M.-A. Einarsrud, Functionalized TiO 2 nanoparticles by single-step hydrothermal synthesis: the role of the silane coupling agents, Beilstein J. Nanotechnol. 8 (2017) 304–312. doi:10.3762/bjnano.8.33.

[378] K. Anane-Fenin, E.T. Akinlabi, N. Perry, A Numerical And Statistical Approach For Optimization Of Tab Design For Non-Crimp Fabric Composites, Procedia Manuf. 35 (2019) 820–825. doi:10.1016/j.promfg.2019.06.027.

[379] C.C. Chamis, J.H. Sinclair, Ten-deg Off-axis Test for Shear Properties in Fiber Composites, Exp. Mech. 17 (1977) 339–346. doi:10.1007/BF02326320.

[380] M.M. Tahir, W.-X. Wang, T. Matsubara, Y. Takao, H. Kushiku, New Design of End Tab for the Tensile Test of Unidirectional Composites, 17th US-Japan Conf. Compos. Mater. (2016) 1–2.

[381] H.M. Kwon, H.A. Jang, Case Studies on Strengths and Weaknesses of Taguchi Method, J. Korean Inst. Ind. Eng. 39 (2013) 383–392. doi:10.7232/jkiie.2013.39.5.383.

[382] D.H. Lee, I.J. Jeong, K.J. Kim, A desirability function method for optimizing mean and variability of multiple responses using a posterior preference articulation approach, Qual. Reliab. Eng. Int. 34 (2018) 360–376. doi:10.1002/qre.2258.

[383] A.D. Ali, I.M.M. El Emary, M.M. Abd El-Kareem, Application of Genetic Algorithm in Solving Linear Equation Systems, 2009. https://pdfs.semanticscholar.org/a62e/d1bea684947fce63f527d7b5388867022607.pdf (accessed July 9, 2019).

[384] ASTM, Standard Test Method for Determining the Charpy Impact Resistance of Notched Specimens of Plastics 1, 2018. doi:10.1520/D6110-18.

[385] S. Laurenzi, R. Pastore, G. Giannini, M. Marchetti, Experimental study of impact resistance in multi-walled carbon nanotube reinforced epoxy, Compos. Struct. 99 (2013) 62–68. doi:10.1016/j.compstruct.2012.12.002.

[386] M.R. Ayatollahi, S. Shadlou, M.M. Shokrieh, M. Chitsazzadeh, Effect of multi-walled carbon nanotube aspect ratio on mechanical and electrical properties of epoxy-based nanocomposites, Polym. Test. 30 (2011) 548–556. doi:10.1016/j.polymertesting.2011.04.008.

[387] K. Friedrich, S. Fakirov, Z. Zhang, Polymer composites : from nano-to-macro-scale, Springer, 2005.

[388] H.D. Wagner, O. Lourie, Y. Feldman, R. Tenne, Stress-induced fragmentation of multiwall carbon nanotubes in a polymer matrix, Appl. Phys. Lett. 72 (1998) 188–190. doi:10.1063/1.120680.

[389] A.C. Roulin-Moloney, Fractography and failure mechanisms of polymers and composites, Elsevier Applied Science, 1989. https://books.google.com.gh/books/about/Fractography_and_failure_mechanisms_of_p.html?id=EM9RAAAAMAAJ&redir_esc=y (accessed June 25, 2019).

[390] P. Carballeira, F. Haupert, Toughening effects of titanium dioxide nanoparticles on TiO 2 /epoxy resin nanocomposites, Polym. Compos. 31 (2010) 1241–1246. doi:10.1002/pc.20911.

[391] M.A. Caminero, G.P. Rodríguez, V. Muñoz, Effect of stacking sequence on Charpy impact and flexural damage behavior of composite laminates, Compos. Struct. 136 (2016) 345–357. doi:10.1016/j.compstruct.2015.10.019.

[392] A. Erkliğ, N.F. Doğan, M. Bulut, Charpy Impact Response of Glass Fiber Reinforced Composite with Nano Graphene Enhanced Epoxy, Period. Eng. Nat. Sci. 5 (2017) 341–346. doi:10.21533/pen.v5i3.121.

[393] K. Morioka, Y. Tomita, Effect of lay-up sequences on mechanical properties and fracture

behavior of CFRP laminate composites, Mater. Charact. 45 (2000) 125–136. doi:10.1016/S1044-5803(00)00065-6.

[394] S.W. Hong, S.S. Ahn, H. Li, J.K. Kim, S.J. Ko, J.M. Koo, C.S. Seok, Charpy impact fracture characteristics of CFRP composite materials according to variations of fiber array direction and temperature, Int. J. Precis. Eng. Manuf. 14 (2013) 253–258. doi:10.1007/s12541-013-0035-9.

[395] J.D. Fuller, M.R. Wisnom, Pseudo-ductility and damage suppression in thin ply CFRP angle-ply laminates, Compos. Part A Appl. Sci. Manuf. 69 (2015) 64–71. doi:10.1016/j.compositesa.2014.11.004.

[396] M. Jalalvand, G. Czél, M.R. Wisnom, Damage analysis of pseudo-ductile thin-ply UD hybrid composites - A new analytical method, Compos. Part A Appl. Sci. Manuf. 69 (2015) 83–93. doi:10.1016/j.compositesa.2014.11.006.

[397] Y. Tomita, K. Morioka, Effect of lay-up sequence on mechanical properties and fracture behaviour of advanced CFRP laminate composite, Mater. Sci. Eng. A. 234–236 (1997) 778–781. doi:10.1016/s0921-5093(97)00411-5.

[398] S.Y. Fu, B. Lauke, E. Mäder, X. Hu, C.Y. Yue, Fracture resistance of short-glass-fiber-reinforced and short-carbon-fiber-reinforced polypropylene under Charpy impact load and its dependence on processing, J. Mater. Process. Technol. 89–90 (1999) 501–507. doi:10.1016/S0924-0136(99)00065-5.

[399] R.K. Nayak, A. Dash, B.C. Ray, Effect of Epoxy Modifiers (Al2O3/SiO2/TiO2) on Mechanical Performance of epoxy/glass Fiber Hybrid Composites, Procedia Mater. Sci. 6 (2014) 1359–1364. doi:10.1016/j.mspro.2014.07.115.

[400] A. Chatterjee, M.S. Islam, Fabrication and characterization of TiO2-epoxy nanocomposite, Mater. Sci. Eng. A. 487 (2008) 574–585. doi:10.1016/j.msea.2007.11.052.

[401] J. Meredith, S. Cozien-Cazuc, E. Collings, S. Carter, S. Alsop, J. Lever, S.R. Coles, B.M. Wood, K. Kirwan, Recycled carbon fibre for high performance energy absorption, Compos. Sci. Technol. 72 (2012) 688–695. doi:10.1016/j.compscitech.2012.01.017.

[402] I.M.K. Ismail, Structure and active surface area of carbon fibers, Carbon N. Y. 25 (1987) 653–662. doi:10.1016/0008-6223(87)90219-3.

[403] X. Tan, Y. Liu, G. Zeng, X. Wang, X. Hu, Y. Gu, Z. Yang, Application of biochar for the removal of pollutants from aqueous solutions, Chemosphere. 125 (2015) 70–85. doi:10.1016/j.chemosphere.2014.12.058.

[404] X. Qian, L. Chen, J. Huang, W. Wang, J. Guan, Effect of carbon fiber surface chemistry on the interfacial properties of carbon fibers/epoxy resin composites, J. Reinf. Plast. Compos. 32 (2013) 393–401. doi:10.1177/0731684412468369.

[405] M. Sharma, S. Gao, E. Mäder, H. Sharma, L.Y. Wei, J. Bijwe, Carbon fiber surfaces and composite interphases, Compos. Sci. Technol. 102 (2014) 35–50. doi:10.1016/j.compscitech.2014.07.005.

[406] J. Jang, H. Yang, Effect of surface treatment on the performance improvement of carbon fiber/polybenzoxazine composites, J. Mater. Sci. 35 (2000) 2297–2303. doi:10.1023/A:1004791313979.

[407] S. Tiwari, J. Bijwe, Surface Treatment of Carbon Fibers - A Review, Procedia Technol. 14 (2014) 505–512. doi:10.1016/j.protcy.2014.08.064.

[408] S.J. Park, B.J. Kim, Roles of acidic functional groups of carbon fiber surfaces in enhancing interfacial adhesion behavior, Mater. Sci. Eng. A. 408 (2005) 269–273. doi:10.1016/j.msea.2005.08.129.

[409] M.C. Paiva, C.A. Bernardo, M. Nardin, Mechanical, surface and interfacial characterization of pitch and PAN-based carbon fibres, Carbon N. Y. 38 (2000) 1323–1337. doi:10.1016/S0008-6223(99)00266-3.

[410] N. Dilsiz, N.K. Erinç, E. Bayramli, G. Akovali, Surface energy and mechanical properties of plasma-modified carbon fibers, Carbon N. Y. 33 (1995) 853–858. doi:10.1016/0008-6223(94)00181-X.

[411] Y. Luo, Y. Zhao, Y. Duan, S. Du, Surface and wettability property analysis of CCF300 carbon fibers with different sizing or without sizing, Mater. Des. 32 (2011) 941–946. doi:10.1016/j.matdes.2010.08.004.

[412] M.K. Almutairi, R.A. Felemban, S.E. Pasha, The Effect of Different Surface Treatments of Carbon Fibers and Their Impact on Composites, Egypt. J. Hosp. Med. 70 (2018) 1275–1281. doi:10.12816/0044635.

[413] B. Lindsay, M.-L. Abel, J.F. Watts, A study of electrochemically treated PAN based carbon fibres by IGC and XPS, Carbon N. Y. 45 (2007) 2433–2444. doi:10.1016/J.CARBON.2007.04.017.

[414] C.L. Weitzsacker, P.M.A. Sherwood, X-ray photoelectron spectroscopic studies of carbon-fiber surfaces. 19. Surface chemical changes during electrochemical oxidation in base, Surf. Interface Anal. 23 (1995) 551–558. doi:10.1002/sia.740230715.

[415] P. Denison, F.R. Jones, J.F. Watts, X-ray photoelectron spectroscopic analysis of barium-labelled carbon fibre surfaces, J. Mater. Sci. 20 (1985) 4647–4656. doi:10.1007/BF00559354.

[416] G. Pavoski, T. Maraschin, F. de C. Fim, N.M. Balzaretti, G.B. Galland, C.S. Moura, N.R. de S. Basso, Few Layer Reduced Graphene Oxide: Evaluation of the Best Experimental Conditions for Easy Production, Mater. Res. 20 (2016) 53–61. doi:10.1590/1980-5373-mr-2015-0528.

[417] M.A. Amaral Junior, J.T. Matsushima, M.C. Rezende, E.S. Gonçalves, J.S. Marcuzzo, M.R. Baldan, Production and Characterization of Activated Carbon Fiber from Textile PAN Fiber, J. Aerosp. Technol. Manag. 9 (2017) 423–430. doi:10.5028/jatm.v9i4.831.

[418] A. Oberlin, M. Villey, A. Combaz, Influence of elemental composition on carbonization. Pyrolysis of kerosene shale and kuckersite, Carbon N. Y. 18 (1980) 347–353. doi:10.1016/0008-6223(80)90006-8.

[419] B.E. Warren, X-ray diffraction in random layer lattices, Phys. Rev. 59 (1941) 693–698. doi:10.1103/PhysRev.59.693.

[420] T.F. Yen, J.G. Erdman, S.S. Pollack, Investigation of the Structure of Petroleum Asphaltenes by X-Ray Diffraction, Anal. Chem. 33 (1961) 1587–1594. doi:10.1021/ac60179a039.

[421] F.R. Ludwig Schoening, X-ray structure of some South African coals before and after heat treatment at 500 and 1000° C, Fuel. 62 (1983) 1315–1320. doi:10.1016/S0016-2361(83)80016-7.

[422] A. Sharma, T. Kyotani, A. Tomita, Comparison of structural parameters of PF carbon from XRD and HRTEM techniques, Carbon N. Y. 38 (2000) 1977–1984. doi:10.1016/S0008-6223(00)00045-2.

[423] A.K. Kercher, D.C. Nagle, Microstructural evolution during charcoal carbonization by X-ray

diffraction analysis, Carbon N. Y. 41 (2003) 15–27. doi:10.1016/S0008-6223(02)00261-0.

[424] J.-S. Roh, Oxidation Kinetics of Carbon Fibers, Carbon Sci. 6 (2005) 1–5. http://citeseerx.ist.psu.edu/viewdoc/download?doi=10.1.1.888.5267&rep=rep1&type=pdf (accessed May 28, 2019).

[425] B.S. Girgis, Y.M. Temerk, M.M. Gadelrab, I.D. Abdullah, X-ray Diffraction Patterns of Activated Carbons Prepared under Various Conditions, Carbon Lett. 8 (2012) 95–100. doi:10.5714/cl.2007.8.2.095.

[426] A. Sadezky, H. Muckenhuber, H. Grothe, R. Niessner, U. Pöschl, Raman microspectroscopy of soot and related carbonaceous materials: Spectral analysis and structural information, Carbon N. Y. 43 (2005) 1731–1742. doi:10.1016/j.carbon.2005.02.018.

[427] A.C. Ferrari, Raman spectroscopy of graphene and graphite: Disorder, electron-phonon coupling, doping and nonadiabatic effects, Solid State Commun. 143 (2007) 47–57. doi:10.1016/j.ssc.2007.03.052.

[428] F. Vautard, S. Ozcan, F. Paulauskas, J.E. Spruiell, H. Meyer, M.J. Lance, Influence of the carbon fiber surface microstructure on the surface chemistry generated by a thermo-chemical surface treatment, Appl. Surf. Sci. 261 (2012) 473–480. doi:10.1016/j.apsusc.2012.08.038.

[429] Y. Kawashima, G. Katagiri, Fundamentals, overtones, and combinations in the Raman spectrum of graphite, Phys. Rev. B. 52 (1995) 10053–10059. doi:10.1103/PhysRevB.52.10053.

[430] M.S. Dresselhaus, A. Jorio, M. Hofmann, G. Dresselhaus, R. Saito, Perspectives on carbon nanotubes and graphene Raman spectroscopy, Nano Lett. 10 (2010) 751–758. doi:10.1021/nl904286r.

[431] C. Beny-Bassez, J.-N. Rouzaud, Characterization of carbonaceous materials by correlated electron and optical microscopy and raman microspectroscopy, Scan. Electron Microsc. 1 (1985) 119–132. https://eurekamag.com/research/018/541/018541432.php (accessed May 28, 2019).

[432] C. Thomsen, S. Reich, Raman Scattering in Carbon Nanotubes, n.d.

[433] O. Beyssac, B. Goffé, J.P. Petitet, E. Froigneux, M. Moreau, J.N. Rouzaud, On the characterization of disordered and heterogeneous carbonaceous materials by Raman spectroscopy, in: Spectrochim. Acta - Part A Mol. Biomol. Spectrosc., Elsevier, 2003: pp. 2267–2276. doi:10.1016/S1386-1425(03)00070-2.

[434] M.A. Montes-Morán, F.W.J. van Hattum, J.P. Nunes, A. Martínez-Alonso, J.M.D. Tascón, C.A. Bernardo, A study of the effect of plasma treatment on the interfacial properties of carbon fibre–thermoplastic composites, Carbon N. Y. 43 (2005) 1795–1799. doi:10.1016/J.CARBON.2005.02.005.

APPENDIX

A1 – Gap statistics and Data Extraction

Gap Statistics

```
close all;
clear all;
clc;
warning off
%% Gap Statistics
load Sample_2a_1000x
x=(Sample_2a_1000x);
rng('default'); % For reproducibility
eva = evalclusters(x,'kmeans','gap','KList',[1:8])
%% Plot the gap criterion values for each number of clusters tested.
figure,
plot(eva)
%%
figure,
plot(eva.InspectedK,eva.ExpectedLogW,'m+-',eva.InspectedK,eva.LogW,'ro-')
xlabel('Number of clusters')
ylabel('obs and exp log(Wk)')
legend('exp log(Wk)','obs')
```

Data Extraction

```
%% Data Extraction from Observed and Expected curves from Gap statistics
clear all;
close all;
clc;
h=openfig('Sample_2c_160x');
h=findobj(gca,'Type','line');
x=get(h,'Xdata');
y=get(h,'Ydata');
```

A2 – Particle Size Dispersity and Particle Spacing Dispersity

```
close all;
clear all;
clc;
warning off
UniDisp=rgb2gray(imread('Sample_2a_1000x.jpg'));
figure, imshow(UniDisp);
[pixelCount, grayLevels] = imhist(UniDisp);
bar(grayLevels, pixelCount)
graph=bar(grayLevels, pixelCount);
%%
imData=reshape(UniDisp,[],1); % Conversion into an array
imData=double(imData); % Conversion from unit8 to double
[IDX nn]=kmeans(imData,4); %Perform kmean with 4 clusters
imIDX=reshape(IDX, size(UniDisp)); % (256*256) matrix of indexes
%%
figure,
imshow(imIDX,[]),title('index image');
%%
figure,
subplot(3,2,1),imshow(imIDX==1,[]);
subplot(3,2,2),imshow(imIDX==2,[]);
subplot(3,2,3),imshow(imIDX==3,[]);
subplot(3,2,4),imshow(imIDX==4,[]);
%%
bw=(imIDX==2);
se=ones(2);
bw=imopen(bw,se);
bw=bwareaopen(bw,10);
figure,imshow(bw);

%%
% Count particles and label them
[L Ne]=bwlabel(bw);
imshow(label2rgb(L));
% Find the properties of the image
prop=regionprops(L);
% feature extraction - size distribution (area, pixels)
stats = regionprops(L);
A = [stats.Area]; % Calculates individual particle sizes
%%

boundaries = bwboundaries(bw);
numberOfBoundaries = size(boundaries, 1);
for k = 1 : numberOfBoundaries
 thisBoundary = boundaries{k};
 plot(thisBoundary(:,2), thisBoundary(:,1), 'r', 'LineWidth', 3);
end
hold off;

% Define object boundaries
numberOfBoundaries = size(boundaries, 1)
% message = sprintf('Found %d boundaries', numberOfBoundaries);
% uiwait(helpdlg(message));
```

```
% Find minimum distance between each pair of boundaries
for b1 = 1 : numberOfBoundaries
 for b2 = 1 : numberOfBoundaries
  if b1 == b2
   % Can't find distance between the region and itself
   continue;
  end
  boundary1 = boundaries{b1};
  boundary2 = boundaries{b2};
  boundary1x = boundary1(:, 2);
  boundary1y = boundary1(:, 1);
  x1=1;
  y1=1;
  x2=1;
  y2=1;
  overallMinDistance = inf; % Initialize.
  % For every point in boundary 2, find the distance to every point in boundary 1.
  for k = 1 : size(boundary2, 1)
   % Pick the next point on boundary 2.
   boundary2x = boundary2(k, 2);
   boundary2y = boundary2(k, 1);
   % For this point, compute distances from it to all points in boundary 1.
   allDistances = sqrt((boundary1x - boundary2x).^2 + (boundary1y - boundary2y).^2);
   % Find closest point, min distance.
   [minDistance(k), indexOfMin] = min(allDistances);
   if minDistance(k) < overallMinDistance
    x1 = boundary1x(indexOfMin);
    y1 = boundary1y(indexOfMin);
    x2 = boundary2x;
    y2 = boundary2y;
    overallMinDistance = minDistance(k);
   end
  end
  % Find the overall min distance
  minDistance = min(minDistance);
  % Report to command window.
  fprintf('The minimum distance from region %d to region %d is %.3f pixels\n', b1, b2, minDistance);

  % Draw a line between point 1 and 2
  line([x1, x2], [y1, y2], 'Color', 'y', 'LineWidth', 3);
 end
end
```

A3 – Fractal Dimension

FRACTAL DIMENSION

```
close all;
clear all;
clc;
warning off
UniDisp=rgb2gray(imread('2-4.jpg'));
figure, imshow(UniDisp);
%%
imData=reshape(UniDisp,[],1); % Conversion into an array
imData=double(imData); % Conversion from unit8 to double
[IDX nn]=kmeans(imData,2); %Perform kmean with 4 clusters
imIDX=reshape(IDX, size(UniDisp)); % (256*256) matrix of indexes
%%
figure,
imshow(imIDX,[]),title('index image');
%%
figure,
subplot(3,2,1),imshow(imIDX==1,[]);
subplot(3,2,2),imshow(imIDX==2,[]);
subplot(3,2,3),imshow(imIDX==3,[]);
subplot(3,2,4),imshow(imIDX==4,[]);
%%
bw=(imIDX==1);
se=ones(1);
bw=imopen(bw,se);
bw=bwareaopen(bw,10);
figure,imshow(bw);
%% Fractal Dimension
axis square
figure
boxcount(bw)
figure
[n,r]=boxcount(bw,'slope');
df = -diff(log(n))./diff(log(r));
disp(['Fractal dimension, Df = ' num2str(mean(df(4:8))) ' +/- ' num2str(std(df(4:8)))]);


function [n,r] = boxcount(c,varargin)
%BOXCOUNT Box-Counting of a D-dimensional array (with D=1,2,3).
% [N, R] = BOXCOUNT(C), where C is a D-dimensional array (with D=1,2,3),
% counts the number N of D-dimensional boxes of size R needed to cover
% the nonzero elements of C. The box sizes are powers of two, i.e.,
% R = 1, 2, 4 ... 2^P, where P is the smallest integer such that
% MAX(SIZE(C)) <= 2^P. If the sizes of C over each dimension are smaller
% than 2^P, C is padded with zeros to size 2^P over each dimension (e.g.,
% a 320-by-200 image is padded to 512-by-512). The output vectors N and R
% are of size P+1. For a RGB color image (m-by-n-by-3 array), a summation
% over the 3 RGB planes is done first.
%
% The Box-counting method is useful to determine fractal properties of a
% 1D segment, a 2D image or a 3D array. If C is a fractal set, with
% fractal dimension DF < D, then N scales as R^(-DF). DF is known as the
```

```
% Minkowski-Bouligand dimension, or Kolmogorov capacity, or Kolmogorov
% dimension, or simply box-counting dimension.
%
% BOXCOUNT(C,'plot') also shows the log-log plot of N as a function of R
% (if no output argument, this option is selected by default).
%
% BOXCOUNT(C,'slope') also shows the semi-log plot of the local slope
% DF = - dlnN/dlnR as a function of R. If DF is contant in a certain
% range of R, then DF is the fractal dimension of the set C. The
% derivative is computed as a 2nd order finite difference (see GRADIENT).
%
% The execution time depends on the sizes of C. It is fastest for powers
% of two over each dimension.
%
% Examples:
%
%  % Plots the box-count of a vector containing randomly-distributed
%  % 0 and 1. This set is not fractal: one has N = R^-2 at large R,
%  % and N = cste at small R.
%  c = (rand(1,2048)<0.2);
%  boxcount(c);
%
%  % Plots the box-count and the fractal dimension of a 2D fractal set
%  % of size 512^2 (obtained by RANDCANTOR), with fractal dimension
%  % DF = 2 + log(P) / log(2) = 1.68 (with P=0.8).
%  c = randcantor(0.8, 512, 2);
%  boxcount(c);
%  figure, boxcount(c, 'slope');
%
% F. Moisy
% Revision: 2.10, Date: 2008/07/09


% History:
% 2006/11/22: v2.00, joined into a single file boxcountn (n=1,2,3).
% 2008/07/09: v2.10, minor improvements

% control input argument
error(nargchk(1,2,nargin));

% check for true color image (m-by-n-by-3 array)
if ndims(c)==3
 if size(c,3)==3 && size(c,1)>=8 && size(c,2)>=8
  c = sum(c,3);
 end
end

warning off
c = logical(squeeze(c));
warning on

dim = ndims(c); % dim is 2 for a vector or a matrix, 3 for a cube
if dim>3
 error('Maximum dimension is 3.');
end
```

```
% transpose the vector to a 1-by-n vector
if length(c)==numel(c)
 dim=1;
 if size(c,1)~=1
  c = c';
 end
end

width = max(size(c)); % largest size of the box
p = log(width)/log(2); % nbre of generations

% remap the array if the sizes are not all equal,
% or if they are not power of two
% (this slows down the computation!)
if p~=round(p) || any(size(c)~=width)
 p = ceil(p);
 width = 2^p;
 switch dim
  case 1
   mz = zeros(1,width);
   mz(1:length(c)) = c;
   c = mz;
  case 2
   mz = zeros(width, width);
   mz(1:size(c,1), 1:size(c,2)) = c;
   c = mz;
  case 3
   mz = zeros(width, width, width);
   mz(1:size(c,1), 1:size(c,2), 1:size(c,3)) = c;
   c = mz;
 end
end

n=zeros(1,p+1); % pre-allocate the number of box of size r

switch dim

 case 1  %------------------- 1D boxcount ----------------------%

  n(p+1) = sum(c);
  for g=(p-1):-1:0
   siz = 2^(p-g);
   siz2 = round(siz/2);
   for i=1:siz:(width-siz+1)
    c(i) = ( c(i) || c(i+siz2));
   end
   n(g+1) = sum(c(1:siz:(width-siz+1)));
  end

 case 2   %------------------- 2D boxcount ----------------------%

  n(p+1) = sum(c(:));
  for g=(p-1):-1:0
   siz = 2^(p-g);
```

```
  siz2 = round(siz/2);
  for i=1:siz:(width-siz+1)
   for j=1:siz:(width-siz+1)
    c(i,j) = ( c(i,j) || c(i+siz2,j) || c(i,j+siz2) || c(i+siz2,j+siz2) );
   end
  end
  n(g+1) = sum(sum(c(1:siz:(width-siz+1),1:siz:(width-siz+1))));
 end

 case 3   %------------------- 3D boxcount ---------------------%

  n(p+1) = sum(c(:));
  for g=(p-1):-1:0
   siz = 2^(p-g);
   siz2 = round(siz/2);
   for i=1:siz:(width-siz+1),
    for j=1:siz:(width-siz+1),
     for k=1:siz:(width-siz+1),
      c(i,j,k)=( c(i,j,k) || c(i+siz2,j,k) || c(i,j+siz2,k) ...
       || c(i+siz2,j+siz2,k) || c(i,j,k+siz2) || c(i+siz2,j,k+siz2) ...
       || c(i,j+siz2,k+siz2) || c(i+siz2,j+siz2,k+siz2));
     end
    end
   end
   n(g+1) = sum(sum(sum(c(1:siz:(width-siz+1),1:siz:(width-siz+1),1:siz:(width-siz+1)))));
  end

end
n = n(end:-1:1);
r = 2.^(0:p); % box size (1, 2, 4, 8...)

if any(strncmpi(varargin,'slope',1))
 s=-gradient(log(n))./gradient(log(r));
 semilogx(r, s, 's-');
 ylim([0 dim]);
 xlabel('r, box size'); ylabel('- d ln n / d ln r, local dimension');
 title([num2str(dim) 'D box-count']);
elseif nargout==0 || any(strncmpi(varargin,'plot',1))
 loglog(r,n,'s-');
 xlabel('r, box size'); ylabel('n(r), number of boxes');
 title([num2str(dim) 'D box-count']);
end
if nargout==0
 clear r n
end
```

A4 – Image segmentation and Centroid location

```
close all;

clear all;

clc;

warning off

UniDisp=rgb2gray(imread('UniformDispCon.jpg'));

figure, imshow(UniDisp);

% Fliping of Image

flippedImage = flipud(UniDisp);

figure, imshow(flippedImage);

 %%

imData=reshape(UniDisp,[],1); % Conversion into an array

imData=double(imData); % Conversion from unit8 to double

[IDX nn]=kmeans(imData,4); %Perform kmean with 4 clusters

imIDX=reshape(IDX, size(UniDisp)); % (256*256) matrix of indexes

%%

figure,

imshow(imIDX,[]),title('index image');

%%

figure,

subplot(3,2,1),imshow(imIDX==1,[]);

subplot(3,2,2),imshow(imIDX==2,[]);
```

```
subplot(3,2,3),imshow(imIDX==3,[]);

subplot(3,2,4),imshow(imIDX==4,[]);

%%

bw=(imIDX==2);

se=ones(2);

bw=imopen(bw,se);

bw=bwareaopen(bw,10);

figure,imshow(bw);

%% Agglomeration Quantity (Aq)

Agglomeration = sum(bw(:)) / numel(bw);

numWhitePixels = nnz(bw); % Sum of non-zero pixels.

 %% Introduction of bounding box to locate centroids

figure,

flippedImage = flipud(bw);

 % Count particles and label them

[L Ne]=bwlabel(flippedImage);

imshow(label2rgb(L));

 % Find the properties of the image

prop=regionprops(L);

 % Rectangular bounding boxes to locate centroids

hold on
```

```
for n=1:length(prop)
 rectangle('Position',prop(n).BoundingBox,'EdgeColor','g','LineWidth',2)
 x=prop(n).Centroid(1);
 y=prop(n).Centroid(2);
 plot(x,y,'*')
end

hold off

%% New Centroid Location to factor in the influence of particle size variation
% Count elements and label them
figure,
[L Ne]=bwlabel(bw);
prop=regionprops(L,'Centroid');
allCentroids = [prop.Centroid];
xCentroids = allCentroids(1:2:end);
yCentroids = allCentroids(2:2:end);
scatter(xCentroids,yCentroids)
CentroidLocation=[xCentroids,yCentroids];
%% feature extraction - size distribution (area, pixels)
stats = regionprops(L);
```

```
A = [stats.Area]; % Calculates individual particle sizes

histfit(A)

 %% New Centroid Location

figure,

xCentroidsTransposed=xCentroids.';

yCentroidsTransposed=yCentroids.';

ATransposed=A.';

CentroidLocation=[xCentroidsTransposed,yCentroidsTransposed];

TransformedCentroid=(ATransposed.*CentroidLocation);

scatter(TransformedCentroid(:,1),TransformedCentroid(:,2))
```

A5 – Elemental Ananlysis Results

	Sample name	Filename	Inj Date	Inj Time	Type	Weight	Protein Facto	None	AS	Vial	Nitrogen%	Carbon%	Hydrogen%
80	k4	k4	12/12/2018	10:08	UNK	1.82	6.25	1			2.987189054	86.69689178	0
81	k1	k1	12/12/2018	10:29	UNK	1.77	6.25	1			3.208420038	79.41575623	0
82	k1	k1	12/12/2018	10:29	UNK	1.76	6.25	1			3.226649761	79.86698151	0
83	k7	k7	12/12/2018	10:59	UNK	1.8	6.25	1			2.537498236	82.07402039	0
84	k7	k7	12/12/2018	10:59	UNK	1.79	6.25	1			2.551674128	82.53253174	0
85	k5	k5	12/12/2018	11:20	UNK	1.78	6.25	1			4.33513689	96.24344635	0
86	k5	k5	12/12/2018	11:20	UNK	1.83	6.25	1			4.21669054	93.6138382	0
87	k2	k2	12/12/2018	11:33	UNK	1.82	6.25	1			2.500644684	79.18656158	0
88	k3	k3	12/12/2018	11:46	UNK	1.8	6.25	1			4.317390442	92.24117279	0
89	k6	k6	12/12/2018	12:07	UNK	1.83	6.25	1			4.436201096	91.80215454	0
90	k6	k6	12/12/2018	12:07	UNK	1.79	6.25	1			4.53533411	93.85359955	0
91	k9	k9	12/12/2018	12:36	UNK	1.82	6.25	1			4.267593861	94.41551208	0
92	k9	k9	12/12/2018	12:36	UNK	1.84	6.25	1			4.221207142	93.38925934	0
93	k11	k11	12/12/2018	12:57	UNK	1.83	6.25	1			4.330005169	96.71881104	0
94	k11	k11	12/12/2018	12:57	UNK	1.85	6.25	1			4.283194065	95.67320251	0
95	k8	k8	12/12/2018	13:17	UNK	1.82	6.25	1			3.315102816	90.66680908	0
96	k8	k8	12/12/2018	13:17	UNK	1.8	6.25	1			3.351937532	91.67422485	0
97	k10	k10	12/12/2018	13:38	UNK	1.77	6.25	1			4.667655468	93.47024536	0
98	k10	k10	12/12/2018	13:38	UNK	1.81	6.25	1			4.564503193	91.40460968	0

	Sulphur%
80	0
81	1.116807342
82	1.123152852
83	1.418008566
84	1.425930381
85	1.205462456
86	1.17252636
87	1.533843637
88	0
89	0
90	0
91	0
92	0
93	0
94	0
95	0
96	0
97	1.813358665
98	1.773284554

A6 – Test Equipment and Test Samples

Instron impact testing machine

KB-45 Band Saw

Thermolyne Thermo Scientific Furnace for Post oxidation

A7 – Waterjet Test Samples

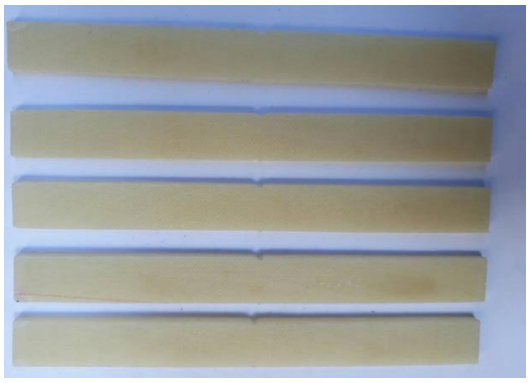

STN

TN

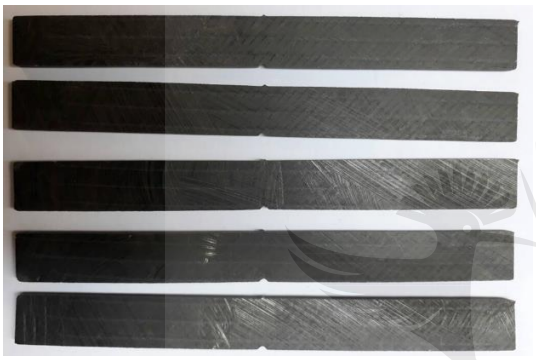

CF-TN

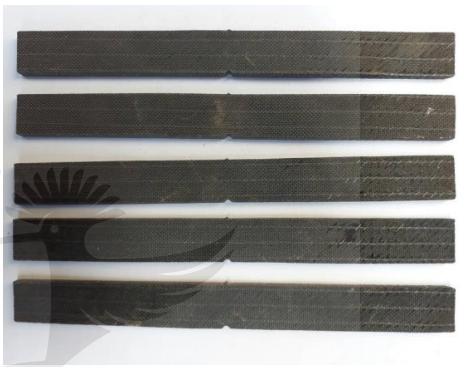

CF-STN